UTPP-50

Measurement of the Cross Section for Charmed Meson Production Associated with a Prompt Photon in 1.8-TeV Proton-Antiproton Collisions

Ryutaro OISHI

A dissertation submitted to the Doctoral Program
in Physics, the University of Tsukuba,
in partial fulfillment of the requirements
for the degree of Doctor of Philosophy (Science)
January 1995

Measurement of the Cross Section for Charmed Meson Production Associated with a Prompt Photon in 1.8-TeV Proton-Antiproton Collisions

Ryutaro OISHI

A dissertation submitted to the Doctoral Program
in Physics, the University of Tsukuba,
in partial fulfillment of the requirements
for the degree of Doctor of Philosophy (Science)
January 1995

Abstract

We measured the cross section for $D^{*\pm}$ meson production associated with a prompt photon in proton-antiproton collisions at a center of mass energy of 1800 GeV.

Charm quark production in proton is poorly known experimentally nowadays. The production of a $D^{*\pm}$ meson associated with a prompt photon can probe a component of the charm quark in proton. In other words, the cross section provides information of charm quark density in proton.

The data were recorded during 1992 and 1993 with the Collider Detector at Fermilab (CDF) detector. The inclusive photon events used in this thesis were collected by a photon trigger with a transverse energy threshold of 16 GeV. The isolated photon candidates were selected using electromagnetic shower profile information.

In the inclusive photon events, we reconstructed $D^{*\pm}$ meson through sequential decays of $D^{*+} \rightarrow D^0(\rightarrow K^-\pi^+$ and $K^-\pi^-\pi^+\pi^+)\pi^+$ and their charge conjugate decays. Clear $D^{*\pm}$ signal peaks were observed in the distributions of the mass difference $\Delta M \equiv M(D^0\pi^\pm) - M(D^0)$ at 145.5 MeV/c^2. The ΔM distributions were fitted to a signal plus a background function. We obtained the fitted mass difference of 145.5 $\pm$ 0.2 MeV/c^2 and 145.4 $\pm$ 0.2 MeV/c^2 in the $D^{*\pm}$ reconstructions using $D^0 \rightarrow K^-\pi^+$ and $D^0 \rightarrow K^-\pi^-\pi^+\pi^+$, respectively. The observed mass differences are consistent with the world average value of 145.52$\pm$0.05 MeV/c^2 within the statistical errors.

The photon candidates contain roughly 50 % signal of prompt photons and 50 % of backgrounds. The background sources against prompt

photons are multi-photons from neutral meson decays. A goodness of fitting, χ^2, which is calculated from a shower profile in the strip chamber, was used to subtract the photon background events statistically. After the photon background subtraction, there are 42 ± 10 and 75 ± 17 events in the $D^{*\pm}$ signal window ($144 < \Delta M < 147$ MeV/c^2) with the reconstructions using $D^0 \rightarrow K^-\pi^+$ and $D^0 \rightarrow K^-\pi^-\pi^+\pi^+$, respectively.

The background source against the $D^{*\pm}$ mesons is a combinatorial background, which comes from random track combinations. The number of the combinatorial background events below the $D^{*\pm}$ signal peak was estimated from a fake $D^{*\pm}$ ΔM distribution. Subtracting the combinatorial background events, we found (30 ± 10) $\gamma + D^{*\pm}$ events in the $D^{*\pm} \rightarrow K^{\mp}\pi^{\pm}\pi^{\pm}$ channel and (32 ± 16) $\gamma + D^{*\pm}$ events in the $D^{*\pm} \rightarrow K^{\mp}\pi^{\mp}\pi^{\pm}\pi^{\pm}\pi^{\pm}$ channel.

The reconstruction efficiencies of $\gamma + D^{*\pm}$ events were estimated using real data and Monte Carlo data. They were 0.120 ± 0.024 and 0.067 ± 0.011 for the reconstructions using $D^0 \rightarrow K^-\pi^+$ and $D^0 \rightarrow K^-\pi^-\pi^+\pi^+$, respectively.

The systematic uncertainty was evaluated using Monte Carlo data and real data. The percent systematic uncertainty was estimated to be $^{+14\%}_{-16\%}$ in our measured cross section.

We calculated the cross section in a kinematical range of 16 GeV/c < $p_{\mathrm{T}}(\gamma) < 40$ GeV/c, $|y(\gamma)| < 0.9$, $p_{\mathrm{T}}(D^{*\pm}) > 6$ GeV/c, and $|y(D^{*\pm})| < 1.2$, where p_{T} and y are the transverse momentum and the rapidity, respectively. The cross section was measured to be 0.48 ± 0.15 (stat.) $^{+0.07}_{-0.08}$ (syst.) nb, where the first and the second errors show the statistical and systematic ones, respectively.

The contamination in $\gamma + D^{*\pm}$ events from non-prompt charm quark production was estimated using a PYTHIA Monte Carlo data sample and a real dijet data sample. The charm quark production from gluon-splitting and bottom quark decay processes was considered. From the PYTHIA Monte Carlo events, the fractions of the gluon splitting and the b quark decay processes were estimated to be 7 % and 3 % in the observed $\gamma+ D^{*\pm}$ events, respectively. The contamination from the gluon splitting was estimated to be 12±4 % using the real dijet events.

The measured cross section was compared to the theoretical predictions calculated with PYTHIA and parton distribution functions. The leading order cross sections are 0.21 nb and 0.18 nb with the CTEQ2M and MRSD_' parton distribution functions, respectively, where the renormalization scale is defined to be a photon transverse momentum.

The measured cross section is 1.5 standard deviation higher than the theoretical leading order calculation.

Acknowledgements

I would like to thank my advisor, Professor Kunitaka Kondo, for his support throughout my thesis work. He provided me the opportunity to join the CDF experiment and support in working on CDF.

I am grateful to Brenna Flaugher, Stephen Kuhlmann, Robert Blair, and Robert Harris for providing the guidance and supports.

I would like to thank Koji Takikawa, Shigeyuki Miyashita, and Shinhong Kim for their supports and discussions on the analysis.

Discussions on physics with Itsuo Nakano, Yoshihiro Seiya, and Mikio Takano were very beneficial for me.

The work in this thesis has been made by the efforts and achievements of the CDF collaborators, the Fermilab Accelerator Division, and the CDF technical staff.

This work was supported by the U.S. Department of Energy and National Science Foundation; the Italian Istituto Nazionale di Fisica Nucleare; the Ministry of Education, Science and Culture of Japan; the Natural Sciences and Engineering Research Council of Canada; the National Science Council of the Republic of China; the A. P. Sloan Foundation; and the Alexander von Humboldt-Stiftung.

Contents

List of Tables

List of Figures

The CDF Collaboration

F. Abe,[13] M. G. Albrow,[7] D. Amidei,[16] J. Antos,[28] C. Anway-Wiese,[4]
G. Apollinari,[26] H. Areti,[7] P. Auchincloss,[25] F. Azfar,[21] P. Azzi,[20]
N. Bacchetta,[18] W. Badgett,[16] M. W. Bailey,[18] J. Bao,[34] P. de Barbaro,[25]
A. Barbaro-Galtieri,[14] V. E. Barnes,[24] B. A. Barnett,[12] P. Bartalini,[23]
G. Bauer,[15] T. Baumann,[9] F. Bedeschi,[23] S. Behrends,[3] S. Belforte,[23]
G. Bellettini,[23] J. Bellinger,[33] D. Benjamin,[32] J. Benlloch,[15] J. Bensinger,[3]
D. Benton,[21] A. Beretvas,[7] J. P. Berge,[7] S. Bertolucci,[8] A. Bhatti,[26]
K. Biery,[11] M. Binkley,[7] F. Bird,[29] D. Bisello,[20] R. E. Blair,[1] C. Blocker,[29]
A. Bodek,[25] V. Bolognesi,[23] D. Bortoletto,[24] C. Boswell,[12] T. Boulos,[14]
G. Brandenburg,[9] E. Buckley-Geer,[7] H. S. Budd,[25] K. Burkett,[16] G. Busetto,[20]
A. Byon-Wagner,[7] K. L. Byrum,[1] J. Cammerata,[12] C. Campagnari,[7]
M. Campbell,[16] A. Caner,[7] W. Carithers,[14] D. Carlsmith,[33] A. Castro,[20]
Y. Cen,[21] F. Cervelli,[23] J. Chapman,[16] M.-T. Cheng,[28] G. Chiarelli,[8]
T. Chikamatsu,[31] S. Cihangir,[7] A. G. Clark,[23] M. Cobal,[23] M. Contreras,[5]
J. Conway,[27] J. Cooper,[7] M. Cordelli,[8] D. Crane,[7] J. D. Cunningham,[3]
T. Daniels,[15] F. DeJongh,[7] S. Delchamps,[7] S. Dell'Agnello,[23] M. Dell'Orso,[23]
L. Demortier,[26] B. Denby,[23] M. Deninno,[2] P. F. Derwent,[16] T. Devlin,[27]
M. Dickson,[25] S. Donati,[23] R. B. Drucker,[14] A. Dunn,[16] K. Einsweiler,[14]
J. E. Elias,[7] R. Ely,[14] E. Engels, Jr.,[22] S. Eno,[5] D. Errede,[10] S. Errede,[10]
Q. Fan,[25] B. Farhat,[15] I. Fiori,[2] B. Flaugher,[7] G. W. Foster,[7] M. Franklin,[9]
M. Frautschi,[18] J. Freeman,[7] J. Friedman,[15] H. Frisch,[5] A. Fry,[29] T. A. Fuess,[1]
Y. Fukui,[13] S. Funaki,[31] G. Gagliardi,[23] S. Galeotti,[23] M. Gallinaro,[20]
A. F. Garfinkel,[24] S. Geer,[7] D. W. Gerdes,[16] P. Giannetti,[23] N. Giokaris,[26]
P. Giromini,[8] L. Gladney,[21] D. Glenzinski,[12] M. Gold,[18] J. Gonzalez,[21]
A. Gordon,[9] A. T. Goshaw,[6] K. Goulianos,[26] H. Grassmann,[6] A. Grewal,[21]
G. Grieco,[23] L. Groer,[27] C. Grosso-Pilcher,[5] C. Haber,[14] S. R. Hahn,[7]

R. Hamilton,[9] R. Handler,[33] R. M. Hans,[34] K. Hara,[31] B. Harral,[21] R. M. Harris,[7] S. A. Hauger,[6] J. Hauser,[4] C. Hawk,[27] J. Heinrich,[21] D. Cronin-Hennessy,[6] R. Hollebeek,[21] L. Holloway,[10] A. Hölscher,[11] S. Hong,[16] G. Houk,[21] P. Hu,[22] B. T. Huffman,[22] R. Hughes,[25] P. Hurst,[9] J. Huston,[17] J. Huth,[9] J. Hylen,[7] M. Incagli,[23] J. Incandela,[7] H. Iso,[31] H. Jensen,[7] C. P. Jessop,[9] U. Joshi,[7] R. W. Kadel,[14] E. Kajfasz,[7a] T. Kamon,[30] T. Kaneko,[31] D. A. Kardelis,[10] H. Kasha,[34] Y. Kato,[19] L. Keeble,[30] R. D. Kennedy,[27] R. Kephart,[7] P. Kesten,[14] D. Kestenbaum,[9] R. M. Keup,[10] H. Keutelian,[7] F. Keyvan,[4] D. H. Kim,[7] H. S. Kim,[11] S. B. Kim,[16] S. H. Kim,[31] Y. K. Kim,[14] L. Kirsch,[3] P. Koehn,[25] K. Kondo,[31] J. Konigsberg,[9] S. Kopp,[5] K. Kordas,[11] W. Koska,[7] E. Kovacs,[7a] W. Kowald,[6] M. Krasberg,[16] J. Kroll,[7] M. Kruse,[24] S. E. Kuhlmann,[1] E. Kuns,[27] A. T. Laasanen,[24] S. Lammel,[4] J. I. Lamoureux,[3] T. LeCompte,[10] S. Leone,[23] J. D. Lewis,[7] P. Limon,[7] M. Lindgren,[4] T. M. Liss,[10] N. Lockyer,[21] O. Long,[21] M. Loreti,[20] E. H. Low,[21] J. Lu,[30] D. Lucchesi,[23] C. B. Luchini,[10] P. Lukens,[7] P. Maas,[33] K. Maeshima,[7] A. Maghakian,[26] P. Maksimovic,[15] M. Mangano,[23] J. Mansour,[17] M. Mariotti,[23] J. P. Marriner,[7] A. Martin,[10] J. A. J. Matthews,[18] R. Mattingly,[15] P. McIntyre,[30] P. Melese,[26] A. Menzione,[23] E. Meschi,[23] G. Michail,[9] S. Mikamo,[13] M. Miller,[5] R. Miller,[17] T. Mimashi,[31] S. Miscetti,[8] M. Mishina,[13] H. Mitsushio,[31] S. Miyashita,[31] Y. Morita,[13] S. Moulding,[26] J. Mueller,[27] A. Mukherjee,[7] T. Muller,[4] P. Musgrave,[11] L. F. Nakae,[29] I. Nakano,[31] C. Nelson,[7] D. Neuberger,[4] C. Newman-Holmes,[7] L. Nodulman,[1] S. Ogawa,[31] S. H. Oh,[6] K. E. Ohl,[34] R. Oishi,[31] T. Okusawa,[19] C. Pagliarone,[23] R. Paoletti,[23] V. Papadimitriou,[7] S. Park,[7] J. Patrick,[7] G. Pauletta,[23] M. Paulini,[14] L. Pescara,[20] M. D. Peters,[14] T. J. Phillips,[6] G. Piacentino,[2] M. Pillai,[25] R. Plunkett,[7] L. Pondrom,[33] N. Produit,[14] J. Proudfoot,[1] F. Ptohos,[9] G. Punzi,[23] K. Ragan,[11] F. Rimondi,[2] L. Ristori,[23] M. Roach-Bellino,[32] W. J. Robertson,[6] T. Rodrigo,[7]

J. Romano,[5] L. Rosenson,[15] W. K. Sakumoto,[25] D. Saltzberg,[5] A. Sansoni,[8] V. Scarpine,[30] A. Schindler,[14] P. Schlabach,[9] E. E. Schmidt,[7] M. P. Schmidt,[34] O. Schneider,[14] G. F. Sciacca,[23] A. Scribano,[23] S. Segler,[7] S. Seidel,[18] Y. Seiya,[31] G. Sganos,[11] A. Sgolacchia,[2] M. Shapiro,[14] N. M. Shaw,[24] Q. Shen,[24] P. F. Shepard,[22] M. Shimojima,[31] M. Shochet,[5] J. Siegrist,[29] A. Sill,[7a] P. Sinervo,[11] P. Singh,[22] J. Skarha,[12] K. Sliwa,[32] D. A. Smith,[23] F. D. Snider,[12] L. Song,[7] T. Song,[16] J. Spalding,[7] L. Spiegel,[7] P. Sphicas,[15] A. Spies,[12] L. Stanco,[20] J. Steele,[33] A. Stefanini,[23] K. Strahl,[11] J. Strait,[7] D. Stuart,[7] G. Sullivan,[5] K. Sumorok,[15] R. L. Swartz, Jr.,[10] T. Takahashi,[19] K. Takikawa,[31] F. Tartarelli,[23] W. Taylor,[11] Y. Teramoto,[19] S. Tether,[15] D. Theriot,[7] J. Thomas,[29] T. L. Thomas,[18] R. Thun,[16] M. Timko,[32] P. Tipton,[25] A. Titov,[26] S. Tkaczyk,[7] K. Tollefson,[25] A. Tollestrup,[7] J. Tonnison,[24] J. F. de Troconiz,[9] J. Tseng,[12] M. Turcotte,[29] N. Turini,[2] N. Uemura,[31] F. Ukegawa,[21] G. Unal,[21] S. van den Brink,[22] S. Vejcik, III,[16] R. Vidal,[7] M. Vondracek,[10] R. G. Wagner,[1] R. L. Wagner,[7] N. Wainer,[7] R. C. Walker,[25] G. Wang,[23] J. Wang,[5] M. J. Wang,[28] Q. F. Wang,[26] A. Warburton,[11] G. Watts,[25] T. Watts,[27] R. Webb,[30] C. Wendt,[33] H. Wenzel,[14] W. C. Wester, III,[14] T. Westhusing,[10] A. B. Wicklund,[1] E. Wicklund,[7] R. Wilkinson,[21] H. H. Williams,[21] P. Wilson,[5] B. L. Winer,[25] J. Wolinski,[30] D. Y. Wu,[16] X. Wu,[23] J. Wyss,[20] A. Yagil,[7] W. Yao,[14] K. Yasuoka,[31] Y. Ye,[11] G. P. Yeh,[7] P. Yeh,[28] M. Yin,[6] J. Yoh,[7] T. Yoshida,[19] D. Yovanovitch,[7] I. Yu,[34] J. C. Yun,[7] A. Zanetti,[23] F. Zetti,[23] L. Zhang,[33] S. Zhang,[15] W. Zhang,[21] and S. Zucchelli[2]

(CDF Collaboration)

[1] *Argonne National Laboratory, Argonne, Illinois 60439*

[2] *Istituto Nazionale di Fisica Nucleare, University of Bologna, I-40126 Bologna, Italy*

[3] *Brandeis University, Waltham, Massachusetts 02254*

[4] *University of California at Los Angeles, Los Angeles, California 90024*

[5] *University of Chicago, Chicago, Illinois 60637*

[6] *Duke University, Durham, North Carolina 27708*

[7] *Fermi National Accelerator Laboratory, Batavia, Illinois 60510*

[8] *Laboratori Nazionali di Frascati, Istituto Nazionale di Fisica Nucleare, I-00044 Frascati, Italy*

[9] *Harvard University, Cambridge, Massachusetts 02138*

[10] *University of Illinois, Urbana, Illinois 61801*

[11] *Institute of Particle Physics, McGill University, Montreal H3A 2T8, and University of Toronto,*

Toronto M5S 1A7, Canada

[12] *The Johns Hopkins University, Baltimore, Maryland 21218*

[13] *National Laboratory for High Energy Physics (KEK), Tsukuba, Ibaraki 305, Japan*

[14] *Lawrence Berkeley Laboratory, Berkeley, California 94720*

[15] *Massachusetts Institute of Technology, Cambridge, Massachusetts 02139*

[16] *University of Michigan, Ann Arbor, Michigan 48109*

[17] *Michigan State University, East Lansing, Michigan 48824*

[18] *University of New Mexico, Albuquerque, New Mexico 87131*

[19] *Osaka City University, Osaka 588, Japan*

[20] *Universita di Padova, Instituto Nazionale di Fisica Nucleare, Sezione di Padova, I-35131*

Padova, Italy

[21] *University of Pennsylvania, Philadelphia, Pennsylvania 19104*

[22] *University of Pittsburgh, Pittsburgh, Pennsylvania 15260*

[23] *Istituto Nazionale di Fisica Nucleare, University and Scuola Normale Superiore of Pisa,*

I-56100 Pisa, Italy

[24] *Purdue University, West Lafayette, Indiana 47907*

[25] *University of Rochester, Rochester, New York 14627*

[26] *Rockefeller University, New York, New York 10021*

[27] *Rutgers University, Piscataway, New Jersey 08854*

[28] *Academia Sinica, Taiwan 11529, Republic of China*

[29] *Superconducting Super Collider Laboratory, Dallas, Texas 75237*
[30] *Texas A&M University, College Station, Texas 77843*
[31] *University of Tsukuba, Tsukuba, Ibaraki 305, Japan*
[32] *Tufts University, Medford, Massachusetts 02155*
[33] *University of Wisconsin, Madison, Wisconsin 53706*
[34] *Yale University, New Haven, Connecticut 06511*

Chapter 1

Introduction

The Standard Model has successfully described many phenomena in high energy particle physics. Quantum Chromodynamics (QCD) is a theory of interactions of quarks and gluons in the Standard Model. In the theoretical frame, physics processes of lepton-hadron and hadron-hadron interactions are formulated by perturbative QCD. The cross section of the processes can be factorized into "elementary process" involving lepton-parton or parton-parton scattering and parton momentum distributions in hadrons. The calculation of the cross section is carried out by convoluting the elementary cross section with the parton distribution functions. The parton distribution functions have mainly been determined from deep inelastic lepton scattering experiments. The NMC collaboration [1] and the CCFR collaboration [2] have accurately measured proton and deuteron structure functions with high statistics to explore inside proton in the range down to $x = 0.006$, where x is a momentum fraction of a parton in proton. The electron-proton collision data at HERA are available from the H1 [3] and the ZEUS [4] collaborations to provide knowledge of parton distribution down to $x = 10^{-4}$ at high Q^2. The accurate measurement of the parton distributions helps a precious test of the Standard Models, because one of the dominant systematic uncertainties comes from knowledge of the parton distribution functions. Recently, the flavor asymmetry of the sea quark distributions in nucleon has been reported by the NMC collaboration [5]. The CTEQ collaboration [6] and CCFR collaboration [7] have independently determined the strange quark distribution function inside nucleon. The flavor dependence of the sea quark distributions has been addressed in global parton distribution analysis. Heavy quark components of distribution functions are important in higher energy collisions to provide predictions of many processes. For example, the charm quark component becomes to be about 18 % of the total quark momenta at a future Large Hadron Collider (LHC).

The charm quark production associated with a prompt photon (γ+c production) can directly probe charm quark inside proton at $\sqrt{s} = 1800$ GeV in proton-antiproton collisions. The Feynman diagrams of the γ+c productions are illustrated in Fig. 1.1. The dominant process is called "Compton" process which is shown in Fig. 1.1-(a). The other sources are called "gluon splitting" and "bottom quark decay" as shown in the Figs. 1.1 (b) and (c), respectively. Events containing a photon and a charm quark in the final state are expected to be produced by a charm quark and a gluon in proton or antiproton, because the Compton process is dominant. The cross section for γ+c production is related with the charm density in proton. The charm quark can be identified by reconstructing a $D^{*\pm}$ meson. The measurement of the cross section for $\gamma + D^{*\pm}$ production can provide a constraint to the charm quark distri-

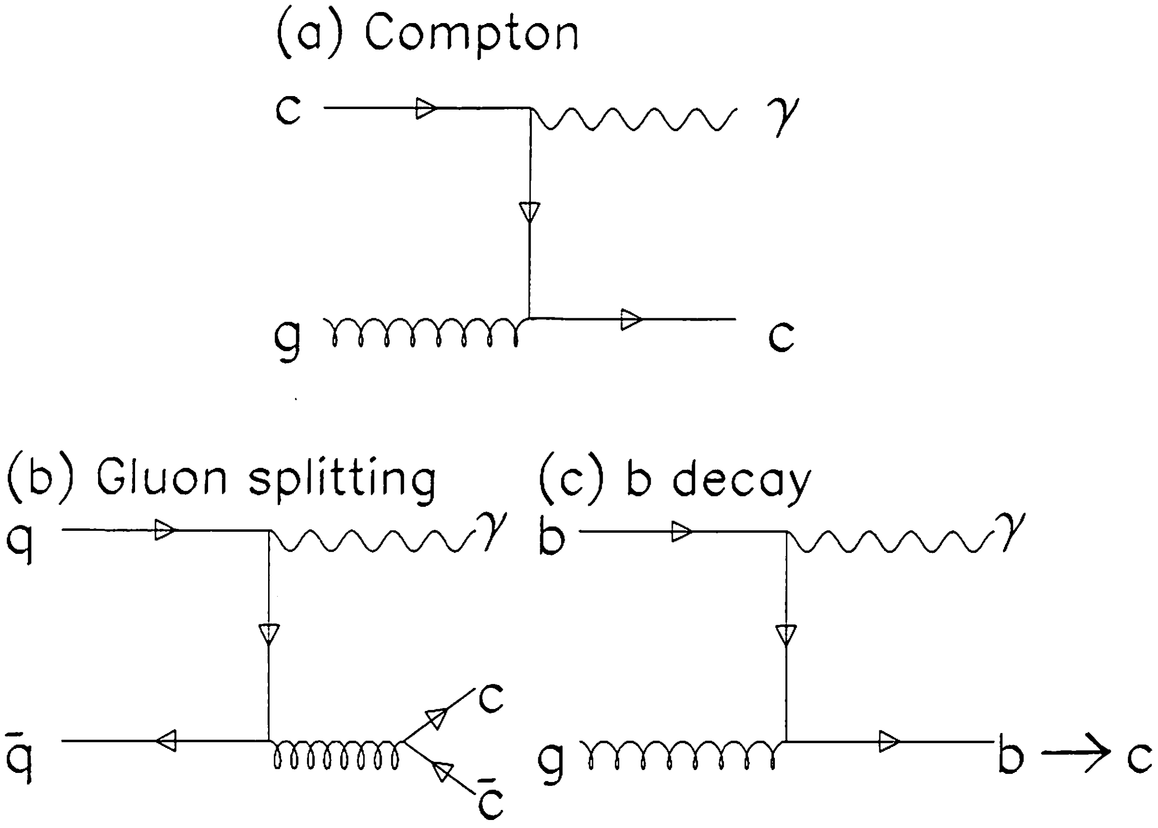

Figure 1.1: Feynman diagrams of the γ+c productions. (a) the Compton process, (b) gluon splitting process, and (c) b-quark decay process.

bution function.

In chapter 2, the CDF detector is described briefly. A photon detection method and a $D^{*\pm}$ reconstruction method are described in chapters 3 and 4, respectively. Extraction of the signal events including a prompt photon and a $D^{*\pm}$ is carried out in chapter 5. The cross section for $\gamma+D^{*\pm}$ production is obtained in chapter 6. The systematic uncertainty in the cross section is evaluated in chapter 7. The contaminations from the gluon splitting and the b-quark decay processes in the $\gamma+D^{*\pm}$ production are discussed in chapter 8. The measured cross section is compared to the theoretical predictions using the PYTHIA Monte Carlo program and the parton distribution functions in chapter 9. Finally, we conclude in chapter 10.

Chapter 2

The CDF Detector

2.1 CDF detector overview

The CDF detector is located at the B0 collision hall in the Fermi National Accelerator Laboratory in the United States of America, in order to detect particles produced by $\bar{p}p$ collisions using the TEVATRON accelerator. The CDF detector can be separated into three parts, which are called "Central," "Plug," and "Forward." The central detector is mainly used in this analysis. Our coordinate system is taken in such a way that the z axis is the proton beam direction, θ and φ are a polar and an azimuthal angles. The central detector covers the pseudorapidity range from -1.2 to 1.2, where the pseudorapidity is defined by $\eta \equiv -\ln\tan(\theta/2)$. The central detector consists of the silicon vertex detector (SVX), the vertex time projection chamber (VTX), the central tracking chamber (CTC), the central preradiator (CPR), the central electromagnetic calorimeter (CEM), and the central hadronic calorimeter (CHA), surrounding the beam pipe symmetrically in azimuth. A solenoidal superconducting magnet is embedded between the CTC and the CEM, producing uniform magnetic field of 1.4 T in the CTC, the VTX, and the SVX, to measure momenta of charged particles. The CEM includes a strip chamber (CES) to determine positions of EM cascade shower precisely.

The construction of the CDF detector was completed in 1987. The VTX was updated, the SVX and the CPR were newly installed in 1992. The cross-sectional view of the CDF central detector is shown in Fig. 2.1. In this chapter, several features of the components which are relevant to the present analysis are briefly described. More detailed descriptions are available in references [8], [9], [10], [11], and [12] for the CTC, the SVX, the VTX, the CEM and CES, and the CHA, respectively. An overall description is given in Ref. [13].

2.2 Tracking detectors

The tracking devices of the SVX, the VTX, and the CTC provide momentum and position information of charged particles produced by $\bar{p}p$ collisions. The CTC globally measures charged particle momenta in large volume. The SVX precisely measures positions of charged particles, and detects secondary vertex positions in the plane perpendicular to the proton beam line. It provides a transverse decay length measurement with an accuracy of about 10 μm. The VTX is used to determine a z-coordinate of a $\bar{p}p$ collision point.

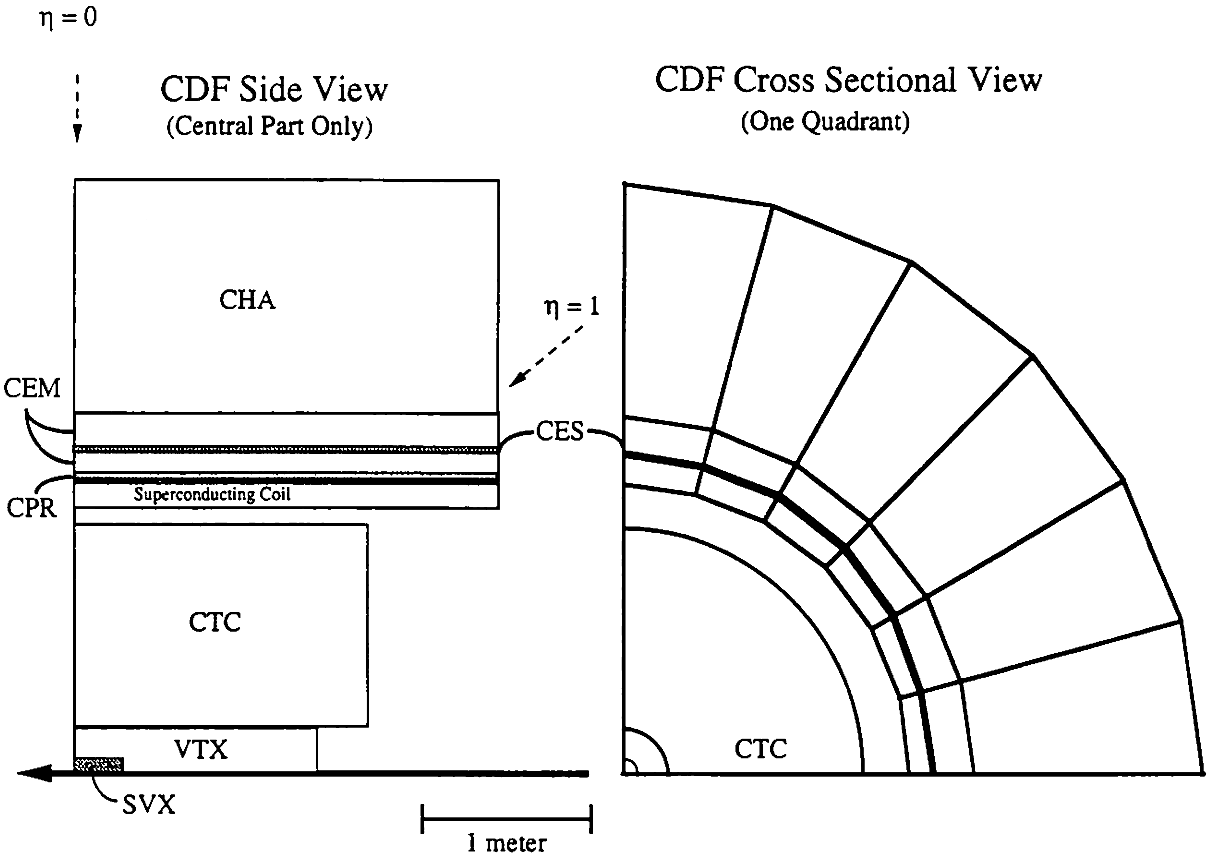

Figure 2.1: Cross-sectional views of the CDF central detector.

2.2.1 SVX

The SVX detector consists of two barrel modules. Each module covers the $|z|$ range between 0 cm and 51 cm, contacting with each other at $z = 0$. The active SVX region covers 60 % of the $\bar{p}p$ collisions for a bunch length of 30 cm. Each barrel consists of four concentric cylindrical layers of DC-coupled silicon microstrips. The innermost layer is placed at a radius of 3.005 cm, middle two layers are located at 4.256 cm and 5.687 cm, and the outermost layer is located at 7.866 cm from the proton beam line. The silicon microstrips are 8.5 cm long and 300 μm thick with a strip pitch of 60 μm for the inner three layers, and 55 μm for the fourth layer. The charge distributions from hits on each layer provide positions of a charged track in the R-φ plane perpendicular to the proton beam line. A z-position of charged particles is estimated by an extrapolation from the external tracking (CTC) measurement. The spatial resolution in the R-φ plane is about 13 μm at a track transverse momentum of 3.5 GeV/c.

2.2.2 VTX

The VTX provides a $\bar{p}p$ collision point in z coordinate along the proton beam line. The VTX system consists of 28 modules of time projection chambers. The VTX, whose length is 2.8 m along the proton beam line, can well cover $\bar{p}p$ collisions. The active area in the R-φ plane extends from 6.8 cm to 21 cm in radius R. The position resolution of an event z-vertex is about 3 mm.

2.2.3 CTC

The CTC is a large multiwire drift chamber in a high magnetic field of 14 kG. It consists of 84 layers of sense wires. The 84 layers are grouped into 9 "superlayers," which are divided into 5 axial superlayers and 4 stereo superlayers. The wires in the stereo superlayers have a stereo angle of 3 degrees with respect to the beam direction in order to supply z-coordinate information. The position resolution in z-direction is about 3 mm. Axial wire hits provide the information for pattern recognition in the R-φ plane. The intrinsic position resolution of a single hit wire is about 200 μm, which provides a momentum resolution of

$$\frac{\delta p_{\mathrm{T}}}{p_{\mathrm{T}}} \sim 0.002 \times p_{\mathrm{T}},$$

where p_{T} is a transverse momentum of a charged particle in units of GeV/c.

2.2.4 Momentum scale

The momentum scale of charged particles was verified using $J/\Psi \rightarrow \mu^+\mu^-$ and $\Upsilon \rightarrow \mu^+\mu^-$ data by comparing the measured masses with their world average masses. The J/Ψ and Υ events were taken by dimuon triggers. Figure 2.2 shows the dimuon mass distributions. The significant peaks of J/Ψ, Υ(1S), Υ(2S), and Υ(3S) are clearly observed in the mass distributions. The distributions were fitted with a gaussian plus a quadratic background functions. The fitted masses and their world average masses [18] are listed in Table 2.1, where the errors of the CDF measured masses are the statistical ones.

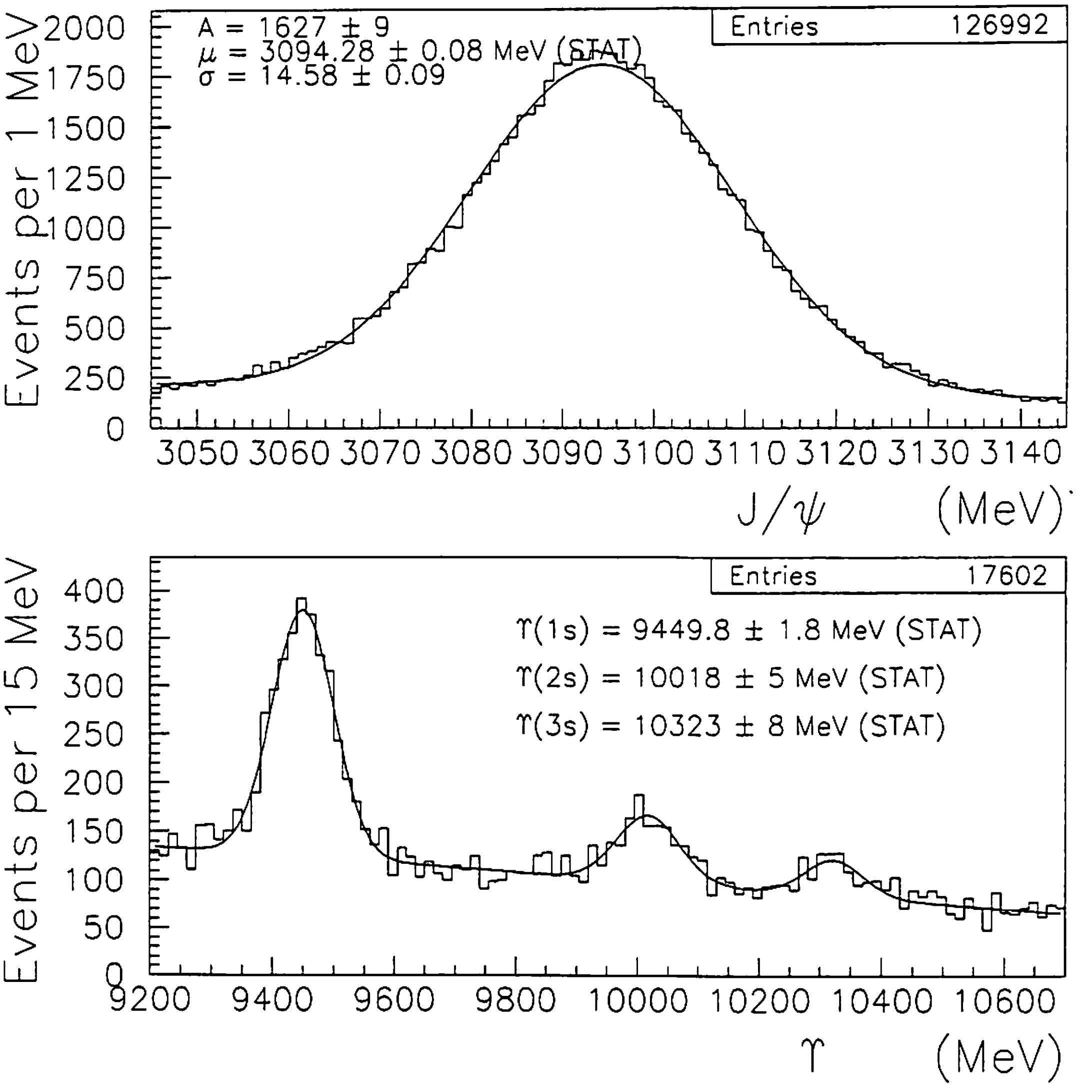

Figure 2.2: Dimuon mass distributions.

Table 2.1: Observed masses of J/Ψ and Υ's, and their world average masses.

	CDF measurement (MeV/c^2)	World average (MeV/c^2)
J/Ψ	3094.6 ± 0.08	3096.93 ± 0.09
Υ(1S)	9449.8 ± 1.8	9460.3 ± 0.2
Υ(2S)	10018 ± 5	10023.3 ± 0.3
Υ(3S)	10323 ± 8	10355.3 ± 0.5

2.3 Calorimetry

The calorimetry devices provide energy and position information of showers originating from electron, photon, and hadron in materials. The CEM is used to measure the energy in the electromagnetic shower component, the CHA is used for the hadronic shower. The CES is used to measure positions of the electromagnetic shower precisely.

2.3.1 CEM

The CEM is a lead-scintillator-type calorimeter with wavelength shifter for light correction, and consists of 48 "wedge" modules. The modules are located outside of the solenoidal magnet surrounding it cylindrically. A ring is constructed by 24 wedge modules. Two rings are contacted with each other at z=0. Each module has 10 towers. The towers are pointing to a center of the CDF detector on the proton beam line. The sizes of the tower are 0.1 in η and 15° in φ. The energy resolution of the

CEM was obtained from the electron test beam data as follows:

$$\frac{\sigma(E_{\rm T})}{E_{\rm T}} = \frac{0.135}{\sqrt{E_{\rm T}}},$$

where $E_{\rm T}$ is the transverse energy in GeV, which is defined by $E_{\rm T} = E\sin\theta$ using the energy (E) and polar angle (θ). Figure 2.3 shows a CEM "wedge" module.

2.3.2 CES

The CES detector precisely measures positions of EM shower at shower maximum (~ 6 radiation lengths) using the charge depositions in orthogonal strip and wire views. The CES is a multi-wire gas proportional chamber with anode wires along the beam direction and cathode strips perpendicular to the wires. That is imbedded into each CEM wedge module. The length of the CES in z-direction is 184 cm. The numbers of the channels are 64 wire channels and 128 strip channels. Figure 2.4 shows a schematic view of the CES.

2.3.3 CEM energy scale

The CEM energy scale was calibrated using the test beam electrons and the $W \to e\nu$ decay electrons. The test beam electrons were mainly used to determine a response map in the CEM towers. The electrons from $W \to e\nu$ decays were used for the tower-by-tower relative responses. Figure 2.5 shows an E/p distribution in the $W \to e\nu$ events, where E is the energy measured with the CEM, and p is the momentum measured with the CTC.

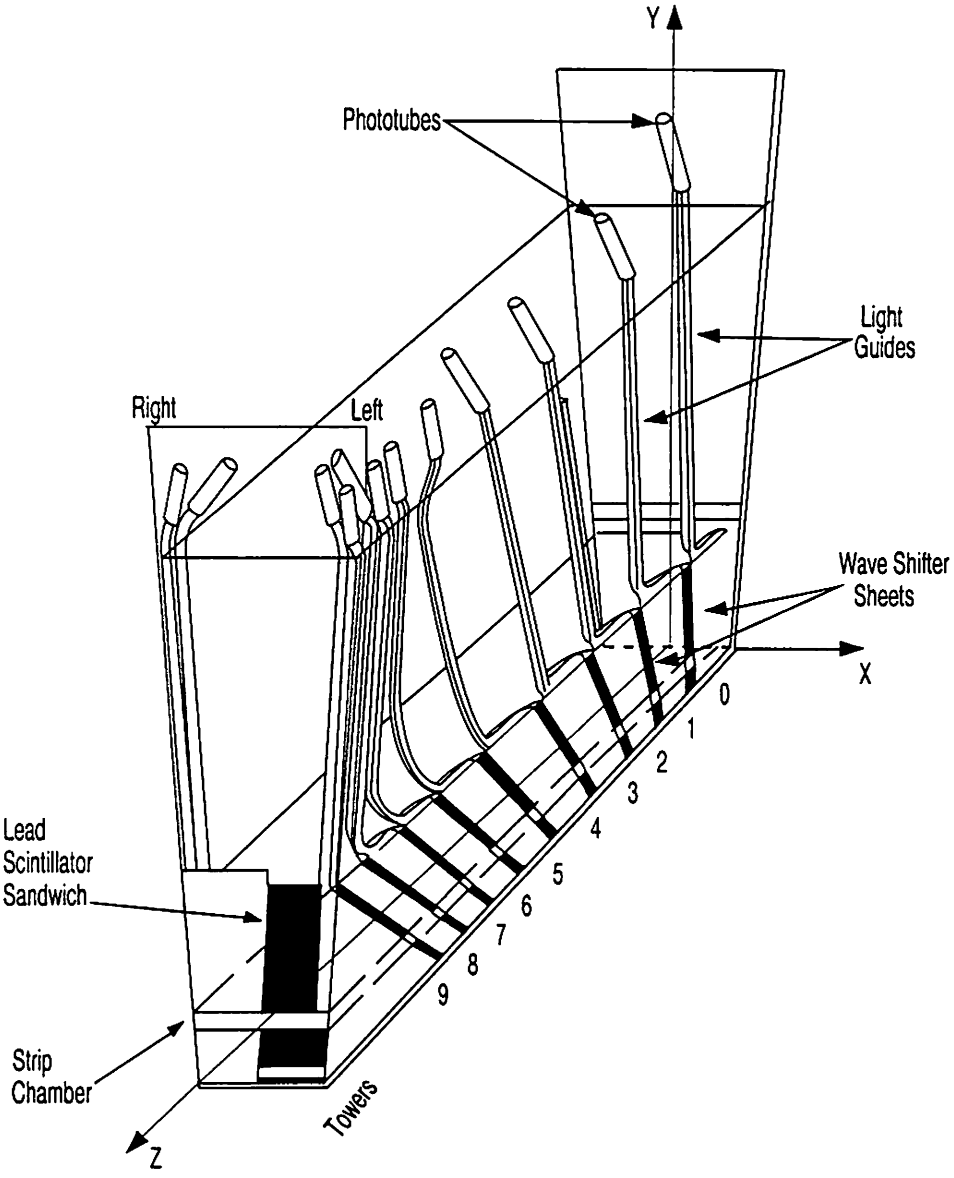

Figure 2.3: Schematics view of a CEM wedge module.

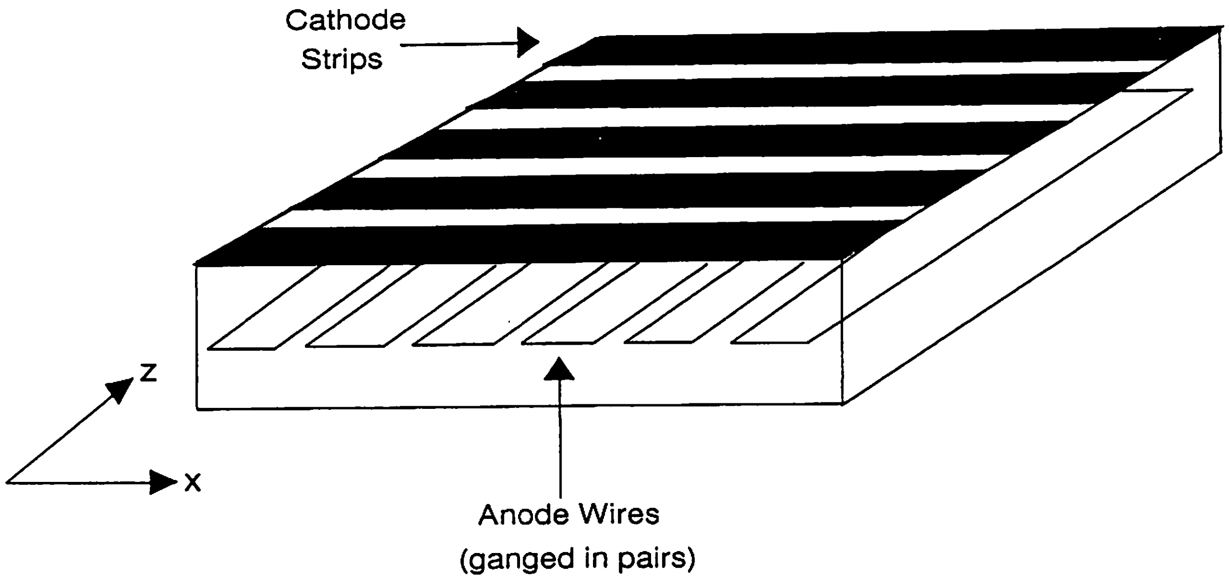

Figure 2.4: Schematic view of a CES detector.

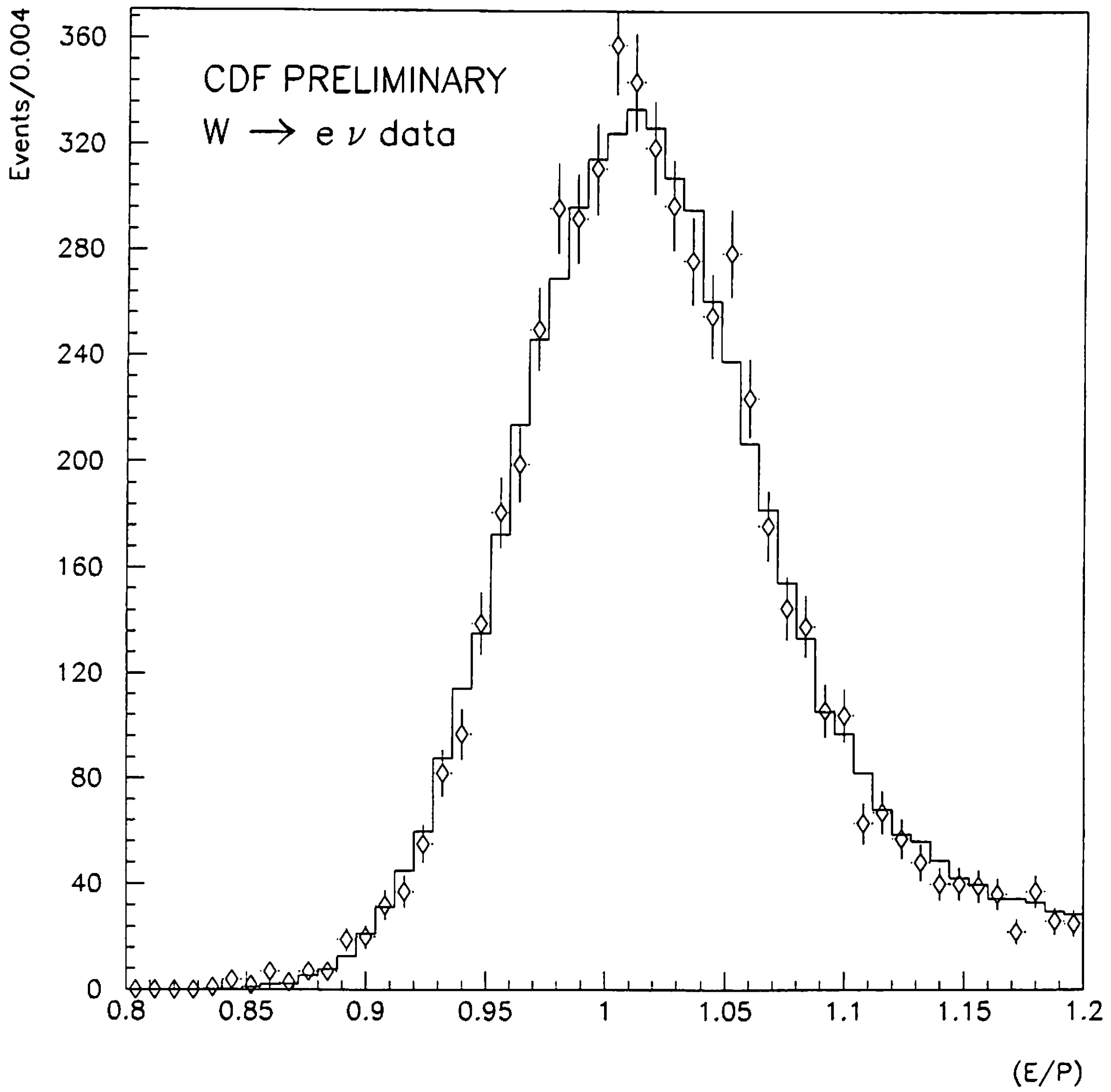

Figure 2.5: E/p distribution of electrons from $W \to e\nu$ decays. The plots show real electrons from the $W \to e\nu$ decays, and the histogram show the simulated electrons.

2.3.4 CHA

The CHA detector is located outside of the CEM and measures the energy deposited in the detector. It has cylindrical symmetry and covers $|\eta|$ range between 0 and 0.9, and 2π in azimuth. The CHA consists of 48 steel-scintillator calorimeters with 2.5 cm steel sampling. Each calorimeter module is divided into projective towers, whose size is $0.1 \times 15^{\circ}$ in $\eta \times \varphi$.

2.4 BBC

The BBC consists of scintillation counters, and are located in the pseudorapidity range $3.3 < |\eta| < 5.9$ on both sides of the interaction region. The BBC detects charged particles scattered into small angle, and measures the coincidence rate between both counters. The timing resolution is about 200 psec. The BBC coincidence gives for a trigger of minimum bias events. The event rate provides the luminosity of the proton and antiproton beams.

2.5 Trigger system

In this experiment, a multi-level trigger system was used to take data. The multi-level trigger system collects data with as little bias as possible at the lower levels, and provides more sophisticated analysis without giving dead time at the next upper level. The trigger systems, which are called "Level_1," "Level_2," and "Level_3," are located in the order of the data taking stream. The triggers of the level_1 and level_2 are hardware triggers, and the level_3 trigger is a software trigger through the CDF reconstruction codes on UNIX machines.

There are 286,000 bunch crossings per second. The decision at the Level_1 has to be made in 3.5 μsec. The Level_1 trigger uses calorimeter information and a coincidence of the BBC detectors. The calorimeter information is a transverse energy of the trigger towers. The size of the trigger tower is 0.2 in η and 15^o in φ. The trigger towers consist of 42 (in η) $\times$ 24 (in φ) array. The accept rate at the Level_1 is 2.4 kHz.

At the Level_2, clustering of the trigger tower energies and the association of stiff tracks with the calorimeter clusters are performed. The Level_2 trigger uses information of the number of clusters with an $E_{\rm T}$ above thresholds, an electromagnetic energy fraction of a cluster, and an existence of a stiff track associated with a cluster. The stiff track is obtained by a fast hardware track processor [14] of the CTC. This trigger reduces the event rate to about 24 Hz in order to handle the events at the Level_3.

The Level_3 trigger performs more sophisticated analysis. The trigger algorithm at the Level_3 is written with FORTRAN-77, and runs on UNIX machine. This program is the same as the offline reconstruction code except that "regional tracking" rather than "global tracking" is used. Events passing through the Level_3 trigger are recorded onto 8mm tapes and disks. The event rate at the Level_3 is about 6 Hz.

2.6 Luminosity measurement

Luminosity of the beam is determined from rates of minimum bias events which are dominantly $\bar{p}p$ inelastic scattering. The luminosity L is related to the event rate R_{BBC} and the effective total cross section $\sigma_{\mathrm{BBC}}^{\mathrm{eff}}$ by

$$L = \frac{R_{\mathrm{BBC}}}{\sigma_{\mathrm{BBC}}^{\mathrm{eff}}}.$$

The measured value $\rho = 0.140 \pm 0.069$ from the E710 collaboration [15], which is the ratio of the real and imaginary part of the forward scattering amplitude, is used for the effective total cross section calculation after correcting to the acceptance [16]. The effective total cross section is

$$\sigma_{\mathrm{BBC}}^{\mathrm{eff}} = 51.2 \pm 1.7 \text{ mb}.$$

The systematic uncertainty in our luminosity measurement is 3.3 % [16].

Chapter 3

Photon Detection

A method of photon identification and an extraction of prompt photons are described in this chapter. A prompt photon, which is produced by a parton-parton collision, is detected in the CEM detector through electromagnetic (EM) cascade showers. The signal of a prompt photon produces an isolated EM cluster in the CEM without an associated charged track in the CTC. The dominant background against prompt photons is multi-photon from neutral meson decays. As the neutral mesons, π^0, η, and K_S^0 mesons are considered. The neutral mesons are produced in hadronization of light quarks or gluons. These backgrounds are subtracted statistically from photon candidates.

3.1 Photon trigger

The inclusive photon sample used in this analysis is an output of a photon trigger at the Level_3. The stream of the data is described in this section.

At the Level_1, the transverse energy of a trigger tower in the CEM calorimeter is required to be larger than an $E_{\rm T}$ threshold. The Level_2 trigger requires one or more EM clusters formed using the EM trigger towers above an $E_{\rm T}$ threshold. The EM cluster must be isolated and located in the CEM to measure the energy and the positions well. The requirements are given by

- $E_{\rm T}^{\rm Total}/E_{\rm T}^{\rm EM} < 1.125$,
- $|\eta| < 1.19$,
- $E_{\rm T}^{\rm EM} > 16$ GeV,
- hardware isolation,

where $E_{\rm T}^{\rm Total}$ is the transverse energy of a cluster, $E_{\rm T}^{\rm EM}$ is that in EM component. A hardware isolation requires that the sum of the transverse energy in the 5×5 trigger tower grid surrounding an EM cluster is less than 5 GeV. The area of the grid is approximately that of a circle with radius $R = \sqrt{(\Delta\eta)^2 + (\Delta\varphi)^2} = 0.65$. The events accepted by the Level_2 are reconstructed and examined to pass a photon filter at the Level_3. A fiducial volume cut of a CES cluster and a tighter isolation cut are applied in addition. The requirements are listed below:

- transverse energy of EM cluster; $E_{\rm T} > 16$ GeV,
- CES cluster position from a center of the CES in the wire view; $|X_{\rm CES}| < 17.5$ cm,
- CES cluster position from a center of the CES in the strip view; $14\ {\rm cm} < |Z_{\rm CES}| < 217$ cm,
- Isolation $(R < 0.7) < 4$ GeV,

where E_{T} is the transverse energy of a photon candidate, X_{CES} and Z_{CES} are the distances between a CES cluster position and a center of the CES module in the wire and the strip views, respectively. The Isolation ($R < 0.7$) is the transverse energy sum around an EM cluster within a radius of 0.7 in η-φ space.

3.2 Clustering in the CEM

In the CEM, a photon is observed as an EM cluster through EM cascade showers. The EM cluster is made by a CDF standard clustering algorithm (EMCLST). This algorithm looks for a seed tower over a transverse energy threshold in the CEM, and gathers the energies of the seed EM tower and its two neighbor towers in pseudorapidity. The EM cluster must satisfy a requirement that the energy of the cluster divided by the CHA tower energy is larger than 1.125.

3.3 Clustering in the CES

The clustering algorithm of a CES cluster gathers 11 wire (or strip) channels around a seed wire (or strip) channel. The energy of a seed wire(or strip) channel is required to be larger than 0.5 GeV. The clustering begins by looking for a seed channel in order of its energy, and sums up all 11 seed wire(or strip) channels. The wire (or strip) channels used in the previous clustering are eliminated. A cluster shape is fitted to a standard shower profile. The standard shower profile was determined from the electron test beam data. The energy of CES clusters is normalized to be unity. Therefore, the fitting depends on the relative pulse height.

The shower profiles are observed to be roughly independent of its energy from the electron test beam experiment.

3.4 Photon identification

The EM clusters constructed by the EMCLST are not enough to be considered as prompt photon candidates yet, because the EM clusters include backgrounds. In the CDF experiment, the following variables are available for prompt photon identification:

- χ^2 of the lateral shower profiles in the CES.
- Isolation of a cluster.
- EM energy fraction of a cluster.
- Absence of charged track in the CTC.
- Associated CES cluster information.
- Missing E_{T} significance.

The above variables are described in detail in the following.

3.4.1 Lateral shower profiles

The information of photon lateral shower profiles in both wire and strip views is available using the CES clusters with fits of the standard shower profiles. The profiles of photon candidates are compared with those of the electron shower measured from the test beam data. The goodness of the fit is expressed by χ^2_{strip} and χ^2_{wire} for the strip and the wire clusters, respectively. The χ^2 value of multi-photon backgrounds is expected to be larger than that of prompt photons, because of the wider shower profile expected for backgrounds. The CES χ^2 is defined by

$$\chi^2 = \frac{\chi^2_{\mathrm{strip}} + \chi^2_{\mathrm{wire}}}{2}.$$

The individual χ^2 in the strip(or the wire) view is given by

$$\chi^2_{\mathrm{strip}}(\mathrm{or}\ \chi^2_{\mathrm{wire}}) = \frac{1}{4}\sum_{i=1}^{11} \frac{(y_i - y(x_i))^2}{\sigma_i^2},$$

where i is an index of CES channels, y_i is the measured profile normalized to the total pulse height, $y(x_i)$ is the standard profile measured by the electron test beam, and σ_i is the estimated variance of the shower profile. The value of σ_i depends on energy of clusters. The dependence is determined from the electron test beam data to be:

$$\sigma_i^2 = 4 \times (0.026^2 + 0.096^2 \times y_i) \times (\frac{10\mathrm{GeV}}{E})^{0.747},$$

where E is a cluster energy in units of GeV.

3.4.2 Isolation

In the CEM, a prompt photon is detected as an isolated cluster. The Isolation($R < 0.7$) is expressed by the sum of the transverse energies around the photon cluster within a cone radius of 0.7 in the η-φ space, namely:

$$\mathrm{Isolation}(R < 0.7) = \sum E_{\mathrm{T}}^i \quad \mathrm{in\ R} < 0.7,$$

where E_{T}^i is the transverse energy of a tower around a photon candidate in $R = 0.7$. A light quark or a gluon occasionally fragments to neutral mesons (π^0, η, and K_{S}^0) without an associated charged particle, and makes an EM cluster in the CEM. This is a main background source against prompt photons. The isolation variable can help to reduce the backgrounds. This Isolation($R < 0.7$) is required to be less than 2 GeV. The efficiency of the cut is estimated from a minimum bias data sample. The estimation method is discussed later.

3.4.3 EM energy fraction

The cluster energy fraction of EM component is useful to eliminate backgrounds from a jet. The fraction is defined by $E^{\mathrm{Had}}/E^{\mathrm{Em}}$ using the energies in the hadronic and electromagnetic components of a cluster.

3.4.4 Absence of a charged track in the CTC

A prompt photon passes through the tracking device of the CTC without providing a signal. Therefore, the absence of an associated charged track in the CTC helps to identify an EM cluster as a prompt photon, and to eliminate electrons, and to reduce backgrounds from a jet.

3.4.5 Associated CES cluster

To eliminate the multi-photon backgrounds from the neutral meson decays, information of extra CES clusters around a CES cluster is useful. We require that there is no extra CES cluster in the same "wedge." The energy of an extra CES cluster is required to be less than 1.0 GeV. This cut provides a significant rejection against the backgrounds from the neutral meson decays. The efficiency of this cut depends on the energy of photon candidates. Figure 3.1 shows the efficiency of the cut as a function of EM cluster energy. These efficiencies were obtained from the real $W \to e\nu$ data, the Monte Carlo $W \to e\nu$ data, and the electron test beam data.

3.4.6 Missing E_{T} significance

To eliminate backgrounds of cosmic ray events which include *bremsstrahlung* photons, a missing E_{T} significance (S) is required to be less than 3. The *bremsstrahlung* photons from cosmic rays deposit a large energy without balancing transverse energy in the R-φ plane. The missing E_{T} significance is a net imbalance of transverse energy on the calorimeter, which is defined by

$$S = \frac{|\sum \vec{E}_{\mathrm{T}}^{i}|}{\sqrt{\sum E_{\mathrm{T}}^{i}}},$$

where E_{T}^{i} is the transverse energy of the calorimeter towers, and the summation is taken over all calorimeter towers.

3.5 Inclusive photon sample

To reduce backgrounds, the photon selection cuts are applied to the inclusive photon data which passed the Level_3 trigger. The transverse momentum of the EM clusters is required to be larger than 16 GeV. The cluster energy ratio of hadronic to electromagnetic calorimeters is less than 0.125. These requirements come from the trigger thresholds at the Level_3. The Isolation ($R < 0.7$) is required to be smaller than 2 GeV. The missing E_{T} significance is required to be smaller than 3. There must be no extra CES cluster above 1 GeV in both strip and wire views, and no associated CTC track. The strip clusters must be in the CES

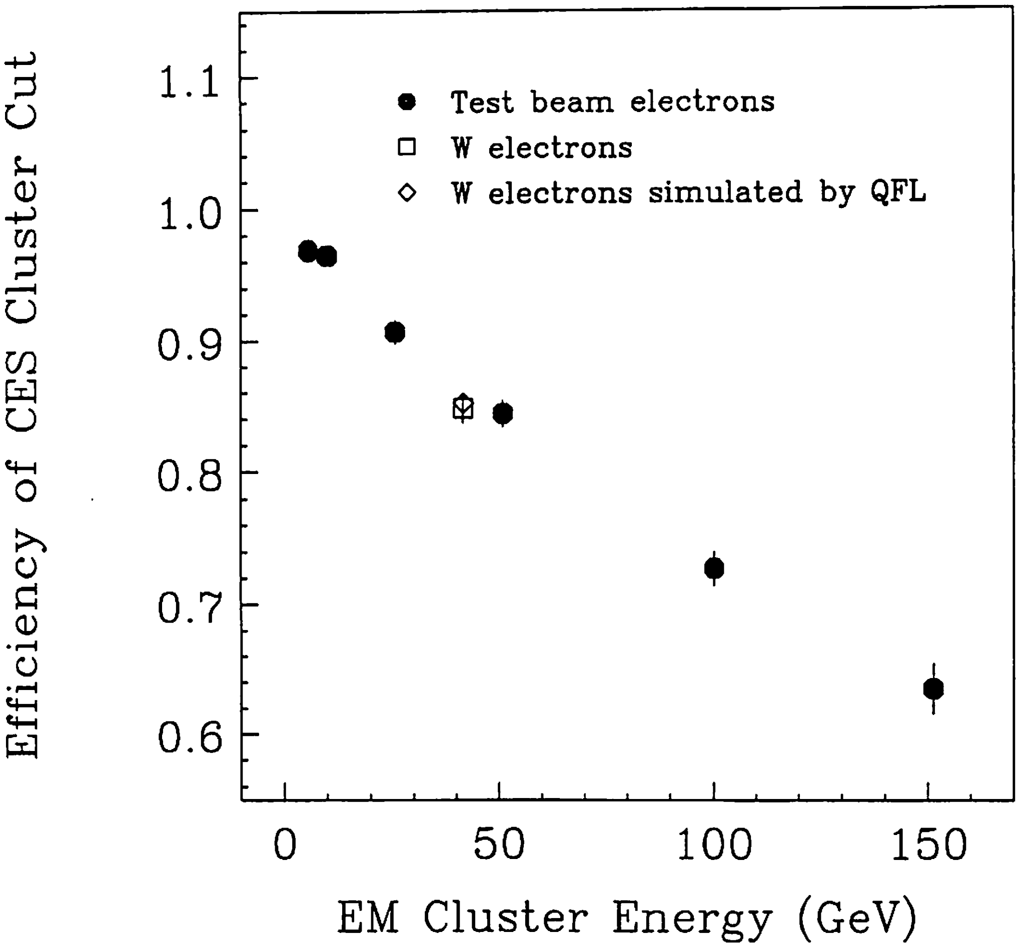

Figure 3.1: The efficiency of the extra CES cluster cut as a function of EM cluster energy. The test beam electrons, and the electrons from $W \rightarrow e\nu$ decay (both measured and simulated) are shown.

fiducial regions to detect the shower well. The photon selection cuts are summarized in Table 3.1.

Table 3.1: Photon selection cuts.

Photon p_{T}	$>$	16 GeV
Isolation($R < 0.7$)	$<$	2 GeV
Number of charged track	$=$	0
$\chi^2 = \frac{1}{2}(\chi^2_{\mathrm{wire}} + \chi^2_{\mathrm{strip}})$	$<$	20.0
E_{T} of the 2nd CES clusters	$<$	1 GeV
Missing E_{T} Significance	$<$	3
14.0 cm $< \lvert Z_{\mathrm{strip}}\rvert < 217.0$ cm		
$\lvert X_{\mathrm{wire}}\rvert < 17.5$ cm		

We show a transverse momentum (p_{T}) distribution of the photon candidates passing the selection cuts except for the p_{T} cut in Fig. 3.2. In this analysis, the photon candidates in the p_{T} range between 16 and 40 GeV/c are used. The p_{T} range is shown as the hatched area in the figure. The lower cut value is the trigger threshold. The upper cut comes from the limitation associated with using the CES χ^2, because the separation of a prompt photon from a background photon using the CES χ^2 becomes worse above $p_{\mathrm{T}} = 40$ GeV/c.

3.6 Background sources

The dominant background sources against prompt photons are multi-photons from the neutral meson decays such as $\pi^0 \to \gamma\gamma$, $\eta \to \gamma\gamma$, and

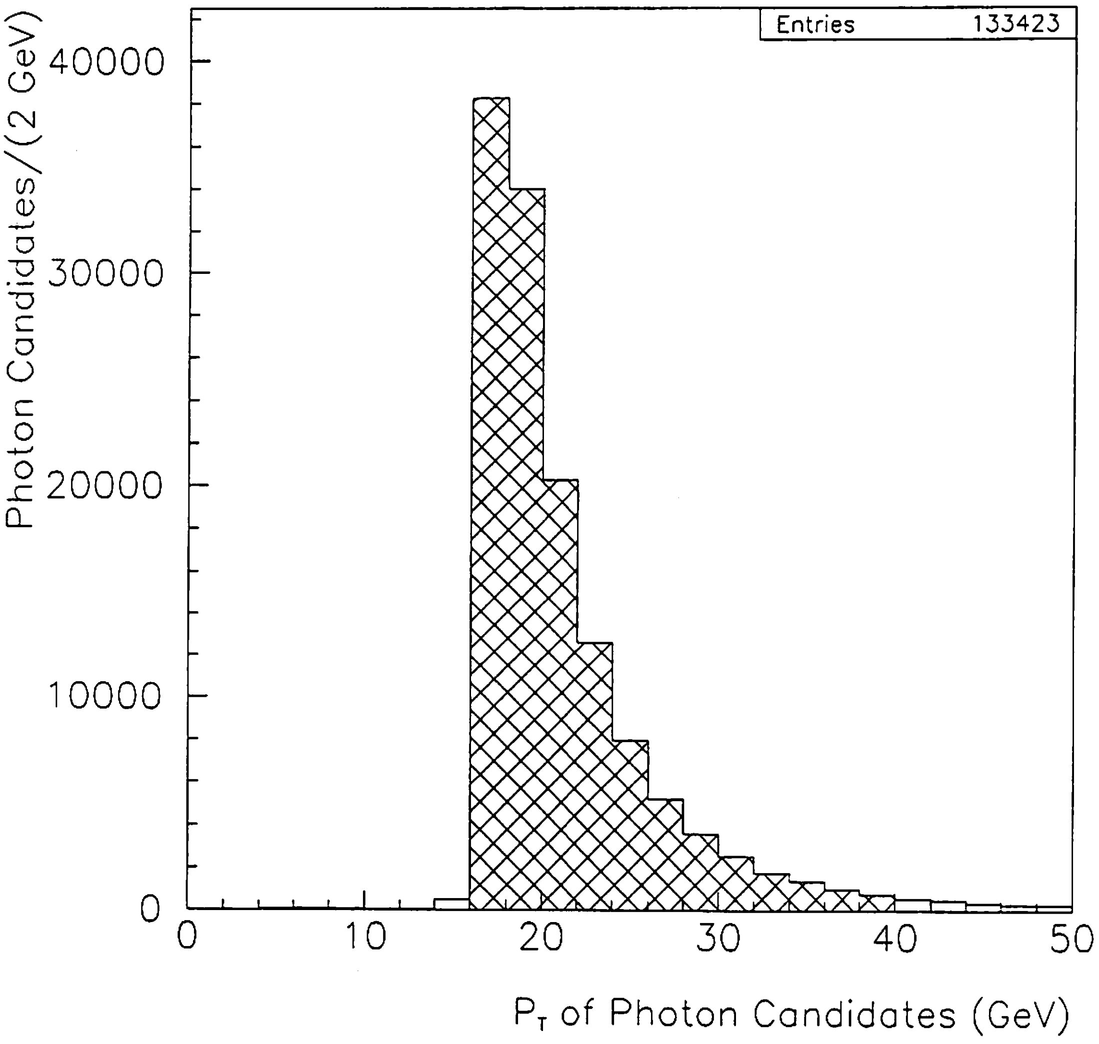

Figure 3.2: p_{T} distribution of the photon candidates which satisfy the photon selection cuts except for the p_{T} cut.

$K^0_S \rightarrow \pi^0\pi^0$. The branching ratios of the neutral mesons decaying into γ's or π^0's are listed in Table 3.6. The mesons are produced in fragmentation of light quarks and gluons. At the CES detector position, the minimum separation of the two photons from a π^0 decay is approximately given by

Table 3.2: Branching ratios of the neutral mesons decaying into γ's or π^0's

Decay Modes	Branching ratios
$\pi^0 \rightarrow \gamma\gamma$	~ 100 %
$\eta \rightarrow \gamma\gamma$	38.8 ± 0.5 %
$\eta \rightarrow \pi^0\pi^0\pi^0$	31.9 ± 0.4 %
$K^0_S \rightarrow \pi^0\pi^0$	31.39 ± 0.28 %

$$S_{\text{min}} = \frac{50}{p_T(\text{GeV}/c)} \quad (\text{cm}),$$

where p_T is the transverse momentum of π^0. Above $p_T = 16$ GeV, it is difficult to separate a prompt photon from two photons of a π^0 decay individually in the CES, because the Molíere radius of the calorimeter of lead-scintillator type is 3.5 cm [18]. However, the average χ^2 for prompt photons is expected to be smaller than that for backgrounds. Figure 3.3 shows the χ^2 distributions of prompt photons and backgrounds obtained by a simulation at $p_T = 15$ GeV/c. In this analysis, the statistical method using the CES average χ^2 is used to separate prompt photons from multi-photon backgrounds.

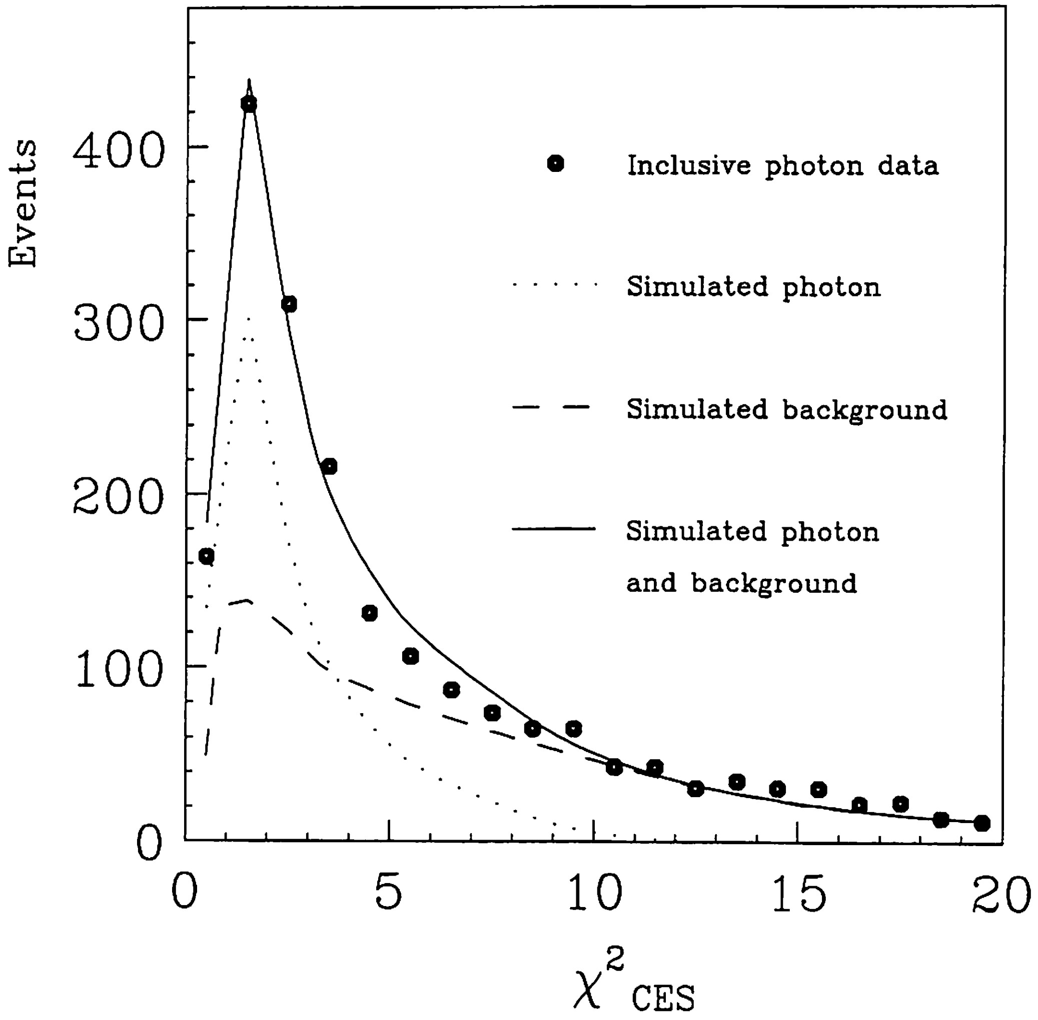

Figure 3.3: CES χ^2 distributions of simulated photons, simulated photon backgrounds and the measured photon candidates.

3.7 Background subtraction

After requiring the photon selection cuts, the photon candidates include roughly half signals and half backgrounds in general. The number of observed photon candidate events (N) is given by

$$N = N_\gamma + N_{\rm B},$$

where N_γ and $N_{\rm B}$ are the numbers of true photons and backgrounds, respectively. Similarly, the number of the events passing the cut ($\chi^2 < 4$) is expressed by

$$N(\chi^2 < 4) = N_\gamma(\chi^2 < 4) + N_{\rm B}(\chi^2 < 4),$$

where $N_\gamma(\chi^2 < 4)$ and $N_{\rm B}(\chi^2 < 4)$ are the numbers of true photon and background events passing the cut ($\chi^2 < 4$), respectively. Combining the above equations, we obtain as follows:

$$\begin{aligned} \epsilon N &= \varepsilon_\gamma \ N_\gamma + \varepsilon_{\rm B} \ N_{\rm B} \\ &= \varepsilon_\gamma \ N_\gamma + \varepsilon_{\rm B} \ (N - N_\gamma), \end{aligned}$$

where ϵ, ε_γ, and $\varepsilon_{\rm B}$ are the χ^2 efficiencies for photon candidates, true photons, and backgrounds to pass the cut $\chi^2 < 4$, respectively. From the above equation, the number of prompt photons N_γ is given by

$$N_\gamma = (\frac{\epsilon - \epsilon_{\rm B}}{\epsilon_\gamma - \epsilon_{\rm B}}) \times N.$$

Figure 3.4 shows the χ^2 efficiencies ε_γ and $\varepsilon_{\rm B}$ as a function of EM cluster $p_{\rm T}$. They were estimated from a detector simulation based on the electron test beam data.

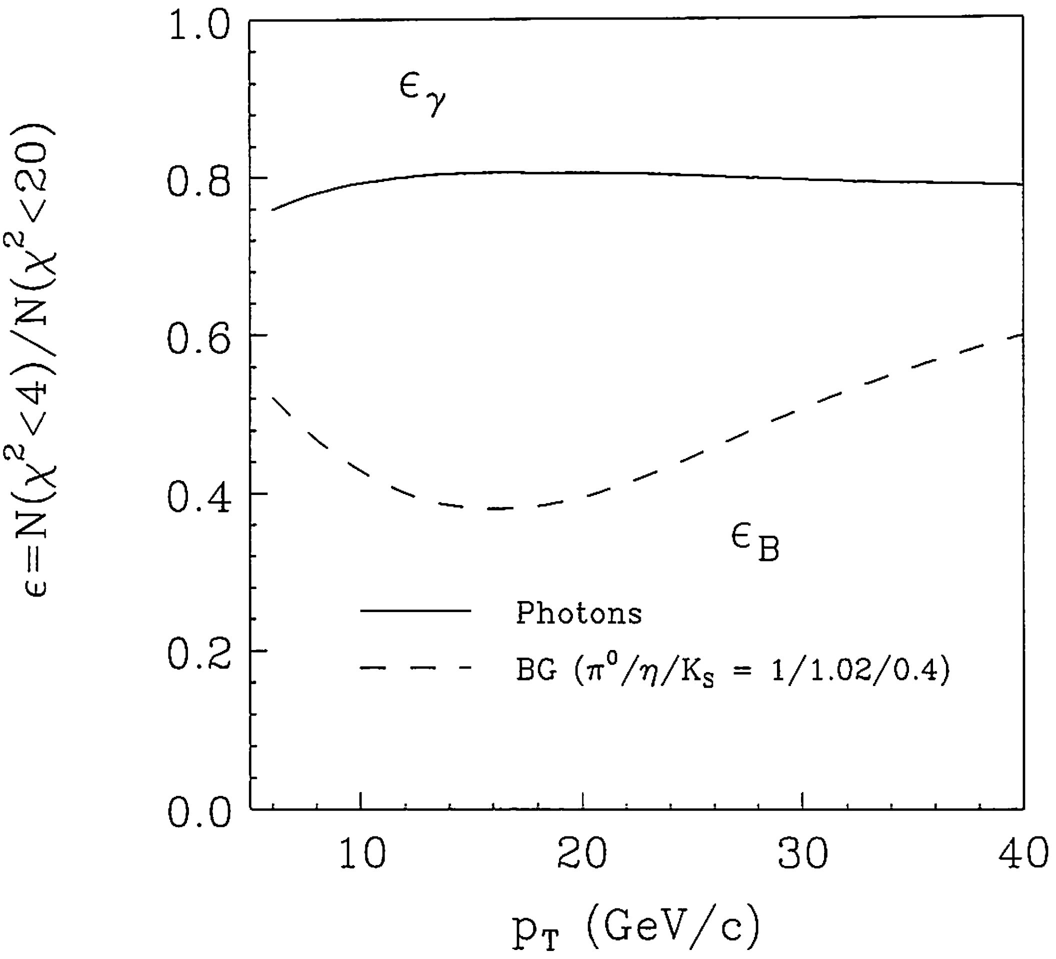

Figure 3.4: Signal and background χ^2 efficiencies obtained by a detector simulation.

3.8 χ^2 efficiencies in profile method

The χ^2 efficiencies ε_γ and $\varepsilon_{\rm B}$ to pass the cut $\chi^2 < 4$ are determined by a detector simulation based on the electron test beam data. The accuracy of the simulation is checked by comparisons with the data of $W \rightarrow e\nu$ and $\eta \rightarrow \gamma\gamma$ for signals and $\rho^\pm \rightarrow \pi^0\pi^\pm$ for backgrounds.

3.8.1 Detector simulation

The simulation program, GEANT 3.14 [17], was used for the simulation of the detector responses. The simulation provides some guidance and intuition into the magnitude of various effects. The information of the real electron showers measured by the electron test beam was installed in the simulation of photons after the correction for the difference between photon and electron.

3.8.2 Signal χ^2 efficiency

The χ^2 efficiency ε_γ for signal (prompt) photons was estimated by the simulation. The validity of the estimation is checked using the CDF real data. The electrons from $W \rightarrow e\nu$ decays provide a check that the data of the test beam electrons are properly installed into the simulation. The photons from $\eta \rightarrow \gamma\gamma$ decay provide a comparison of remaining details of the simulation.

3.8.2.1 Electron sample from $W \rightarrow e\nu$

The electrons from the $W \rightarrow e\nu$ decays were collected by a high transverse energy ($E_{\rm T}$) electron trigger, and were selected by the following selection cuts:

- Transverse energy of the EM cluster; $E_{\mathrm{T}}^{\mathrm{EM\ cluster}} > 25$ GeV.
- Isolation; $E_{\mathrm{T}}(R < 0.7)/E_{\mathrm{T}}^{\mathrm{EM\ cluster}} < 0.15$,

  where $E_{\mathrm{T}}(R < 0.7)$ is the transverse energy sum around a cluster within a radius of 0.7 in η-φ space.
- Number of associated CTC tracks; $N_{\mathrm{track}} = 1$.
- Comparison of the cluster energy (E) and the track momentum (p); $0.8 < E/p < 1.2$.
- Fiducial volume cuts for a CES cluster;

  $14 < |Z_{\mathrm{CES}}| < 217$ cm,
  $|X_{\mathrm{CES}}| < 17.5$ cm,
  where X_{CES} and Z_{CES} are CES cluster positions in the wire and strip views, respectively.
- Shower shape in the CES strip view; $\chi^2_{\mathrm{strip}} < 20$.

The CES χ^2 distributions of the W decay electrons were compared with those of the simulated electrons from the W decays. The simulation includes the effects of internal and external photon radiations and the gas saturation. Figs. 3.5 (a) and (b) show the strip χ^2_{strip} and the wire χ^2_{wire} distributions, respectively. Fig. 3.5 (c) shows their average χ^2 distribution, where the average is calculated by

$$\chi^2 = (\chi^2_{\mathrm{strip}} + \chi^2_{\mathrm{wire}})/2.$$

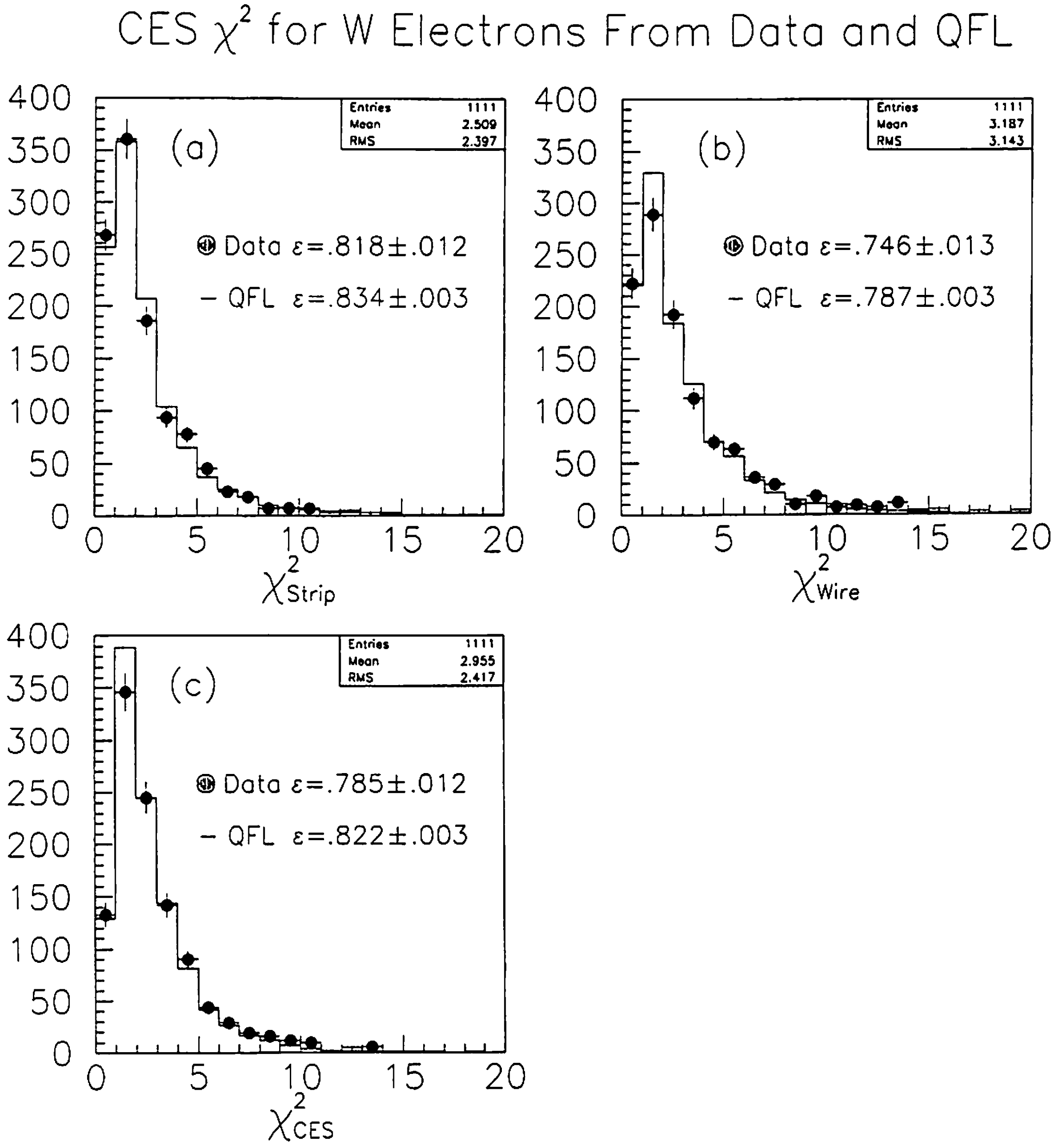

Figure 3.5: Comparison of electron χ^2's from $W \rightarrow e\nu$ decays (points) with a radiative W Monte Carlo plus detector simulation (histogram): (a) strip χ^2, (b) wire χ^2, (c) average of both the strip and the wire χ^2's.

The real W electron data agree with the simulation data in the strip χ^2_{strip} distribution. However, these are slightly different in the wire χ^2_{wire} and the average χ^2 distributions. The efficiencies for the real and the simulated electrons to satisfy the cut $\chi^2 < 4$ are 0.785 ± 0.012 and 0.822 ± 0.003, respectively, where the errors show the statistical ones.

3.8.2.2 Photon sample from $\eta \rightarrow \gamma\gamma$

The $\eta \rightarrow \gamma\gamma$ data were taken by a low transverse energy photon trigger in the previous run during 1988~1989. The E_{T} threshold of the trigger is 10 GeV. The trigger also required the small hadronic energy fraction and the isolation of an EM cluster. The energy fraction is defined by the fraction of the transverse energy ($E_{\text{T}}^{\text{Had}}$) in the CHA divided by that (E_{T}^{Em}) in the CEM. The isolation is the energy sum in $R = 0.7$ in η-φ space around a cluster divided by the cluster E_{T}. The photon candidates were required to have no associated CTC track. The events including the photon candidates were required to have an event z vertex within 50 cm from the detector center, and to have a small missing E_{T}. The trigger requirements and the selection cuts for the EM clusters from the $\eta \rightarrow \gamma\gamma$ decays are summarized as follows:

Trigger requirement:

- Transverse energy of EM cluster; $E_{\text{T}} > 9$ GeV.
- Energy fraction; $E_{\text{T}}^{\text{had}}/E_{\text{T}}^{\text{Em}} < 0.125$.
- Isolation; $E_{\text{T}}(R < 0.7)/E_{\text{T}}^{\text{cluster}} < 0.15$.

Photon selection cuts in offline:

- Number of associated CTC track; $N_{\text{track}} = 0$.
- Central photons; $|\eta^{\gamma}| < 0.9$.
- Event vertex z position; $|z_{\text{vertex}}| < 50$ cm.
- Missing E_{T} significance < 3.

To provide information of the single photon from $\eta \to \gamma\gamma$ decays, we required that each photon landed in two separate CEM towers in an EM cluster. A schematic view of the $\eta \to \gamma\gamma$ detection is shown in Fig. 3.6. The additional cuts are applied to the events for the two photon analysis. The transverse energy of the EM cluster is restricted to between 9 GeV and 15 GeV. The lower cut comes from the extremely low trigger efficiency, and the upper one is introduced to separate the photons from $\pi^0 \to \gamma\gamma$ decays. To suppress the backgrounds from $\eta \to \pi^0\pi^0\pi^0$ decay and other neutral meson decays, only two CES clusters in the strip view were required in the EM cluster. The clusters in the wire view presumably are overlapped, thus we require one or two clusters for the wire view. The CES clusters are imposed to be in the fiducial region of the CES. The additional cuts are summarized as follows:

- Transverse energy; 9 GeV $< E_{\text{T}}^{\text{cluster}} <$ 15 GeV.
- Number of strip clusters; $N_{\text{strip}} = 2$.
- Number of wire clusters; $N_{\text{wire}} = 1$ or 2.
- Each CES strip cluster landed in two separate towers.
- Fiducial volume cuts in the CES;

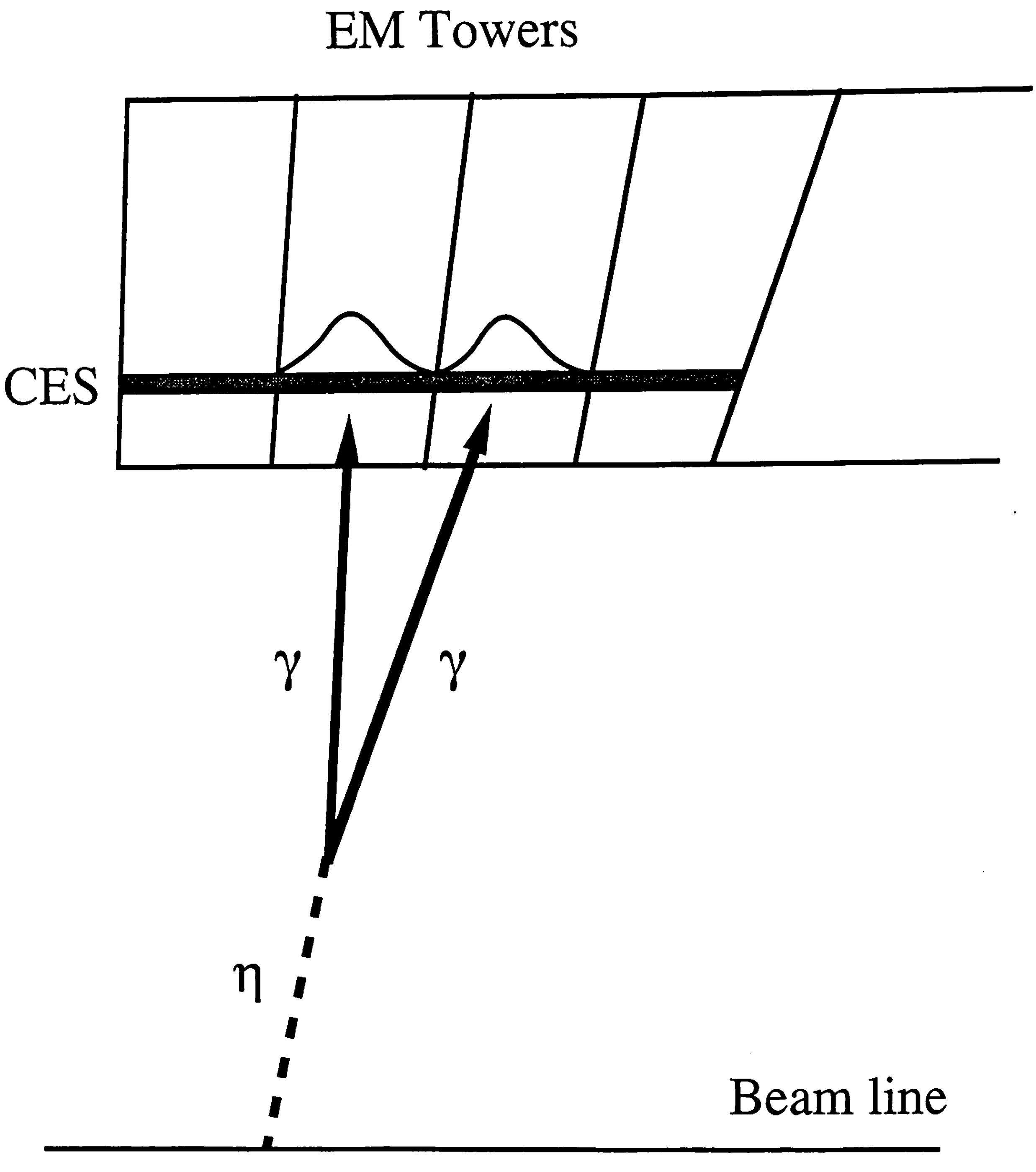

Figure 3.6: Schematic view for the $\eta \rightarrow \gamma\gamma$ detection.

$14 < |Z_{\mathrm{CES}}| < 217$ cm,
$|X_{\mathrm{1st\ CES}}| < 20$ cm and $|X_{\mathrm{2nd\ CES}}| < 20$ cm,
$|X_{\mathrm{1st\ CES}}| < 17.5$ cm or $|X_{\mathrm{2nd\ CES}}| < 17.5$ cm.

The two photon mass $M_{\gamma\gamma}$ is calculated by

$$M_{\gamma\gamma} = \sqrt{2E_1E_2 \times (1 - \cos\theta_{12})},$$

where θ_{12} is an angle between two photons in the laboratory frame, $E_i (i = 1 \text{ or } 2)$ is the tower energy of each photon. The tower energy is corrected individually for CEM response variations. The $\cos\theta_{12}$ is expressed using the positions of the CES clusters (Z and X) as follows:

$$\cos\theta_{12} = \frac{R^2 + Z_1Z_2 + X_1X_2}{\sqrt{(R^2 + Z_1^2 + X_1^2)(R^2 + Z_2^2 + X_2^2)}},$$

where R (=183.9 cm) is a distance between the proton beam line to the CES position in the R-φ plane. Figure 3.7 shows the two photon invariant mass distributions. A significant $\eta \to \gamma\gamma$ peak is observed. The distribution is fitted to a gaussian plus quadratic function. The fitted mass is obtained to be 549 ± 6 MeV/c^2, where the error shows statistical one. This is consistent with the world average mass of η meson 547.45 ± 0.19 MeV/c^2 [18]. The width of the peak is roughly the expected one from the CEM energy resolution. A peak of $\pi^0 \to \gamma\gamma$ is suppressed by a large CES clustering window (11 channels). In order to remove the contribution of backgrounds in the $\eta \to \gamma\gamma$ events, the χ^2 distribution of the side band events around the η mass region was subtracted from that of the events in the η mass region. The signal and the side band regions are indicated in the figure. The strip χ^2_{strip} distribution of the

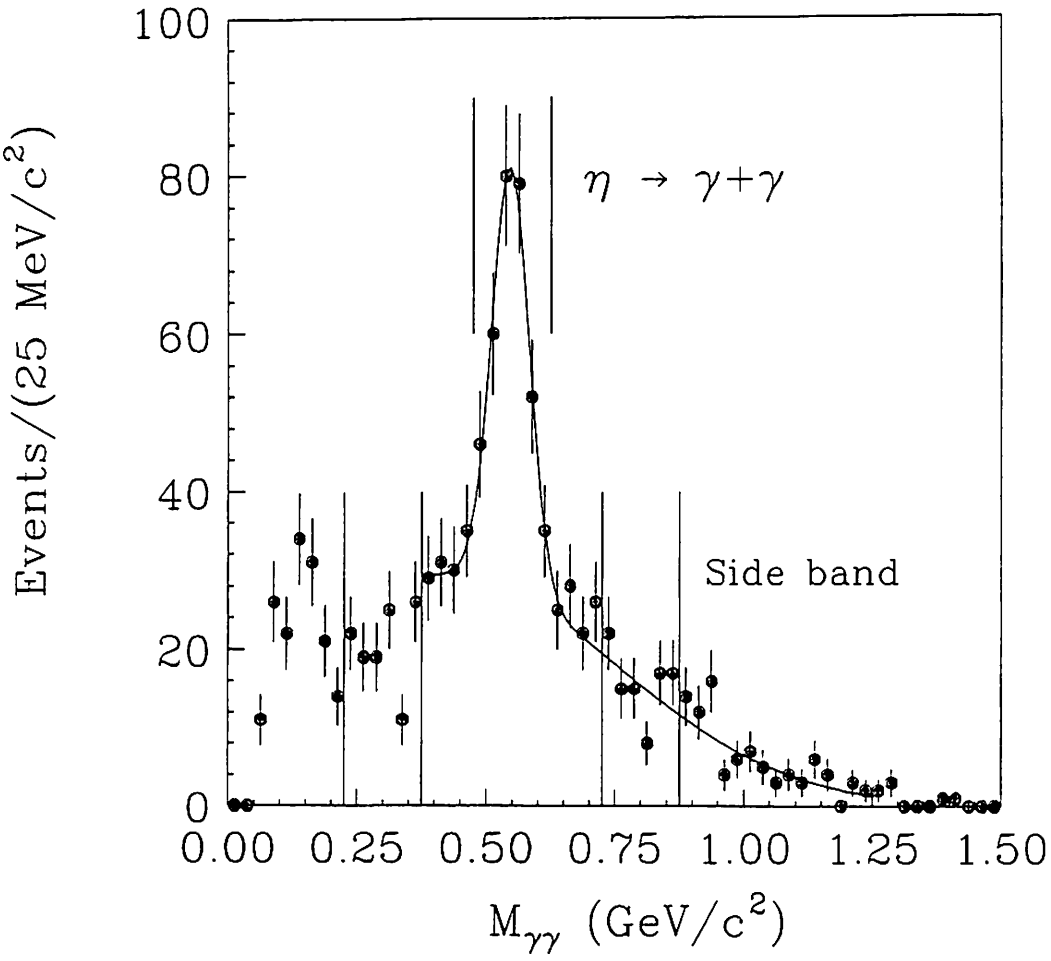

Figure 3.7: Two photon mass distribution. The distribution was fitted to a gaussian plus quadratic function. A clear $\eta \to \gamma\gamma$ peak can be seen at $M_{\gamma\gamma} = 0.549$ GeV/c^2.

photons obtained from the $\eta \rightarrow \gamma\gamma$ events is compared with that of the simulated $\eta \rightarrow \gamma\gamma$ events in Figure 3.8. The χ^2_{strip} distribution of the simulated photons well produces that of the real photons obtained from the $\eta \rightarrow \gamma\gamma$ events.

3.8.3 Background efficiency

Sources of the photon backgrounds against prompt photons are mainly multi-photons from the neutral meson decays such as $\pi^0 \rightarrow \gamma\gamma$, $\eta \rightarrow \gamma\gamma$, and $K^0_S \rightarrow \pi^0\pi^0$. The compositions of these backgrounds were obtained from the CDF measurements. At the CDF, the π^0 and η mesons decaying into two photons have been reconstructed using a narrow CES cluster (3 channels). The two CES clusters are required to be in the adjoining CEM towers. Figure 3.9 shows the two photon invariant mass distribution with the significant π^0 and η peaks at 139 and 547 MeV/c^2, respectively. After the acceptance corrections, the production ratio of π^0 and η was obtained [20]:

$$\eta/\pi^0 = 1.02 \pm 0.15(\mathrm{stat.}) \pm 0.23(\mathrm{syst.}),$$

where the first and the second errors show the statistical and systematic ones, respectively. The production of K^0_S has also been measured at the CDF using charged decay mode [21]. The production ratio of K^0_S and π^0 from the K^0_S measurement with an assumption of isospin invariance was measured to be

$$K^0_S/\pi^0 = 0.4.$$

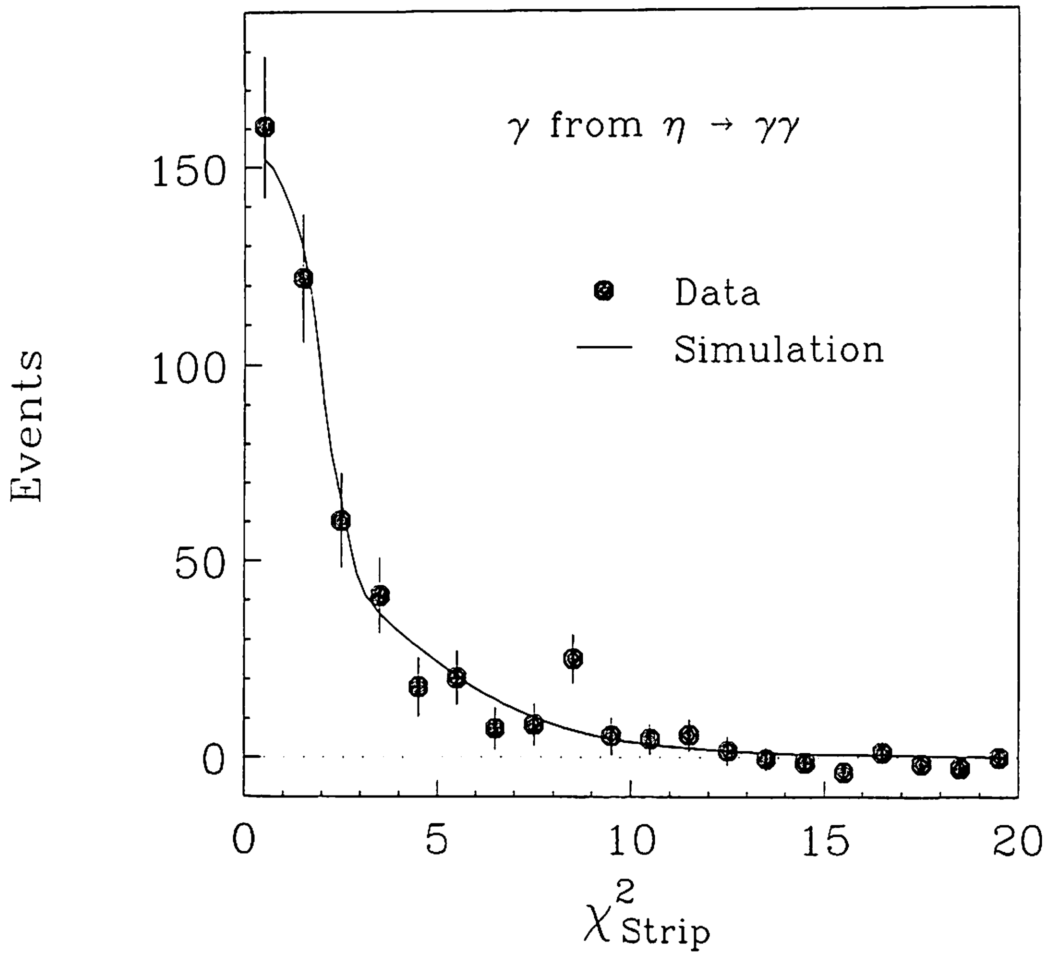

Figure 3.8: Strip $\chi^2_{\rm strip}$ distribution of the photons obtained from the $\eta \to \gamma\gamma$ events is shown as the points. The solid line shows the $\chi^2_{\rm strip}$ distribution of the simulated $\eta \to \gamma\gamma$ events.

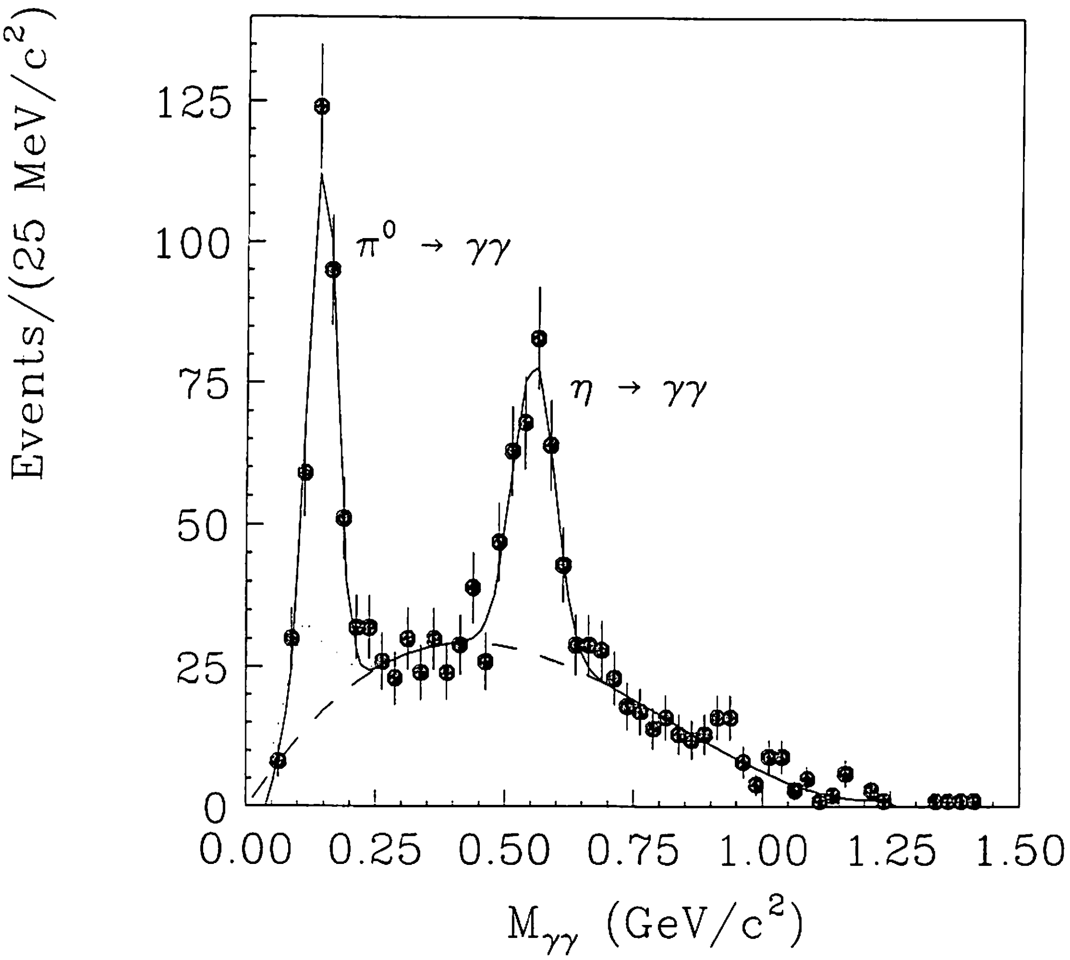

Figure 3.9: Two-photon invariant mass distribution using three CES channel cluster. The significant $\eta \rightarrow \gamma\gamma$ and $\pi^0 \rightarrow \gamma\gamma$ signals can be seen. The smooth dashed curve shows the estimated background, and the dotted line is the sum of single photon contribution.

3.8.3.1 π^0 sample from $\rho^\pm \to \pi^\pm\pi^0$

A $\rho^\pm$ meson decaying to $\pi^\pm$ π^0 is a good sample for checking the χ^2 distribution of π^0's. The $\rho^\pm$ meson was reconstructed using a single charged track and an associated EM cluster. Figure 3.10 shows the mass distribution of a track and an EM cluster, where the masses of the track and the EM cluster are assigned to be charged pion and neutral pion masses, respectively. A clear $\rho^\pm \to \pi^\pm\pi^0$ peak is observed. The distribution was fitted with a Breit-Wigner plus polynomial function. The fitted mass is 772 ± 9 MeV/c^2, where the error shows statistical one. It is consistent with the world average ρ^+ mass 766.9 ± 1.2 MeV/c^2[18]. The χ^2 distribution of the reconstructed π^0's in the $\rho^\pm$'s mass window of $0.7 < M_{\pi^\pm\pi^0} < 1.2$ GeV/c^2 and that of the simulated π^0's are shown in Figure 3.11.

3.8.3.2 Combined background efficiency

The background χ^2 efficiency was evaluated using the measured production ratios and each background source by simulation. Figure 3.12 shows the efficiencies of each source and the combined efficiency.

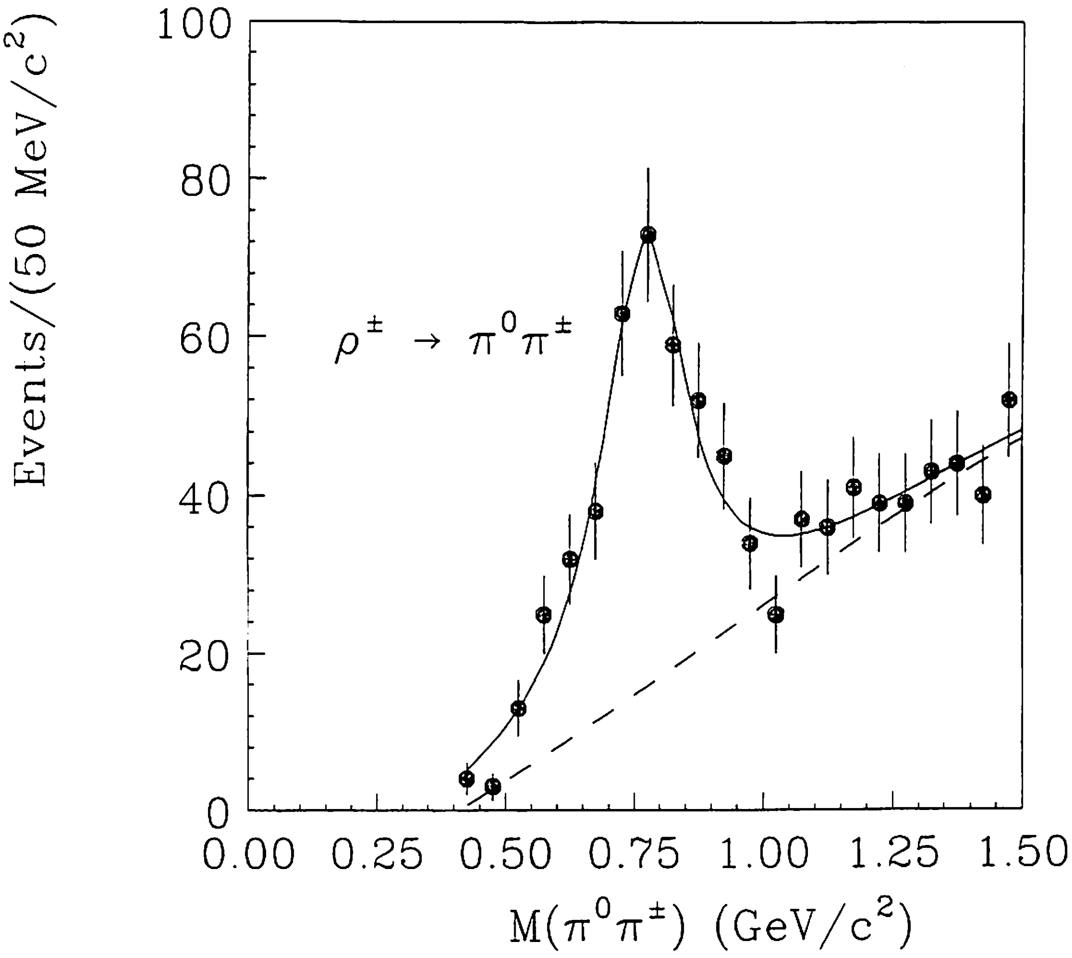

Figure 3.10: Photon-charged pion mass distribution. The significant $\rho^{\pm} \to \pi^{\pm}\pi^{0}$ peak is observed.

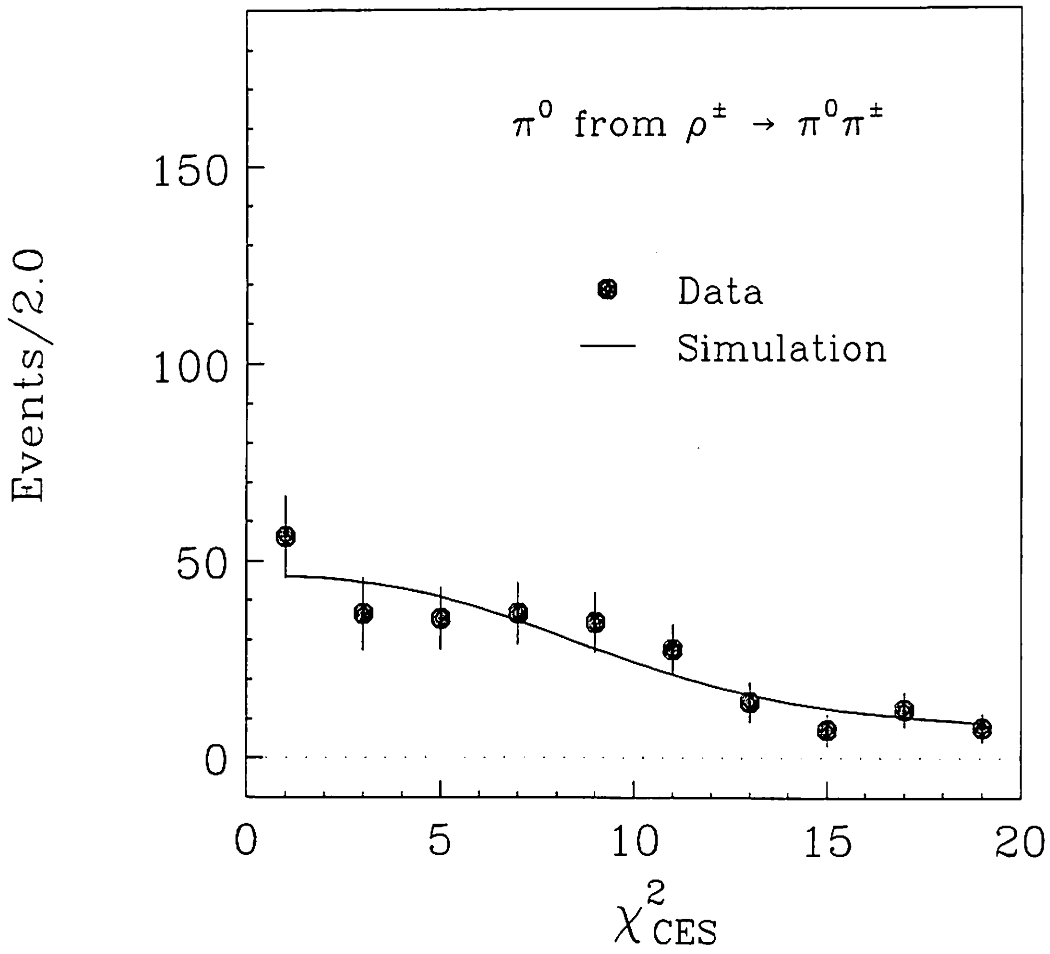

Figure 3.11: CES χ^2 distribution for the π^0's obtained from the observed $\rho^\pm \longrightarrow \pi^\pm\pi^0$ events(points). That is compared with the simulated single π^0's (solid line).

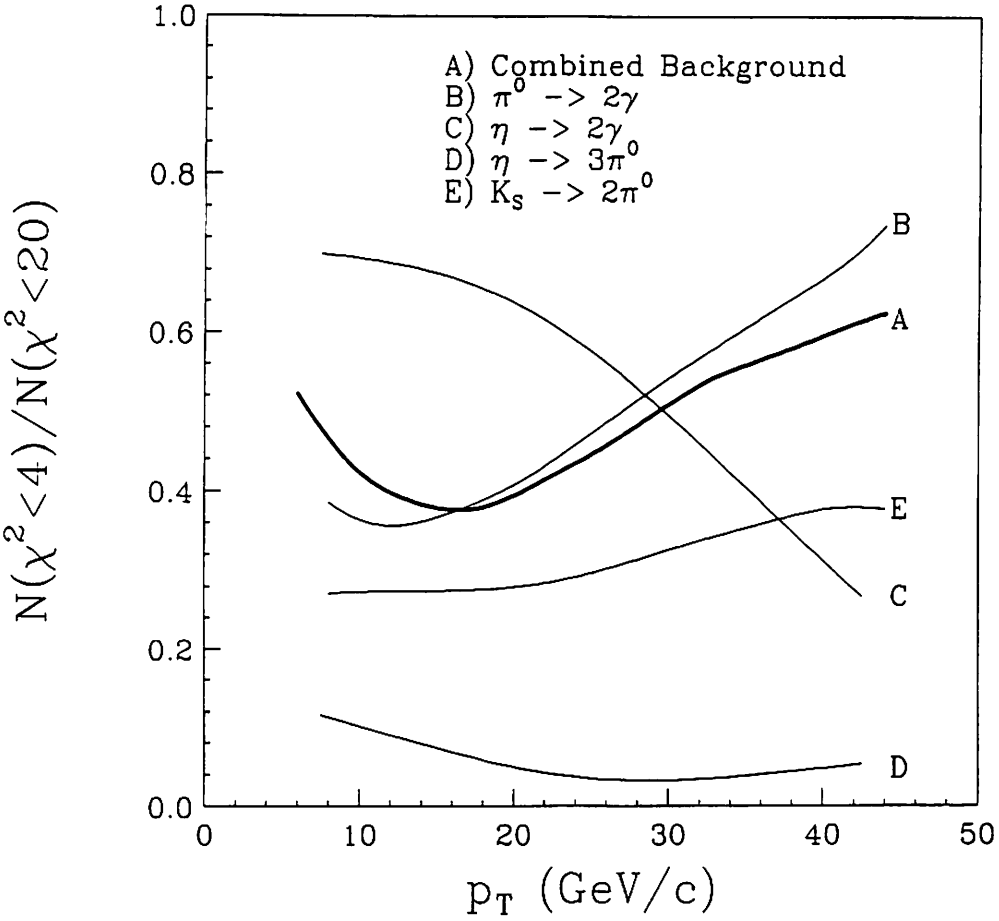

Figure 3.12: Efficiencies for the combined background and the individual particles to pass the cut $\chi^2 < 4$.

Chapter 4

$D^{*\pm}$ Reconstruction

In this chapter the $D^{*\pm}$ reconstruction method is described. Quarks are never seen in free state, although the existence of quarks have indirectly been established [22]. Charm quark as well as other quarks form mesons or baryons rapidly after the production. The charm mesons or baryons decay into stable hadrons, baryons, or leptons. We reconstructed a $D^{*\pm}$ meson in the inclusive photon events in order to identify the event containing a charm quark. In the CDF experiment, there are several charm quark identification methods. One is a full reconstruction of charm mesons using their invariant mass distributions. Characteristics of a lepton (electron or muon) from semileptonic decays of charm quark are also useful to identify charm quark signals with an advantage of the relative large branching ratios of the charm meson or baryon decays. The other uses a charm quark jet with its secondary vertex position due to the finite lifetime of the charm mesons or baryons ($c\tau \sim 200$ μm).

A $D^{*\pm}$ meson was fully reconstructed using the sequential decays of

$$\begin{cases} D^{*+} \to D^0\pi_s^+ \to & K^-\pi^+\pi_s^+, \\ D^{*+} \to D^0\pi_s^+ \to & K^-\pi^-\pi^+\pi^+\pi_s^+, \end{cases}$$

and their charge conjugate decays. Charge-conjugate modes are implied hereafter. In order to distinguish the pions from $D^{*+} \to D^0\pi^+$ and $D^0 \to K^-\pi^+$ (or $K^-\pi^-\pi^+\pi^+$), the pion from the $D^{*\pm}$ decay is represented by a symbol π_s. An existence of a $D^{*\pm}$ meson is a direct evidence of a charm quark production, and can be used to select an event containing a charm quark. A $D^{*\pm}$ meson can be reconstructed without particle identification equipment. It is based on the small Q-value in the decay of $D^{*+} \to D^0\pi^+$. A mass difference between D^{*+} and D^0 mesons, $\Delta M \equiv M_{D^*} - M_{D^0}$, is 145.42 ± 0.05 MeV/$c^2$ [18], that is nearly pion mass. Therefore, random combinations which accidentally come in a $D^{*\pm}$ signal window are expected to be relatively small. However, the branching ratio of the decay is relatively small. It is 2 % [18]. The analysis is limited by statistics.

4.1 $D^{*\pm}$ reconstruction method

The $D^{*\pm}$ reconstruction using the sequential decay of $D^{*+} \to D^0\pi_s^+ \to K^-\pi^+\pi_s^+$ (or $\to K^-\pi^-\pi^+\pi^+\pi_s^+$) was performed by taking a combination of charged tracks to simultaneously form a D^0 and a D^{*+} using two and three tracks (or four and five tracks), respectively. We took all possible combinations in an event. The tracks used in the combination were assumed to be a kaon or a pion, and their masses were assumed to be kaon mass (=0.493646 GeV/c^2) or pion mass (=0.1395675 GeV/c^2) [18].

In the assignments of a π_s, only tracks which have the opposite electric charge as that of a K track were considered, namely;

$$\begin{array}{ll} K^-\pi^+\pi_s^+ & \text{for } D^0 \to K^-\pi^+, \\ K^-\pi^-\pi^+\pi^+\pi_s^+ & \text{for } D^0 \to K^-\pi^-\pi^+\pi^+. \end{array}$$

A mass difference of

$$\Delta M(D^0\pi_s^+ - D^0) \equiv M(D^0\pi_s^+) - M(D^0),$$

was calculated for each track combination, where $M(D^0\pi_s^+)$ and $M(D^0)$ are invariant masses of a $D^0(\to K^-\pi^+$ or $K^-\pi^-\pi^+\pi^+)\pi_s^+$ and a $D^0(\to K^-\pi^+$ or $K^-\pi^-\pi^+\pi^+)$ systems, respectively. Part of the common track momentum errors tends to cancel in the ΔM.

4.2 Track selection

Charged particles are detected in the SVX and the CTC. The momentum is reconstructed by fitting the CTC hit positions to an arch. Good tracks passing some quality cuts were used for the $D^{*\pm}$ reconstruction. The good track selection cuts are described in this section.

4.2.1 Good track selection

The goodness of fitting is given by the number of hits used for the fitting. The good track conditions are given by

- 3 dimensional fitted track.
- Number of stereo layers having more than 4 hits ≥ 2.
- Number of axial layers having more than 2 hits ≥ 2.

In this experiment, the reconstructed tracks can be separated into two types. One is a CTC track which was reconstructed in the CTC. The other is an SVX-CTC track which was a CTC track having SVX hits successfully combined in the track fitting. For SVX-CTC tracks, additional cuts were required as follows:

- χ^2 of combining fit of CTC and SVX tracks ≤ 20.
- Number of hits on the SVX ≥ 2.

If there exists an SVX-CTC track, then the track was used, otherwise a CTC track was used.

4.2.2 Removal of photon conversion tracks

Charged tracks contain "photon conversion" tracks. The photon conversion is caused by a process of $\gamma X(\text{material}) \rightarrow e^+e^-X'$ in material, where the photon is produced in fragmentation of a quark or a gluon. The photon conversion tracks were not used for the $D^{*\pm}$ reconstruction, because they are secondary particles. The track pairs were removed by the following procedures. An invariant mass of an opposite charged track pair is calculated at a point of the closest approach between two helixes of a track pair. The tracks are assumed to have the electron mass. The track parameters, the curvature C, the azimuthal angle φ, and the cotangent of the polar angle $\cot\theta$ are calculated at the point. The cuts for removing the conversion track pairs are summarized in Table 4.1, where δS_{min} is the minimum separation distance between two helixes in the R-φ plane, δz is the z position difference between two tracks at the closest point, $\delta(\cot\theta)$ is the difference in track parameter $\cot\theta$'s between two tracks,

Table 4.1: Conversion selection cuts

Variables		Cut Values
$\lvert\delta S_{\min}\rvert$	$\leq$	0.1 cm
$\lvert\delta z\rvert$	$\leq$	3.0 cm
$\lvert\delta(\cot\theta)\rvert$	$\leq$	0.04
$M_{e^+e^-}$	$\leq$	0.1 GeV/c^2

and $M_{e^+e^-}$ is the invariant mass of a track pair assuming the tracks to be an electron and a positron. Figure 4.1 shows the distributions of the conversion selection variables in the photon candidate events. The track pairs in each plot passed all conversion selection cuts expect for the one in the plot. The distribution of a conversion radius R is shown in Fig. 4.2, where R is a distance from the center of the detector to the closest point of the two tracks in the R-φ plane. In the region of 20 cm $< R <$ 30 cm between the VTX and the CTC, the track pairs are enhanced after the conversion selection cuts (See solid line in Fig. 4.2). The track pairs which passed the conversion selection cuts and had in the range of 20 cm $< R <$ 30 cm were removed in the $D^{*\pm}$ reconstruction. Some signal tracks from the $D^{*\pm}$ decay are lost by the conversion cut. From a study using Monte Carlo events, the fraction of the signal which is excluded by the conversion cut is 3 % .

4.2.3 Removal of K^0_S and Λ candidate tracks

Particles from $\Lambda \rightarrow p\pi^-$ and $K^0_S \rightarrow \pi^+\pi^-$ decays were also removed in the $D^{*\pm}$ reconstruction. The candidates of $\Lambda \rightarrow p\pi^-$ and $K^0_S \rightarrow \pi^+\pi^-$

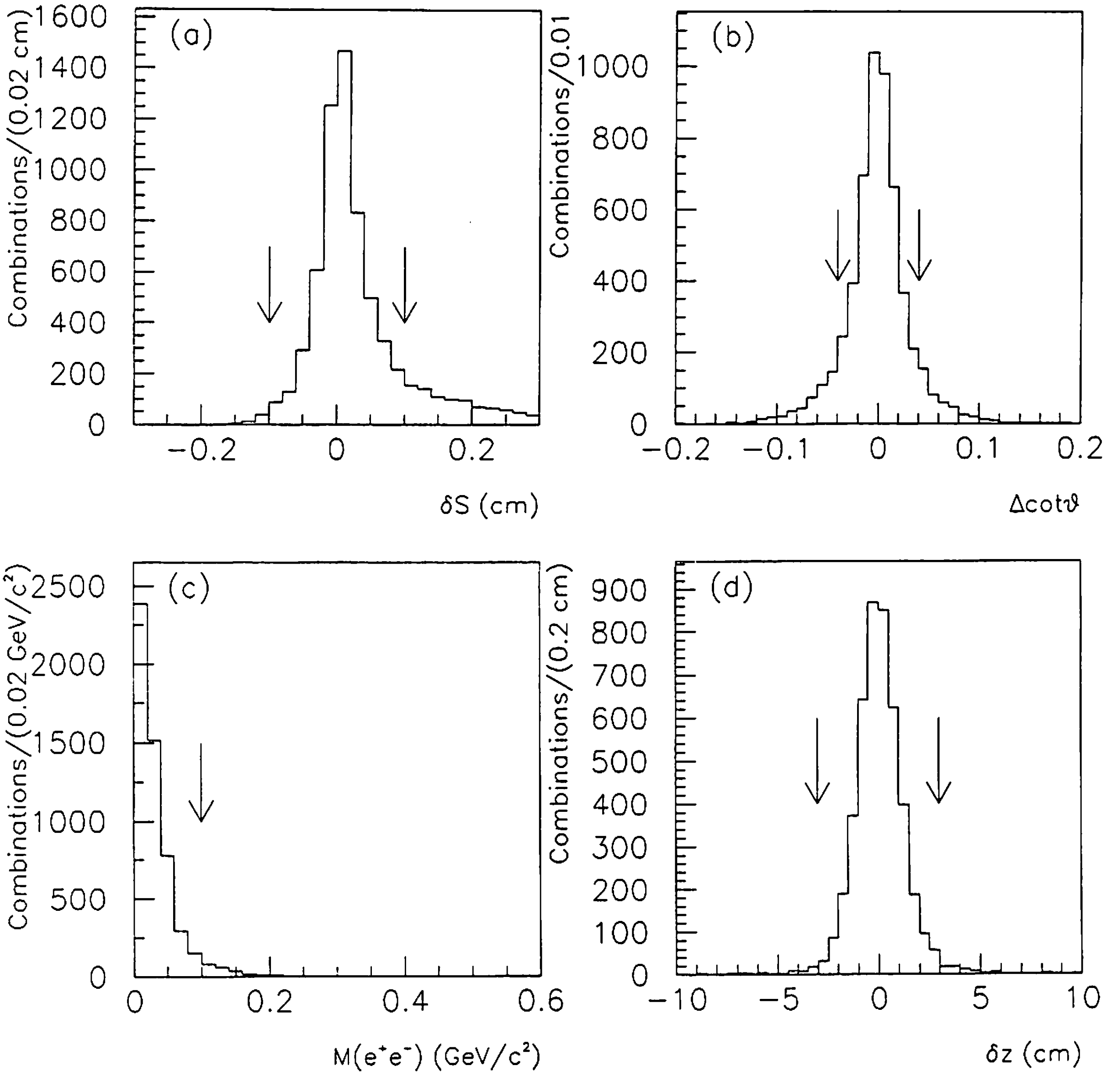

Figure 4.1: Distributions of the conversion selection variables: (a) separation distance, (b) difference of $\cot\theta$, (c) mass of two tracks, and (d) difference of z positions at the closest approach point of two tracks.

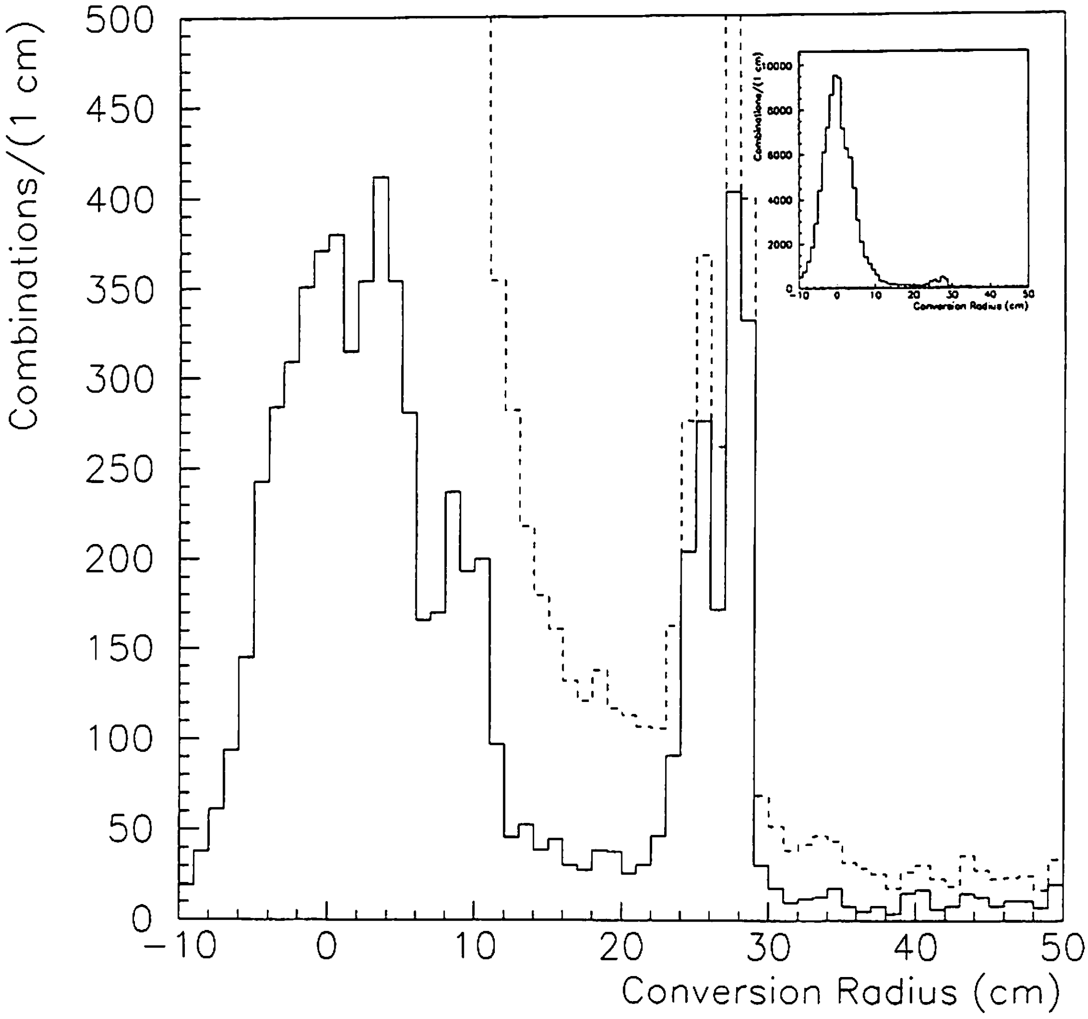

Figure 4.2: Conversion radius distributions. The broken line and the inset histogram show the distributions with the cuts of only δz and δS. The solid line shows that with all conversion selection cuts including $\delta(\cot\theta)$ and $M_{e^+e^-}$ cuts.

can be identified by reconstructing their secondary vertex positions. The secondary vertex fitting was carried out for all opposite electric charged track pairs. The momenta of the tracks were calculated using the fitted secondary vertex point. Figures 4.3 (a) and (b) show the invariant mass distributions of $\pi^+\pi^-$ and $p\pi^-$(and its charge conjugate), respectively, where the tracks were assumed to be a proton or a pion. The track p_T was required to be greater than 0.4 GeV/c. A fitted function of a gaussian plus a linear function was superimposed in each figure. The fitted masses were obtained to be 0.49649±0.00004 GeV/c^2 and 1.11580±0.00005 GeV/c^2 from the $\pi^+\pi^-$ and the $p\pi^-$ mass distributions, respectively, where the errors show only statistical ones. They are consistent with the world average K^0_S mass 0.49767 GeV/c^2 and Λ mass 1.11563 GeV/c^2 [18] within systematic errors. In order to exclude the K^0_S and the Λ candidate tracks, the combinations in the mass windows listed in Table 4.2 were removed in the $D^{*\pm}$ reconstruction.

Table 4.2: Mass cuts to select K^0_S and Λ candidates.

0.483	$\leq$	$M_{\pi^+\pi^-}$	$\leq$	0.513 (GeV/c^2)
1.112	$\leq$	$M_{p\pi}$	$\leq$	1.120 (GeV/c^2)

4.3 Constraint fit

The track position resolution in z direction is relatively worse than the R-φ position resolution in the CTC. In order to improve the position measurement of tracks, a constraint fit is used. The tracks assigned to

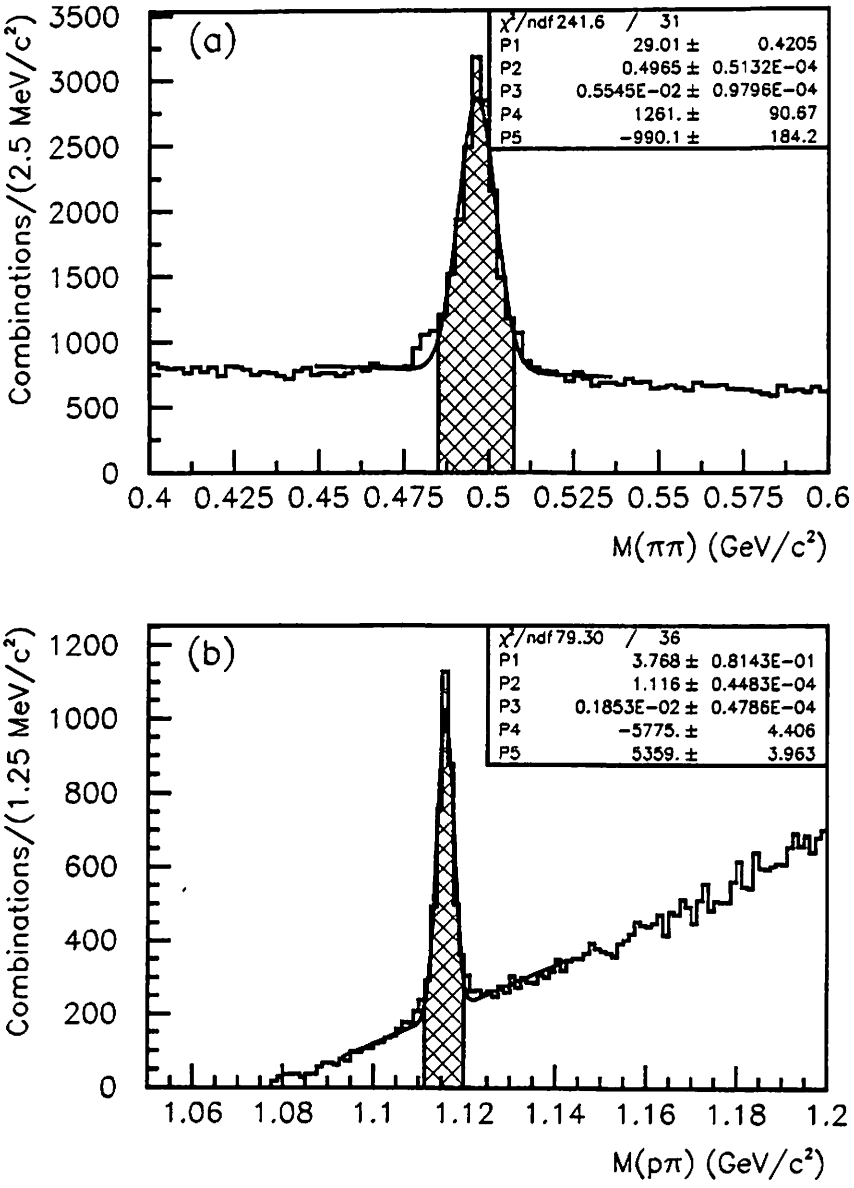

Figure 4.3: Mass distributions of $\pi^+\pi^-$ in (a) and $p\pi^-$ in (b). The transverse momenta of the tracks were required to be greater than 0.4 GeV/c.

a π_s particle from the $D^{*+} \to D^0\pi_s^+$ decay were constrained to pass the primary vertex positions in three-dimension. The tracks assigned to a K and a π particles from the $D^0 \to K^-\pi^+$(or $\to K^-\pi^-\pi^+\pi^+$) decay were constrained only to pass the primary vertex z position, because D^0 particle has a finite decay length. A Monte Carlo event sample was used for the study of the constraint fits. The particles from the decay of $D^{*+} \to D^0(\to K^-\pi^+)\pi_s^+$ were generated according to a predicted p_T distribution for the $\gamma + D^{*\pm}$ production with the PYTHIA event generator [23], and were simulated for the CDF detector. The distributions of the $K^-\pi^+$ mass M($K^-\pi^+$) and the mass difference $\Delta M = M(K^-\pi^+\pi_s^+) - M(K^-\pi^+)$ of the Monte Carlo events are shown in Fig. 4.4 . The distributions were fitted to a gaussian function. Figures 4.4 (a) and (b) show the distributions of the $K^-\pi^+$ mass and the mass difference which were calculated using the original fitted track parameters before the constraint fit. Figures 4.4 (c) and (d) show those which were calculated using the constraint fit track parameters. The mass resolutions are improved after the constraint fit as shown in Fig. 4.4.

4.4 $D^{*+} \to D^0(\to K^-\pi^+) + \pi^+$

In a photon candidate event, a $D^{*\pm}$ meson through the sequential decay of $D^{*+} \to D^0\pi_s^+ \to K^-\pi^+\pi_s^+$ was reconstructed by taking combinations of tracks. We took all possible combinations of the tracks, retaining the electric charge correlation, namely; $K^\mp\pi^\pm\pi_s^\pm$. The masses of tracks assigned to K and π were assumed to be kaon mass (=0.493646 GeV/c^2) and pion mass (=0.1395675 GeV/c^2), respectively. For a $K^-\pi^+\pi_s^+$ or

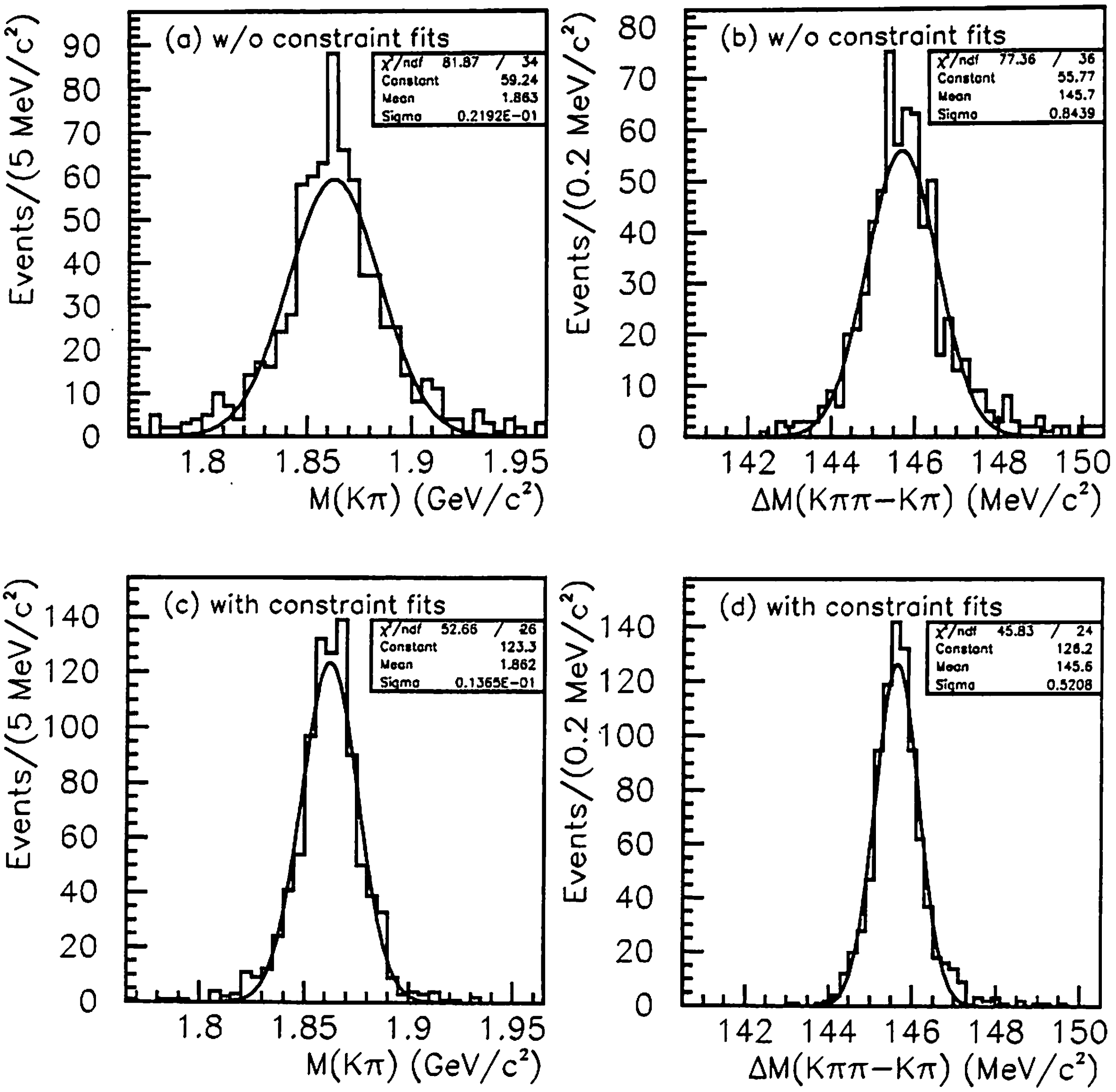

Figure 4.4: $M(K^-\pi^+)$ and $\Delta M(K^-\pi^+\pi_s^+ - K^-\pi^+)$ distributions of the simulated $D^{*+} \to D^0(\to K^-\pi^+)\pi_s^+$ events: (a) and (b) show those before the constraint fits; (c) and (d) show those after the constraint fits.

$K^+\pi^-\pi_s^-$ combination, a $K^\mp\pi^\pm$ invariant mass and a mass difference between $K^\mp\pi^\pm\pi_s^\pm$ and $K^\mp\pi^\pm$ systems were calculated.

4.4.1 Kinematical cuts

As a main background in the $D^{*\pm}$ detection, "combinatorial background" is considered. The combinatorial background is an event in which random track combinations accidentally fall onto the mass window. Figure 4.5 shows a track multiplicity distribution in the photon candidate events, where the photon candidates passed the photon selection cuts and the track transverse momentum p_T was required to be larger than 0.4 GeV/c. The photon candidate sample mainly contains a prompt photon (or a neutral meson) + a light quark (or gluon) events. The average charged track multiplicity is about 20. Therefore, the combinations of the tracks become around 900 in an event, and the combinatorial background events will be much larger than the expected signal events without any cuts. In order to eliminate the combinatorial background events, some kinematical cuts were applied. The kinematical cuts were determined from their distributions of real events or $\gamma + D^{*\pm}$ Monte Carlo events. The variables of the kinematical cuts are described below:

- p_T : Transverse momenta of tracks.

  The transverse momentum cut is effective to reduce the combinatorial background. The track momenta of K, π, and π_s were required to be larger 1.0 GeV/c, 0.7 GeV/c, and 0.4 GeV/c, respectively. The transverse momentum p_T distributions of K, π, and π_s in the Monte Carlo

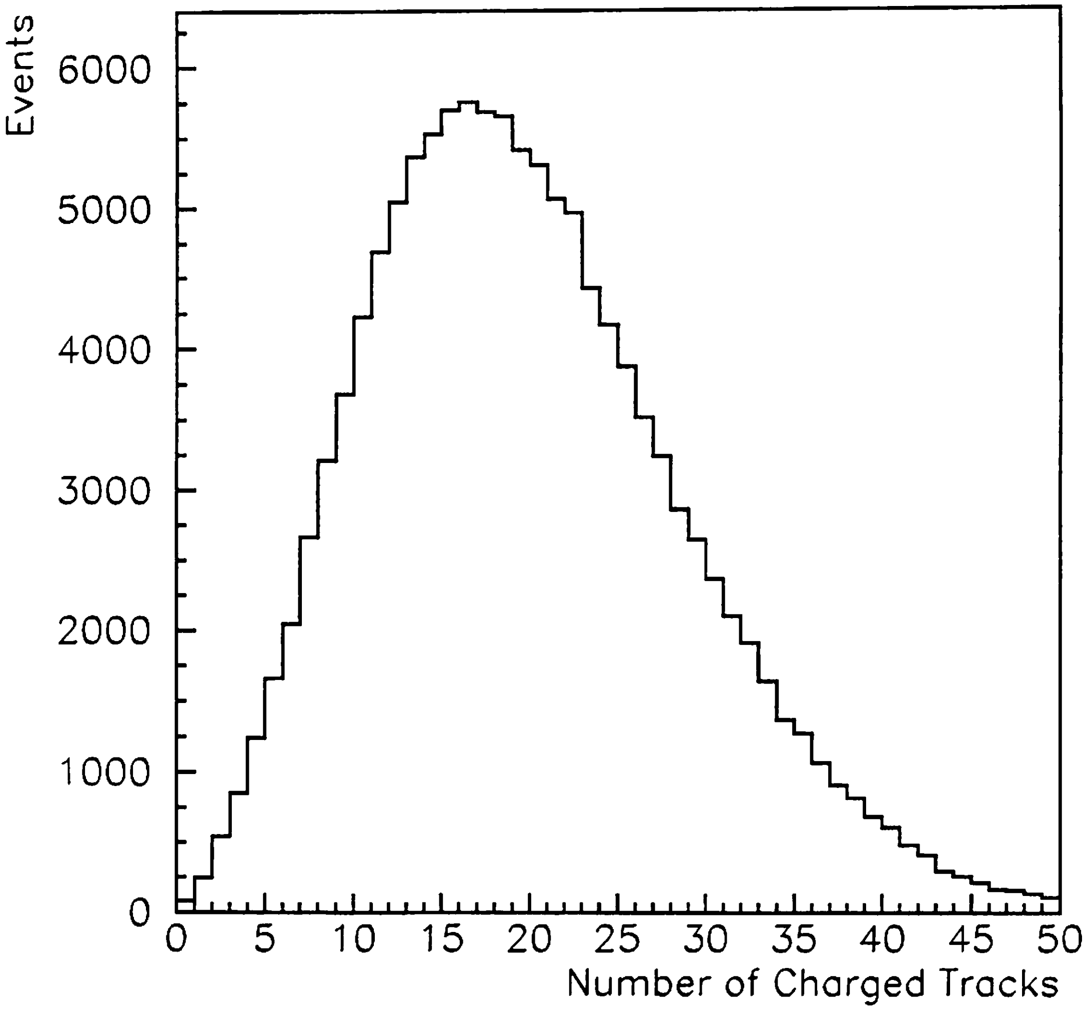

Figure 4.5: Track multiplicity distribution in the photon candidate events.

$\gamma+D^{*\pm}$ events are shown in Figs. 4.6 (a), (b), and (c), respectively. The p_T cut values were taken to be relatively low for the Monte Carlo events. In order to study the combinatorial background events, we prepared a loose track p_T cut, which is $p_T > 0.4$ GeV/c for K, π, and π_s.

- $M(K^-\pi^+)$: Invariant mass of $K^-\pi^+$.

  An invariant mass of the assigned $K^-\pi^+$ system was restricted in a mass window around true D^0 mass. A combination whose $M(K^-\pi^+)$ is within 30 MeV/c^2 around true D^0 mass 1.8646 GeV/c^2 [18] was used for the reconstruction.

- $p_T(D^{*\pm})$: Transverse momentum of a $D^{*\pm}$.

  The transverse momentum of a $D^{*\pm}$ system was required to be larger than 6 GeV/c. The $D^{*\pm}$ p_T distribution in the $\gamma + D^{*\pm}$ Monte Carlo events are shown in Fig. 4.7.

The $D^{*\pm}$ selection cut values are summarized into the Table 4.3.

4.4.2 Elimination of duplicate events

The $D^{*\pm}$ reconstruction was carried out through all possible combinations of tracks without particle identification. Therefore, some duplicate combinations in an event come in a ΔMdistribution. To eliminate the duplicate entries, we chose a $K\pi$ combination with the closest D^0 mass to the P.D.G. value of 1.8646 GeV/c^2 [18] and chose π_s by requiring the highest $D^{*\pm}$ momentum in an event.

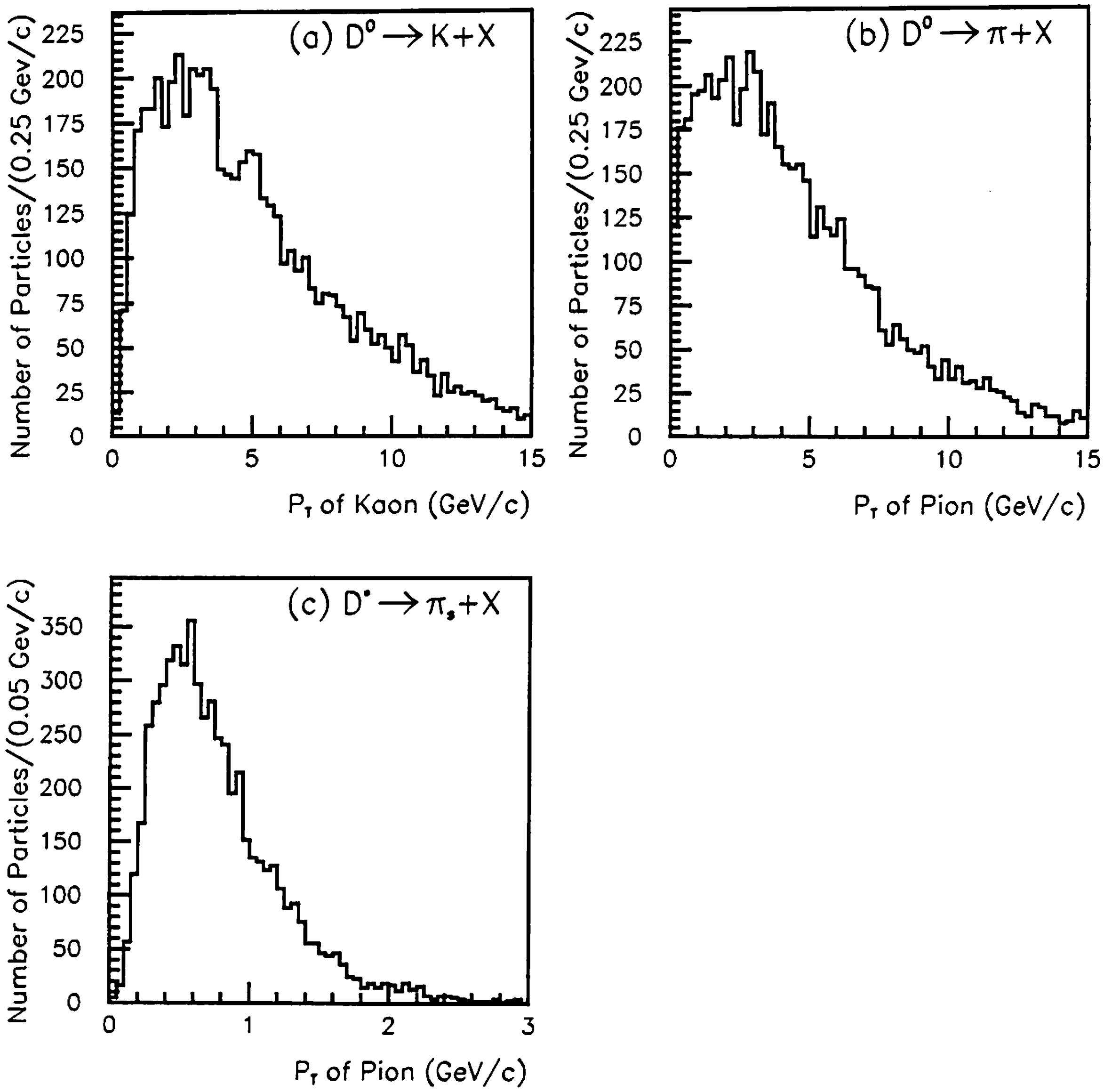

Figure 4.6: p_T distributions of K,π, and π_s in the $\gamma+D^{*\pm}$ events generated with PYTHIA.

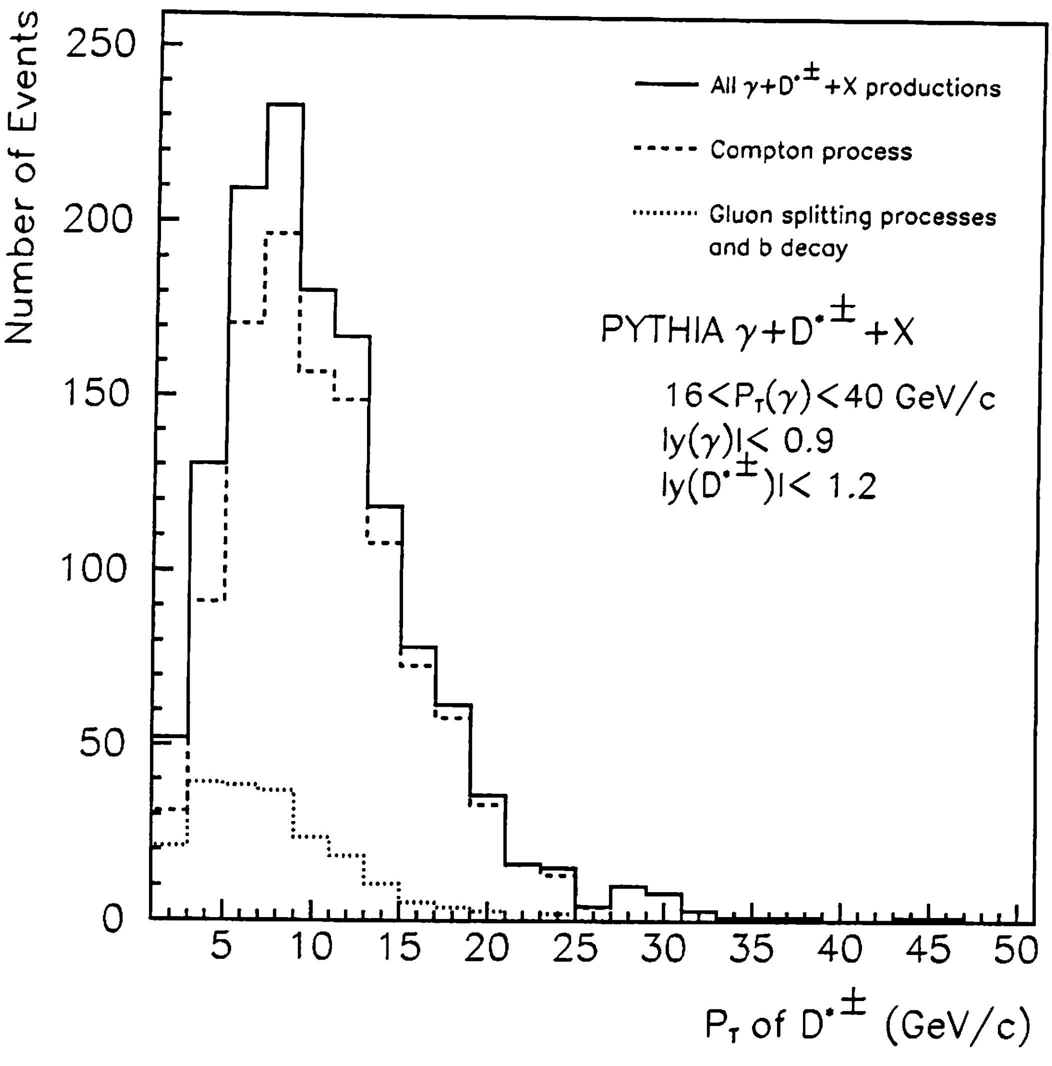

Figure 4.7: $p_T(D^{*\pm})$ distribution in the $\gamma + D^{*\pm}$ Monte Carlo events. The solid line shows that containing the Compton, the gluon splitting, and b quark decay processes. The dashed line shows that of the Compton process, and the dotted line shows that of the gluon splitting and b quark decay processes.

Table 4.3: Summary of the $D^{*\pm}$ selection cuts.

		Loose cut	Tight cut (A)	Tight cut (B)
p_T of K	$>$	0.4	1.0	1.0 GeV/c
p_T of π	$>$	0.4	0.7	0.7 GeV/c
p_T of π_s	$>$	0.4	0.4	0.4 GeV/c
$\lvert M(K^-\pi^+) - M_{D^0}\rvert$	$<$	30	30	30 MeV/c^2
$p_T(D^{*\pm})$	$>$	0	0	6 GeV/c

4.4.3 Reconstruction with loose cut

First of all, we show the ΔM distribution with the loose cut. Figure 4.8 shows the $M(K^-\pi^+)$ distribution of all combinations and the $\Delta M(K^-\pi^+\pi_s^+ - K^-\pi^+)$ distribution in the photon candidate events with the loose cut, where the photons pass the photon selection cuts. In Fig. 4.8 (b), the $K^-\pi^+$ mass was restricted in the D^0 mass window, $1.835 < M(K^-\pi^+) < 1.895$ GeV/c^2, shown as the shaded area in Fig. 4.8 (a). A significant peak was observed at $\Delta M = 145.5$ MeV/c^2. The ΔM distribution was fitted to a function of

$$\frac{\mathrm{P1}}{\sqrt{2\pi}\mathrm{P3}} \times \exp\left(-\frac{1}{2}\left(\frac{\Delta M - \mathrm{P2}}{\mathrm{P3}}\right)^2\right) + \mathrm{P4} \times (\Delta M - m_\pi)^{\mathrm{P5}},$$

where P1, P2, P3, P4, and P5 are the fitting parameters, and m_π is the pion mass. The fitted function was superimposed in Fig. 4.8 (b). The fitted ΔM value was obtained to be 145.5 ± 0.3 MeV/c^2, where the error shows statistical one. This is consistent with the world average mass difference $M(D^{*+}) - M(D^0)$=145.42 MeV/c^2 [18] within the statistical error.

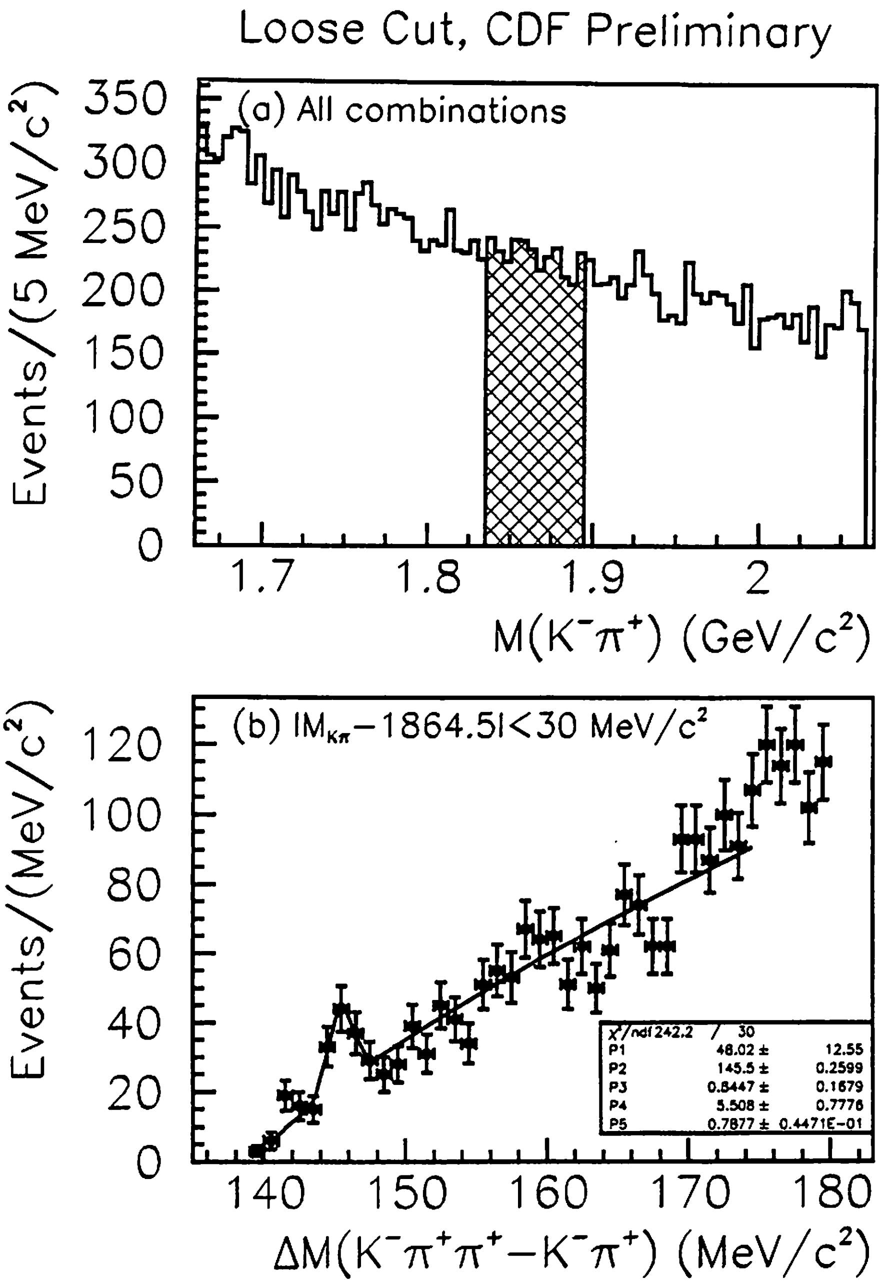

Figure 4.8: $M(K^-\pi^+)$ and ΔM distributions in the photon candidate events: (a) $K^-\pi^+$ mass distribution of all combinations, (b) mass difference $\Delta M(K^-\pi^+\pi_s^+ - K^-\pi^+)$ distribution of the events selected within the D^0 mass window. The D^0 mass window is shown as the hatched area in (a).

In order to confirm that the $D^{*\pm}$ signal contains $D^0 \to K^-\pi^+$, the $K^-\pi^+$ mass was relaxed, and the mass difference was restricted within 1.5 MeV/c^2 around $\Delta M = 145.5$ MeV/c^2 as seen in Fig. 4.9 (a) (hatched area). Figure 4.9 (b) shows the $K^-\pi^+$ mass distribution of the events in the $D^{*\pm}$ signal window of $144 < \Delta M < 147$ MeV/c^2. In the figure, the $D^0 \to K^-\pi^+$ signal peak was observed at $M(K\pi) = 1.865$ GeV/c^2. The distribution was fitted to a function of

$$\frac{\mathrm{P1}}{\sqrt{2\pi}\mathrm{P3}} \times \exp\left(-\frac{1}{2}\left(\frac{M_{K\pi} - \mathrm{P2}}{\mathrm{P3}}\right)^2\right) + \mathrm{P4} + \mathrm{P5} \times M_{K\pi},$$

where $M_{K\pi}$ is the $K\pi$ mass, and P1, P2, P3, P4, and P5 are the fitting parameters. The fitted function was superimposed in Fig. 4.9 (b). The fitted D^0 mass was 1.863 ± 0.006 GeV/c^2, which is consistent with the D^0 world average mass of 1.8646 GeV/c^2 [18] within the statistical error.

Figure 4.10 shows a scatter plot of azimuthal angles of the photon and the $D^{*\pm}$ candidates. The $D^{*\pm}$ candidates were selected within 1.5 MeV/c^2 around $\Delta M = 145.5$ MeV/c^2 in the ΔM distribution, which was shown as the hatched area in the inset histogram. Most of the $D^{*\pm}$ candidates are in opposite side of the photon candidates in the R-φ plane. This indicates that the photon and the $D^{*\pm}$ (or charm quark) are produced back-to-back in the R-φ plane.

4.4.4 Reconstruction with tight cut(A)

We require the tight p_T cuts for the charged tracks without the $p_\mathrm{T}(D^{*\pm})$ cut. The requirements are $p_\mathrm{T} > 1.0$ GeV/c, 0.7 GeV/c, and 0.4 GeV/c for assigned K, π, and π_s tracks, respectively. The ΔM and the $K^-\pi^+$ mass distributions after applying the tight p_T cuts are shown in Figs. 4.11

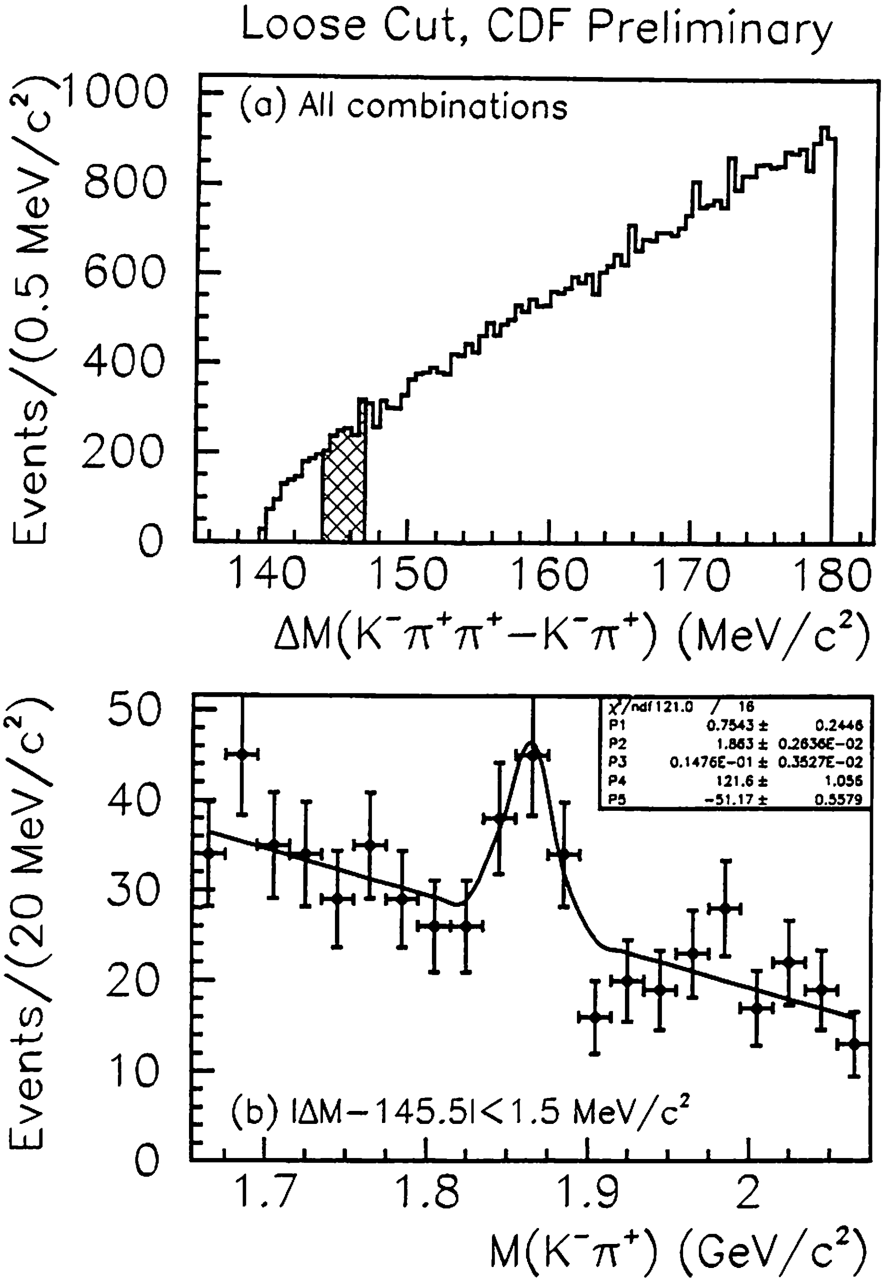

Figure 4.9: ΔM and $M(K^-\pi^+)$ distributions in the photon candidate events: (a) Mass difference $\Delta M(K^-\pi^+\pi_s^+ - K^-\pi^+)$ distribution of all combinations, (b) $K^-\pi^+$ mass distribution of the events selected within the $D^{*\pm}$ signal window($|\Delta M - 145.5| < 1.5$ MeV/c^2). The window is shown as the hatched area in (a).

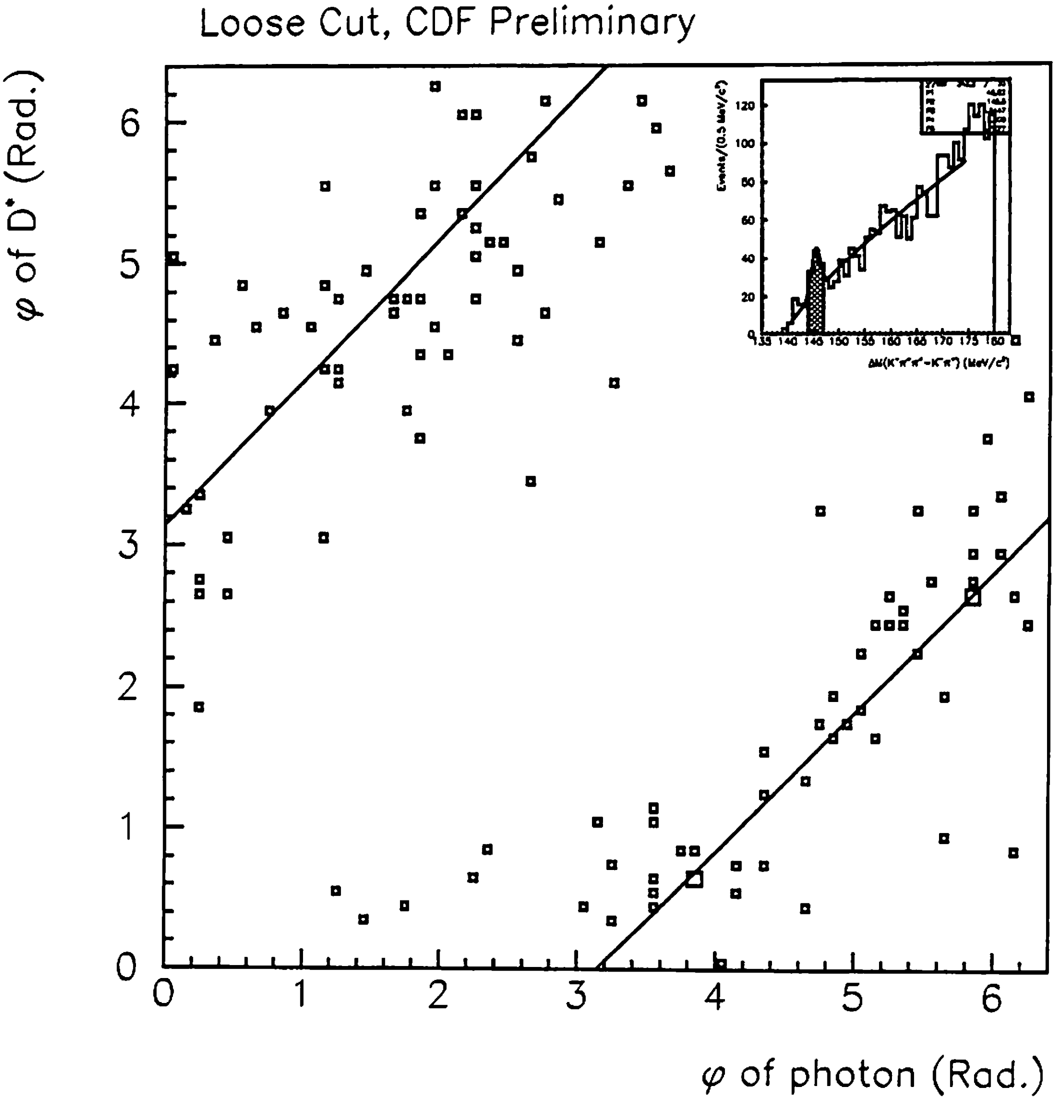

Figure 4.10: Scatter plot between azimuthal angles of the photon and the $D^{*\pm}$ candidates. The $D^{*\pm}$ candidates were selected in the $D^{*\pm}$ signal window, which is shown in the inset histogram as the hatched area.

and 4.12. The $D^{*\pm}$ and the D^0 signals are observed. The ratio of signal and background is improved after the tight p_{T} cuts.

4.4.5 Reconstruction with tight cut(B)

Furthermore, the $p_{\mathrm{T}}(D^{*\pm})$ cut was applied to $K^-\pi^+\pi_s^+$ systems in order to reduce the combinatorial backgrounds. Figures 4.13 (a) and (b) show the $p_{\mathrm{T}}(D^{*\pm})$ distributions of the $D^{*\pm}$ candidates and backgrounds, respectively, where the background events were taken by combining the D^0 candidate with a track in another event. We chose the $p_{\mathrm{T}}(D^{*\pm})$ threshold to be 6 GeV/c.

After all the selection cuts including the $p_{\mathrm{T}}(D^{*\pm})$ cut, the $K^-\pi^+$ mass distribution for all combinations and the ΔM distribution in the photon candidate events are shown in Fig. 4.14, where the $K^-\pi^+$ mass forming a D^0 particle was required to be in the D^0 mass window. The D^0 mass window ($|M(K^-\pi^+)-1865| < 30$ MeV/c^2) was shown as the hatched area in Fig. 4.14 (a). On the other hand, $M(K^-\pi^+)$ distribution with a mass difference ΔM within $|\Delta M - 145.5| <1.5$ MeV/c^2 is shown in Fig. 4.15. The significant peaks at $\Delta M = 145.5$ MeV/c^2 and at $M(K^-\pi^+) = 1.865$ GeV/c^2 are observed in Fig. 4.14 (b) and Fig. 4.15 (b) after the $p_{\mathrm{T}}(D^{*\pm})$ cut, respectively. The fitted D^0 mass and mass difference are $M(K^-\pi^+) = 1.862 \pm 0.004$ GeV/c^2 and $\Delta M = 145.5 \pm 0.2$ MeV/c^2, respectively, where the errors are statistical ones. They are consistent with the world averages [18] of $M(D^0) = 1.8645$ GeV/c^2 and $M(D^{*+}) - M(D^0)$=145.42 MeV/c^2 within statistical errors.

To show that the peaks do not accidentally come out, the ΔM and the $K^-\pi^+$ mass distributions in the side band region are shown in Fig. 4.16.

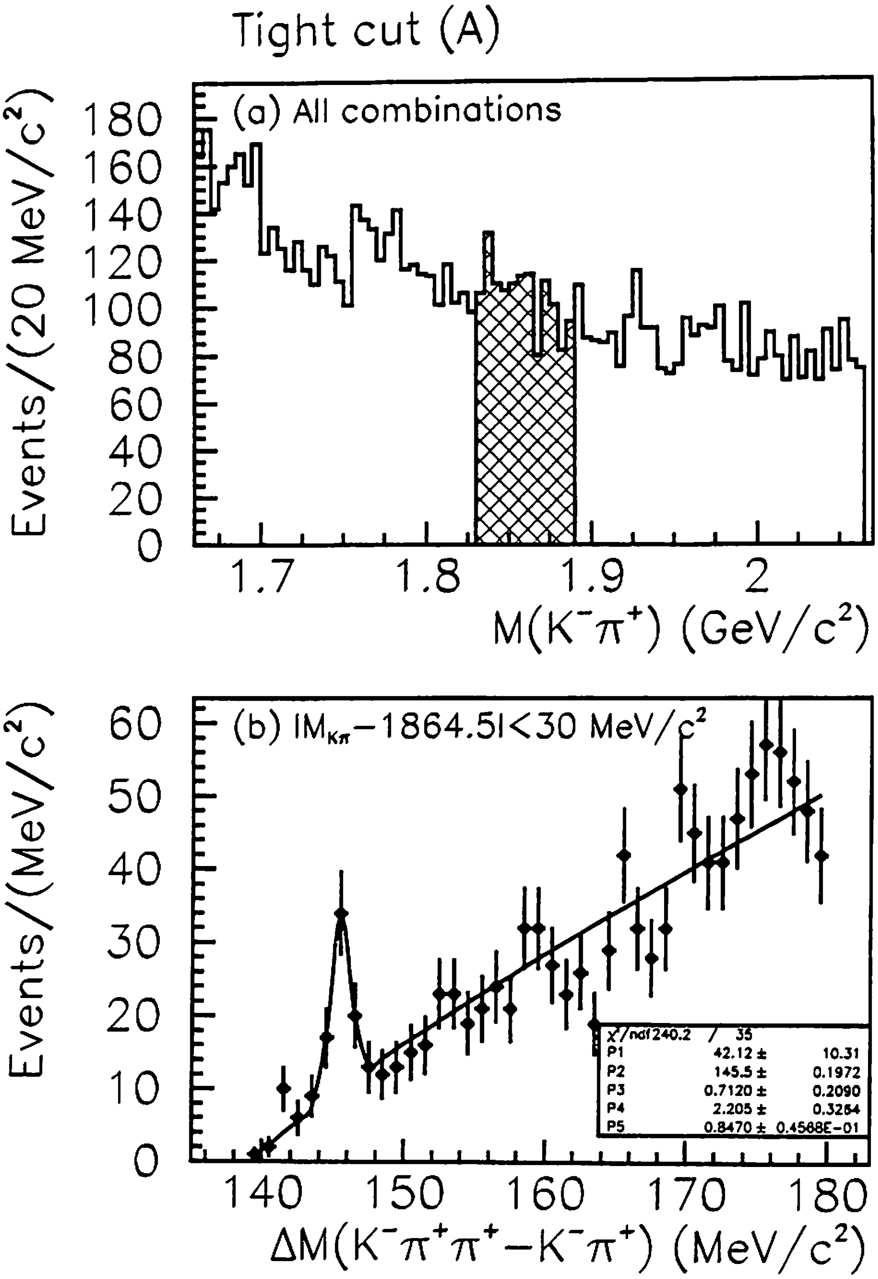

Figure 4.11: $M(K^-\pi^+)$ and ΔM distributions in the photon candidate events: (a) $K^-\pi^+$ mass distribution of all combinations, (b) mass difference $\Delta M(K^-\pi^+\pi_s^+ - K^-\pi^+)$ distribution of the events selected within the D^0 mass window. The window is shown as the hatched area in (a). The tight p_T cuts were applied.

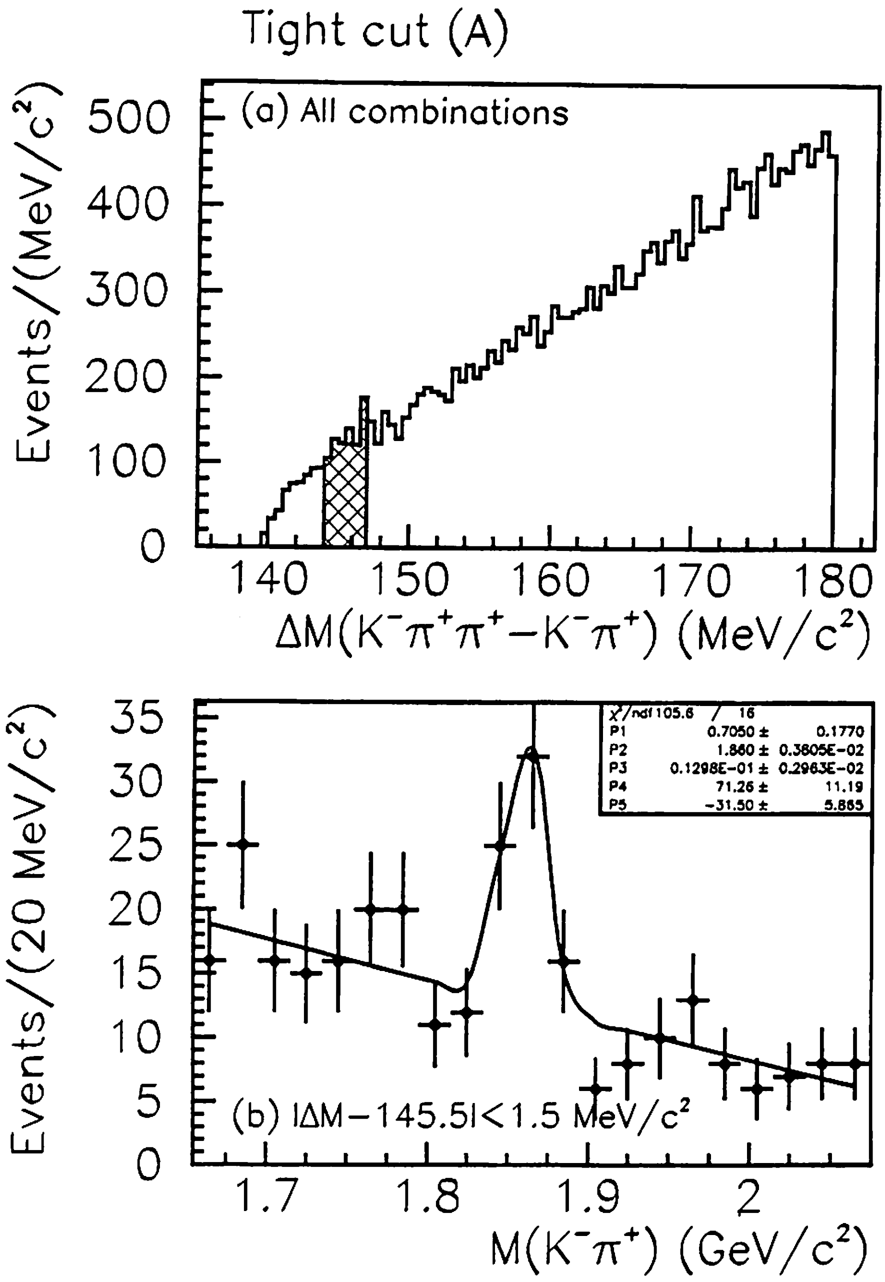

Figure 4.12: ΔM and $M(K^-\pi^+)$ distributions in the photon candidate events: (a) Mass difference $\Delta M(K^-\pi^+\pi_s^+ - K^-\pi^+)$ distribution of all combinations, (b) $K^-\pi^+$ mass distribution of the combinations selected within the $D^{*\pm}$ signal window($|\Delta M - 145.5| < 1.5\,\mathrm{MeV}/c^2$). The window is shown as the hatched area in (a). The tight p_T cuts were applied.

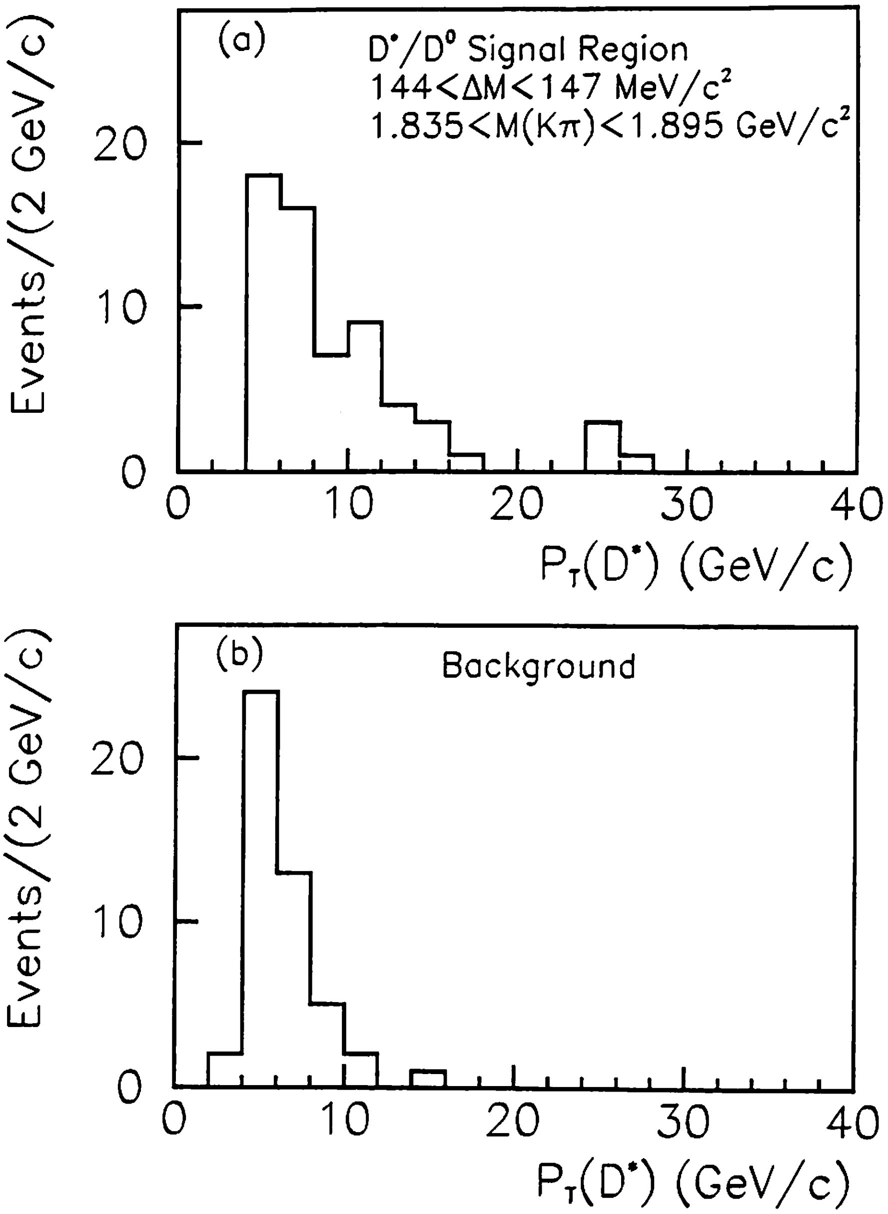

Figure 4.13: $p_T(D^{*\pm})$ distributions of (a) the $D^{*\pm}$ candidates (b) the background. The $D^{*\pm}$ candidates were selected within 144 < ΔM< 147 MeV/c^2.

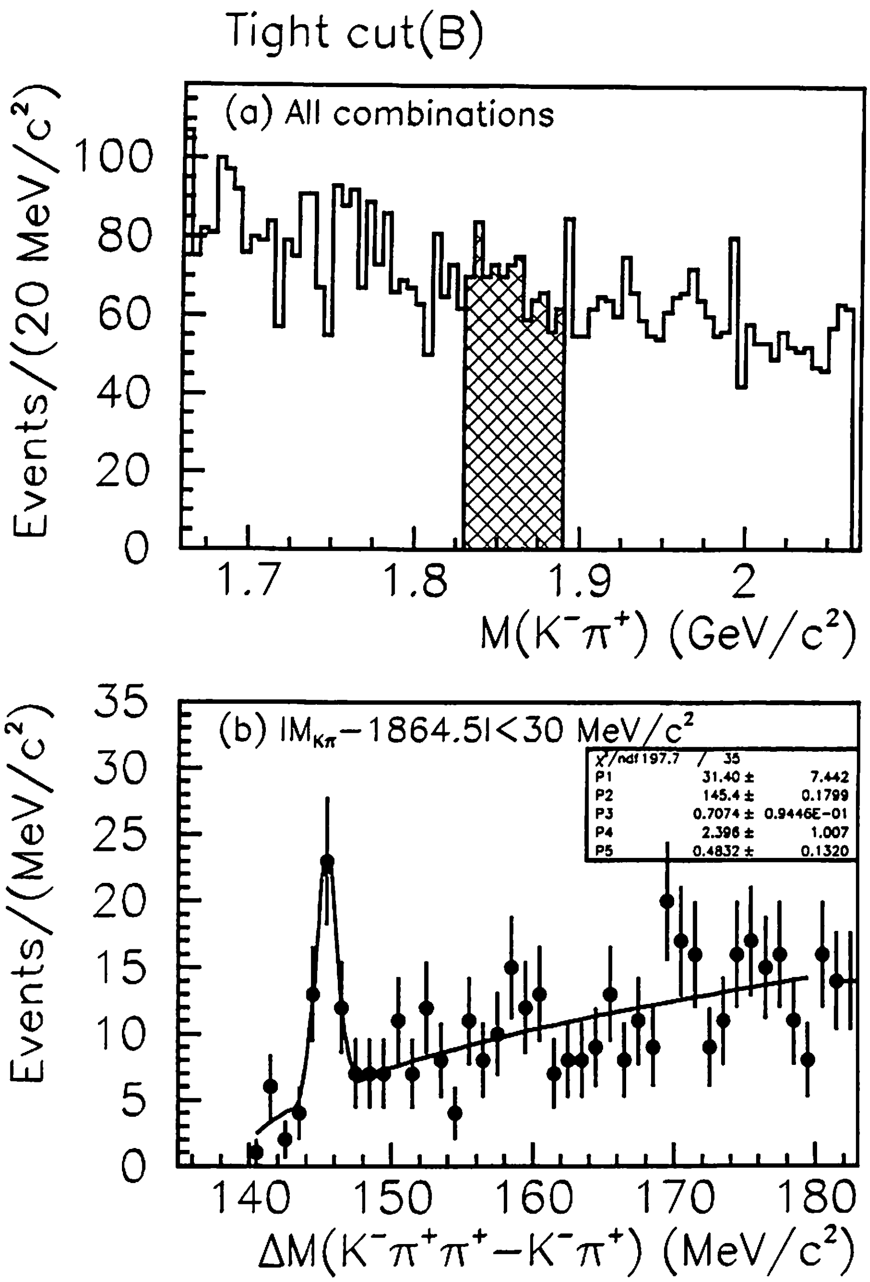

Figure 4.14: $M(K^-\pi^+)$ and $\Delta M(K^-\pi^+\pi_s^+ - K^-\pi^+)$ distributions in the photon candidate events after the tight track p_T cuts and the $p_T(D^{*\pm})$ cut: (a) $K^-\pi^+$ mass distribution for all combinations, (b) mass difference $\Delta M(K^-\pi^+\pi_s^+ - K^-\pi^+)$ distribution of the events which are selected in the D^0 mass window ($|M(K\pi) - 1.865)|$ <30 MeV/c^2) of the hatched area in (a).

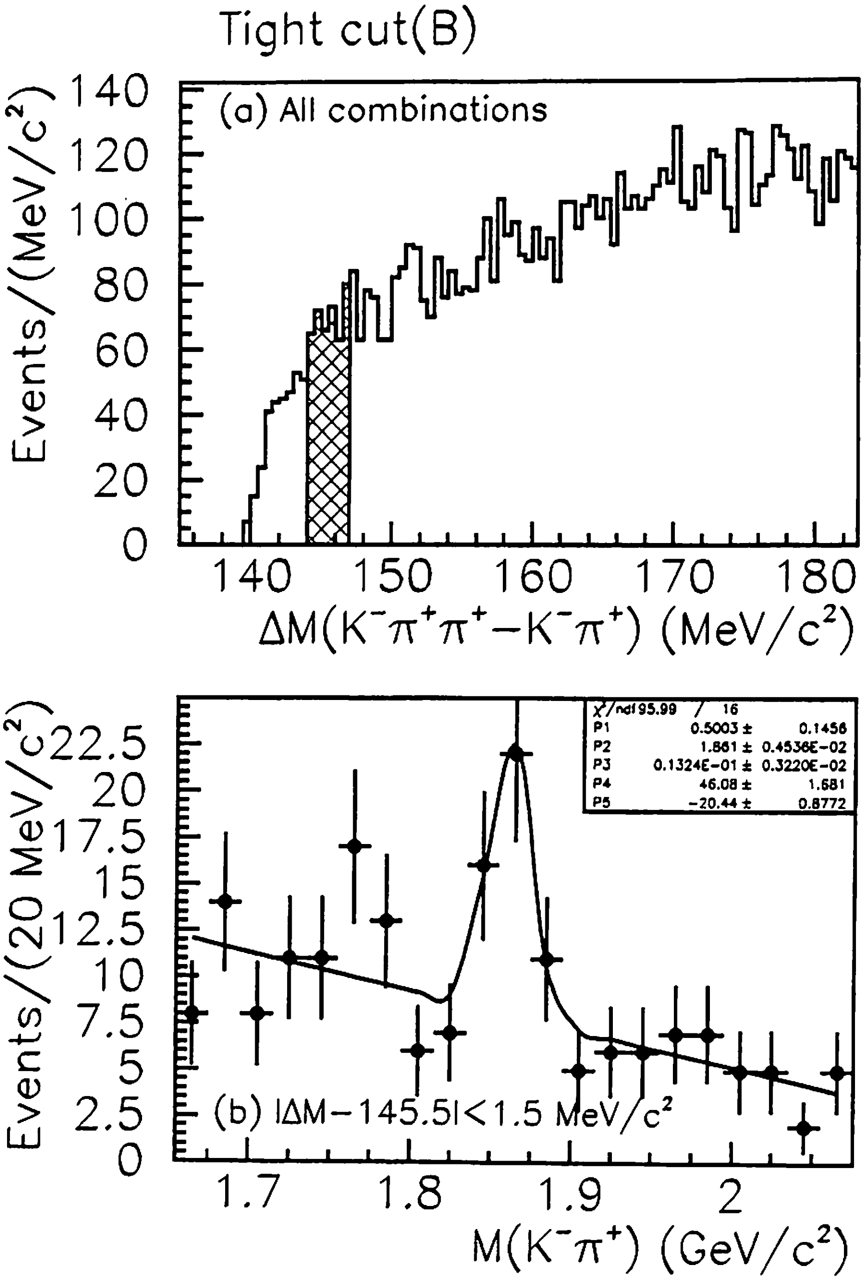

Figure 4.15: $\Delta M(K^-\pi^+\pi_s^+ - K^-\pi^+)$ and $M(K^-\pi^+)$ distributions in the photon candidate events after the tight track p_T cuts and the $p_T(D^{*\pm})$ cut: (a) $\Delta M(K^-\pi^+\pi_s^+ - K^-\pi^+)$ distribution for all combinations, (b) $K^-\pi^+$ mass distribution of the events which are selected in the $D^{*\pm}$ signal window ($|\Delta M - 145.5| < 1.5$ MeV/c^2) of the hatched area in (a).

The side band events were taken in $1.895 < M(K^-\pi^+) < 1.915$ GeV/c^2 for the ΔM distribution in Fig. 4.16 (a), and $3.5< |\Delta M - 145.5| < 5$ MeV/c^2 for the $M(K^-\pi^+)$ distribution in Fig. 4.16 (b). These side band regions are shown as the shaded areas in the inset histograms.

We show a background ΔM distribution using a fake $D^{*\pm}$, where the fake $D^{*\pm}$ is made by a D^0 candidate and a track in another event. The background ΔM distribution is shown in Fig. 4.17 as a hatched histogram. The number of the fake $D^{*\pm}$ events were normalized by that of the data out of the signal region.

No peak is observed in the side band ΔM and the background ΔM distributions. We conclude that the observed $D^{*\pm}$ peak does not accidentally come up from random track combinations.

We also show that the particles from other charm meson or baryon decays do not make a significant peak in the ΔM distribution. We checked this by using PYTHIA Monte Carlo data. The Monte Carlo events were generated with PYTHIA and were simulated for the CDF detector. They contain all charm mesons and baryon decays except for the $D^{*+} \to D^0(\to K^-\pi^+)\pi^+$ decay. The event sample corresponds to 38.4 pb^{-1} data. No significant peak was seen in the plot around the $D^{*\pm}$ signal region as shown in Fig. 4.18. Therefore, we conclude that other charm meson and baryon decays do not contribute to the peak in the ΔM distribution.

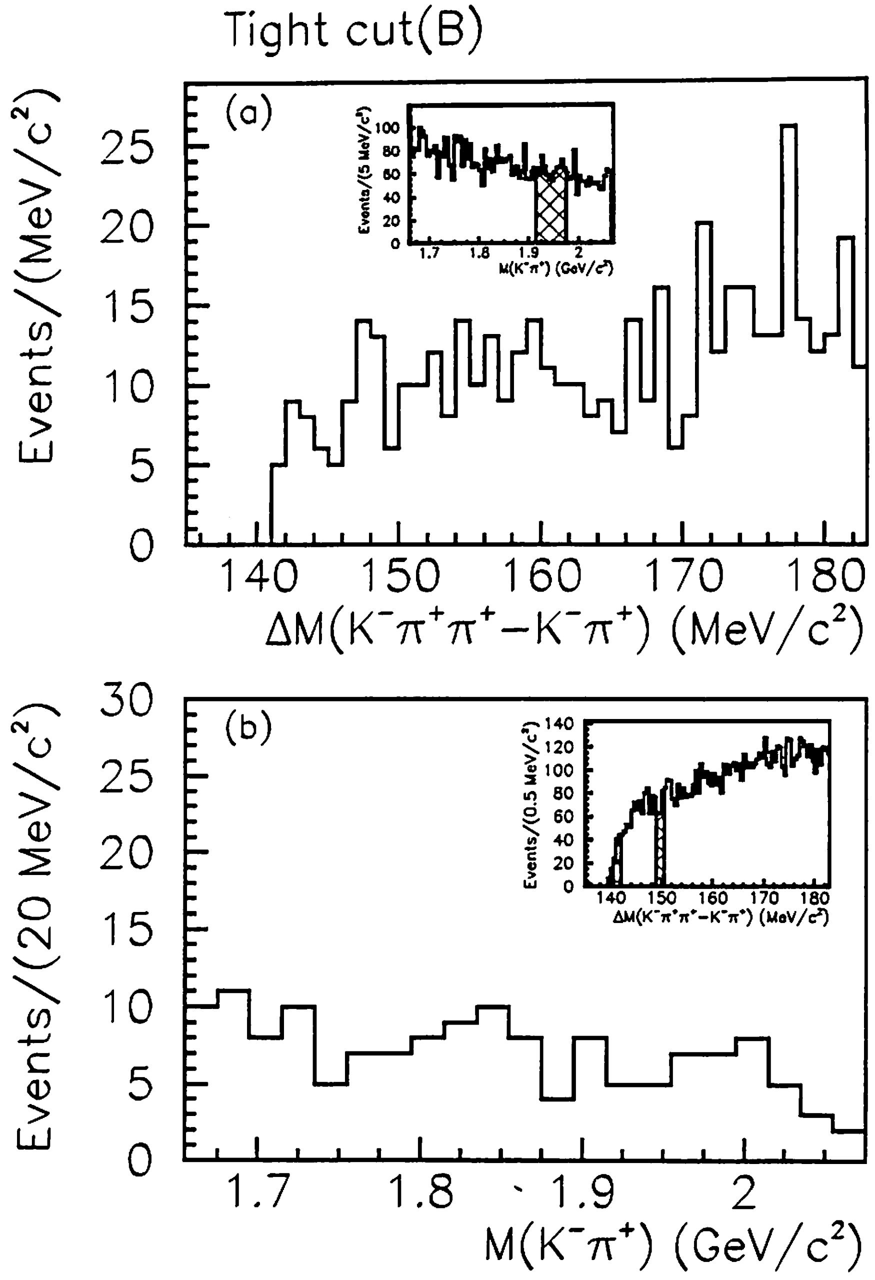

Figure 4.16: $\Delta M(K^-\pi^+\pi_s^+ - K^-\pi^+)$ and $M(K^-\pi^+)$ distributions in the side band regions shown as the hatched areas in the inset histograms.

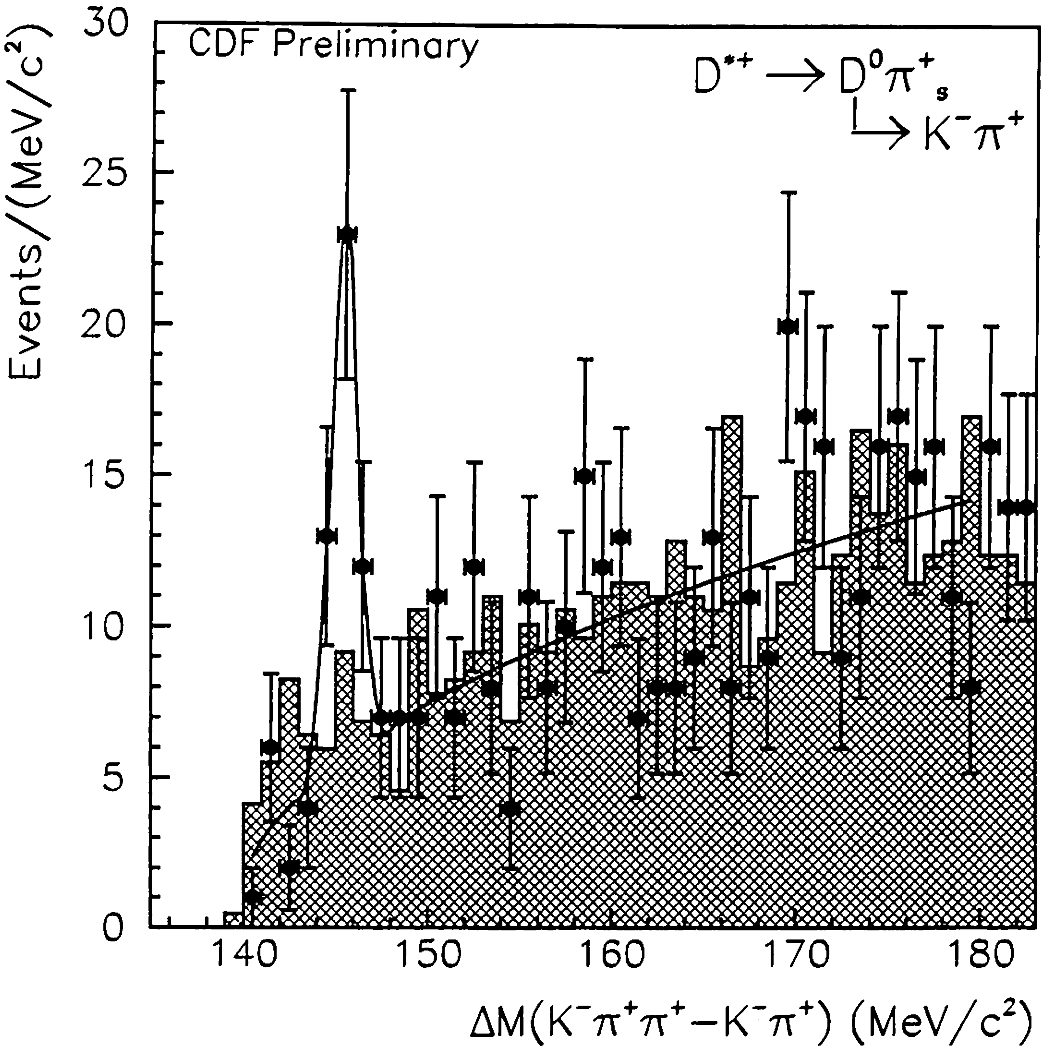

Figure 4.17: The background ΔM distribution compared with the data. The plots show the data, and the hatched histogram shows the background.

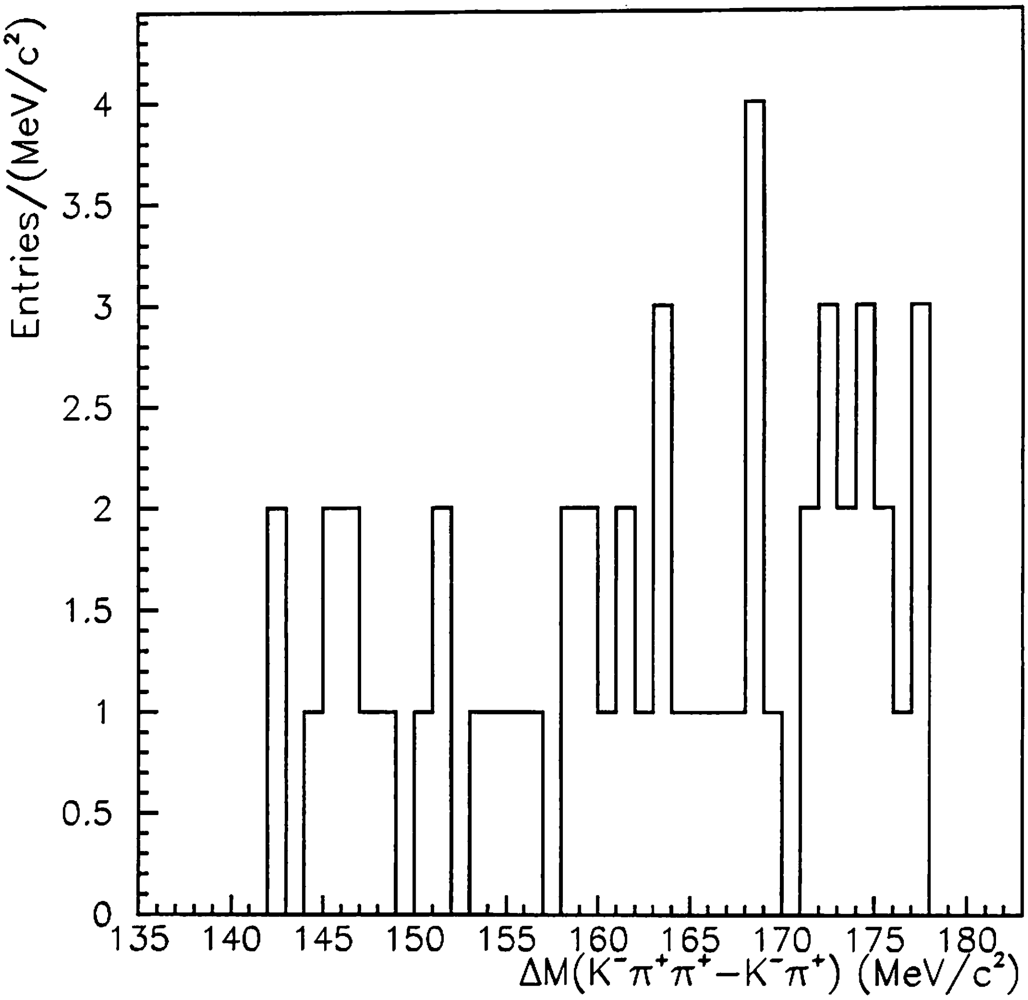

Figure 4.18: ΔM distribution of the Monte Carlo $\gamma + D^{*\pm}$ events, whose events do not contain the decay of $D^{*\pm} \rightarrow D^0\pi^\pm \rightarrow K^\mp\pi^\pm\pi^\pm$.

4.5 $D^{*+} \to D^0(\to K^-\pi^-\pi^+\pi^+) + \pi_s^+$

For the $D^{*\pm}$ reconstruction using the $D^0 \to K^-\pi^-\pi^+\pi^+$ decay mode, we also took all possible track combinations, retaining the electric charge correlation, namely,

$$K^\mp\pi^\mp\pi^\pm\pi^\pm + \pi_s^\pm.$$

The tracks were assumed to be a kaon or a pion. The kinematical cuts are summarized in Table 4.4, which contain the charged track p_T cuts, the D^0 mass restriction, the $D^{*\pm}$ transverse momentum cut. The kinematical cuts are tighter than those for the reconstruction using $D^0 \to K^-\pi^+$, because of a larger number of combinations. Figure 4.19 shows p_T distributions of K, π, and π_s particles in the $\gamma + D^{*\pm}$ Monte Carlo events.

Table 4.4: $D^{*\pm}$ selection cuts for the $D^0 \to K^-\pi^-\pi^+\pi^+$ mode.

		Cuts
p_T of K	$>$	2.0 GeV/c
Leading p_T of π's	$>$	1.5 GeV/c
p_T of π's	$>$	0.5 GeV/c
p_T of π_s	$>$	0.4 GeV/c
$\lvert M(D^0) - 1864.5\rvert$	$<$	20 MeV/c^2
$p_T(D^{*\pm})$	$>$	6 GeV/c

We show the ΔM distributions in the inclusive photon events after the kinematical cuts except for the $p_T(D^{*\pm})$ cut in Figure 4.20. A $D^{*\pm}$ signal was observed at $\Delta M = 145.5$ MeV/c^2 above a large number of the combinatorial background events.

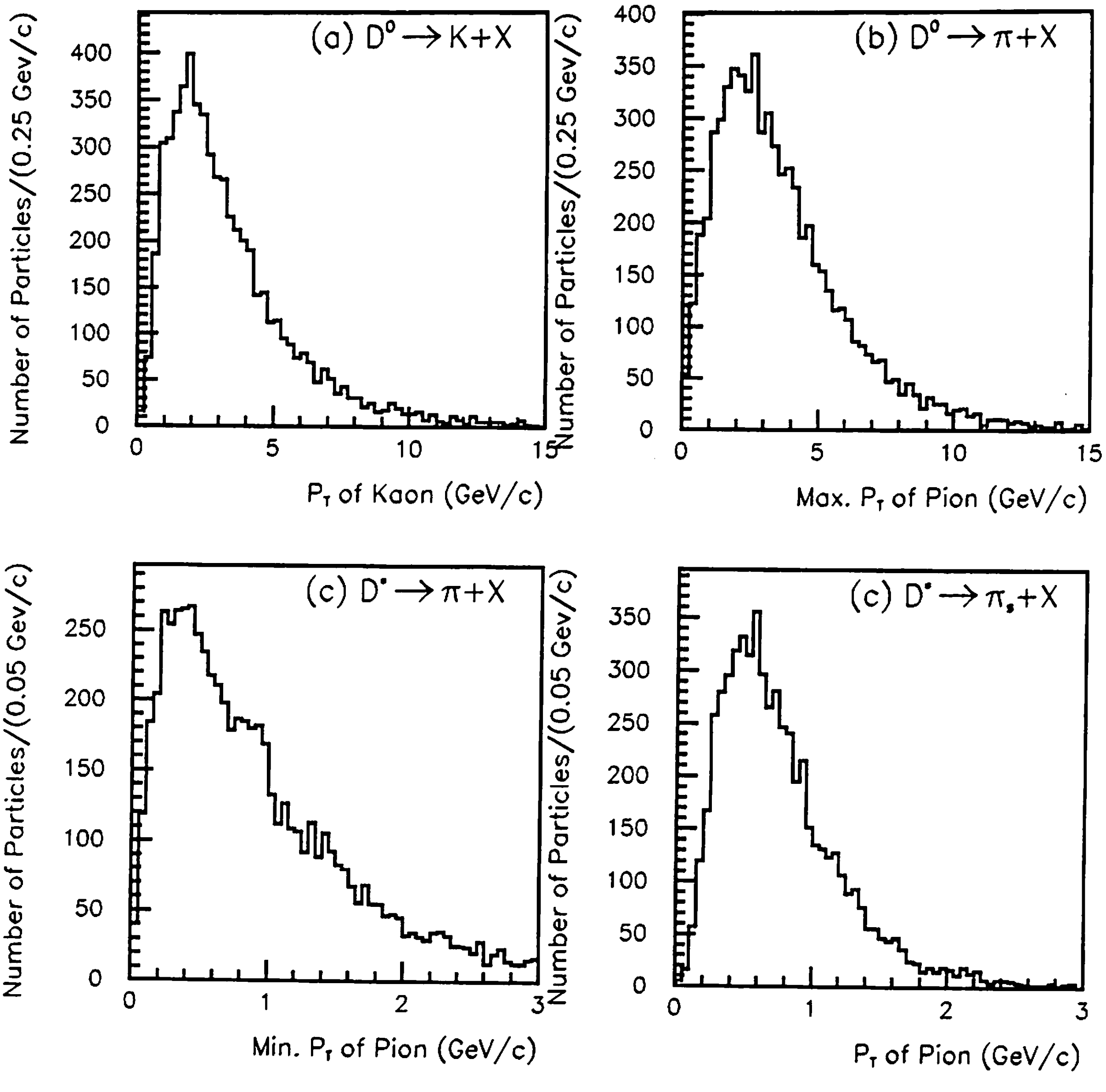

Figure 4.19: p_T distributions of K,π, and π_s in the γ+$D^{*\pm}$ events generated with PYTHIA.

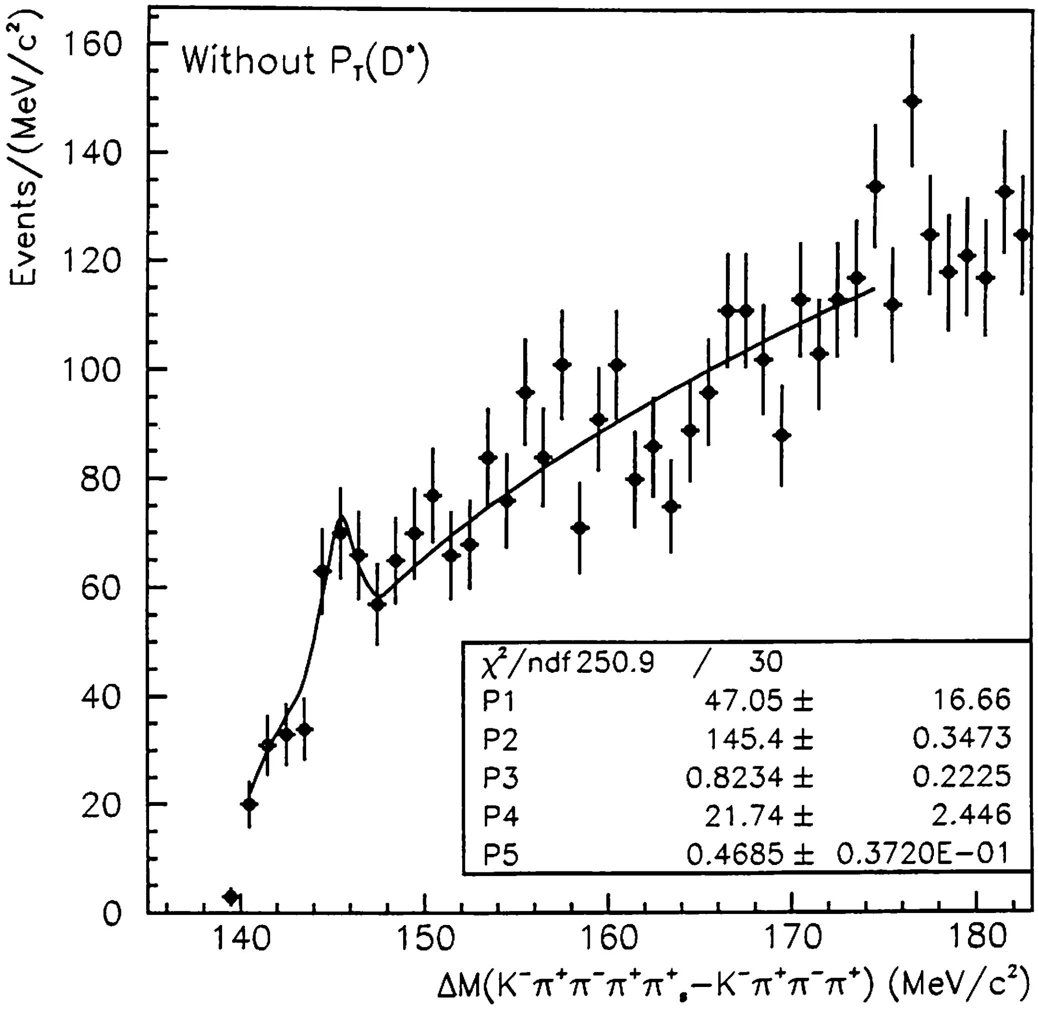

Figure 4.20: $\Delta M(K^-\pi^-\pi^+\pi^+\pi_s^+ - K^-\pi^-\pi^+\pi^+)$ distributions in the photon candidate events after the kinematical cuts except for the $p_T(D^{*\pm})$ cut.

In order to eliminate the backgrounds, we applied the $p_{\mathrm{T}}(D^{*\pm})$ cut. Figure 4.21 shows the ΔM distribution together with the background. The background events were generated by combining a D^0 candidate with a track in another event. We observe the $D^{*\pm}$ signal at $\Delta M =$ 145.5 MeV/c^2, however, do not observed in the fake $D^{*\pm}$ events. The ratio of signal to background was improved after the $p_{\mathrm{T}}(D^{*\pm})$ cut. The distribution was fitted to the function of

$$\frac{\mathrm{P1}}{\sqrt{2\pi}\mathrm{P3}} \times \exp\left(-\frac{1}{2}\left(\frac{\Delta M - \mathrm{P2}}{\mathrm{P3}}\right)^2\right) + \mathrm{P4} \times (\Delta M - m_\pi)^{\mathrm{P5}},$$

where P1, P2, P3, P4, and P5 are the fitting parameters, and m_π is the pion mass. The fitted ΔM is 145.4 ± 0.3 MeV/c^2, where the error is the statistical one. The fitted ΔM is consistent with the world average of 145.42 MeV/c^2 [18].

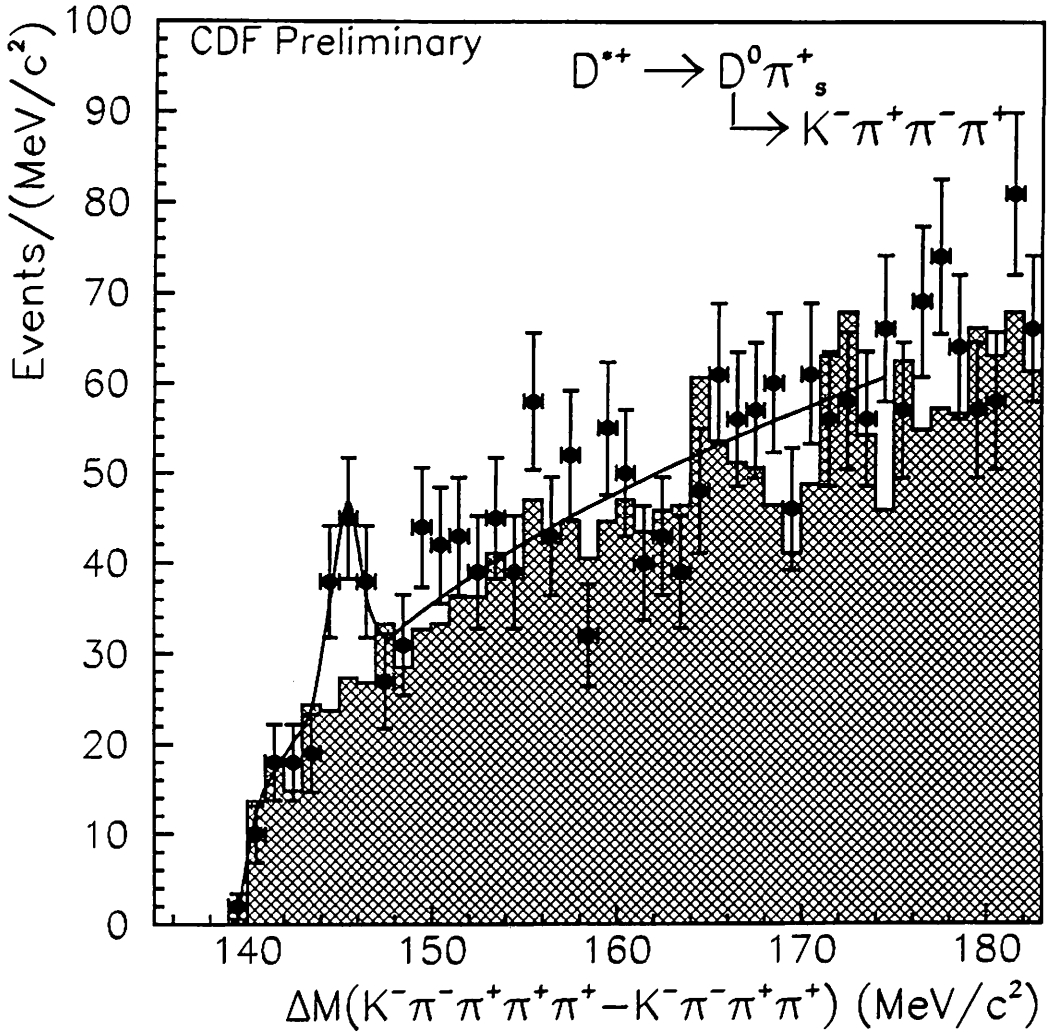

Figure 4.21: ΔM distribution of the data with the background. The plots show that of the data, and the histogram show that of the background events. The $p_T(D^{*\pm})$ cut was applied.

Chapter 5

Extraction of $\gamma + D^{*\pm}$ Events

The $D^{*\pm}$ mesons were successfully reconstructed as the significant peaks above backgrounds in the ΔM distributions. The backgrounds are mainly track combinations due to accidentally falling into the ΔM mass window. The photon candidates include the multi-photon backgrounds from the neutral meson decays such as $\pi^0 \to \gamma\gamma$, $\eta \to \gamma\gamma$, and $K_S^0 \to \pi^0\pi^0$. In order to obtain the number of events containing a prompt photon and a $D^{*\pm}$, the photon backgrounds are subtracted from the photon candidates by using the CES χ^2, and the combinatorial backgrounds are subtracted in the ΔM distribution by using the background ΔM distribution. In this chapter the methods to subtract the backgrounds and to estimate the number of the $\gamma + D^{*\pm}$ candidate events are described.

5.1 Subtraction of photon background

The photon candidates which passed the photon selection cuts still include backgrounds. The fraction of prompt photons in the photon candidates is roughly 50 %. The photon backgrounds were statistically subtracted from the photon candidates by the method using the CES χ^2. The number of prompt photons (N_γ) in photon candidates (N) is given by

$$N_\gamma = (\frac{\epsilon - \epsilon_{\mathrm{B}}}{\epsilon_\gamma - \epsilon_{\mathrm{B}}}) \times N,$$

where ε_γ, ε_{B}, and ε are χ^2 efficiencies for true photons, backgrounds, photon candidates to pass the cut $\chi^2 < 4$, respectively. That was described in section 3.7. The χ^2 efficiency is defined as the number of photon candidates with $\chi^2 < 4$ divided by that with $\chi^2 < 20$. Figure 5.1 shows the χ^2 efficiencies for true photons, true backgrounds, and the photon candidates in the inclusive photon events. From the efficiency curves, the prompt photon fraction can be determined in a photon p_{T} range. The curves were obtained by a simulation. The errors of the efficiencies will be discussed in chapter of systematic uncertainty.

The numbers of the events which passed and failed the $\chi^2 < 4$ cut are given by

$$\begin{cases} N(\chi^2 < 4) & = \varepsilon_\gamma\ N_\gamma + \varepsilon_{\mathrm{B}}\ N_{\mathrm{B}}, \\ N(4 \leq \chi^2 < 20) & = (1 - \varepsilon_\gamma)N_\gamma + (1 - \varepsilon_{\mathrm{B}})N_{\mathrm{B}}, \end{cases}$$

where N_γ (N_{B}) is the number of true photons (backgrounds). From these equations, the number of true photons is given by

$$N_\gamma = w_{\mathrm{p}}\ N(\chi^2 < 4)\ + w_{\mathrm{f}}\ N(4 \leq \chi^2 < 20),$$

where w_{p} and w_{f} are weights of the events which passed or failed the $\chi^2 < 4$ cut, respectively. The weights are calculated by

$$\begin{cases} w_{\mathrm{p}} & = \frac{1-\varepsilon_{\mathrm{B}}}{\varepsilon_\gamma - \varepsilon_{\mathrm{B}}} \quad (\chi^2 < 4), \\ w_{\mathrm{f}} & = \frac{-\varepsilon_{\mathrm{B}}}{\varepsilon_\gamma - \varepsilon_{\mathrm{B}}} \quad (4 \leq \chi^2 < 20), \end{cases}$$

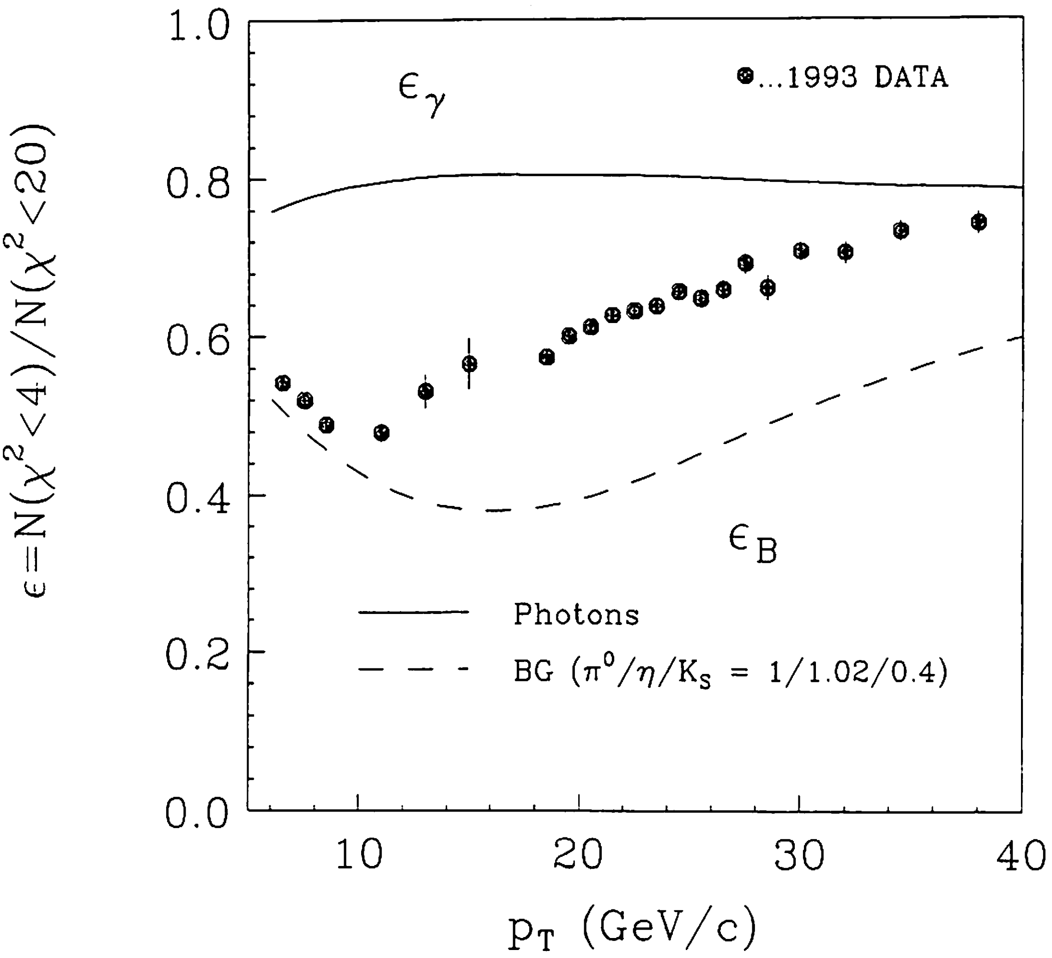

Figure 5.1: χ^2 efficiencies of prompt photons, backgrounds, and the photon candidates. The measured efficiency obtained from the photon candidate data are shown as the points.

using the efficiencies.

The photon candidate sample can be separated into two groups. One is a prompt photon sample, and the other is a background sample. Separating photon candidates into the two groups, the number of prompt photons is calculated by summing the weight $w^i_{\mathrm{p/f}}(w^i_{\mathrm{p}}$ or $w^i_{\mathrm{f}})$ over all photon candidates, namely:

$$N_\gamma = \sum_{i;\chi^2<4} w^i_{\mathrm{p}} + \sum_{j;4<\chi^2<20} w^j_{\mathrm{f}}.$$

Similarly, the number of backgrounds is given by

$$N_{\mathrm{B}} = \sum_{i;\chi^2<4} (1-w^i_{\mathrm{p}}) + \sum_{j;4<\chi^2<20} (1-w^j_{\mathrm{f}})$$

The statistical error ΔN_γ is given by

$$\Delta N_\gamma = \sqrt{\sum_{i:\chi^2<4} (w^i_{\mathrm{p}})^2 + \sum_{j:4<\chi^2<20} (w^j_{\mathrm{f}})^2}.$$

The weights of the photon candidates in the ΔM distribution were calculated by filling the events with the weights ($w^i_{\mathrm{p/f}}$ and $1-w^i_{\mathrm{p/f}}$) in the ΔM distributions. We show the ΔM distributions in the prompt photon and the photon background samples. Figures 5.2 (a) and 5.3 (a) show the $\Delta M(K^-\pi^+\pi^+_s - K^-\pi^+)$ and $\Delta M(K^-\pi^-\pi^+\pi^+\pi^+_s - K^-\pi^-\pi^+\pi^+)$ distributions in the prompt photon sample, respectively. Figures 5.2 (b) and 5.3 (b) show those in the photon background sample, respectively. In the plots, the fake $D^{*\pm}$ ΔM distributions were shown as histograms. The vertical axis corresponds to the number of the prompt photons or the backgrounds. The $D^{*\pm}$ signals still remain at $\Delta M = 145.5$ MeV$/c^2$ in the prompt photon samples with significant excesses. However, no excess in the $D^{*\pm}$ signal region ($144 < \Delta M < 147$ MeV$/c^2$) is observed in the

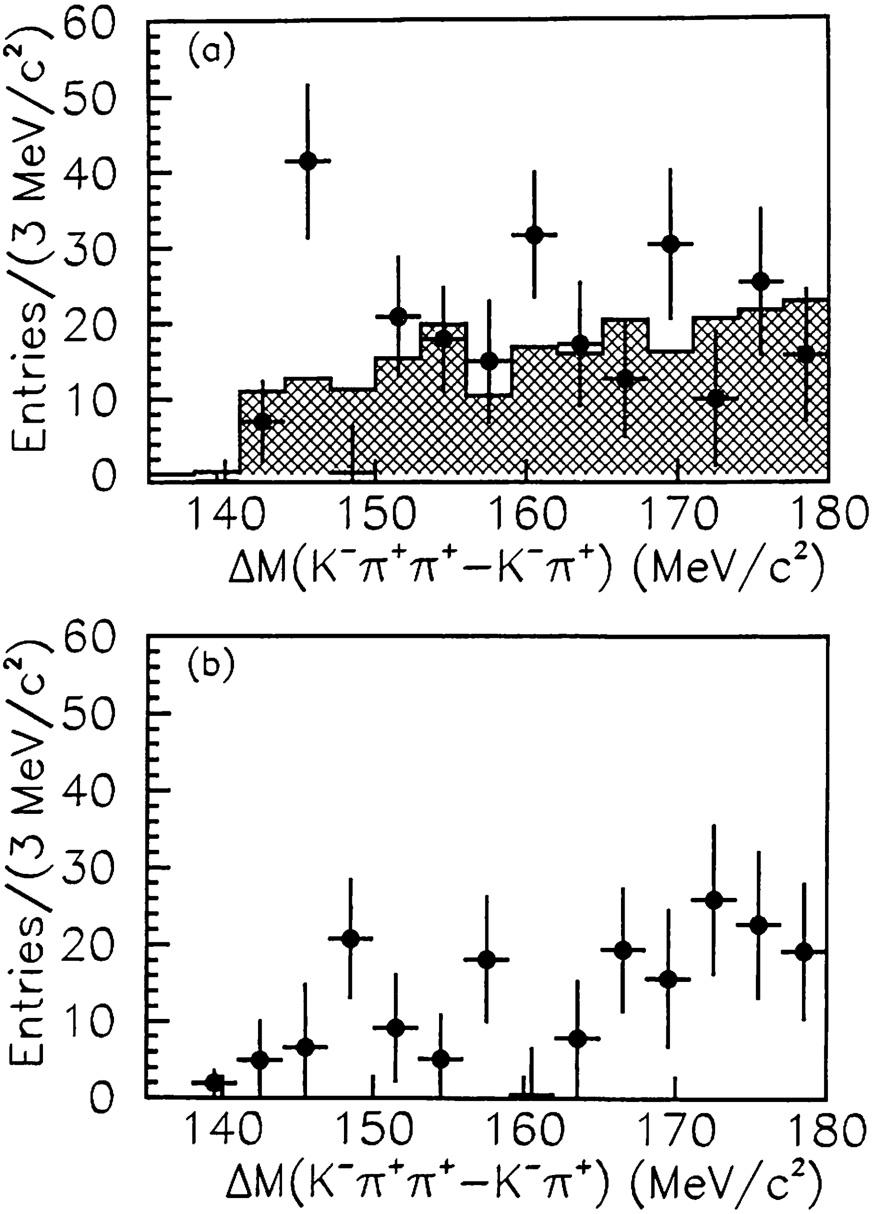

Figure 5.2: $\Delta M(K^-\pi^+\pi_s^+ - K^-\pi^+)$ distributions in the prompt photon sample (a), and in the background sample (b). The histogram shows the fake $D^{*\pm}$ events.

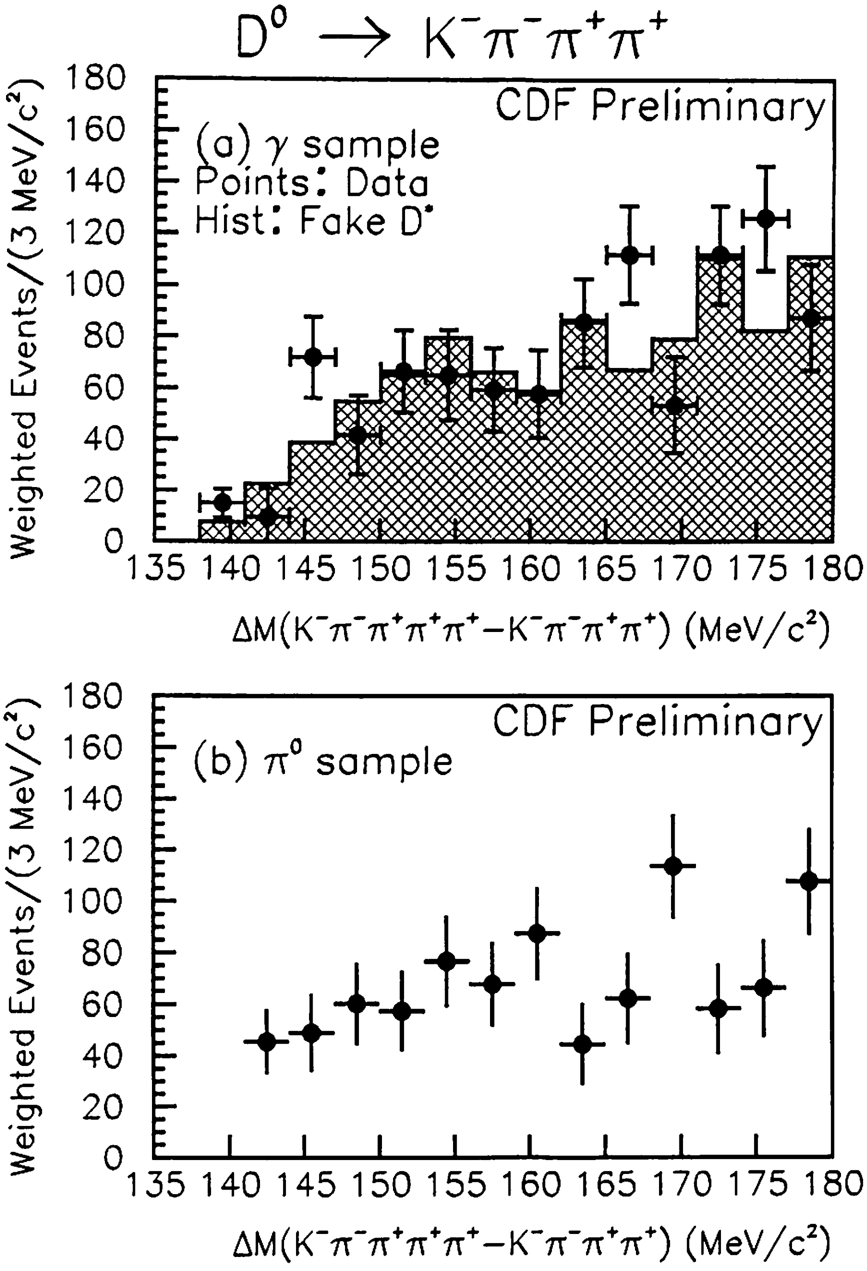

Figure 5.3: $\Delta M(K^-\pi^-\pi^+\pi^+\pi_s^+ - K^-\pi^-\pi^+\pi^+)$ distributions in the prompt photon sample (a), and in the background sample (b). The hatched histogram shows the fake $D^{*\pm}$ events.

background samples. It indicates that the $D^{*\pm}$ candidates are produced with prompt photons. The numbers of the $D^{*\pm}$ events associated with prompt photons are calculated using the weights to be

$$N(\gamma) = 41.4 \pm 10 \quad (D^0 \to K^-\pi^+).$$
$$N(\gamma) = 72.0 \pm 16 \quad (D^0 \to K^-\pi^-\pi^+\pi^+).$$

where the errors are statistical ones.

5.2 Subtraction of combinatorial background

The $D^{*\pm}$ signals associated with prompt photons have been observed as significant excesses in the ΔM distributions at ΔM=145.5 MeV/c^2. The background against prompt photons has already been subtracted with the statistical method using the CES χ^2. The remaining background is combinatorial background. The shape of the combinatorial background events in the ΔM distribution was determined from the ΔM distributions of the fake $D^{*\pm}$ mesons. The fake $D^{*\pm}$ events were made by combining a D^0 candidate of the data with a track in another event. We assume that the fake $D^{*\pm}$ events have the same ΔM distribution as the combinatorial background events.

5.2.1 $D^0 \to K^-\pi^+$

We have showed the ΔM distribution of the fake $D^{*\pm}$ events together with the data in Fig. 5.2 (a). The excess at ΔM = 145.5 MeV/c^2 is clearly observed in the data (points) however, no excess was observed in the backgrounds (histogram).

In order to estimate the number of the $D^{*\pm}$ candidates above the combinatorial backgrounds, the background ΔM distribution was parameterized by various functions. The functions are listed in Table 5.1 together with the estimated number of background events in the $D^{*\pm}$ signal window for each parameterization. In the parameterization functions, a, b, c, and d are the fitting parameters, and m_π is pion mass. The

Table 5.1: Number of the combinatorial background (C.B.) events

	Functions	# of the C.B. events
(a)	$a \times (\Delta M - m_\pi)^b$	12.0 ± 2.0
(b)	$a \times (\Delta M - m_\pi)^b \times (1 + c(\Delta M - m_\pi))$	12.1 ± 2.0
(c)	$a \times (\Delta M - m_\pi)^b \times (1 + c(\Delta M - m_\pi) + d(\Delta M - m_\pi)^2)$	12.6 ± 2.3
(d)	$a \times (\Delta M - m_\pi) + b \times (\Delta M - m_\pi)^2 + c \times (\Delta M - m_\pi)^3$	11.1 ± 1.8
(e)	$a \times (1 - e^{-b(\Delta M - m_\pi)})$	12.3 ± 3.0
(f)	$a \times \sqrt{\Delta M - m_\pi}$	9.1 ± 0.7
	Average	11.5 ± 2.0

fitted functions are superimposed on the ΔM distributions. They are shown in Figs. 5.4 (a)~(f) and Figs. 5.5 (a)~(f) for the ΔM distributions of the data and the background, respectively. The number of the combinatorial background events in the $D^{*\pm}$ signal window ($144 < \Delta M < 147$ MeV/c^2) was determined by averaging the results from these six functions. The average number was

$$N(\gamma + \text{C.B.}) = 11.5 \pm 2.0 \quad \text{events,}$$

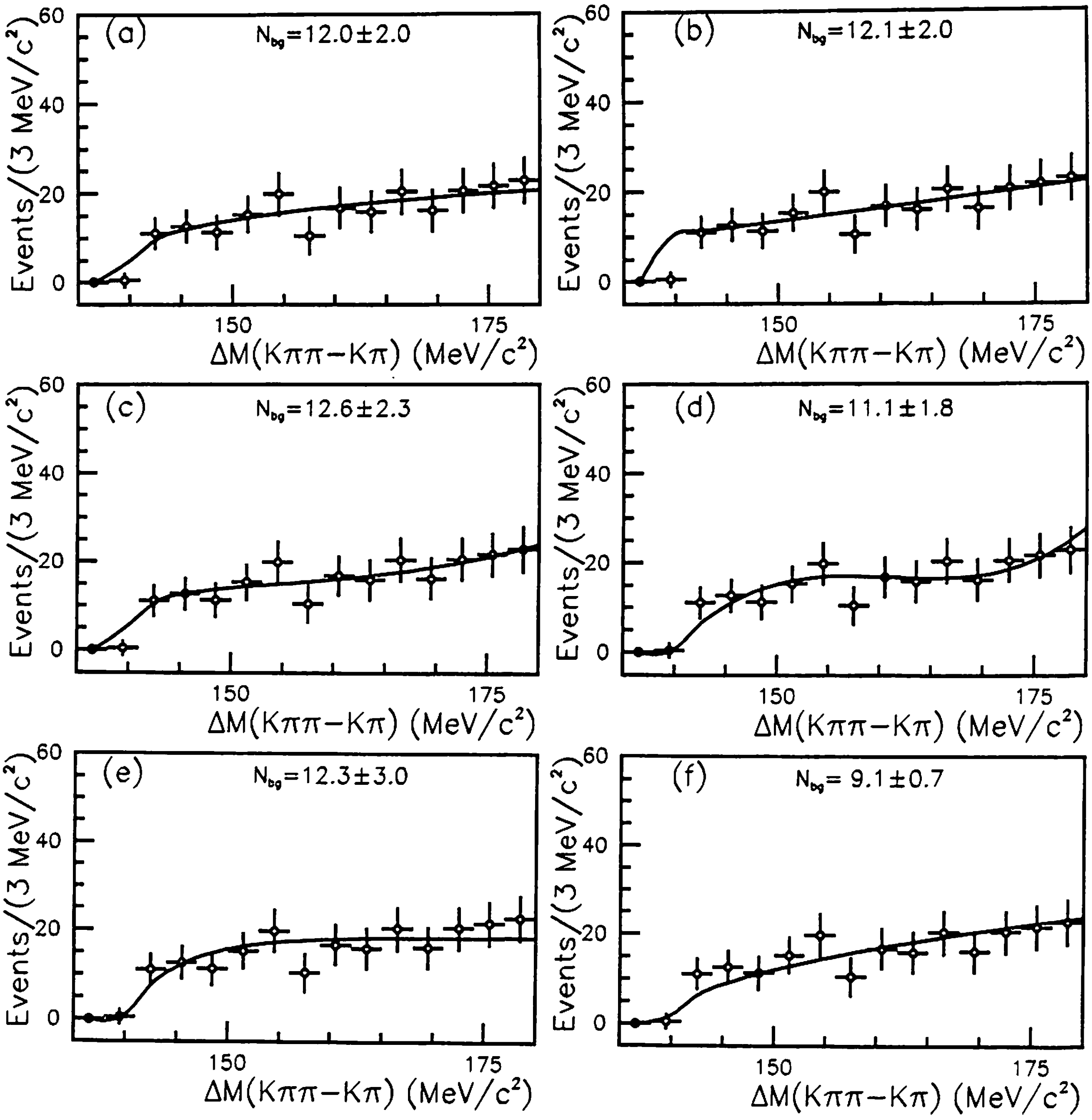

Figure 5.4: ΔM distribution of the fake $D^{*\pm}$ events. The distribution was fitted to the parameterized functions. The functions are shown in the text. N_{bg} denotes the estimated number of the combinatorial background events in the $D^{*\pm}$ signal window using each parameterization.

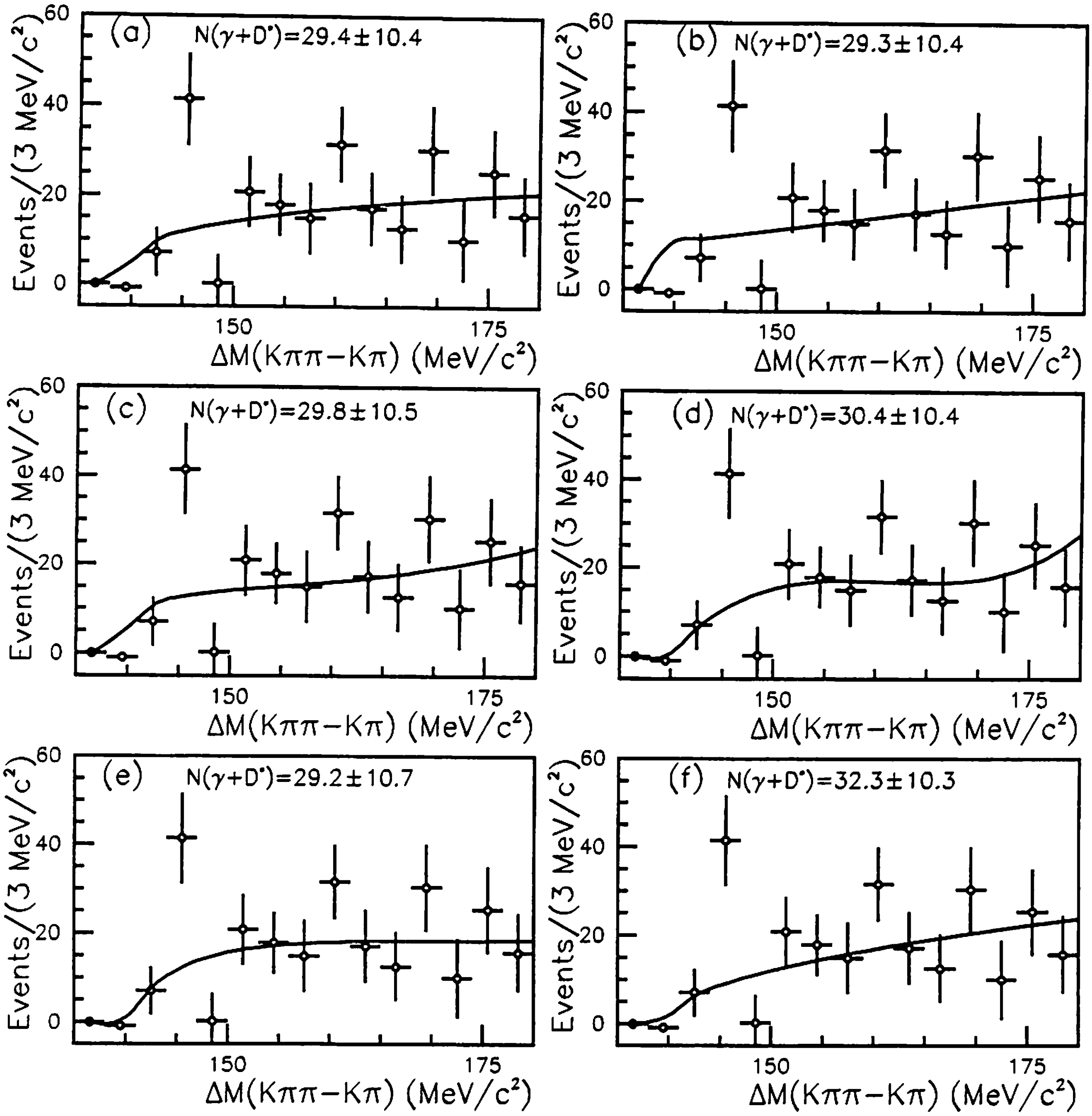

Figure 5.5: ΔM distribution of the data. The fitted functions using the background ΔM distribution are superimposed. $N(\gamma + D^*)$ denotes the estimated number of the $D^{*\pm}$ signal events subtracted the parameterized background events.

where the error shows statistical one. Subtracting the number of the combinatorial background events $N(\gamma + \mathrm{C.B.})$ from the number of the prompt photon events $N(\gamma)$, the number of $\gamma + D^{*\pm} \rightarrow D^0(\rightarrow K^{\mp}\pi^{\pm})\pi^{\pm}$ candidate events was obtained:

$$N(\gamma + D^{*\pm}) = 29.9 \pm 10.4 \quad \text{events},$$

where the error shows only statistical one.

The ΔM distribution of the data was used for another parameterization of the combinatorial background distribution. The ΔM distribution of the events outside of the $D^{*\pm}$ signal window was fitted to the same six functions listed in Table 5.1. The fitted functions are superimposed on the ΔM distributions in Figs. 5.6 (a)~(f). The number of the combinatorial background events is

$$N(\gamma + \mathrm{C.B.}) = 8.6 \pm 1.9 \quad \text{events},$$

from the average of the numbers estimated with the six parameterized functions. The number of the $\gamma + D^{*\pm}$ candidates is

$$N(\gamma + D^{*\pm}) = 32.8 \pm 10.4 \quad \text{events},$$

where the error is also statistical one.

The numbers of the $\gamma + D^{*\pm}$ candidate events were estimated by these two ways. The numbers of the candidates are consistent with each other within the statistical errors. Finally, we took the number of the candidates estimated using the fake $D^{*\pm}$ events in this analysis, because the fake ΔM distribution has more statistics.

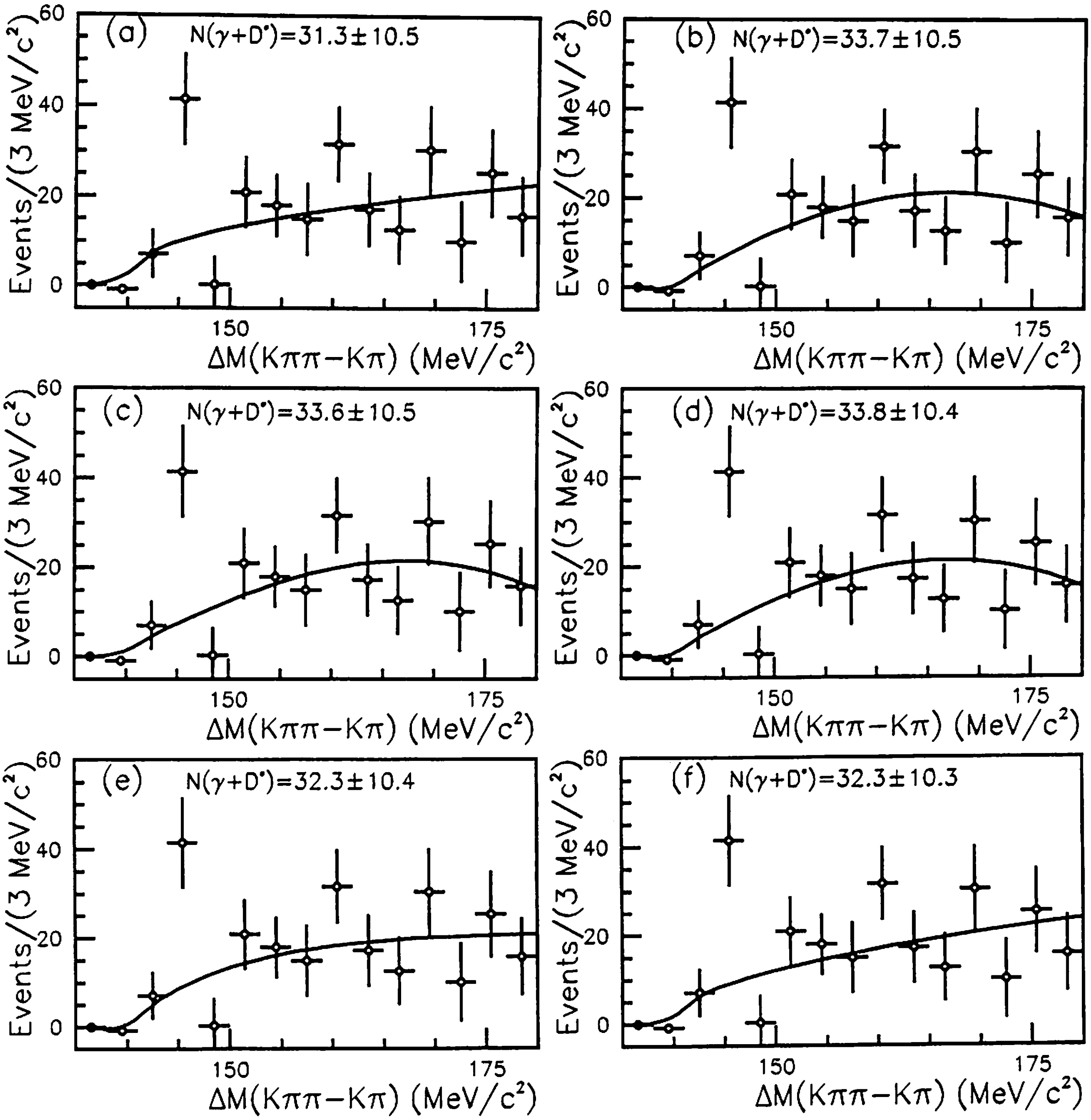

Figure 5.6: $\Delta M(K^-\pi^+\pi_s^+ - K^-\pi^+)$ distributions of the data. The distributions were fitted with the functions (See text) excluding the signal bin.

5.2.2 $D^0 \to K^-\pi^-\pi^+\pi^+$

For the reconstruction using $D^0 \to K^-\pi^-\pi^+\pi^+$, we also subtracted the photon backgrounds by the same procedure as that for the analysis using $D^0 \to K^-\pi^+$. To subtract the combinatorial background events, we used the fake $D^{*\pm}$ ΔM distribution. We have shown the ΔM distributions of the data (points) and the fake $D^{*\pm}$ events (histogram) in Fig. 5.3 (a). To estimate the number of the combinatorial background events, the background ΔM distribution was parameterized by various functions. In Table 5.2, we summarized the numbers of the combinatorial background events.

Table 5.2: Number of the combinatorial background (C.B.) events

	Parameterization functions	C.B. events
(a)	$a \times (\Delta M - m_\pi)^b$	40.6 ± 3.3
(b)	$a \times (\Delta M - m_\pi)^b \times (1 + c(\Delta M - m_\pi))$	40.1 ± 3.4
(c)	$a \times (\Delta M - m_\pi)^b \times (1 + c(\Delta M - m_\pi) + d(\Delta M - m_\pi)^2)$	41.2 ± 3.7
(d)	$a \times (\Delta M - m_\pi) + b \times (\Delta M - m_\pi)^2 + c \times (\Delta M - m_\pi)^3$	41.1 ± 3.2
(e)	$a \times (1 - e^{-b(\Delta M - m_\pi)})$	38.1 ± 3.3
(f)	$a \times \sqrt{\Delta M - m_\pi}$	39.5 ± 1.3
	Average	40.1 ± 3.0

The average of these results is

$$N(\gamma + \text{C.B.}) = 40.1 \pm 3.0,$$

where the error is statistical one. Subtracting the combinatorial background events, the number of the γ+$D^{*\pm}$ events was obtained:

$$N(\gamma + D^{*\pm}) = 31.9 \pm 16.0.$$

5.2.3 Combining the two D^0 decay modes

We combined the $D^{*\pm}$ events reconstructed using the two D^0 decay modes. Figure 5.7 shows the ΔM distribution combining the two D^0 decay modes before the photon background subtraction. Figures 5.8 (a) and (b) show the ΔM distribution in the prompt photon and the background samples, respectively. The shaded histograms show the fake $D^{*\pm}$ ΔM distributions.

5.3 Summary of the γ + $D^{*\pm}$ candidate events

We summarize the number of the γ + $D^{*\pm}$ candidate events in Table 5.3.

Table 5.3: Summary of the $\gamma + D^{*\pm}$ candidates.

Decay modes	$N(\gamma + D^{*\pm})$
$K^{\mp}\pi^{\pm}$	29.9 ± 10.4
$K^{\mp}\pi^{\pm}\pi^{\pm}\pi^{\pm}$	31.9 ± 16.0
$(K^{\mp}\pi^{\pm})$+$(K^{\mp}\pi^{\pm}\pi^{\pm}\pi^{\pm})$	61.8 ± 19.1

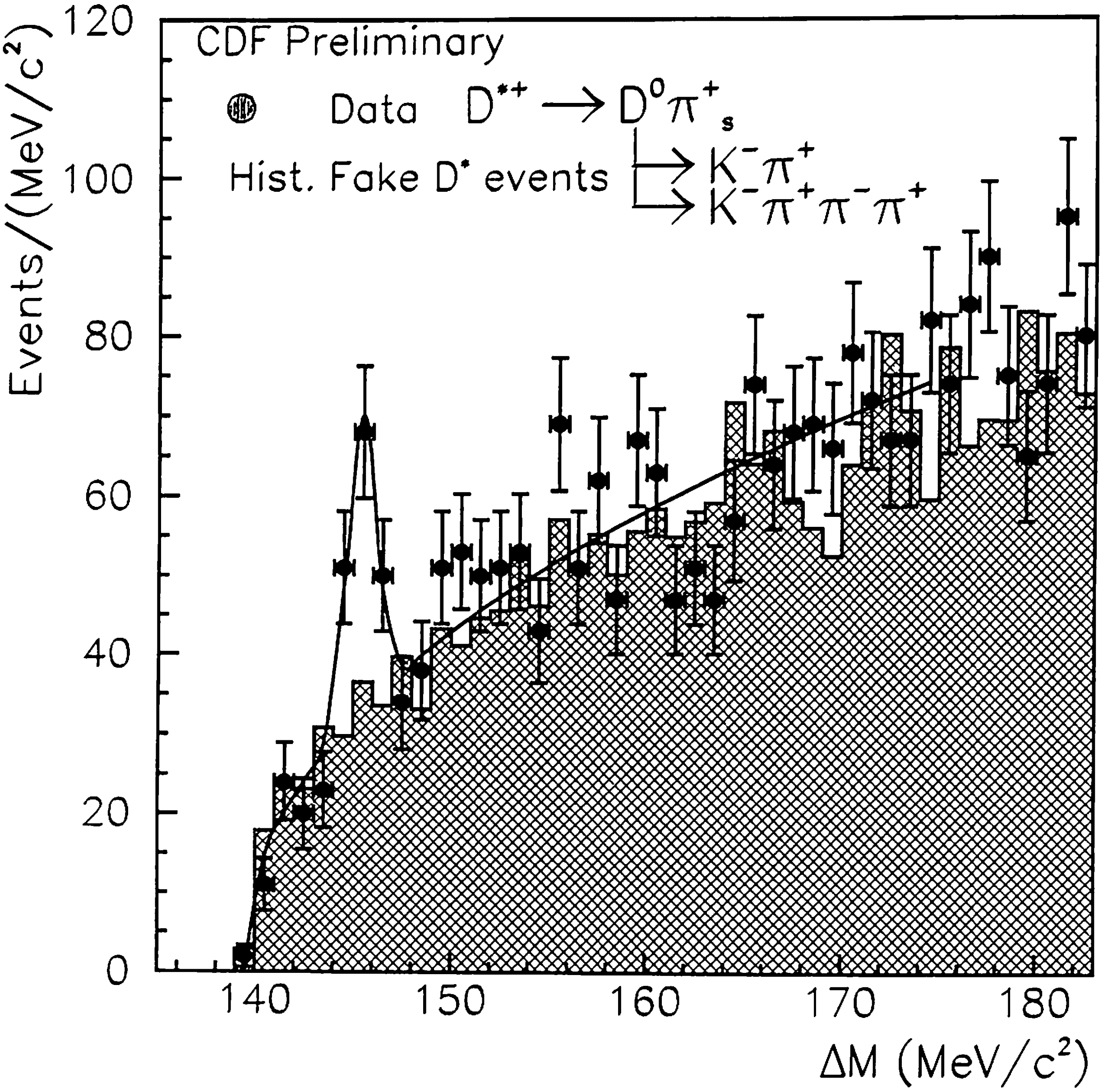

Figure 5.7: ΔM distributions combining the two D^0 decay modes before the photon background subtraction. The points and the hatched histogram show those of the data and the fake $D^{*\pm}$'s, respectively.

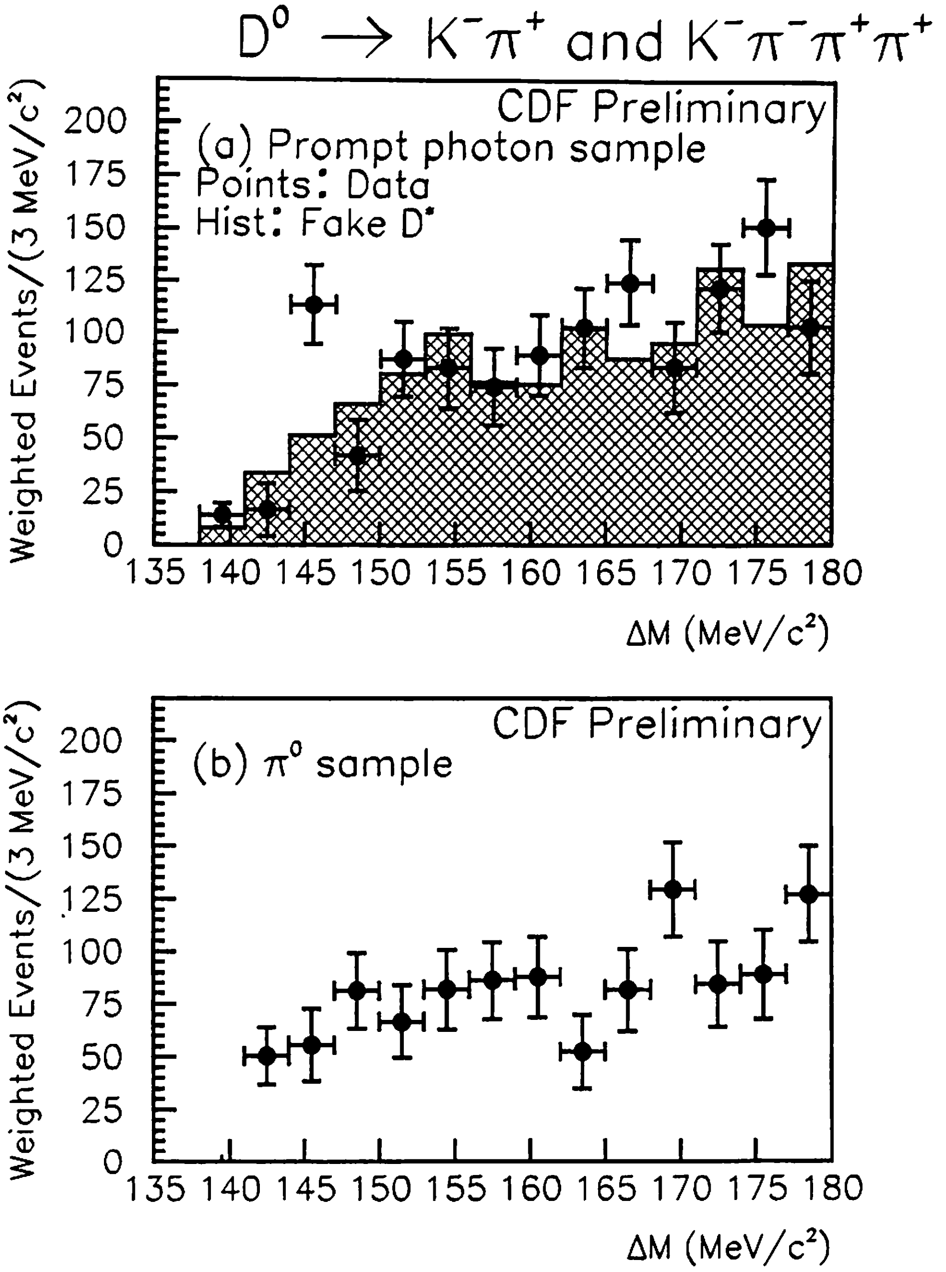

Figure 5.8: ΔM distributions in the prompt photon sample (a), and in the background sample (b). The histogram in (a) shows the fake $D^{*\pm}$ events.

Chapter 6

Measurement of the Cross Section

We measure the cross section for $\gamma + D^{*\pm}$ production in this chapter. To derive the cross section from the observed $\gamma + D^{*\pm}$ events, the efficiency of the reconstruction has to be estimated. The efficiency $\epsilon_{\gamma+D^{*\pm}}$ of reconstructing $\gamma + D^{*\pm}$ events can be decomposed into two efficiencies. One is an efficiency for the photon detection, and the other is a $D^{*\pm}$ detection efficiency. The efficiencies of the photon and the $D^{*\pm}$ detections are estimated from real data, electron test beam data, and Monte Carlo data.

6.1 Efficiency of photon detection

The efficiency for the photon detection is broken down into two parts:

$$\varepsilon = \varepsilon_{\mathrm{sel}} \times \varepsilon_{\mathrm{trig}},$$

where $\varepsilon_{\rm sel}$ is an efficiency for the photon selection cuts, $\varepsilon_{\rm trig}$ is a photon trigger efficiency. These estimations are described below.

6.1.1 Photon trigger

The trigger efficiency was estimated from the data taken by a lower transverse energy ($E_{\rm T}$) threshold trigger. In this experiment, an inclusive electron trigger was prepared at a low $E_{\rm T}$ threshold of 10 GeV. The behavior of electrons in the detector can be considered to be similar with that of photons except for an existence of a charged track in the CTC. The requirements for the electrons are summarized in Table 6.1. The variable $\rm L_{shr}$ is a measure of the lateral shower profile for the electron candidate, which is defined by

Table 6.1: Electron selection cuts

$\rm L_{shr}$	$<$	0.2
E/p	$<$	1.5
Number of CTC track	$=$	1
$E_{\rm Had}/E_{\rm Em}$	$<$	0.125
$\chi^2 = (\chi^2_{\rm strip} + \chi^2_{\rm wire})/2$	$<$	20
$\sum E_{\rm T}$ in $R = 0.7$	$<$	2 GeV
CES fiducial volume cuts		

$$\mathrm{L_{shr}} = 0.14 \sum_k \frac{M_k - P_k}{\sqrt{0.14^2 E + (\Delta P_k)^2}},$$

where the sum is taken over towers adjacent to the seed tower, M_k is the measured energy in the adjacent tower, P_k is the expected energy in adjacent tower, E is the EM cluster energy, ΔP_k is the estimate of the error in P_k. These estimations were obtained from the electron test beam data.

The trigger efficiency in a photon p_T bin was calculated by

$$\varepsilon = \frac{N_{p_T>16}}{N_{p_T>10}},$$

where $N_{p_T>10}$ is the number of the electrons which fired the electron trigger with the p_T threshold of 10 GeV/c and passed the electron selection cuts, and $N_{p_T>16}$ is the number of the electrons which fired both the photon and electron triggers and passed the electron selection cuts. The efficiency is calculated in each photon p_T bin, and is shown in Fig. 6.1. The overall trigger efficiency was estimated to be

$$\varepsilon_{\text{trig}} = 0.80 \pm 0.03,$$

in a range of 16 GeV/c $< p_T <$ 40 GeV/c, where the error shows the statistical one.

6.1.2 Photon selection

The efficiency for the photon selection cuts was estimated from the data taken by a minimum bias trigger and other photon triggers, and from the observed $W \rightarrow e\nu$ data and the electron test beam data.

The efficiencies for the isolation cut and the associated track cut were estimated using the minimum bias data and other inclusive photon samples. In the minimum bias events, a cone radius of 0.7 in η-φ space was taken randomly, and the energy sum and the multiplicity of charged tracks in the cone were obtained. The energy sum distribution was compared with that in a cone at 90 degrees with respect to a photon candidate

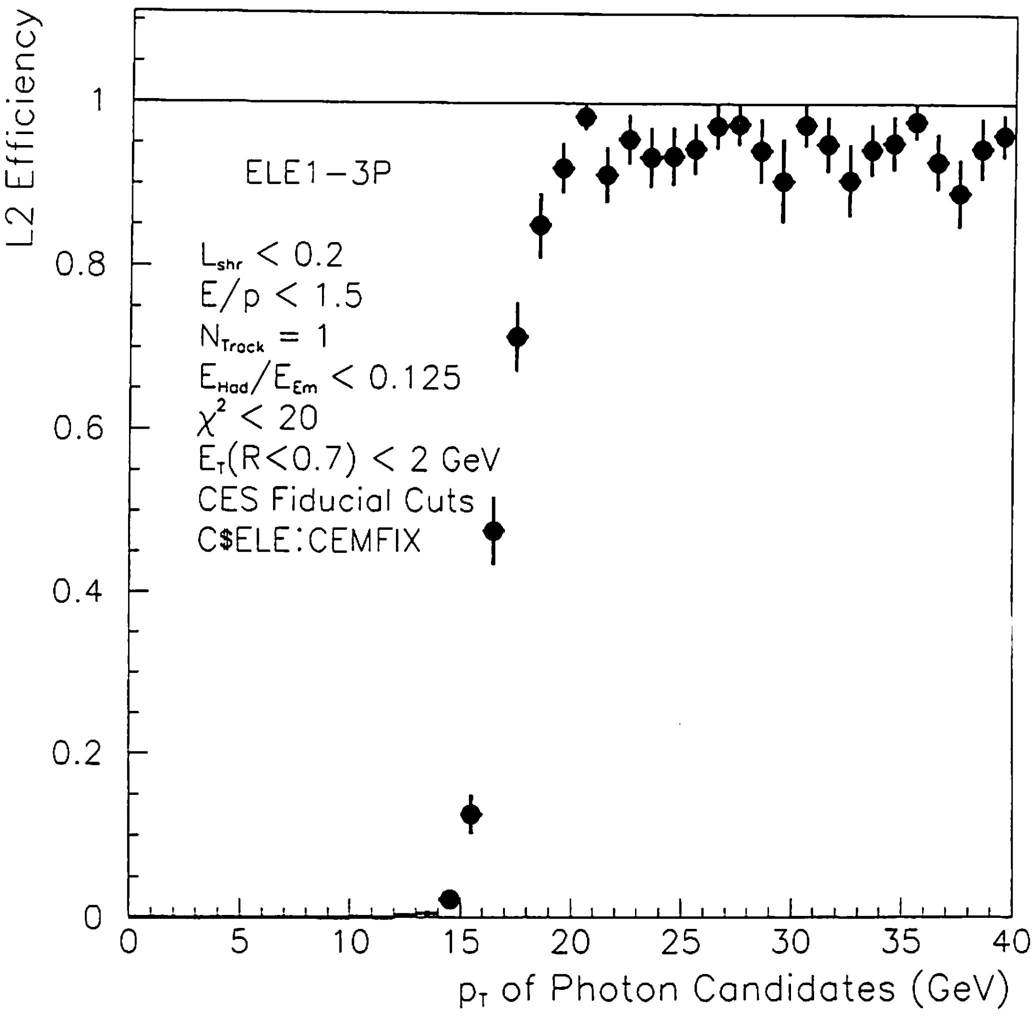

Figure 6.1: Trigger efficiencies in each p_T bin for the photon $p_T > 16$ GeV trigger. These were obtained from the lower E_T electron trigger data.

Table 6.2: Photon selection efficiencies

Cuts		Efficiency
$E_T(R < 0.7) < 2$ GeV	=	0.78
CES fiducial volume cuts	=	0.64
Extra strip/wire cluster	=	0.9
Associated CTC track	=	0.95
Conversion in material	=	0.9
$\lvert z_{\text{vertex}}\rvert < 60$ cm	=	0.9
total	=	0.35

in the inclusive photon events taken by other photon trigger. The energy distribution does not depend on photon p_T. The dependence of the energy sum on luminosities was taken into account for the calculation.

The efficiency for the extra CES cluster cut was obtained from $W \rightarrow e\nu$ data and the electron test beam data. The probability of photon conversion inside the CTC was calculated from the amount of material inside of the CTC. The efficiency of the event z vertex position cut was estimated using the z vertex distribution. The photon selection efficiencies for each cut are summarized in Table 6.2. The total efficiency for the photon selection cuts is

$$\varepsilon_{\text{sel}} = 0.35.$$

6.2 Efficiency for the $D^{*\pm}$ selection cuts

The efficiency for the $D^{*\pm}$ selection cuts was estimated using the Monte Carlo data. The Monte Carlo events were simulated for the CDF detector, and were imbedded into the real events in order to introduce the actual detector effects. The imbedded data include the effects caused by low p_{T} tracks in the inner layer of the CTC, noise in the CTC and SVX, and density of track multiplicity. The efficiency of the $D^{*\pm}$ reconstruction can be decomposed as follows:

$$\varepsilon = \epsilon_{\mathrm{Track\&Mass}} \times \varepsilon_{\mathrm{kaon}},$$

where $\epsilon_{\mathrm{Track\&Mass}}$ is an efficiency for the track p_{T} cuts and the mass reconstruction, $\varepsilon_{\mathrm{kaon}}$ is a probability that a kaon exits the CTC without decay. The studies of the efficiencies are described below.

6.2.1 Single track reconstruction

The studies of a single track are described. Some basic distributions of simulated tracks were compared with those of the real tracks. The accuracy of the detector simulation for a single track is checked by the comparisons. In this study, low p_{T} tracks are considered. A single $\pi^{\pm}$ particle was generated with a flat η distribution and a flat p_{T} distribution in a range of $0.4\ \mathrm{GeV}/c < p_{\mathrm{T}} < 1.5\ \mathrm{GeV}/c$. The Monte Carlo single tracks were simulated for the CDF detector simulation without a detector noise, and were imbedded into the real events taken by a minimum bias trigger. The simulated tracks were reconstructed with the same tracking algorithm as the real data. The CTC intrinsic position resolutions were set to about 200 μm as listed in Table 6.3. They were obtained from the residuals of the track fitting in the real events. The simulated tracks were

Table 6.3: CTC intrinsic position resolutions

Superlayer	0	1	2	3	4	5	6	7	8
Resolution (μm)	217	192	200	193	179	235	195	188	189

compared with the isolated real tracks in the distributions of the TDC counts, the residual of fitting, and the number of hits. The real tracks were taken from the minimum bias data. The track isolation $\cos\theta_{\mathrm{track}}$, which is a cosine of an angle between a track and the nearest track, was required to be less than 0.85. Figures 6.2, 6.3, and 6.4 show the distributions of the TDC counts, the numbers of hits, and the residuals of the simulated tracks and the real tracks, respectively. Figure 6.5 shows a wire hit efficiency on each wire layer. The wire efficiency is defined by

$$\varepsilon = N_{\mathrm{used}}/N_{\mathrm{hits}},$$

where N_{used} is the number of hits used in the track reconstruction, N_{hits} is the number of hits. The wire efficiency and other distributions of the simulated tracks well reproduce those of the real tracks.

6.2.2 SVX hit efficiency

An SVX hit efficiency was obtained using the real tracks in the minimum bias events. The SVX hit efficiencies on each layer are listed in the Table 6.4. The hit efficiency on a layer n is defined by

$$\varepsilon_n = N_{\mathrm{Hit}}/N_{\mathrm{Track}},$$

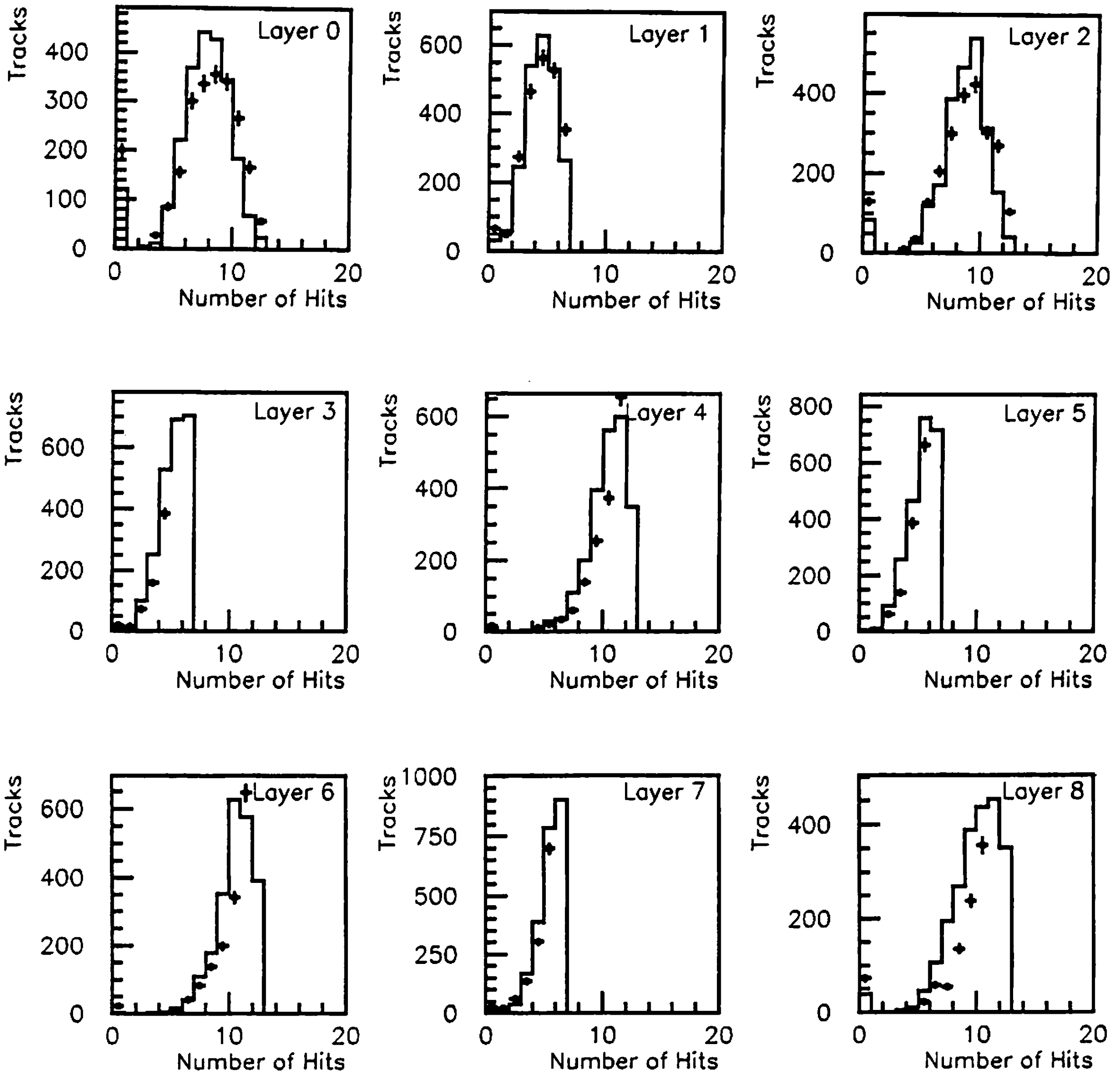

Figure 6.2: Number of hits on axial (0, 2, 4, 6, and 8) and stereo (1, 3, 5, and 7) superlayers. The points show those of the real tracks in the minimum bias events, and the histograms show those of the simulated tracks.

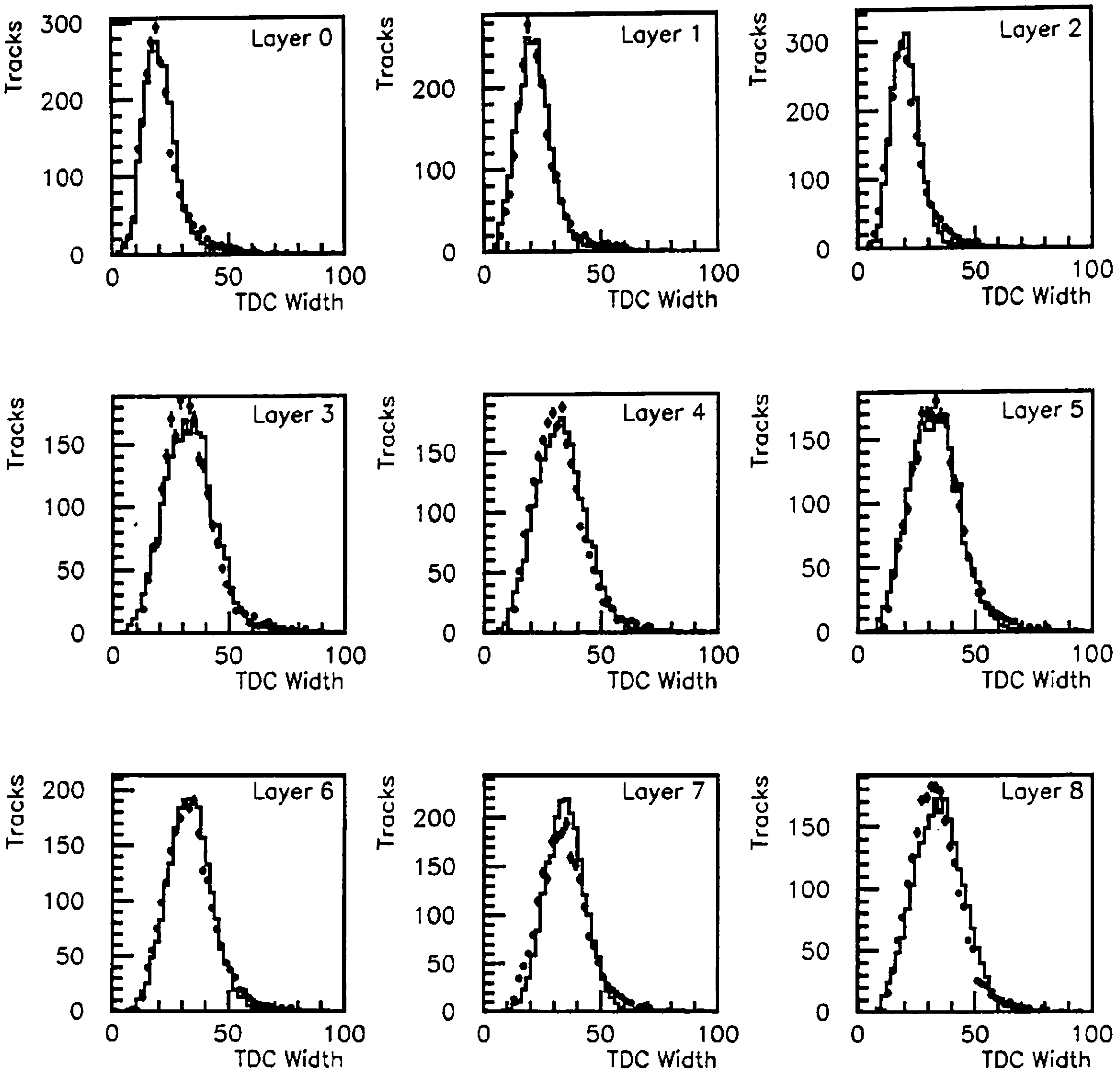

Figure 6.3: TDC width distributions in axial (0, 2, 4, 6, and 8) and stereo (1, 3, 5, and 7) superlayers. The points show those of the real tracks in the minimum bias events, and the histograms show those of the simulated tracks.

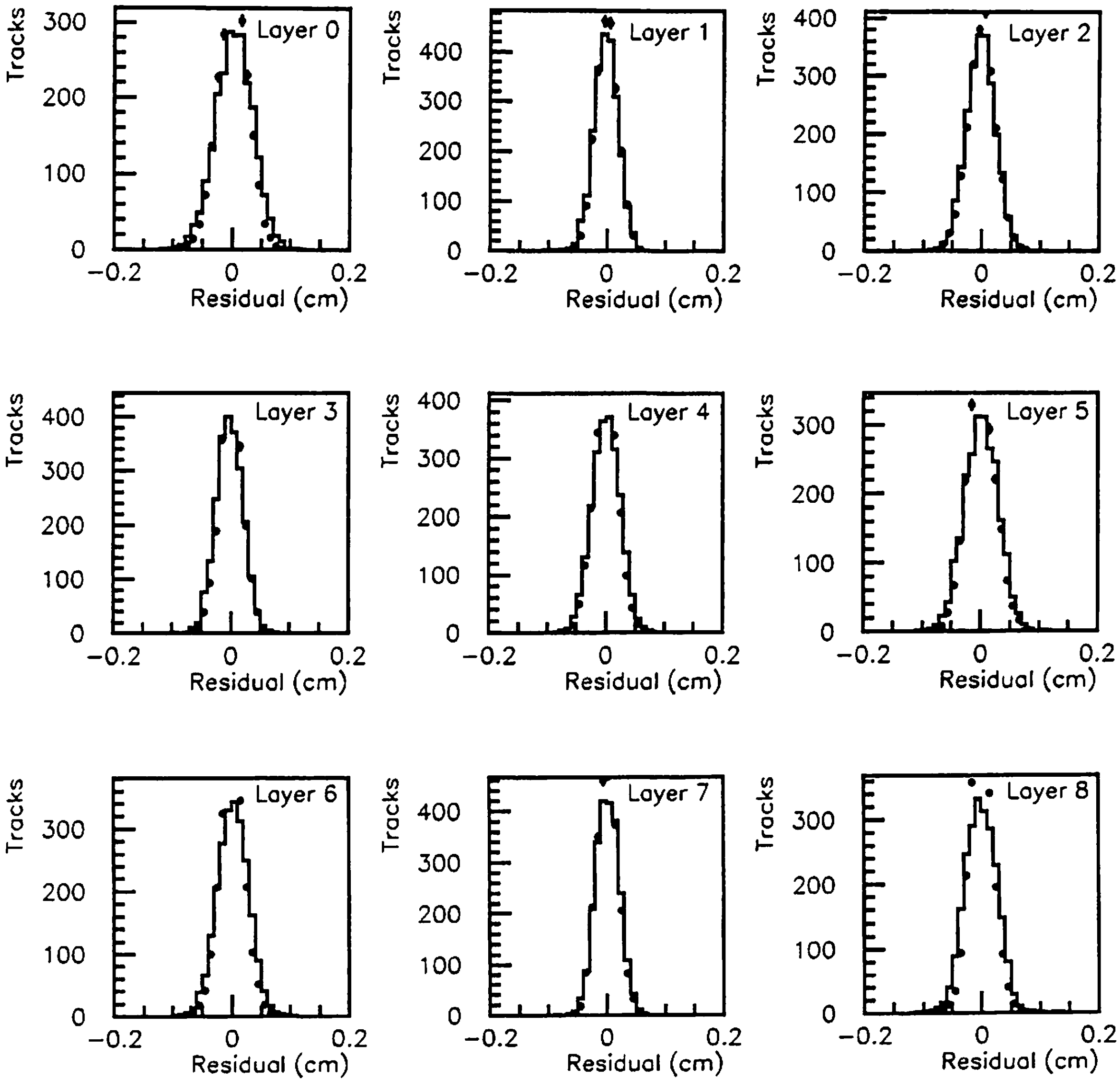

Figure 6.4: Residual distributions in axial (0, 2, 4, 6, and 8) and stereo (1, 3, 5, and 7) superlayers. The points show those of the real tracks in the minimum bias events, and the histograms show those of the simulated tracks.

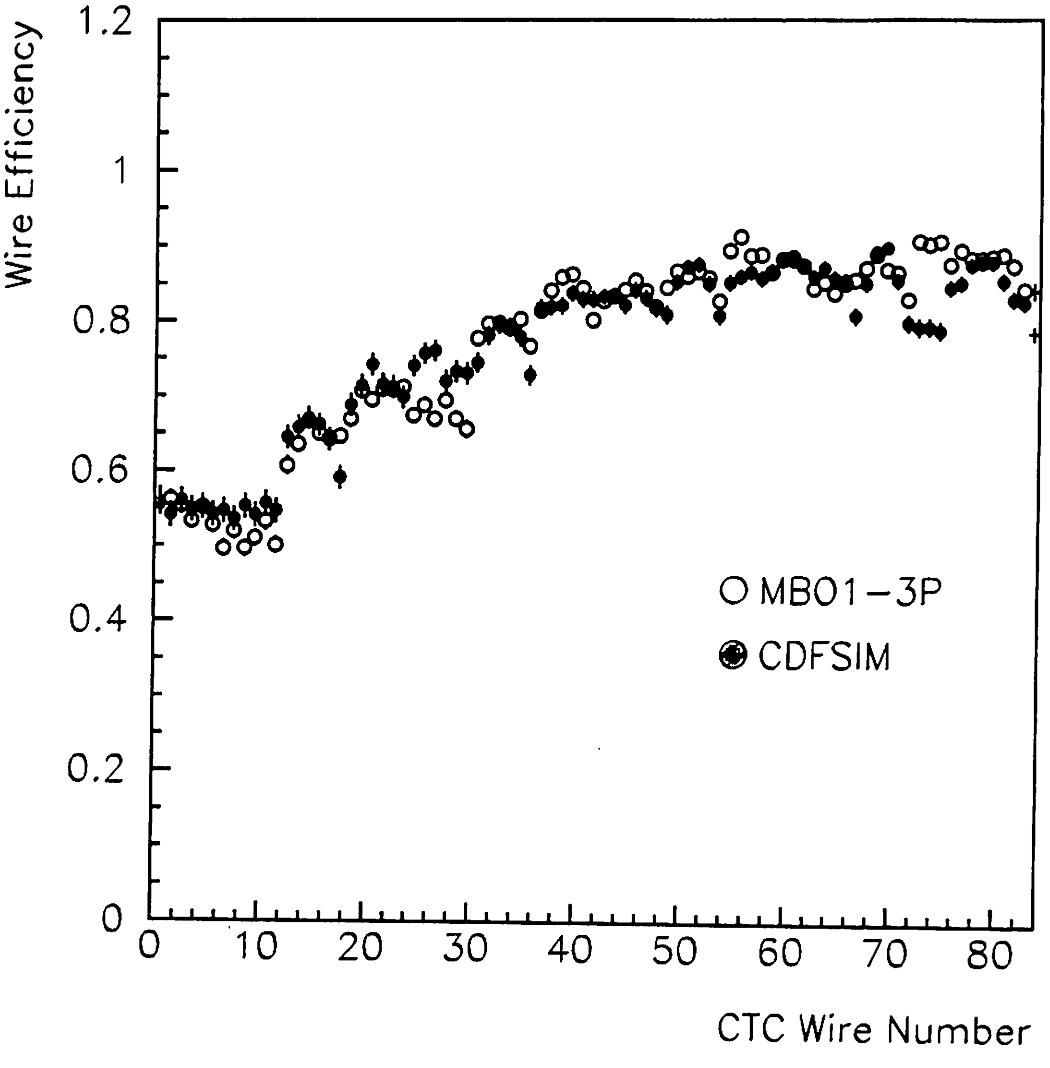

Figure 6.5: Wire efficiency on each layer. The open circles show those of the real tracks in the minimum bias events, and the filled circles show those of the simulated tracks.

where N_{Hit} is the number of the tracks which have a hit on the layer n, and N_{Track} is the number of all tracks which passed the SVX fiducial volume on the layer n. The SVX hit efficiencies were installed in the SVX detector simulation program. Figure 6.6 shows a comparison of the SVX hit efficiencies between the simulated tracks and the real tracks. The simulated tracks were imbedded into the minimum bias events. The SVX hit efficiencies of the simulated tracks are consistent with those of the real tracks.

Table 6.4: SVX hit efficiency in the minimum bias events. The errors show the statistical ones.

SVX Layer	Efficiency
0	0.742 ± 0.002
1	0.854 ± 0.002
2	0.903 ± 0.001
3	0.878 ± 0.002

6.2.3 Mass reconstruction

The efficiency $\epsilon_{\text{Track\&Mass}}$ for the track p_T cuts and the mass reconstruction is defined by

$$\epsilon_{\text{Track\&Mass}} = \frac{N_{\text{rec.}}}{N_{\text{prod.}}},$$

where $N_{\text{prod.}}$ is the number of the produced $D^{*\pm}$ events in the kinematical range of $p_T(D^{*\pm}) > 6$ GeV/c and $|y(D^{*\pm})| < 1.2$, and $N_{\text{rec.}}$ is the number of the reconstructed events in the $D^{*\pm}$ signal window (144 <

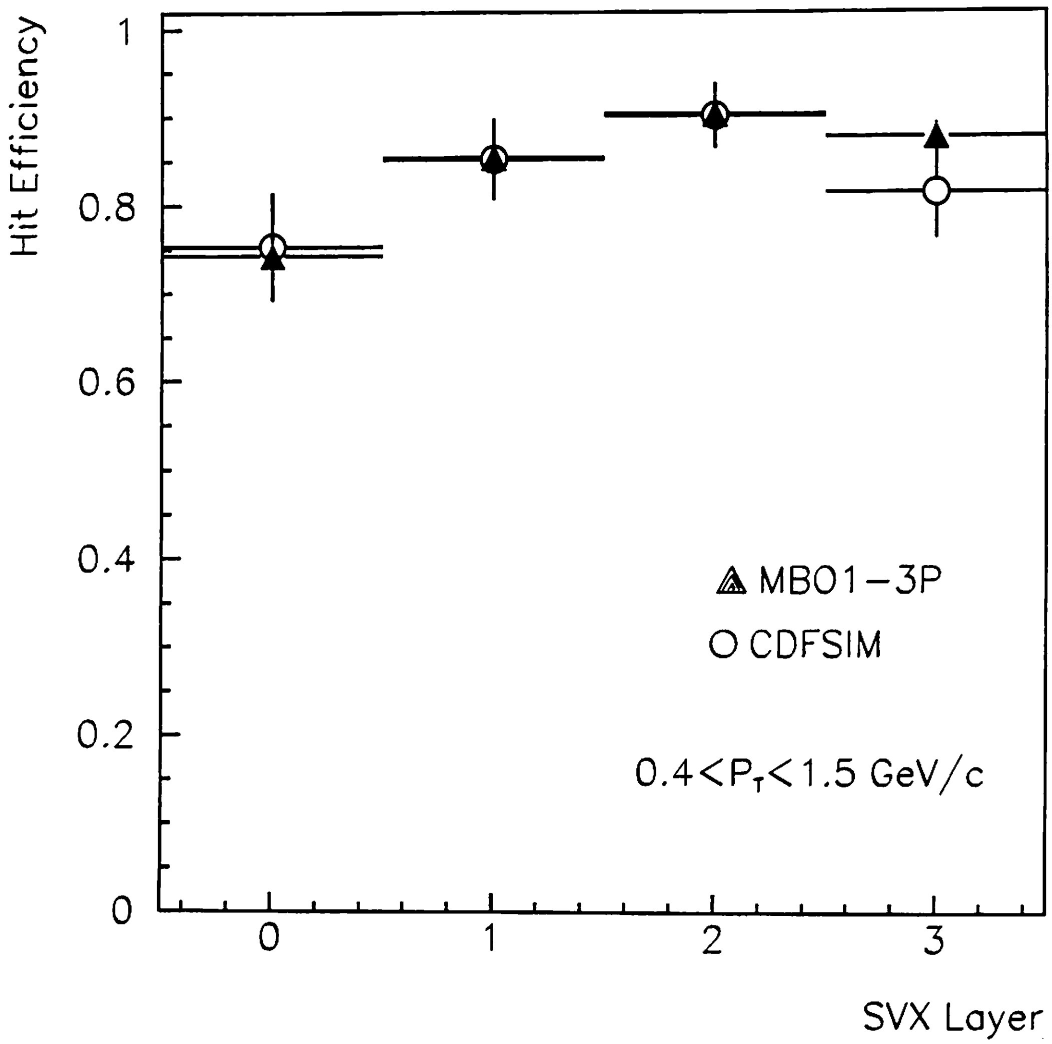

Figure 6.6: SVX hit efficiencies of the simulated tracks imbedded in the minimum bias events (open circles), and those of the isolated real tracks in the minimum bias events (filled triangles).

$\Delta M < 147$ MeV/c^2) with the $D^{*\pm}$ selection cuts. The efficiency contains the geometrical acceptance of the charged tracks for the CTC and the mass resolution effect. The $D^{*\pm}$ Monte Carlo events were generated with PYTHIA through the following processes:

$$\begin{aligned} q+g &\rightarrow \gamma+q, \\ q+q' &\rightarrow \gamma+g, \end{aligned}$$

with initial and final gluon radiations, where q expresses u,d,s,c, or b quarks. The generated events were simulated for the CDF detector. The simulated events were imbedded into the inclusive photon events in order to introduce the actual detector effects. Figures 6.7 and 6.8 show the reconstructed $D^0(\rightarrow K^-\pi^+$ or $\rightarrow K^-\pi^-\pi^+\pi^+)$ mass and the mass difference distributions of the Monte Carlo events. From these distributions, the efficiencies ($\epsilon_{\mathrm{Track\&Mass}}$) were estimated:

$$\left\{ \begin{aligned} \epsilon_{\mathrm{Track\&Mass}} &= 0.57 \pm 0.01 \quad (D^0 \rightarrow K^-\pi^+). \\ \epsilon_{\mathrm{Track\&Mass}} &= 0.26 \pm 0.01 \quad (D^0 \rightarrow K^-\pi^-\pi^+\pi^+). \end{aligned} \right.$$

6.3 Surviving probability of kaon inside the CTC

A kaon is required to be inside the CTC without decaying. The probability of a kaon surviving inside the CTC was estimated using the Monte Carlo data. The momentum distribution of the kaon were obtained with the PYTHIA. The probability surviving inside the CTC, $\varepsilon_{\mathrm{kaon}}$, was calculated:

$$\varepsilon_{\mathrm{kaon}} = 0.95.$$

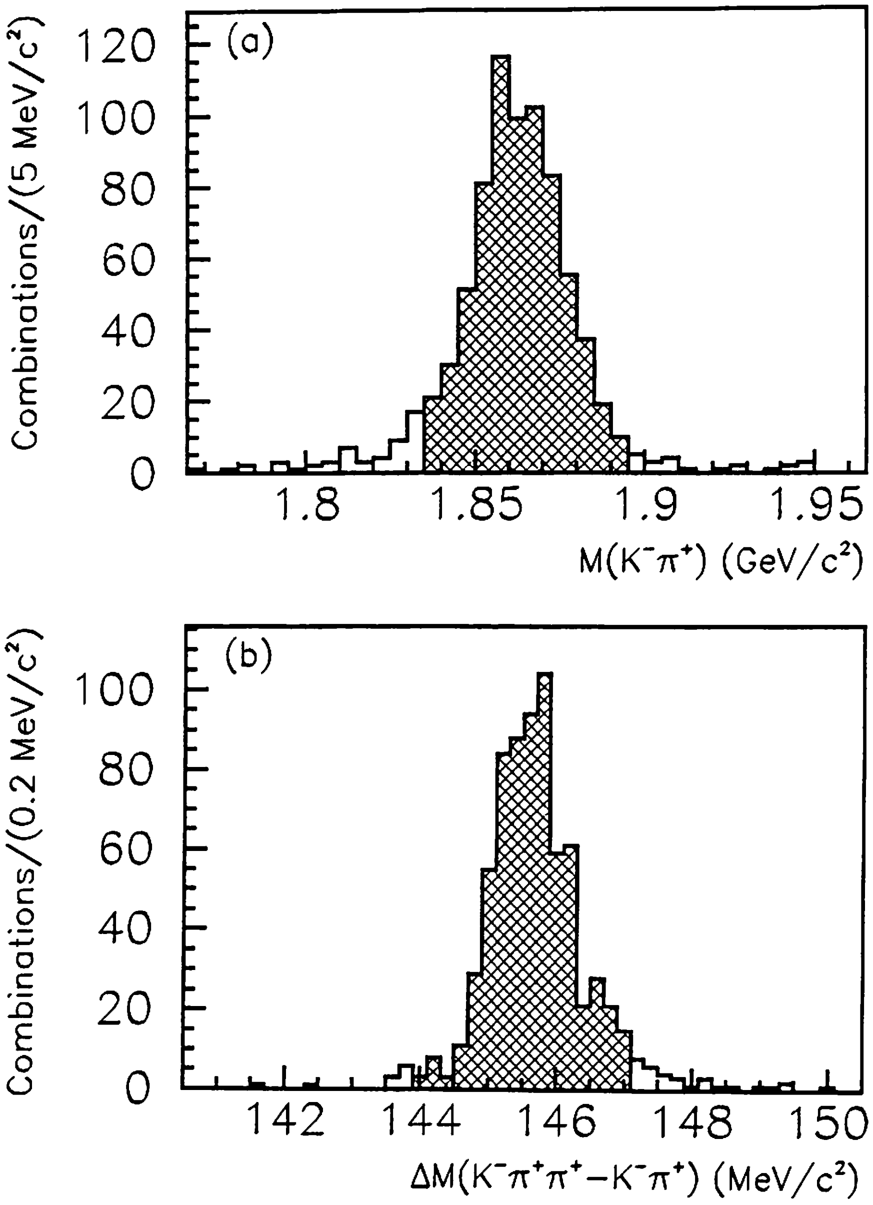

Figure 6.7: Monte Carlo mass distributions; (a) $K^-\pi^+$ mass distribution, (b) mass difference $\Delta M(K^-\pi^+\pi_s^+ - K^-\pi^+)$ distribution. The Monte Carlo events containing $D^{*\pm} \rightarrow K^-\pi^+\pi_s^+$ were simulated and were imbedded into the inclusive photon events.

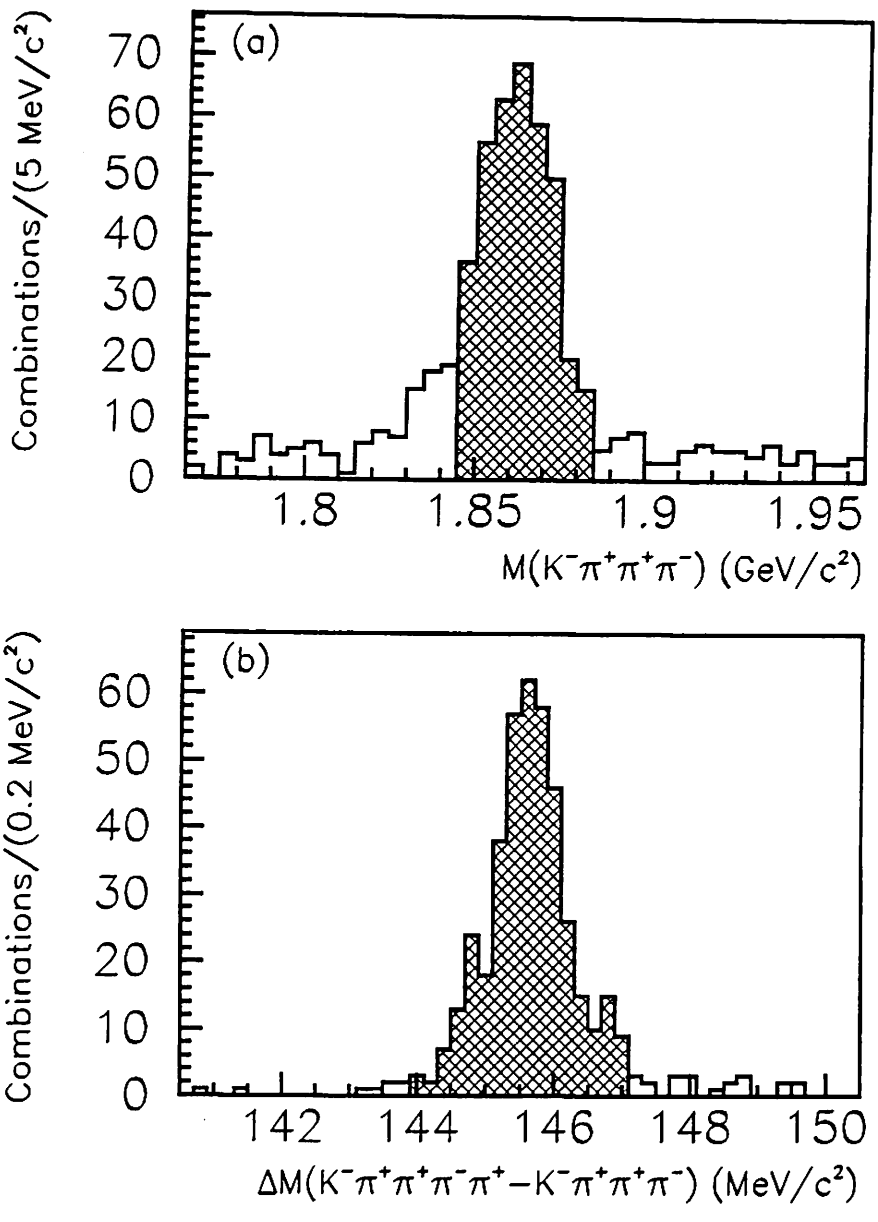

Figure 6.8: Monte Carlo mass distributions; (a) $K^-\pi^-\pi^+\pi^+$ mass distribution, (b) mass difference $\Delta M(K^-\pi^-\pi^+\pi^+\pi_s^+ - K^-\pi^-\pi^+\pi^+)$ distribution. The Monte Carlo events containing $D^{*\pm} \rightarrow K^-\pi^-\pi^+\pi^+\pi_s^+$ were simulated and were imbedded into the inclusive photon events.

6.4 Overall efficiency

The overall efficiency for the $\gamma + D^{*\pm}$ detection was calculated by

$$\epsilon_{\gamma+D^{*\pm}} = \varepsilon_{\rm sel} \times \varepsilon_{\rm trig} \times \epsilon_{\rm Track\&Mass} \times \varepsilon_{\rm kaon}.$$

The overall efficiencies $\epsilon_{\gamma+D^{*\pm}}$ are summarized in Table 6.5.

Table 6.5: Summary of the efficiencies

Channels	overall ε
$D^0 \to K^-\pi^+$	0.150 ± 0.024
$D^0 \to K^-\pi^-\pi^+\pi^+$	0.067 ± 0.011

6.5 Calculation of the cross section

We derived the cross section for $\gamma + D^{*\pm}$ production from the reconstructions using the $D^0 \to K^-\pi^+$ and $D^0 \to K^-\pi^-\pi^+\pi^+$ decay modes. The cross section was calculated by

$$\sigma(\bar{p}p \to \gamma D^{*\pm} + X) = \frac{N(\gamma + D^{*\pm})}{\varepsilon \times Br(D^{*+})Br(D^0) \times \mathcal{L}}$$

where $N(\gamma + D^{*\pm})$ is the number of the $\gamma + D^{*\pm}$ candidates, $\mathcal{L}$ is the integrated luminosity, ε is the overall efficiency for the reconstruction of the $\gamma + D^{*\pm}$ events, and Br expresses the branching ratio of the D^{*+} or the D^0 decays. The branching ratios were taken from Particle Data Book [18]. The values used to derive the cross section are summarized in Table 6.6.

Table 6.6: The values used to derive the cross section.

	$D^0 \to K^-\pi^+$	$D^0 \to K^-\pi^-\pi^+\pi^+$
$N(\gamma + D^{*\pm})$	29.9 ± 10.4	31.9 ± 16.0
ε	0.150 ± 0.024	0.067 ± 0.011
$Br(D^0 \to K^-\pi^+)$	4.01 ± 0.14 %	
$Br(D^0 \to K^-\pi^-\pi^+\pi^+)$		8.1 ± 0.5 %
$Br(D^{*+} \to D^0\pi^+)$	68.1 ± 1.3 %	
$\mathcal{L}$	16.4 pb^{-1}	

6.5.1 $D^0 \to K^-\pi^+$

From the $D^{*\pm}$ reconstruction using $D^0 \to K^-\pi^+$, the $\gamma + D^{*\pm}$ production cross section was found to be

$$\sigma(\bar{p}p \to \gamma D^{*\pm} + X) = 0.45 \pm 0.16 \text{ (stat.)} \pm 0.08 \text{ (syst.)} \quad \text{nb},$$

in a kinematical range of $16 < p_{\mathrm{T}}(\gamma) < 40$ GeV/c, $|y(\gamma)| < 0.9$, $p_{\mathrm{T}}(D^{*\pm}) > 6$ GeV/c, and $|y(D^{*\pm})| < 1.2$, where the first and second errors show the statistical and systematic ones, respectively. The systematic error is discussed in the chapter of systematic uncertainty.

6.5.2 $D^0 \to K^-\pi^-\pi^+\pi^+$

From the $D^{*\pm}$ reconstruction using $D^0 \to K^-\pi^-\pi^+\pi^+$, we obtained the cross section to be

$$\sigma(\bar{p}p \to \gamma D^{*\pm} + X) = 0.53 \pm 0.26(\text{stat.})^{+0.12}_{-0.11}(\text{syst.}) \text{ nb},$$

in the same kinematical range as above.

6.5.3 Combining $D^0 \to K^-\pi^+$ and $D^0 \to K^-\pi^-\pi^+\pi^+$

The cross section using the two D^0 decay modes was calculated by

$$\sigma = \frac{N(\gamma + D^{*\pm})}{Br_{D^{*+}\to D^0\pi^+} \times (Br_{D^0\to K\pi} \times \varepsilon_{D^0\to K\pi} + Br_{D^0\to K3\pi} \times \varepsilon_{D^0\to K3\pi}) \times \mathcal{L}},$$

where the $\varepsilon_{D^0\to K\pi}$ and $\varepsilon_{D^0\to K3\pi}$ are the efficiencies for the reconstructions using $D^0 \to K^-\pi^+$ and $D^0 \to K^-\pi^-\pi^+\pi^+$, respectively. We determined the cross section to be

$$\sigma(\bar{p}p \to \gamma D^{*\pm} + X) = 0.48 \pm 0.15(\text{stat.}) {}^{+0.07}_{-0.08}(\text{syst.})\ \text{nb}.$$

6.5.4 Summary of the cross section

We summarize the measured cross sections as follows:

$$\sigma(\gamma + D^{*\pm}) = \begin{cases} 0.45 \pm 0.16(\text{stat.}) & \pm 0.08 & (\text{syst.})\ (\text{nb}) & (\ D^0 \to K\pi), \\ 0.53 \pm 0.26(\text{stat.}) & {}^{+0.12}_{-0.11} & (\text{syst.})\ (\text{nb}) & (\ D^0 \to K3\pi), \\ 0.48 \pm 0.15(\text{stat.}) & {}^{+0.07}_{-0.08} & (\text{syst.})\ (\text{nb}) & (\ \text{above two}), \end{cases}$$

in the kinematical range of

$$\begin{cases} 16 < p_T(\gamma) < 40\ \text{GeV}/c, \\ |y(\gamma)| < 0.9, \\ p_T(D^{*\pm}) > 6\ \text{GeV}/c, \\ |y(D^{*\pm})| < 1.2. \end{cases}$$

Chapter 7

Systematic Uncertainty

The systematic uncertainty in the $\gamma + D^{*\pm}$ production cross section is discussed. The systematic error can be decomposed into the uncertainties in the photon detection and those in the $D^{*\pm}$ detection. These are estimated from real data, electron test beam data, and Monte Carlo data.

7.1 Photon selection

The major source of systematic error in the photon selection efficiency comes from the uncertainty in the isolation cut efficiency. The isolation cut efficiency was estimated from the distribution of the extra energy around photon in the minimum bias events. The distribution is almost independent of the photon transverse momentum. However, it depends on the number of interactions or instantaneous luminosity of the beam. The extra energy distributions were obtained from the minimum bias data with various luminosities. The extra energy was calculated by a combination of different luminosity samples. We compared the distributions of the data taken at the average luminosity and those combining different luminosity samples. The difference results in 3 % change in the isolation cut efficiency. It is assigned to the systematic uncertainty in the photon selection cut efficiency.

7.2 Subtraction of photon background

The sources of systematic uncertainty in the photon background subtraction can be broken down to:

- CES χ^2 efficiency of photons,
- CES χ^2 efficiency of backgrounds,
- Subtraction of backgrounds against prompt photons.

Each term is discussed below.

7.2.1 Photon χ^2 efficiency

The systematic uncertainties from all known sources were evaluated by varying the sources in the detector simulation. The sources are the shower fluctuation, the shower shape, and the gas saturation. Figure 7.1 shows the systematic uncertainties from the sources in the photon χ^2 efficiency. These uncertainties are discussed below.

Shower Fluctuation

> The variable of the CES χ^2 depends on the number of shower electrons in the CES. The difference of shower electrons between electron and photon is based on their shower maximum

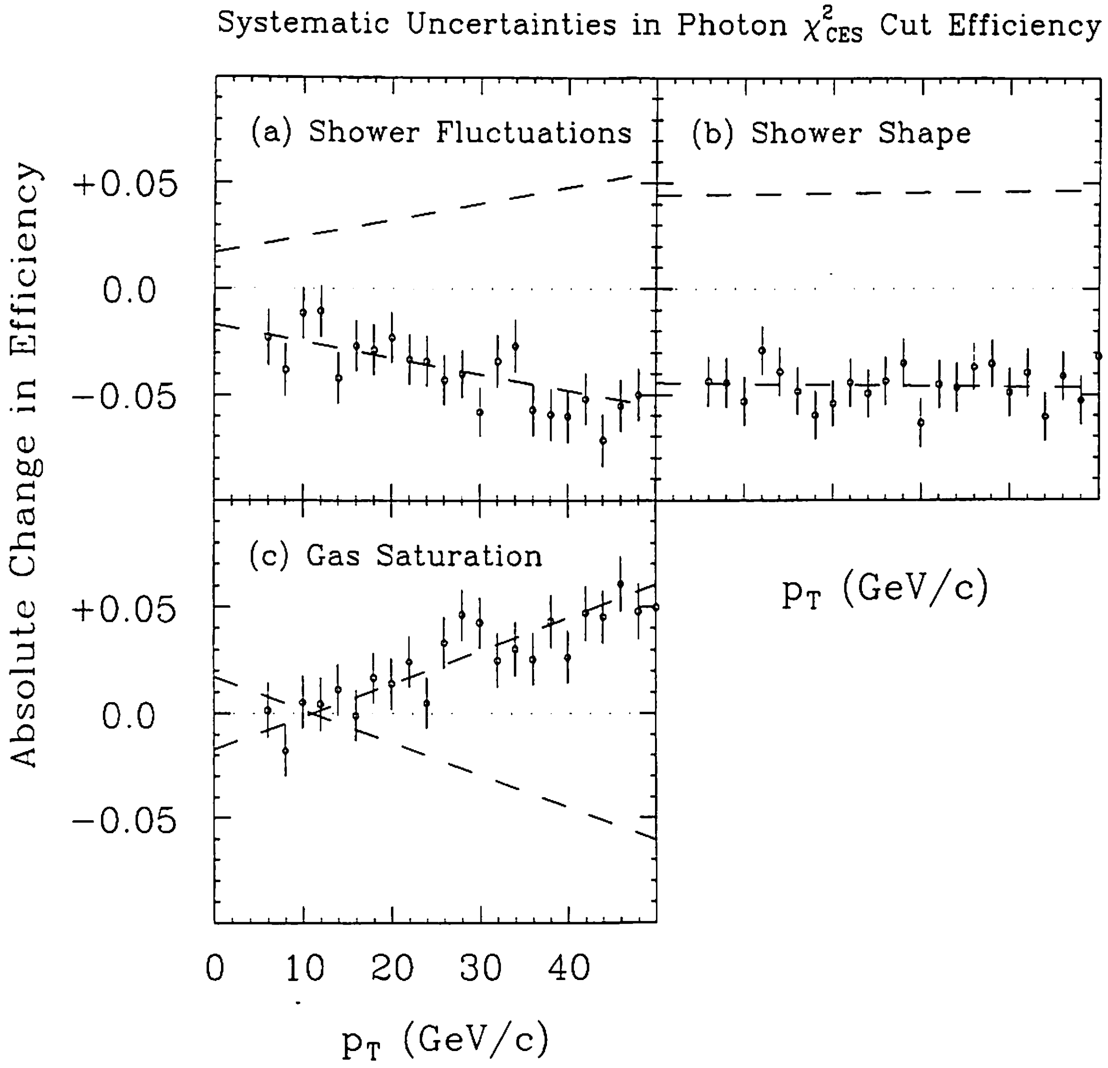

Figure 7.1: The systematic uncertainties in the photon CES χ^2 efficiency from the known three sources. (a) The amount of statistical fluctuations in photon shower, (b) the transverse shape of photon shower, and (c) the effect of CES gas saturation.

positions. The shower of electron in the CEM starts faster than that of photon. A parameterization of the shower fluctuations from the electron test beam data was used for the simulation of photon. The parameterization was installed in the simulation program, taking account of the difference of the shower maximum positions between electron and photon. The shower maximum position difference ΔT was estimated to be $\Delta T = 0.6$ (X_0). The Particle Data Group, on the other hand, estimates $\Delta T = 1$ [18]. The difference between the CES χ^2 efficiencies for $\Delta T = 0.6$ and $\Delta T = 1.0$ gave the absolute change in the χ^2 efficiency. That was evaluated with the simulation, and are shown in Fig. 7.1 (a). The data in Fig. 7.1 (a) were fitted with a linear function. The fitted results are

$$\begin{cases} \text{intercept} & = & -0.0170 \pm 0.0047, \\ \text{slope} & = & -0.00077 \pm 0.00011, \end{cases}$$

where the errors come from the statistics of the Monte Carlo events.

Shower Shape

The systematic uncertainty in the CES χ^2 efficiency from the difference of transverse shower profiles between electron and photon was studied. The χ^2 efficiency of photon is sensitive to the shape of the transverse profile. The shower profile of the test beam electron was used for the estimation of the systematics by varying amounts of material in front of the

CES. The χ^2 efficiencies for 10 GeV test beam electrons are shown in Figure 7.2 as a function of material thickness in front of the CES. The point marked "A" corresponds to the amount of material for the electron test beam data. The change in the χ^2 efficiency with increasing (or decreasing) amount of material is linear, where the same linear relation is assumed in decreasing the amount of material. The point marked "B" shows the χ^2 efficiency at the amount of material in the CDF detector at the collision hall. A shower maximum position of photon shower in material is expected to be larger than that of electron. The difference corresponds to 0.6 radiation length. The point "D" is moved by 0.6 radiation length along the line from the point "B." Then, the difference between the points of "B" and "C," which corresponds to 0.55 radiation length, was defined to the systematic uncertainty in the χ^2 efficiency of photons. The lower systematic uncertainties were evaluated by changing the thickness of material within 0.55 X_0 in the simulation, which are shown in Fig. 7.1 (b). The data were fitted with a linear function, the fitting result is

$$\left\{ \begin{array}{lcl} \text{intercept} & = & -0.0443 \pm 0.0044, \\ \text{slope} & = & -0.00005 \pm 0.00009, \end{array} \right.$$

where the errors show the statistical ones.

Gas Saturation

The pulse heights of the CES channels are normalized before the χ^2 calculation. The effect reducing the pulse height due

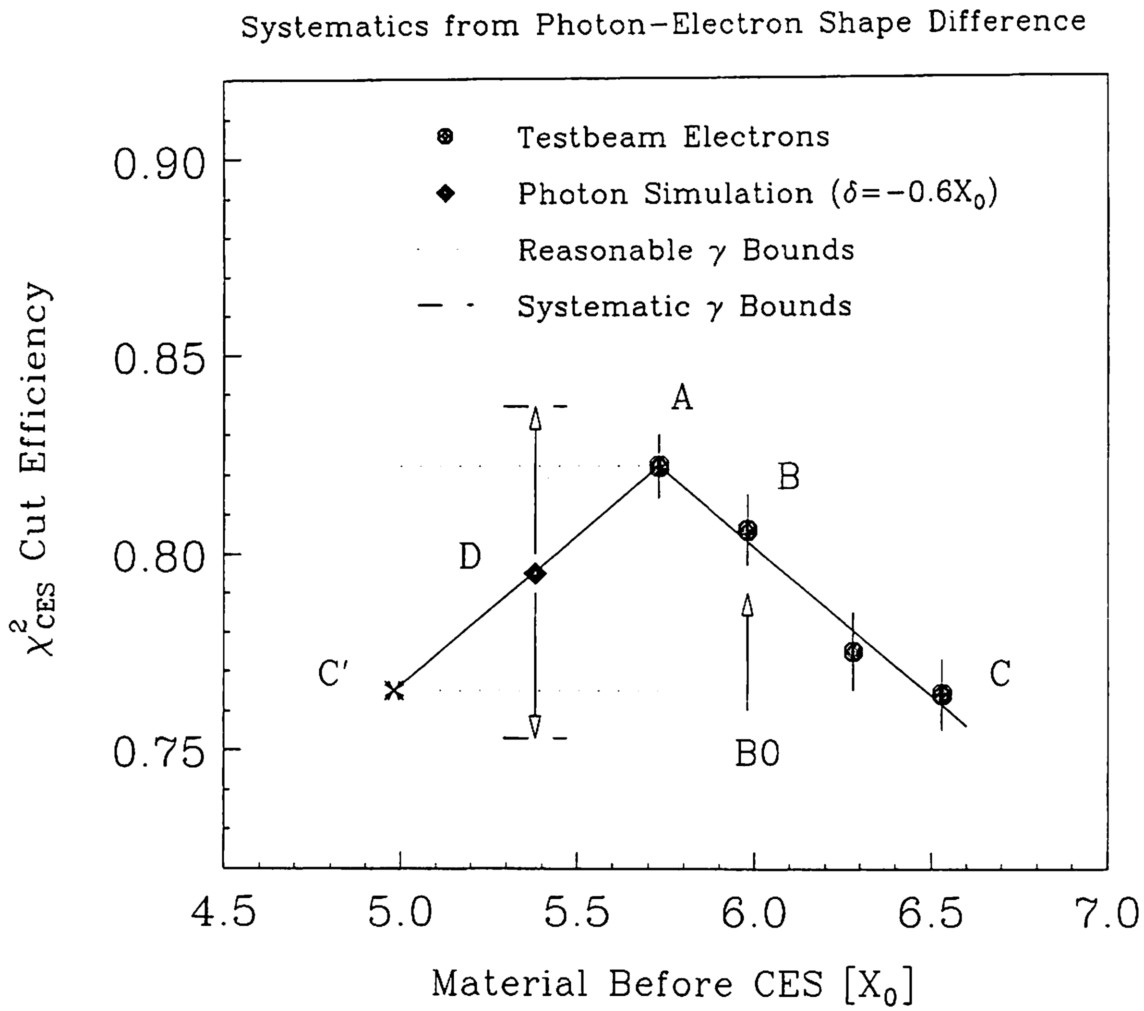

Figure 7.2: The CES χ^2 efficiency for 10 GeV test beam electrons when changing the amount of material in front of the CES detector. The symbols are explained in the text.

to saturation of gas gain depends on the pulse height. The electron test beam data were taken at a relatively low voltage (1390 Volts), where the saturation effect in the CES was small, and were used in the detector simulation of photons. The saturation effect was installed in the detector simulation as a correction to a nominal shower. The correction was carried out on the CES χ^2 by multiplying a factor K. Assuming that the factor is proportional to the photon energy, the factor K is expressed by

$$K = 1 + (K_1 - 1)\frac{E - 10}{50 - 10},$$

where E is the energy of photon in units of GeV. The value of K_1 was obtained from the electron test beam data to be 1.12 ± 0.03. The systematic uncertainty was defined as the value of the correction factor, that was taken conservatively. The absolute difference between the photon efficiencies with and without the corrections was shown in Fig. 7.1 (c). The distribution was fitted with a linear function. The fitted parameters are

$$\begin{cases} \text{intercept} & = & -0.0173 \pm 0.0048, \\ \text{slope} & = & -0.00155 \pm 0.00011, \end{cases}$$

where errors show statistical ones.

We summarize the systematic uncertainties from the known sources in the photon χ^2 efficiency. Figure 7.3 shows the CES χ^2 efficiency of photons for the cut $\chi^2 < 4$, and one standard deviation upper systematic uncertainties obtained by the simulation.

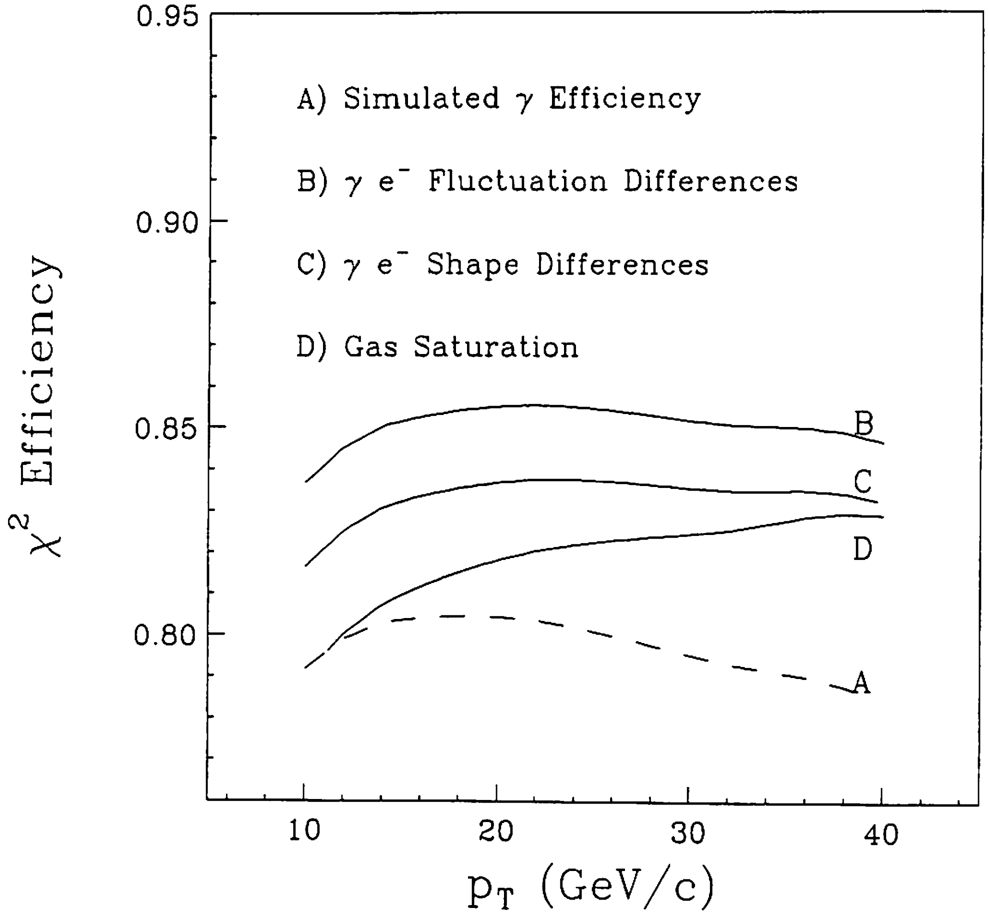

Figure 7.3: CES χ^2 efficiency of photons and 1σ upper systematic uncertainties in the χ^2 efficiency obtained by the simulation.

7.2.2 Background χ^2 efficiency

The systematic uncertainties in the background χ^2 efficiency were also evaluated by varying the sources of the uncertainty in the detector simulation. The absolute differences in the background χ^2 efficiency are shown in Figs. 7.4 (a),(b), and (c) for the shower fluctuation, the shower shape, and the gas saturation, respectively. A remaining source of the systematic uncertainty is a background composition. The CDF collaboration has already measured the ratio of η and π^0 production [20]. The number is

$$\eta/\pi^0 = 1.02 \pm 0.15 \text{ (stat.)} \pm 0.23 \text{ (syst.)},$$

where the first and the second errors are statistical and systematic ones, respectively. The measurement error after combining the statistical and the systematic errors was assigned to the systematic uncertainty in the composition of η and π^0. The absolute difference in the background χ^2 efficiency by varying the background composition is shown in Fig. 7.4 (d). Figure 7.5 shows the χ^2 efficiency of the photon backgrounds with one standard deviation upper systematic uncertainties in the χ^2 efficiency obtained by the simulation.

7.2.3 Subtraction of photon backgrounds

We used the CES method for the photon background subtraction in this analysis. A CPR method using hit rates in the CPR detector is also useful to subtract the photon background.

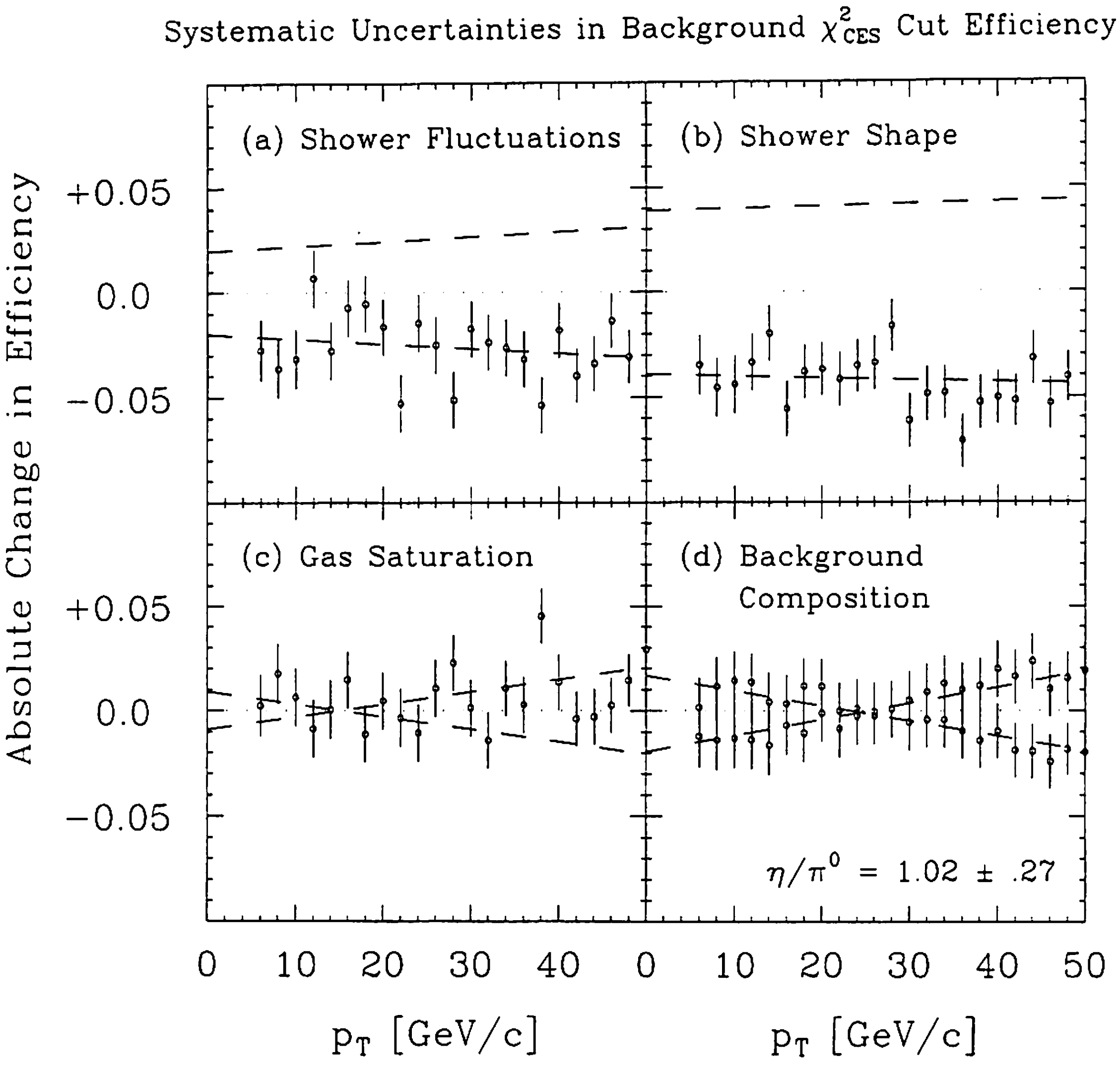

Figure 7.4: Absolute changes in the background CES χ^2 efficiencies for the known sources; (a) the amount of statistical fluctuations in photon shower, (b) the transverse shape of the photon shower, (c) the effect of CES gas saturation, and (d) the background composition.

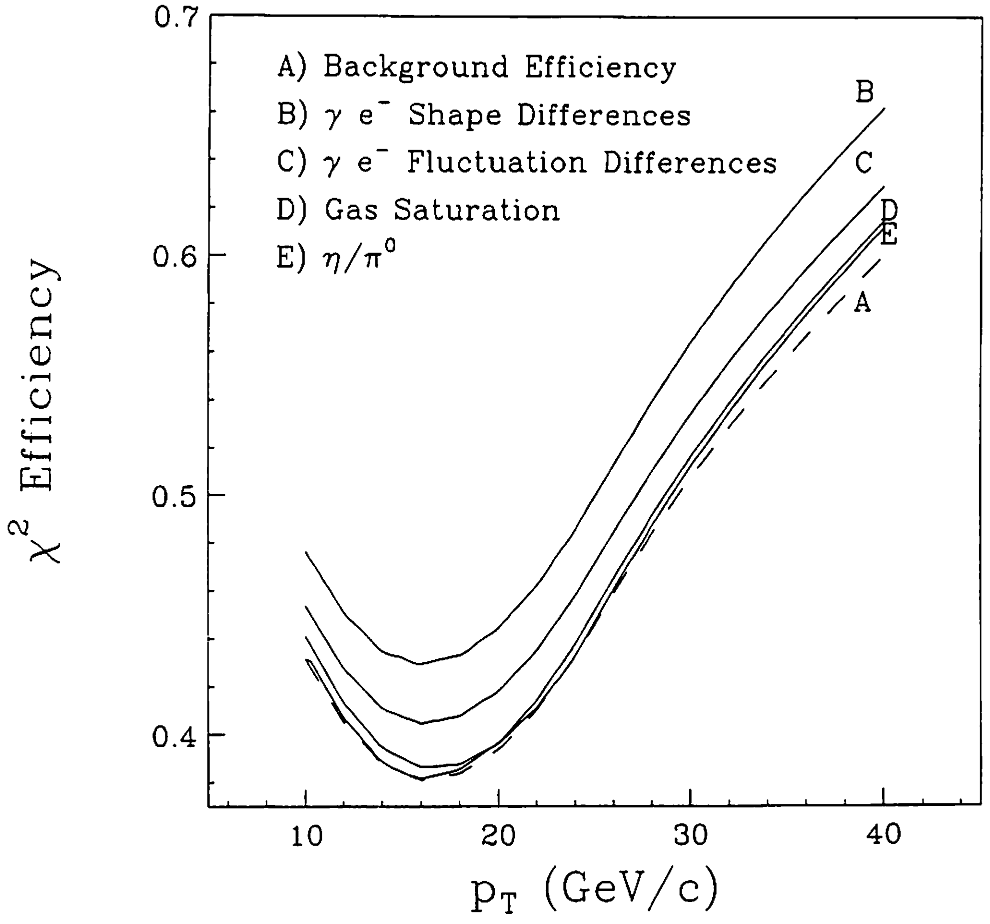

Figure 7.5: CES χ^2 efficiency of the backgrounds, and 1σ upper systematic uncertainties in the χ^2 efficiency obtained by the simulation.

7.2.3.1 CES method

The systematic uncertainty in the photon background subtraction comes from the systematic uncertainties in the photon χ^2 efficiency (ε_γ) and the background χ^2 efficiency (ε_B). The systematic bound (N'_γ) on the number of prompt photons (N_γ) is expressed by

$$\frac{N'_\gamma}{N_\gamma} = (\frac{\epsilon - \epsilon'_B}{\epsilon'_\gamma - \epsilon'_B})/(\frac{\epsilon - \epsilon_B}{\epsilon_\gamma - \epsilon_B}),$$

where ϵ'_γ and ϵ'_B are the systematic bounds on the photon and the background χ^2 efficiencies, respectively. The systematic bounds were obtained by varying the known systematic uncertainty sources in the simulation program, and are shown as the dashed lines in Figure 7.6. The percent systematic uncertainty in the number of photons is given by

$$100 \times (\frac{N'_\gamma}{N_\gamma} - 1).$$

Figure 7.7 shows the percent changes in the number of prompt photons for the known sources. For clarity, only positive changes are shown in the figure, the negative changes are similar.

7.2.4 CPR method

The CPR method utilizes the difference of the CPR hit rates between single photon and multi-photon. The algebra to determine the number of prompt photons is the same as that in the CES method. The major source of systematic uncertainty comes from the uncertainty in the expected hit rate of single photon. The expected hit rate was checked by using the observed $\pi^0 \to \gamma\gamma$, $\eta \to \gamma\gamma$, and $\rho^\pm \to \pi^0\pi^\pm$ events. Figure 7.8 shows the $\gamma\gamma$ and $\pi^0(\to \gamma\gamma)\pi^\pm$ mass distributions. From the π^0 and the

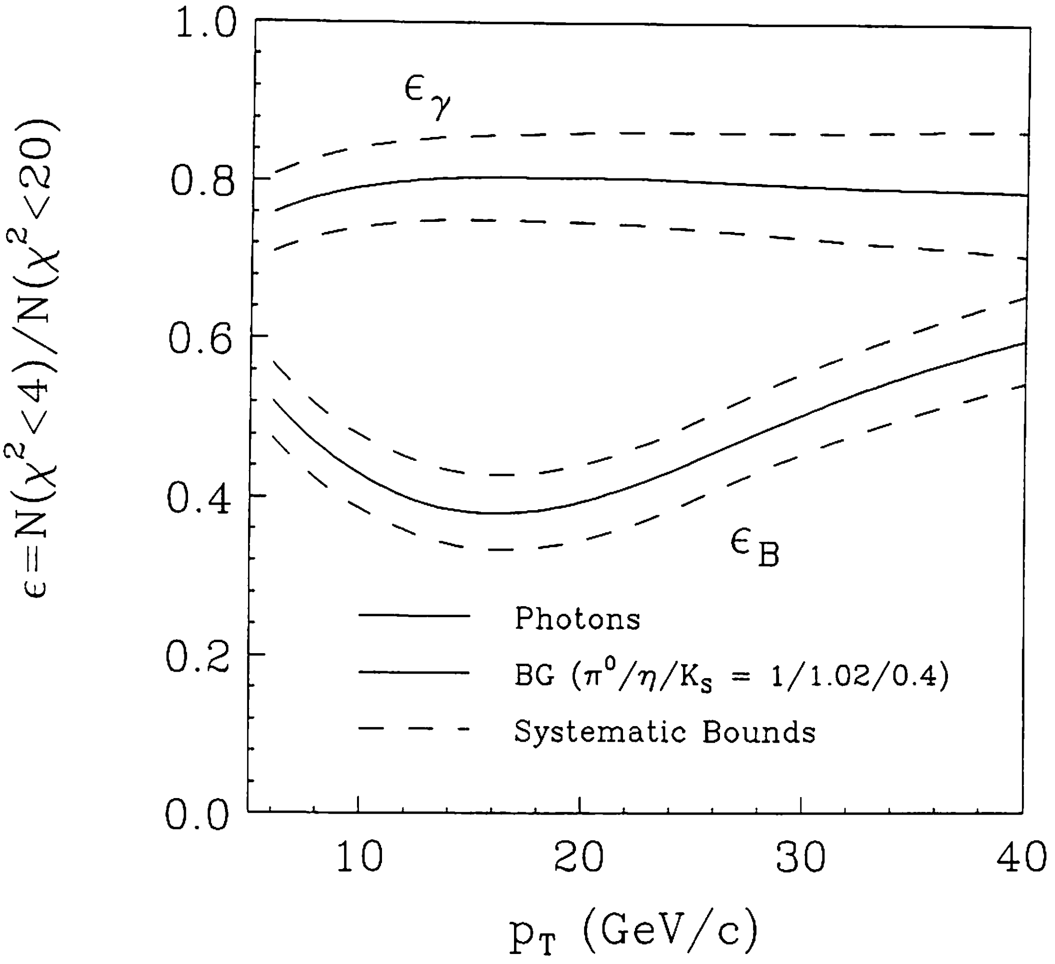

Figure 7.6: χ^2 efficiencies for photons and backgrounds (solid lines), and their systematic bounds (dashed lines).

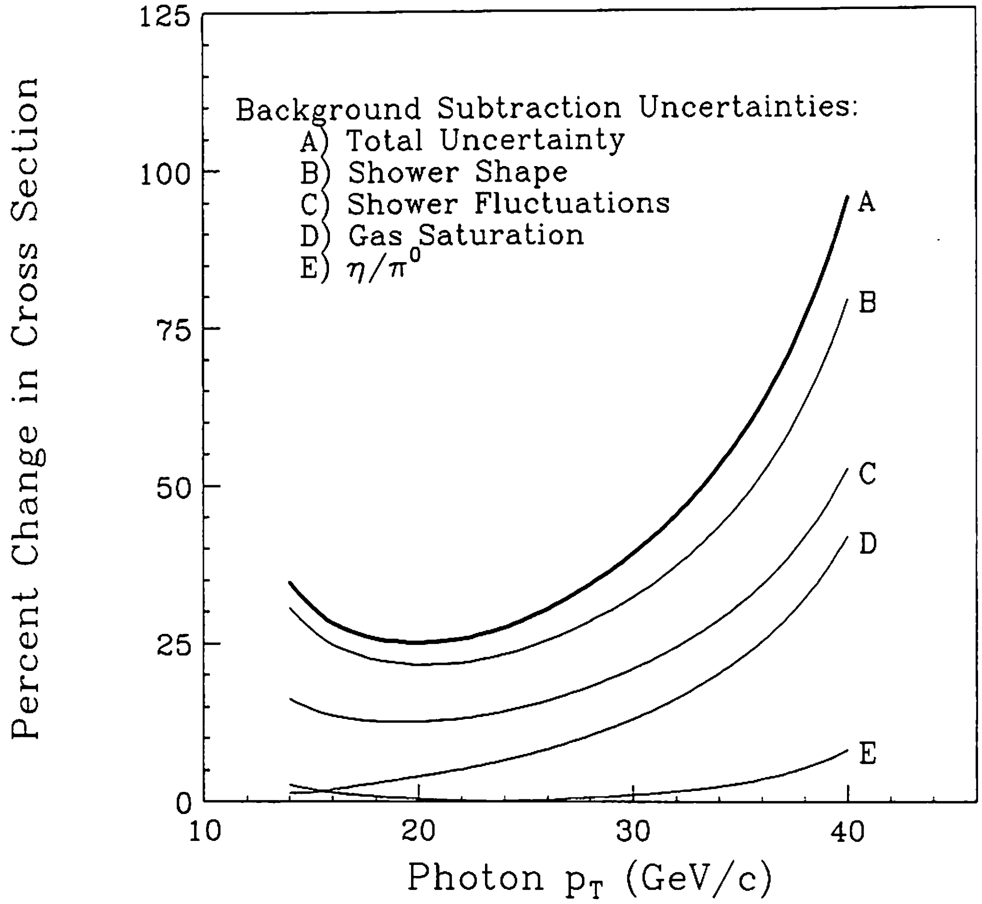

Figure 7.7: Percent changes due to the uncertainties on the background subtraction. (Only positive systematic uncertainties are shown.)

$\rho^{\pm}$ peaks, we obtained the conversion probabilities to be 0.842 ± 0.008 for π^0. From the error on the measurements, the systematic uncertainty on the cross section is 10 % at photon transverse momentum of 16 GeV/c.

7.2.5 Systematics of photon background subtraction

We have measured the inclusive photon cross section with the CES and the CPR methods [24]. We show the inclusive photon cross section in Fig. 7.9. The systematic uncertainty in the CPR method is smaller than that in the CES method. The cross sections using both methods agree to within 5 %. Therefore, we assigned the systematic uncertainty in the CPR method to that of photon background subtraction, which is 9 %.

7.3 $D^{*\pm}$ detection

The systematic uncertainty in the $D^{*\pm}$ detection efficiency is discussed in this section. The sources of the uncertainty are listed below:

- Models of parton distribution function.
- Charm quark fragmentation models.
- Branching ratios of $D^{*+} \to D^0\pi^+$, $D^0 \to K^-\pi^+$, and $D^0 \to K^-\pi^-\pi^+\pi^+$ decays.
- Renormalization scale.
- Track reconstruction efficiency.

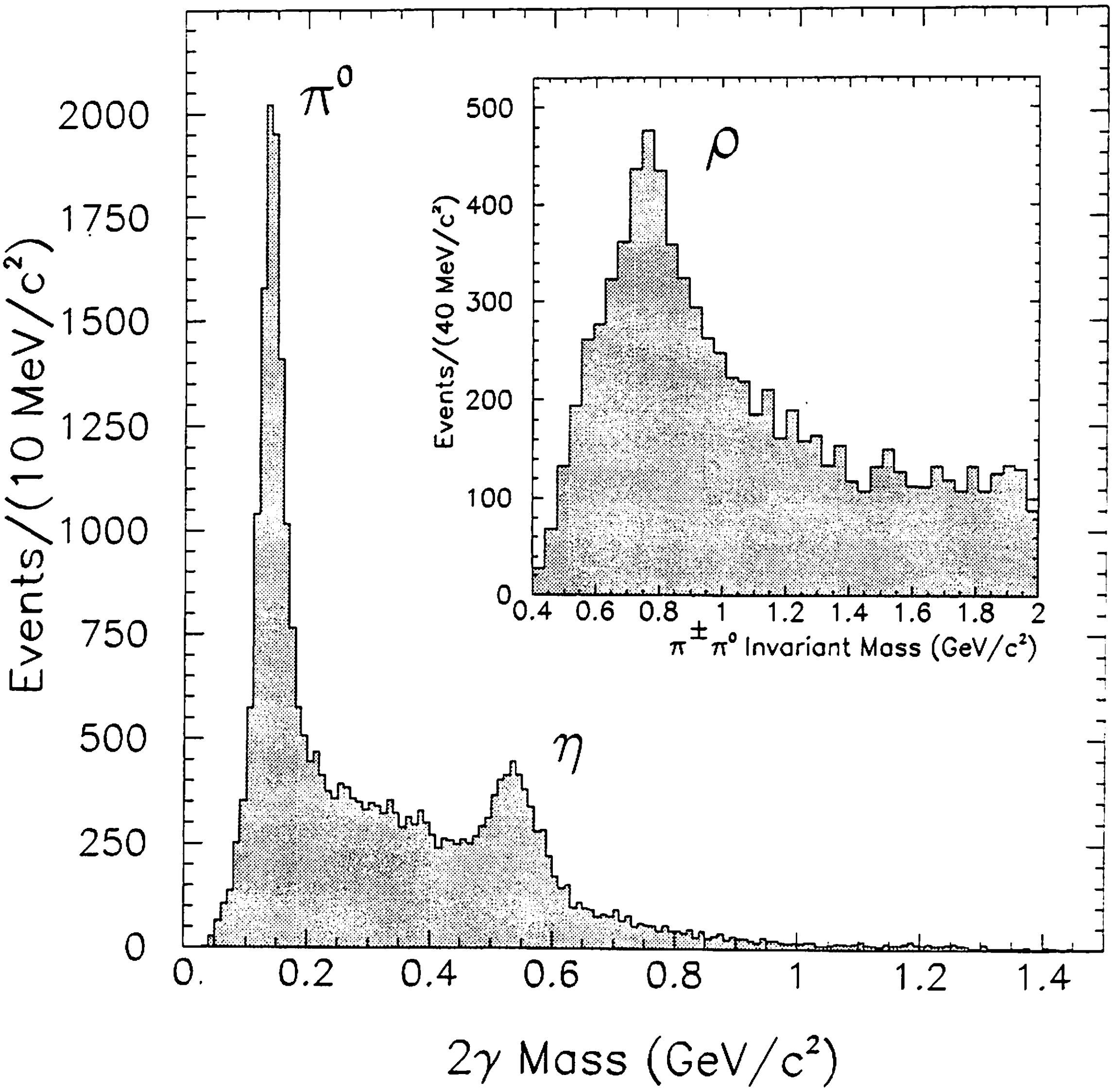

Figure 7.8: $\gamma\gamma$ and $\pi^0\pi^\pm$ mass distributions.

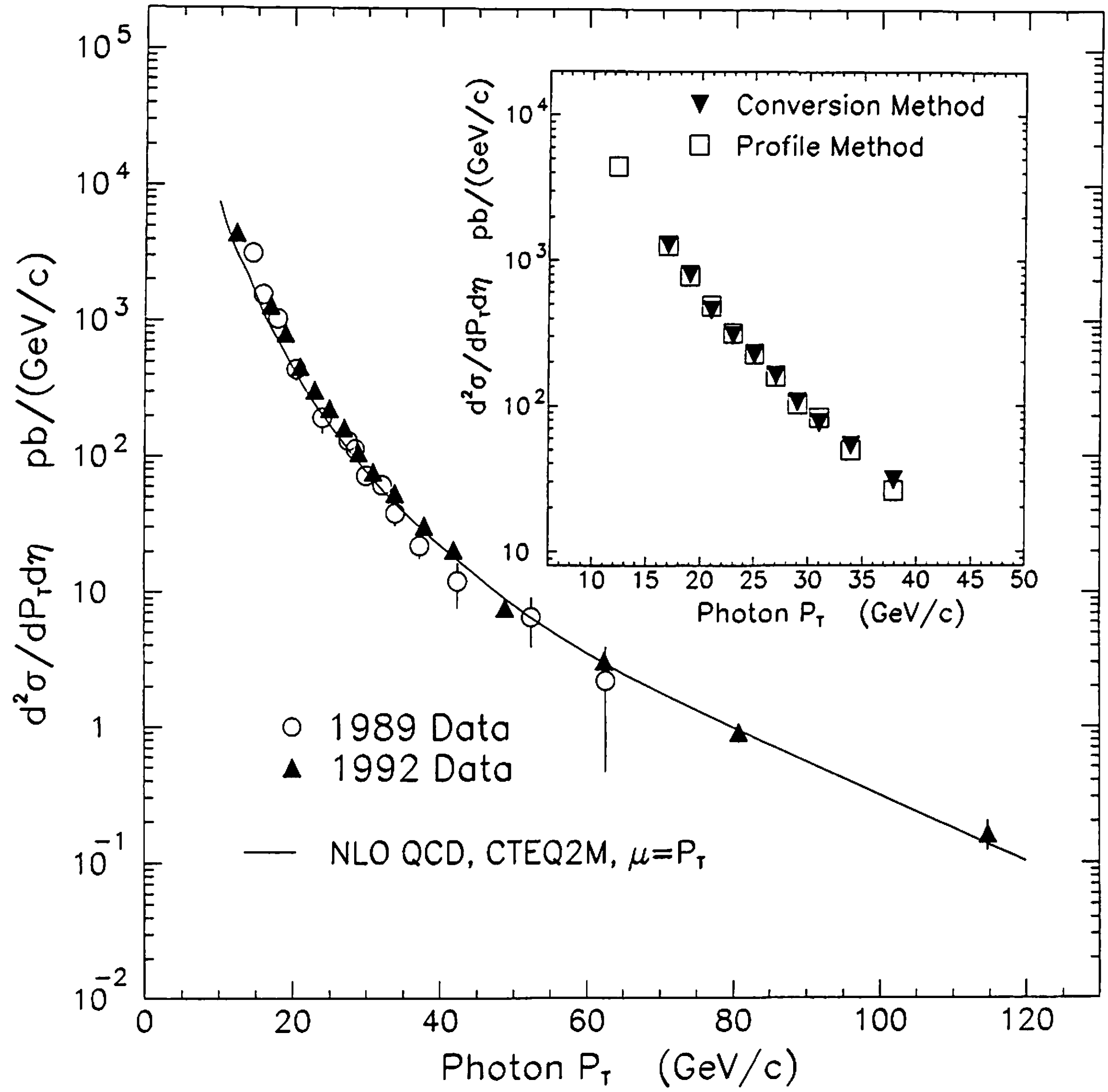

Figure 7.9: Inclusive photon cross section measured at the CDF.

- Subtraction of combinatorial backgrounds.

The uncertainties were estimated from PYTHIA Monte Carlo data and real data.

7.3.1 Choice of parton distribution function

We have used the CTEQ2M parton distribution function for the estimation of the track p_{T} cut and the mass reconstruction efficiency ($\epsilon_{\mathrm{Track\&Mass}}$). Figure 7.10 shows the $D^{*\pm}$ transverse momentum (p_{T}) distribution in the Monte Carlo $\gamma + D^{*\pm}$ events generated with PYTHIA, where the photons were selected with $16 < p_{\mathrm{T}}(\gamma) < 40$ GeV/c and $|y(\gamma)| < 0.9$, and the rapidity of $D^{*\pm}$'s was required to be less than 1.2. Using three parton distribution functions, the percent uncertainty due to the choice of the functions was estimated to be 4.7 % and 5.3 % in $\epsilon_{\mathrm{Track\&Mass}}$ for the reconstructions for $D^0 \to K^-\pi^+$ and $D^0 \to K^-\pi^-\pi^+\pi^+$, respectively. We used CTEQ2M, MRSD$_0$', and MRSD$_-$' in PDFLIB.

7.3.2 Charm quark fragmentation

The Peterson model was used as fragmentation function, which is given by

$$\mathrm{D_c}(z) = \frac{N}{z[1-(1/z)-\epsilon_c/(1-z)]^2},$$

where z is a scaling variable, $z = (E+p)_{\mathrm{hadron}}/(E+p)_{\mathrm{quark}}$, and ϵ_c is a parameter determined by other measurements. The parameter ϵ_c was set to

$$\epsilon_c = 0.078 \pm 0.008,$$

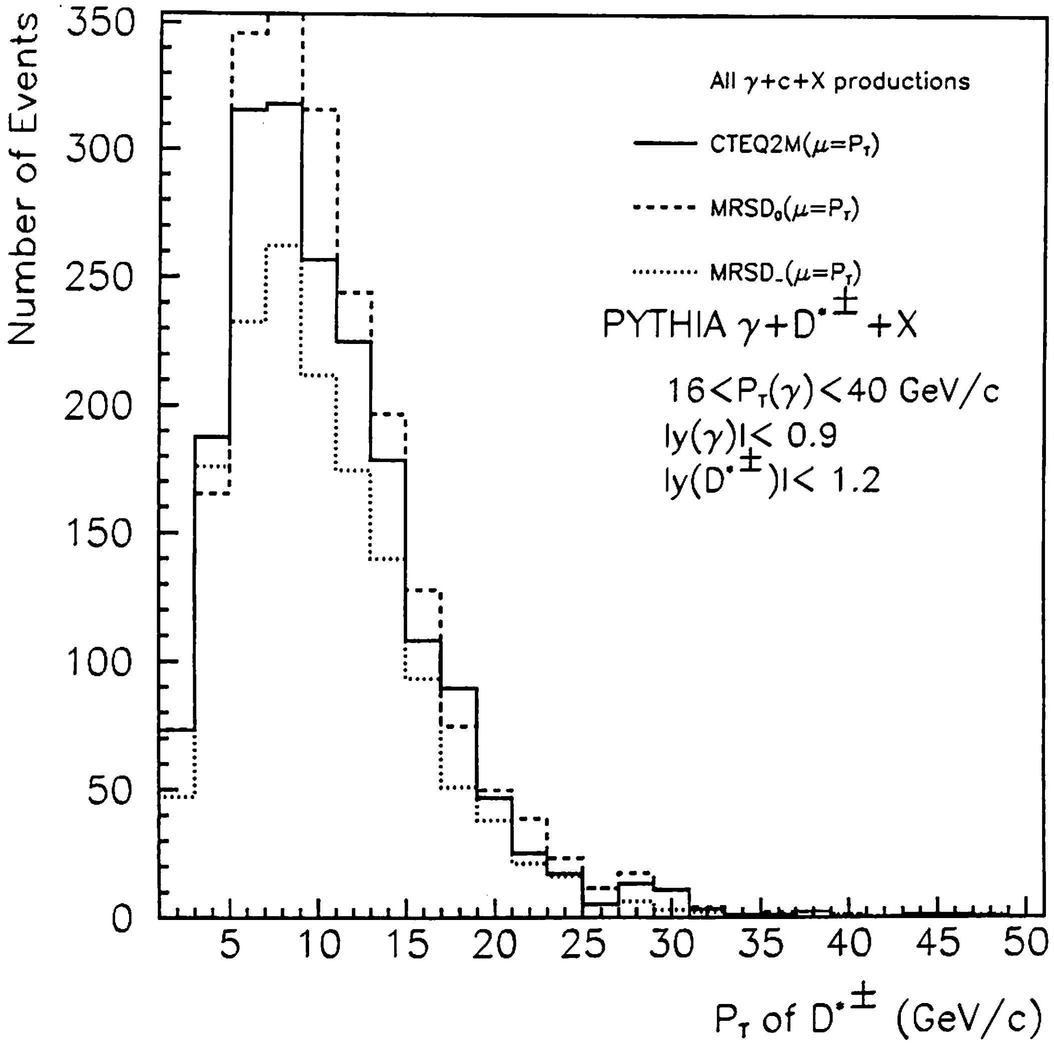

Figure 7.10: $D^{*\pm}$ p_T distribution using the CTEQ2M, MRSD$_0$', and MRSD$_-$'.

which was taken from Particle Data Book [18]. In Fig. 7.11 we show the fragmentation function for three cases of the parameter ϵ_c. Figure 7.12 shows the $D^{*\pm}$ p_T distributions using the two sets of the ϵ_c values in the fragmentation function. By varying the value of ϵ_c within one standard deviation, the changes in the $\epsilon_{\mathrm{Track\&Mass}}$ using $D^0 \to K^-\pi^+$ and $D^0 \to K^-\pi^-\pi^+\pi^+$ are 2.7 % and 5.1 %, respectively.

7.3.3 Branching ratios

The branching ratios of the D^{*+} and D^0 decays were taken from Particle Data Book [18], which are measurements from other experiments. The measurement errors were assigned to the systematic uncertainty in the branching ratios. The systematic uncertainties are 3.6 % and 6.5 % in the branching ratios of $D^{*+} \to D^0(\to K^-\pi^+)\pi^+$ and $D^{*+} \to D^0(\to K^-\pi^-\pi^+\pi^+)\pi^+$ decays, respectively.

7.3.4 Choice of renormalization scale

The photon transverse momentum p_T was taken as the renormalization scale μ and the factorization scale M in the efficiency calculation, namely;

$$\mu = M = p_T.$$

The systematic uncertainty due to the choice was estimated to be 4.8 % and 2.0 % for the reconstructions through $D^0 \to K^-\pi^+$ and $D^0 \to K^-\pi^-\pi^+\pi^+$ decays, respectively, by varying both scales simultaneously from $p_T/2$ to $2 \times p_T$. Figure 7.13 shows a $D^{*\pm}$ transverse momentum distribution in the Monte Carlo $\gamma + D^{*\pm}$ events with the choices of $\mu = p_T/2$ and $2 \times p_T$.

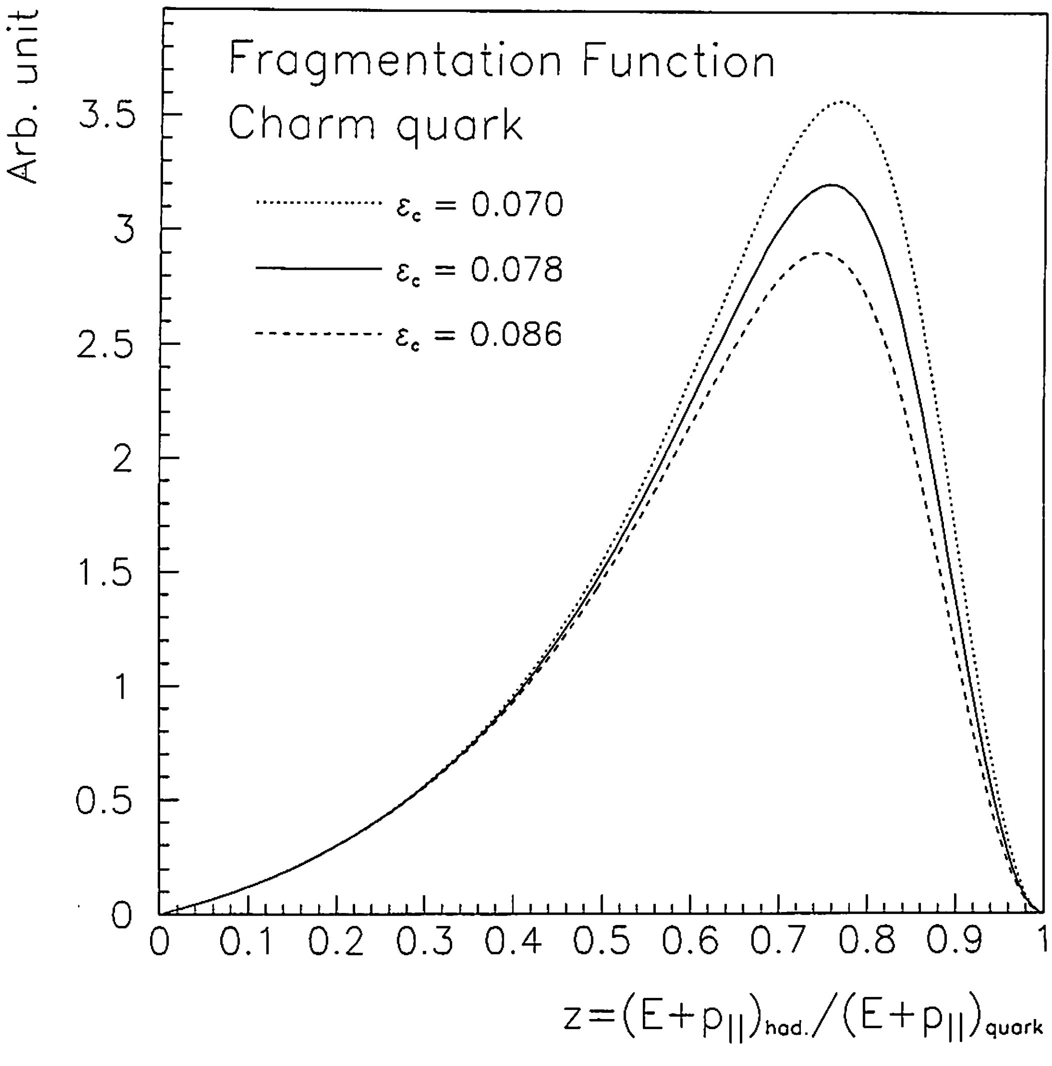

Figure 7.11: Peterson fragmentation function for $\epsilon_c = 0.078 \pm 0.008$.

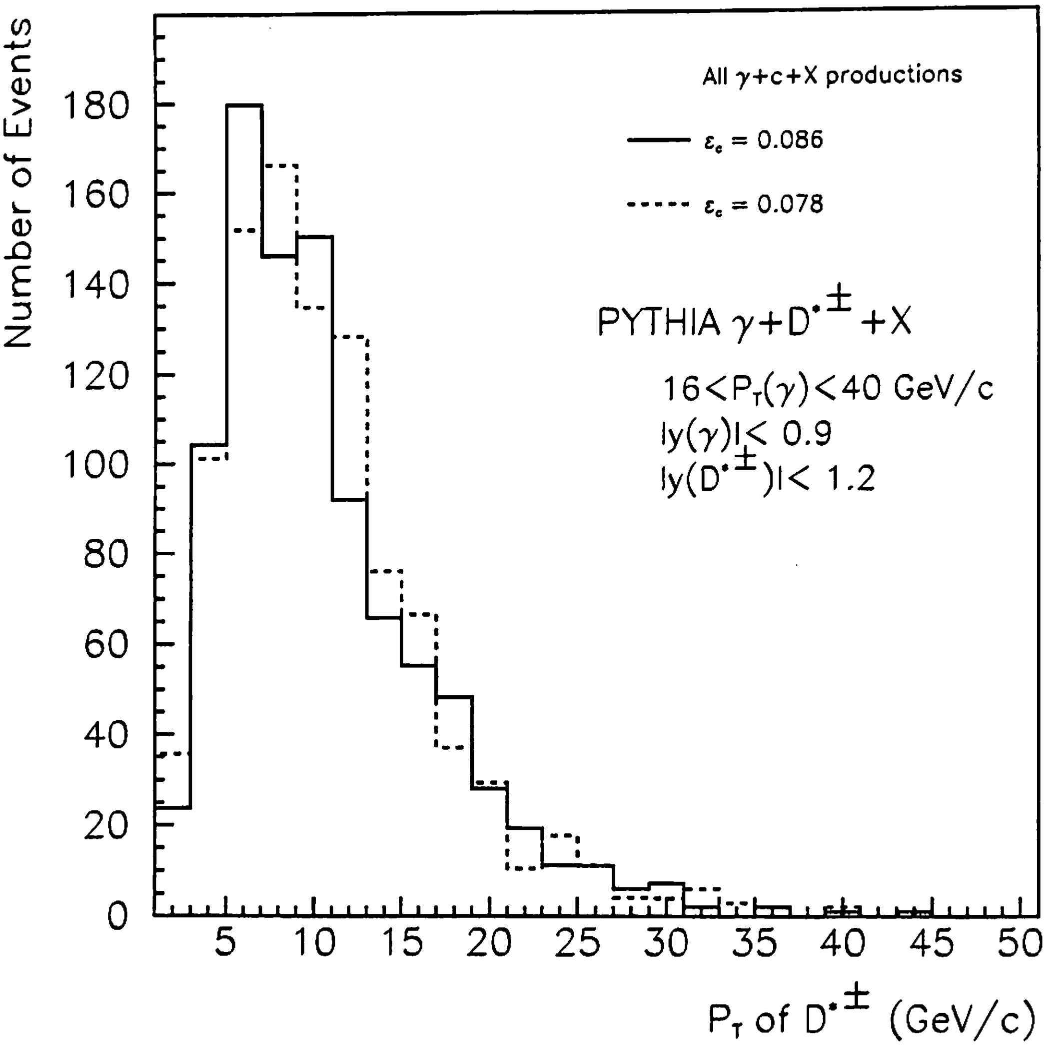

Figure 7.12: $D^{*\pm}$ p_T distributions of the Monte Carlo γ+$D^{*\pm}$ events for the two cases of ϵ_c parameters, corresponding to $\epsilon_c \pm 1\sigma$.

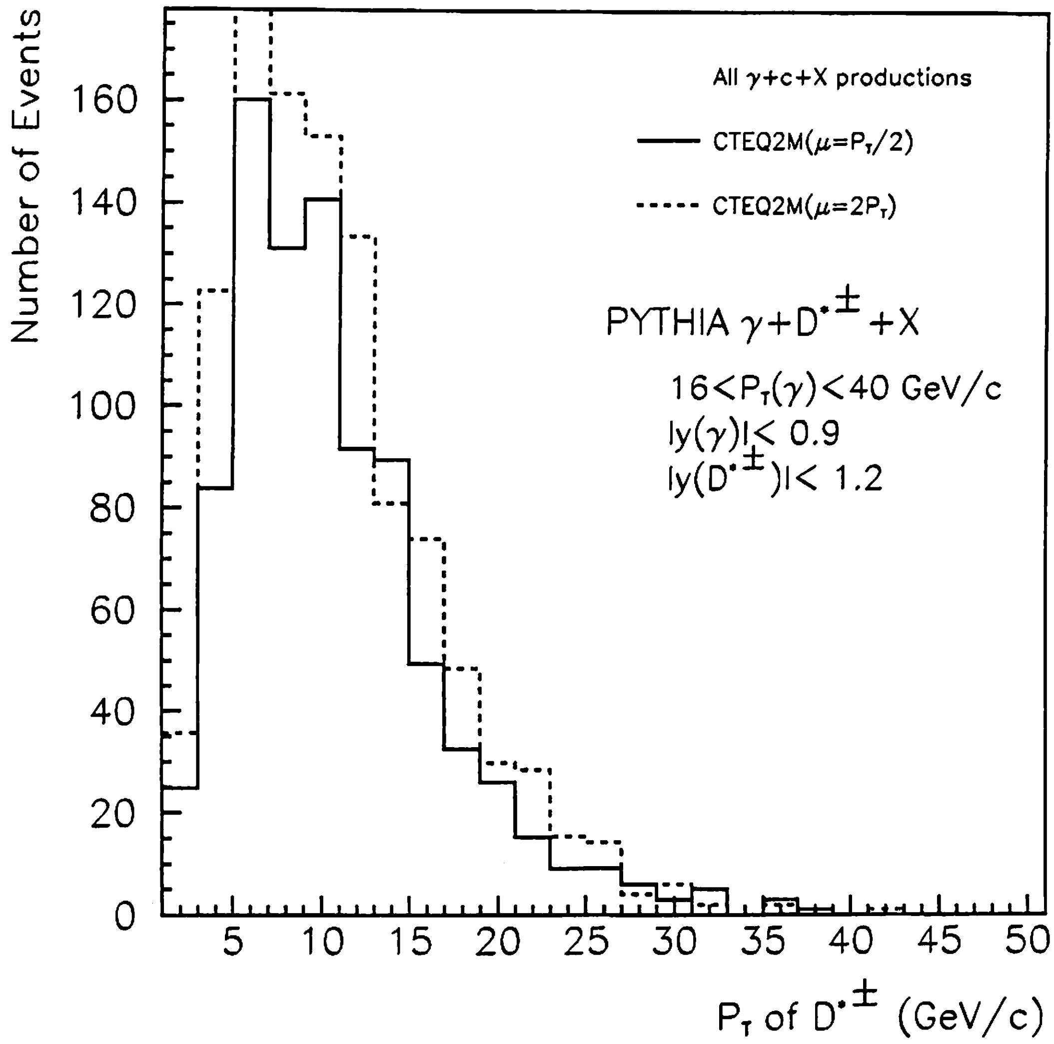

Figure 7.13: p_T distributions of $D^{*\pm}$'s in the Monte Carlo $\gamma + D^{*\pm}$ events in the kinematical range of $16 < p_T(\gamma) < 40$ GeV/c, $|y(\gamma)| < 0.9$, and $|y(D^{*\pm})| < 1.2$. The renormalization scale μ was taken to be $p_T/2$ or $2p_T$.

7.3.5 Track simulation and reconstruction efficiency

The systematic uncertainty in the track reconstruction was estimated to be 10 % by a comparison of the efficiency using the CDFSIM events with that using the CDFSIM events imbedded into the inclusive photon events. The difference between the two efficiencies was assigned to the systematic uncertainty in the track reconstruction efficiency.

7.4 Subtraction of combinatorial backgrounds

The systematic error of the combinatorial background subtraction comes from the uncertainty in the determination of the ΔM shape. The uncertainty was obtained from the various parameterization functions.

7.4.1 $D^0 \to K^-\pi^+$

Figure 7.14 shows the background ΔM distribution using fake $D^{*\pm}$'s together with the upper and the lower systematic bounds obtained from the different parameterized functions. The upper and the lower curves correspond to the functions which give the least and the most numbers of the $\gamma+$ $D^{*\pm}$ candidates, respectively. We take into account of the change in the fitted parameter by $\pm 1\sigma$. The range of the upper and the lower curves in the number of the events was assigned to the systematic uncertainty in the determination of the background shape. The systematic uncertainty is $^{+10}_{-11}$ %.

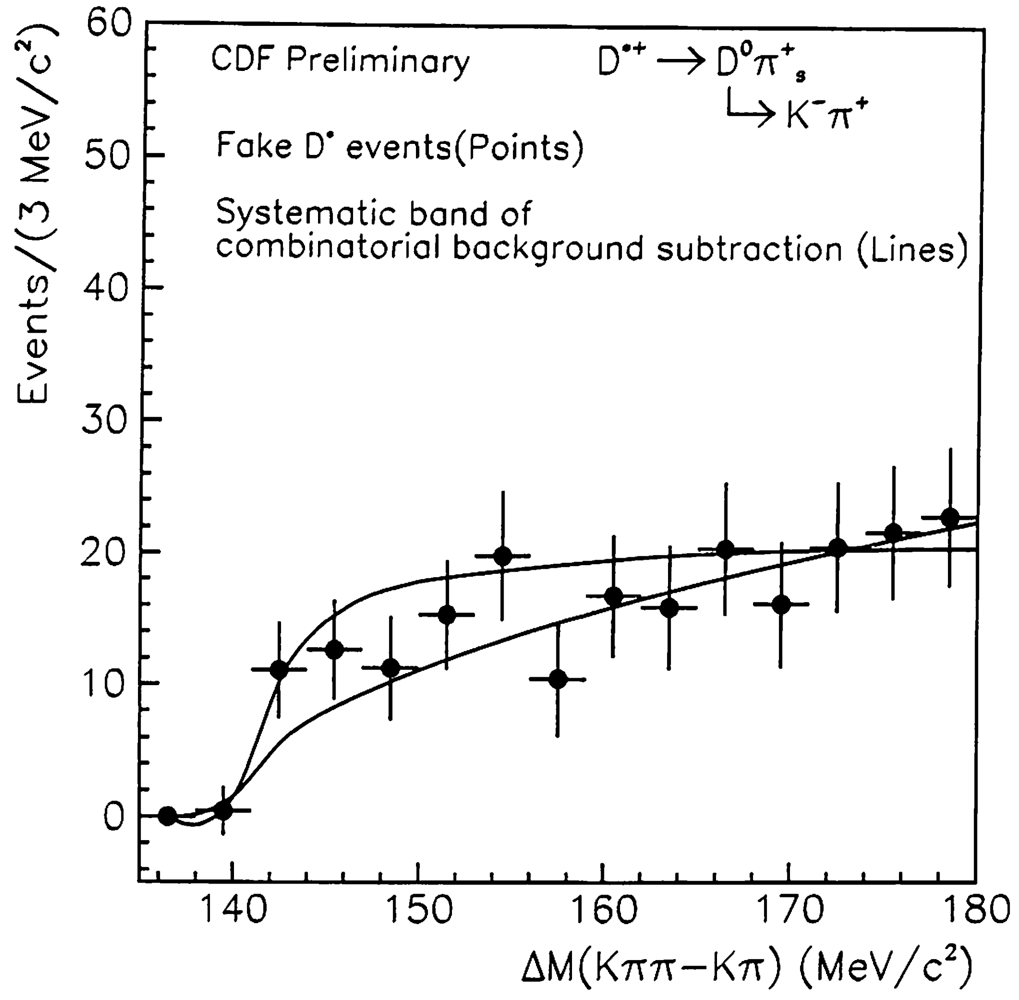

Figure 7.14: ΔM distribution together with the combinatorial background curves obtained from the parameterized functions. The upper and the lower curves correspond to the functions which give the least and the most numbers of the $\gamma + D^{*\pm}$ candidates.

7.4.2 $D^0 \to K^-\pi^-\pi^+\pi^+$

For the $D^{*\pm}$ reconstruction using $D^0 \to K^-\pi^-\pi^+\pi^+$, the systematic uncertainty in the combinatorial background subtraction was evaluated by the same method as that of $D^0 \to K^-\pi^+$. Figure 7.15 shows the fake $D^{*\pm}$ ΔM distribution. In the plot, the upper and the lower curves were obtained from the different parameterized functions, which give the least and the most numbers of the $\gamma + D^{*\pm}$ candidate events. From the range of the upper and the lower curves, we evaluated the systematic uncertainty to be $^{+16}_{-15}$ %.

7.4.3 $D^0 \to K^-\pi^+$ and $D^0 \to K^-\pi^-\pi^+\pi^+$

Combining the two D^0 decay modes, we show the fake $D^{*\pm}$ ΔM distribution together with the upper and the lower curves in Figure 7.16. From the range of the upper and the lower curves, we estimated the systematic uncertainty to be $^{+7}_{-10}$ %.

7.5 Summary of systematic uncertainty

The systematic uncertainties are summarized in Table 7.1. The total systematic uncertainties are $^{+19}_{-20}$ %, $^{+24}_{-21}$ %, and $^{+14}_{-16}$ % in the cross sections obtained from $D^0 \to K^-\pi^+$, $D^0 \to K^-\pi^-\pi^+\pi^+$, and combining the two D^0 decay modes.

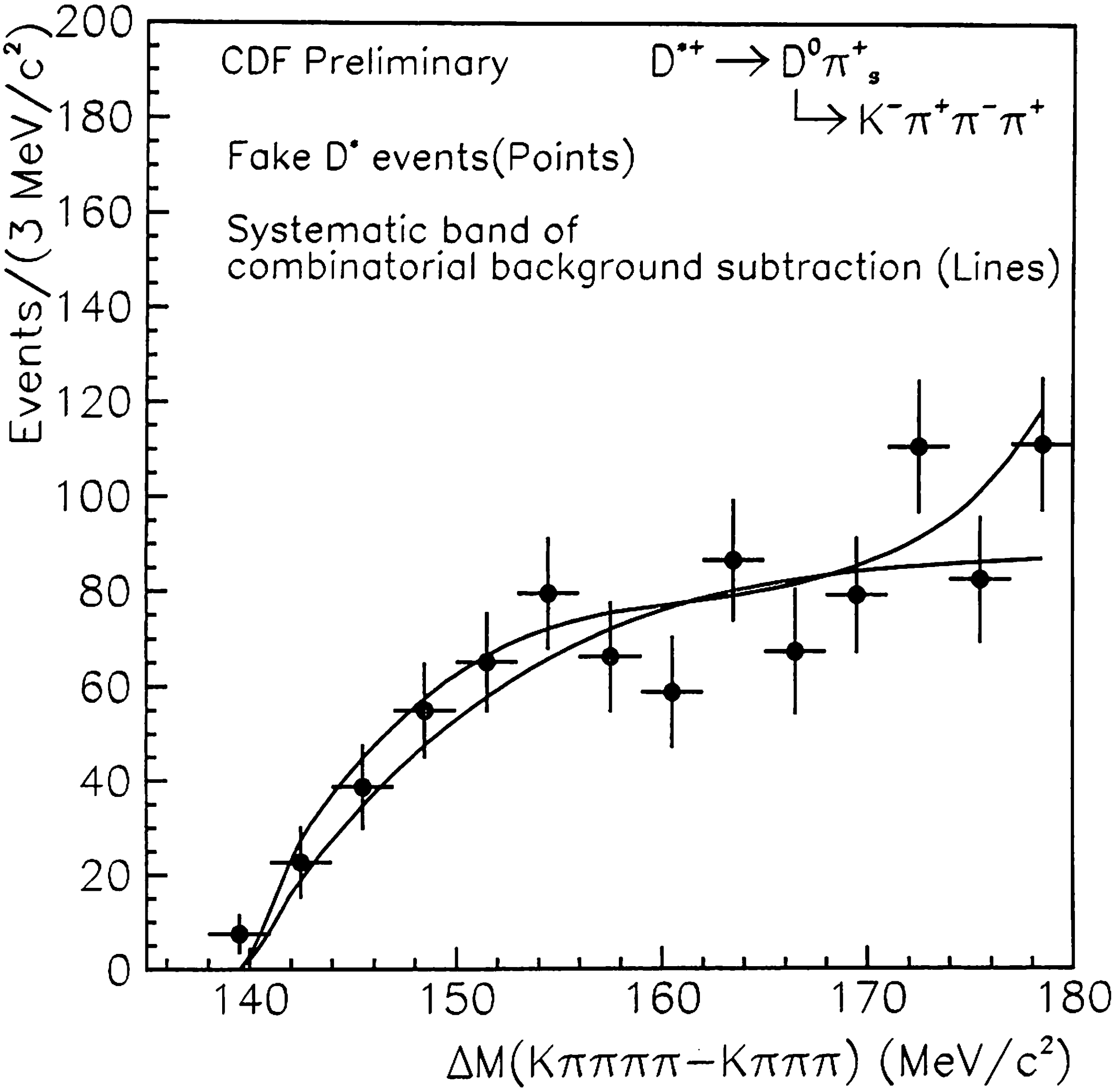

Figure 7.15: ΔM distribution together with the combinatorial background curves obtained from the parameterized functions. The upper and the lower curves correspond to the functions which give the least and the most numbers of the $\gamma + D^{*\pm}$ candidates.

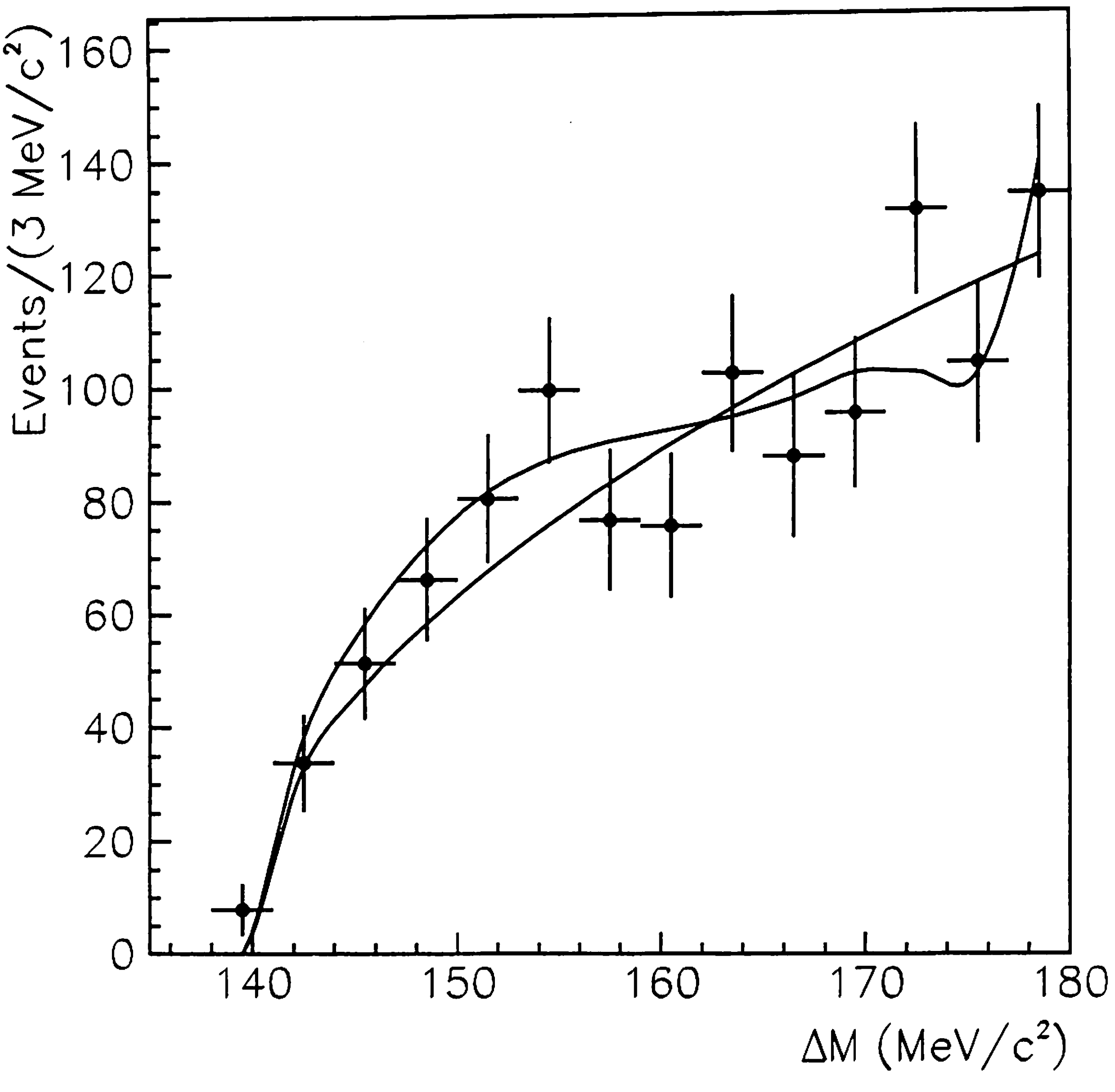

Figure 7.16: ΔM distribution together with the combinatorial background curves obtained from the parameterized functions. The upper and the lower curves correspond to the functions which give the least and the most numbers of the $\gamma + D^{*\pm}$ candidates.

Table 7.1: Summary of the Systematic Uncertainties

	Systematic uncertainties	
Luminosity	3.3 %	
Photon selection efficiency	3 %	
Photon trigger	5 %	
Photon background subtraction	9 %	
	$D^0 \rightarrow K^-\pi^+$	$D^0 \rightarrow K^-\pi^-\pi^+\pi^+$
$D^{*\pm}$ reconstruction	12.3 %	12.5 %
Combinatorial background subtraction	$^{+10\%}_{-11\%}$	$^{+16\%}_{-15\%}$
Branching ratio	3.6 %	6.5 %
Total systematic uncertainty	$^{+19\%}_{-20\%}$	$^{+24\%}_{-21\%}$

Chapter 8

Non-Prompt Charm Quark Productions

We studied the non-prompt charm quark productions, which are the gluon splitting and the bottom quark decay processes. We considered the contributions of the gluon splitting and the bottom quark decay processes in the $\gamma + D^{*\pm}$ production. The number of the non-prompt charm quark events was estimated from a Monte Carlo data sample and a real jet sample. The event fractions from the non-prompt charm quark processes are estimated in following sections.

8.1 Estimation from Monte Carlo events

For the estimation, we used the PYTHIA and the CLEO QQ programs [26]. The CLEO QQ program carries out B meson decays. The program is adjusted from the e^+e^- collision data recorded on the CLEO detector at

$\sqrt{s}$=10 GeV. The Peterson model formulated by

$$\mathrm{D_Q}(z) = \frac{N}{z[1-(1/z)-\epsilon_{\mathrm{Q}}/(1-z)]^2},$$

was used as the fragmentation function for heavy quarks (c and b), where ϵ_{Q} is the parameter determined by other experiments, and z is the scale variable. The parameter ϵ_{Q} values in the $\mathrm{D_Q}(z)$ used in this study are listed as follows:

$$\begin{aligned}\epsilon_b &= 0.006 \pm 0.002. \\ \epsilon_c &= 0.078 \pm 0.008.\end{aligned}$$

They were taken from the Particle Data Book [18].

The $\gamma + D^{*\pm}$ Monte Carlo events from the gluon splitting and the b decay processes were generated through the following processes:

- $q + \bar{q}' \rightarrow g + \gamma$,
- $g + q \rightarrow q + \gamma$,

where q represents u, d, s, c, or b quarks, and these processes include initial and final gluon radiations. The events were generated in a kinematical range of 5 GeV/c < $p_{\mathrm{T}}(\gamma)$ < 45 GeV/c and $|y(\gamma)| < 2.0$ for photons, and were selected with the cuts of 16 GeV/c < $p_{\mathrm{T}}(\gamma)$ < 40 GeV/c and $|y(\gamma)| < 0.9$. The predicted differential cross section for the inclusive photon production is shown in Fig. 8.1, together with the CDF measurements [27]. The Monte Carlo cross section was normalized by the CDF measurement value at p_{T} = 27.5 GeV/c. The slope of the predicted cross section reproduces the CDF measurements. The events containing a $D^{*\pm}$ meson were selected from this Monte Carlo events. The event fractions for each process are summarized in Table 8.1. After the

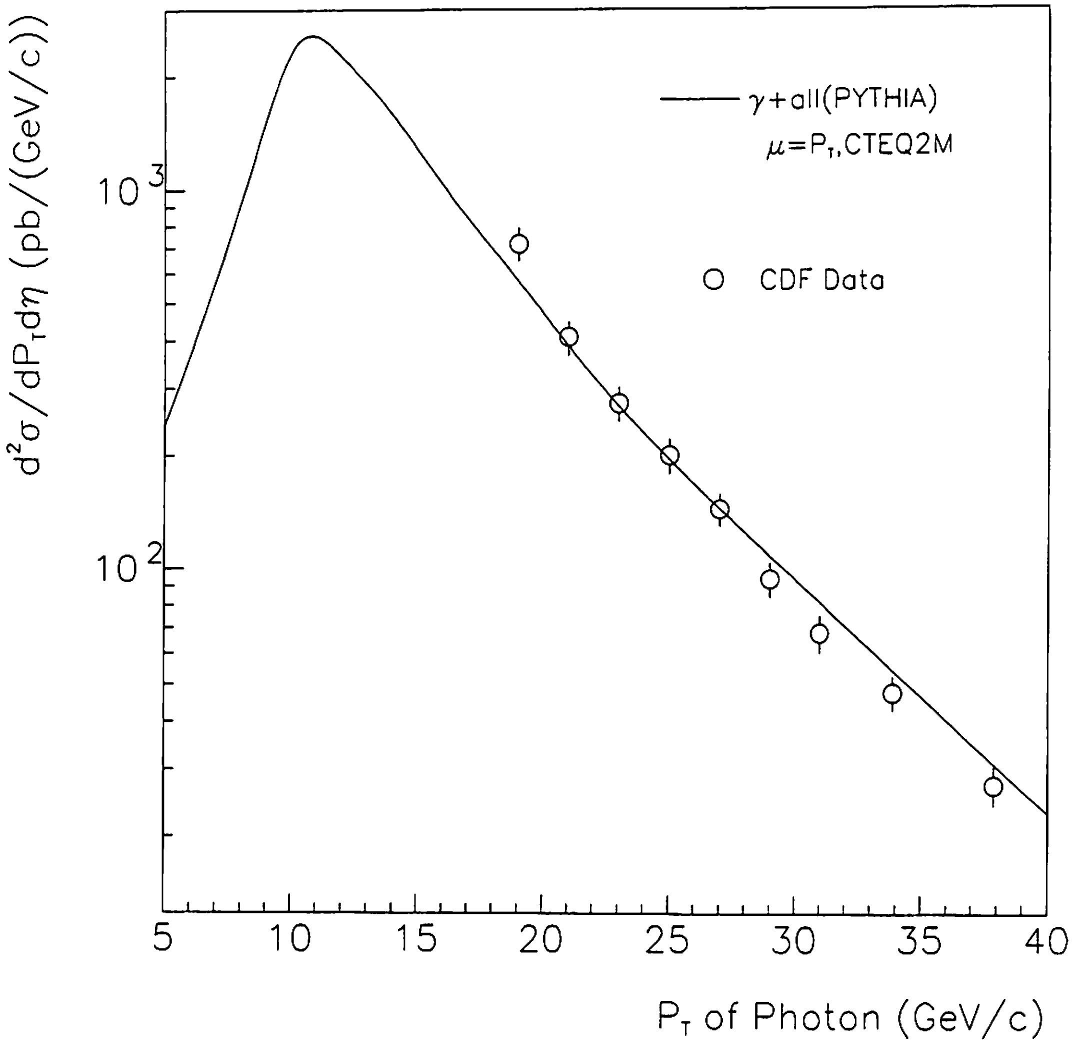

Figure 8.1: The differential cross section for the incisive photon production as a function of photon p_T. The solid line shows the prediction by PYTHIA, and the open circles show the measurements at the CDF.

Table 8.1: Fractions of inclusive photon processes

Processes	γ+X	$\gamma+D^{*\pm}$	$\gamma+D^{*\pm}$
	$16<p_T(\gamma)<40$	$p_T(D^{*\pm})>6$	$D^{*\pm}$ cuts
	$\|y(\gamma)\| <1.2$	$\|y(D^{*\pm})\| < 1.2$	
γ+g	12.9 %	2.7 %	2.4 %
$\gamma+u$	54.6 %	4.0 %	3.8 %
$\gamma+d$	11.4 %	0.9 %	0.9 %
$\gamma+s$	6.2 %	0.5 %	0.3 %
$\gamma+c$	13.2 %	87.9 %	89.3 %
$\gamma+b$	1.7 %	4 %	3.3 %

$D^{*\pm}$ selection cuts, the non-prompt charm quark contributions in the observed $\gamma + D^{*\pm}$ events were estimated to be 7 % and 3 % from the gluon splitting and the b decay processes, respectively.

8.2 Estimation from real data

A real dijet sample was used for another estimation of the non-prompt charm quark events. The dijet data were taken by an inclusive jet trigger. The jet trigger required the transverse energy of a jet to be larger than 20 GeV at the Level_2. The $D^{*\pm}$ production in the dijet events can be considered to come from a gluon splitting. The gluons are produced directly at a hard collision or from a quark by bremsstrahlung. The 75 percent of the jets in the dijet events is expected to be a gluon from a PYTHIA calculation with the CTEQ2M parton distribution function.

The gluon splitting processes can be separated into following two. One is "direct" production, and the other is "bremsstrahlung" production. These are illustrated in Fig. 8.2.

The number of $D^{*\pm}$ events from gluon splitting in the prompt photon events was estimated from the dijet events. The issues on the estimation are listed as follows:

- Average jet E_{T} difference.

$$\text{Average } E_{\mathrm{T}} = \begin{cases} 18 \text{ GeV} & \text{for} \quad \gamma + \text{jet} \quad \text{events.} \\ 30 \text{ GeV} & \text{for} \quad \text{dijet} \quad \text{events.} \end{cases}$$

- Gluon fraction difference.

$$\text{Gluon fraction} = \begin{cases} 13\ \% & \text{in} \quad \gamma + \text{jet} \quad \text{events.} \\ 75\ \% & \text{in} \quad \text{dijet} \quad \text{events.} \end{cases}$$

The differences were corrected using the Monte Carlo data, which are discussed later.

8.2.1 $D^{*\pm}$ reconstruction in dijet events

The $D^{*\pm}$ reconstruction in the dijet events was performed with the same cuts as that of the inclusive photon analysis. Figure 8.3 shows the ΔM distribution in the dijet events after the $D^{*\pm}$ selection cuts. A peak of the $D^{*\pm}$ signal was observed at 145.5 MeV/c^2. The distribution was fitted to a function of

$$\frac{\mathrm{P1}}{\sqrt{2\pi}\mathrm{P3}} \times \exp\left(-\frac{1}{2}\left(\frac{\Delta M - \mathrm{P2}}{\mathrm{P3}}\right)^2\right) + \mathrm{P4} \times (\Delta M - m_\pi)^{\mathrm{P5}},$$

(a) Direct production.

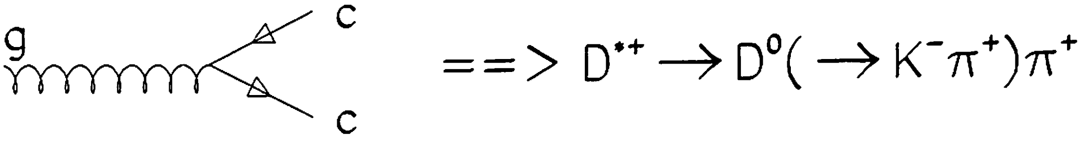

(b) bremsstrahlung production.

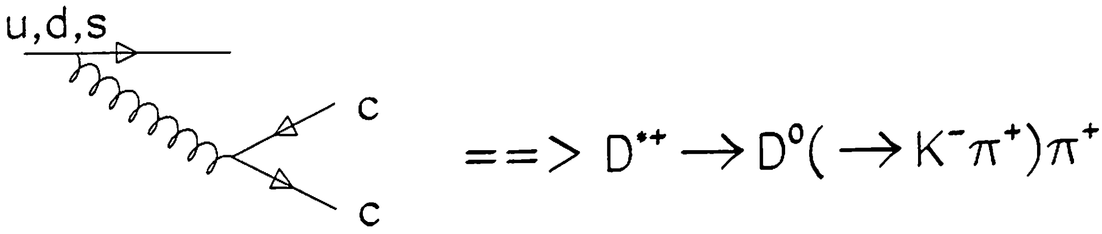

Figure 8.2: Schematic diagrams of gluon splitting.

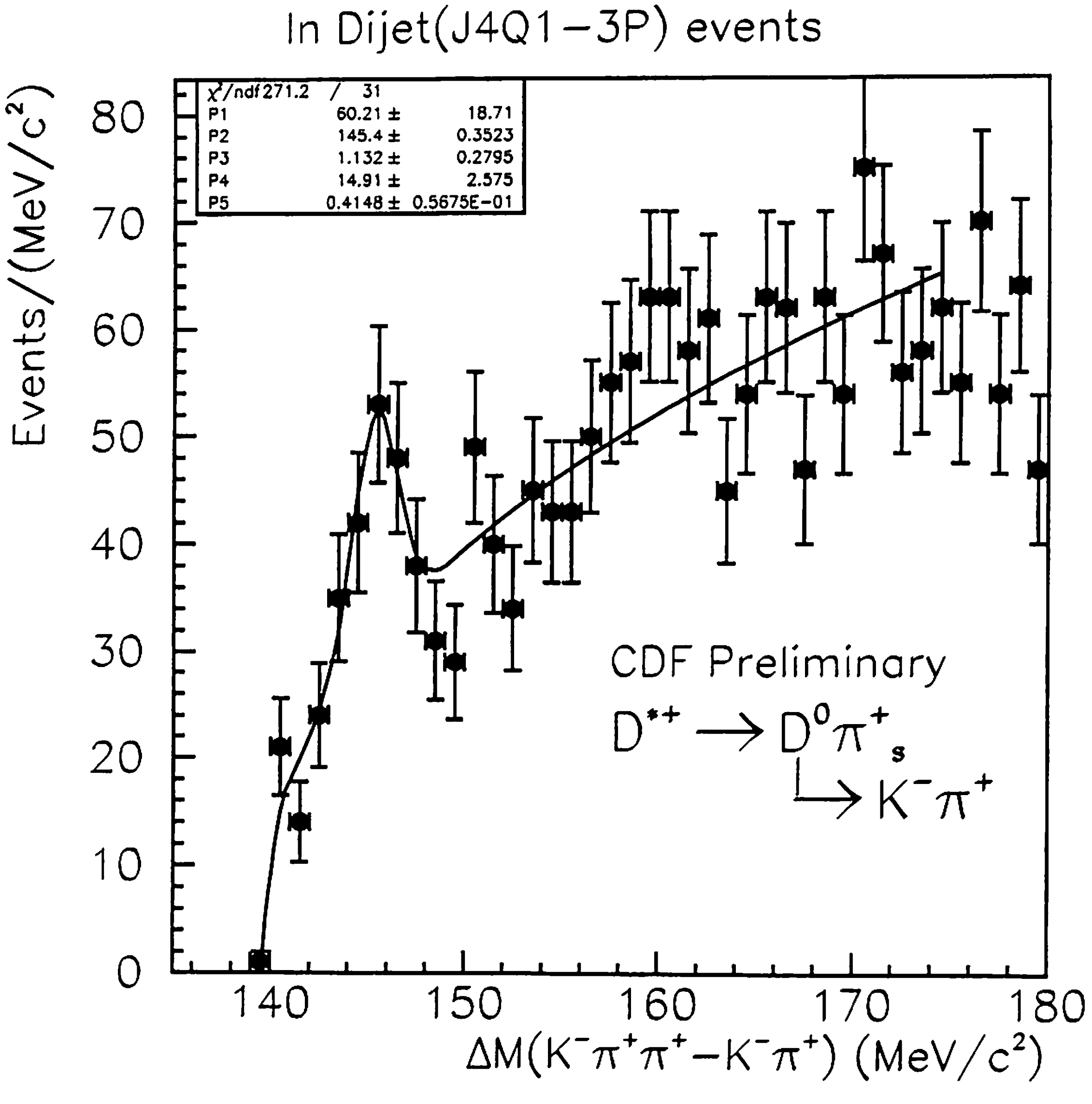

Figure 8.3: ΔM distribution in the dijet events.

where m_π is the pion mass, and P1, P2, P3, P4, and P5 are the fitting parameters. The fitted ΔM is 145.5 ± 0.2 MeV/c^2, where the error shows statistical one. From the fitting, the number of $D^{*\pm}$ events is obtained:

$$N_{D^{*\pm}} = 60.2 \pm 19,$$

where the error shows statistical one.

8.2.2 $D^{*\pm}$ fraction in a jet

From the observed $D^{*\pm}$ events, a $D^{*\pm}$ fraction in the dijet events was obtained. The $D^{*\pm}$ fraction ($F_{D^{*\pm}}$) is defined to be an average number of $D^{*\pm}$ mesons per jet. Figure 8.4 (a) shows a distribution of the number of jets in the dijet events. The jets were required to have the transverse energy larger than 20 GeV and the pseudorapidity smaller than 0.9. The average number of jets ($\langle N_{\rm jet}\rangle$) in an event is

$$\langle N_{\rm jet}\rangle = 1.29.$$

The $D^{*\pm}$ fraction was calculated by

$$\begin{aligned} F_{D^{*\pm}}(\langle E_{\rm T}\rangle = 30 \text{ GeV}) &= \frac{N_{D^{*\pm}}}{\langle N_{\rm jet}\rangle \times N_{\rm ev}} \\ &= \frac{60.2}{1.29 \times 111209} \\ &= (4.20 \pm 1.30) \times 10^{-4}, \end{aligned}$$

where $N_{\rm ev}$ is the number of the observed dijet events.

8.2.3 Average jet $E_{\rm T}$

The inclusive photon data were taken with the $E_{\rm T}$ threshold of 16 GeV, while the dijet data were taken with that of 20 GeV. Figure 8.4 (b) shows

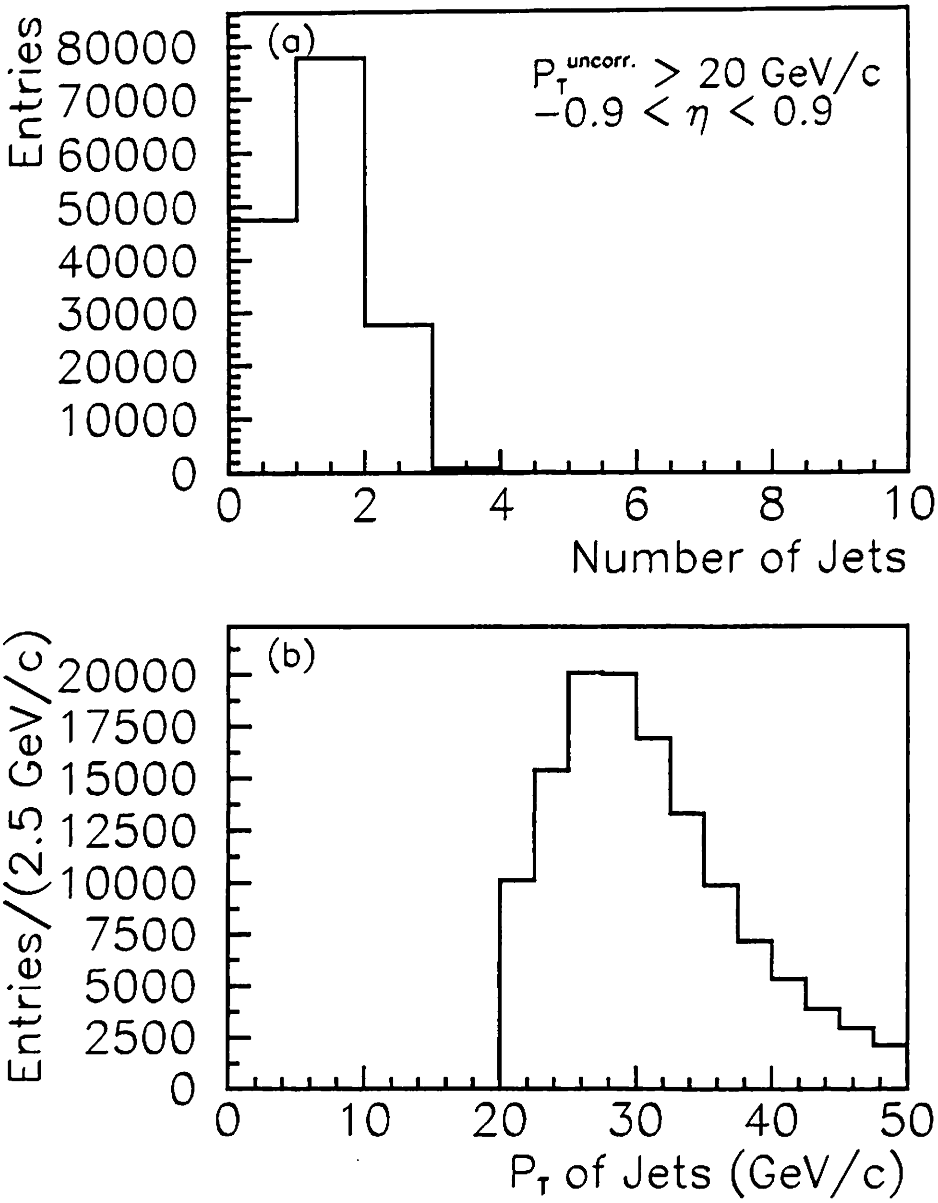

Figure 8.4: (a) The number of jets and (b) jet E_T distribution in the real dijet events.

the jet E_{T} distribution, where the jet E_{T} and $|\eta|$ were required to be greater than 20 GeV and to be less than 0.9, respectively. The average jet E_{T} is different in the photon and the dijet data. The difference affects the $D^{*\pm}$ reconstruction efficiency, because the $D^{*\pm}$ reconstruction efficiency is expected to be higher at higher E_{T} jet sample. The difference in the reconstruction efficiencies was estimated using the $D^{*\pm}$ Monte Carlo events of dijet production. Two sets of the dijet Monte Carlo events were generated with PYTHIA at the average jet E_{T}'s of 18 GeV and 30 GeV. The reconstruction efficiencies were obtained:

$$\begin{cases} \epsilon_{D^{*\pm}}(\langle E_{\mathrm{T}}\rangle = 30\ \mathrm{GeV}) = 46.7 \pm 0.7\% \ \text{at} \ \langle E_{\mathrm{T}}\rangle = 30\ \mathrm{GeV}. \\ \epsilon_{D^{*\pm}}(\langle E_{\mathrm{T}}\rangle = 18\ \mathrm{GeV}) = 35.7 \pm 0.7\% \ \text{at} \ \langle E_{\mathrm{T}}\rangle = 18\ \mathrm{GeV}. \end{cases}$$

The $D^{*\pm}$ fraction at $\langle E_{\mathrm{T}}\rangle = 18$ GeV was obtained as follows:

$$\begin{aligned} & F_{D^{*\pm}}(\langle E_{\mathrm{T}}\rangle = 18\ \mathrm{GeV}) \\ = \ & F_{D^{*\pm}}(\langle E_{\mathrm{T}}\rangle = 30\ \mathrm{GeV}) \times \frac{\epsilon_{D^{*\pm}}(\langle E_{\mathrm{T}}\rangle = 18\ \mathrm{GeV})}{\epsilon_{D^{*\pm}}(\langle E_{\mathrm{T}}\rangle = 30\ \mathrm{GeV})} \\ = \ & 4.20 \times 10^{-4} \times \frac{0.357}{0.467} \\ = \ & (3.21 \pm 1.00) \times 10^{-4}. \end{aligned}$$

8.2.4 Gluon fraction

The gluon fractions in the inclusive photon and the dijet events are different. The gluon fractions were estimated with PYTHIA:

$$\begin{cases} 13\ \% \ \text{in} \ \gamma + \text{jet events.} \\ 75\ \% \ \text{in} \ \text{dijet events.} \end{cases}$$

The difference affects the $D^{*\pm}$ fraction. From the PYTHIA Monte Carlo events, the efficiencies of the track p_{T} cuts for K, π, and π_{s} from the $D^{*\pm}$ decay were estimated to be:

$$\begin{cases} \epsilon_g(g \to c\bar{c} \to D^{*\pm} \to K\pi\pi_{\mathrm{s}}, p_{\mathrm{T}} \text{ cuts}) & = \ 0.69 \ \%. \\ \epsilon_q(q \to gq \to c\bar{c} + q \to D^{*\pm} \to K\pi\pi_{\mathrm{s}}, p_{\mathrm{T}} \text{ cuts}) & = \ 0.13 \ \%. \end{cases}$$

The efficiencies include a probability of $c\bar{c}$ production from a gluon or a light quark, but the branching ratios of $D^{*+} \to D^0\pi^+$ and $D^0 \to K^-\pi^+$ are not included. The quark and gluon fractions (f_g and f_q) in the inclusive photon events were estimated with the PYTHIA:

$$\begin{cases} f_g & = \ 0.13. \\ f_q & = \ 0.87. \end{cases}$$

Taking account of the gluon fraction difference, the $D^{*\pm}$ fraction in the inclusive photon events ($F_{D^{*\pm} \text{ in } \gamma+X}$) was calculated as follows:

$$\begin{aligned} & F_{D^{*\pm} \text{ in } \gamma+X} \\ = \ & \frac{0.75\epsilon_g}{0.75\epsilon_g + 0.25\epsilon_q} F_{D^{*\pm}} \times f_g + \frac{0.25\epsilon_q}{0.75\epsilon_g + 0.25\epsilon_q} F_{D^{*\pm}} \times f_q \\ = \ & (5.58 \pm 1.73) \times 10^{-5} \end{aligned}$$

8.2.5 $D^{*\pm}$ from gluon splitting in γ+$D^{*\pm}$ events

The number of the prompt photon events is

$$N_\gamma = 65879 \pm 494.$$

Using the $D^{*\pm}$ fraction ($F_{D^{*\pm} \text{ in } \gamma+X}$) and the number of the inclusive photon events (N_γ), the number of γ+$D^{*\pm}$ events from the gluon splitting

(G.S.) is estimated to be:

$$\begin{aligned} N(\gamma + D^{*\pm} \text{ from G.S.}) &= 2 \times F_{D^{*\pm} \text{ in } \gamma+X} \times N_\gamma \\ &= 2 \times 5.58 \times 10^{-5} \times 65879 \\ &= 7.4 \pm 2.3, \end{aligned}$$

in the observed 61.8 ± 19.1 $\gamma + D^{*\pm}$ events. We have estimated the number of gluon splitting events using the $D^0 \to K^-\pi^+$ decay mode. For $D^0 \to K^-\pi^-\pi^+\pi^+$, we can expect the same number of gluon splitting events, because of $\varepsilon_{D^0 \to K3\pi} \times Br(D^0 \to K3\pi) \simeq \varepsilon_{D^0 \to K\pi} \times Br(D^0 \to K\pi)$, where ε is the reconstruction efficiency and Br is the branching ratio of the D^0 decay. Therefore, we multiplied $F_{D^{*\pm} \text{ in } \gamma+X}$ as shown above.

On the other hand, the number estimated with PYTHIA in the previous section was

$$N(\gamma + D^{*\pm} \text{ from G.S.}) = 4.3 \pm 0.3.$$

They are consistent within the statistical errors.

Chapter 9

Predictions of the $\gamma + D^{*\pm}$ Production Cross Section

The measured $\gamma + D^{*\pm}$ production cross section is compared to theoretical predictions. The PYTHIA and the PDFLIB programs [25] are used for the calculations. The factorization scale M and the renormalization scale μ are assigned to outgoing parton transverse momentum, namely, $\mu = M = p_{\mathrm{T}}$. The dependences of the predicted cross section on the choices of the renormalization scale and the parton distribution functions are studied.

9.1 Parton distribution function

Parton distribution functions have been determined by other experiments of deep inelastic scattering. Figures 9.1 and 9.2 show the charm quark and the gluon distribution functions with μ dependence in the CTEQ2M [6] and the MRSD$_0$' [28] parton distribution functions, respectively. Comparisons of different parton distribution functions, CTEQ2M [6], MRSD$_0$' [28], and MRSD$_-$' for charm quark and gluon are shown in Figures 9.3 and 9.4, respectively.

9.2 Choice of parton distribution function

Various parton distribution functions were used in the calculations of the $\gamma + D^{*\pm}$ production cross section. The predicted cross sections are summarized in Table 9.1. The renormalization scale μ was taken as parton transverse momentum.

Table 9.1: Cross sections for $\gamma + D^{*\pm}$ production for various parton distribution functions

PDF Set Name	$\sigma(\gamma + D^{*\pm})$ (nb)
CTEQ2M	0.211 ± 0.003
MRSD$_0$'	0.224 ± 0.003
MRSD$_-$'	0.181 ± 0.003

9.3 Choice of the scales

The predicted cross sections were calculated for the scale definitions of $\mu = p_T/2$ and $\mu = 2 \times p_T$. The CTEQ2M was used in the calculations. The predicted cross sections are

$$\begin{aligned} \sigma(\gamma + D^{*\pm}) &= 0.196 \pm 0.003 \quad \text{(nb) with } \mu = P_T/2, \\ \sigma(\gamma + D^{*\pm}) &= 0.248 \pm 0.003 \quad \text{(nb) with } \mu = 2P_T. \end{aligned}$$

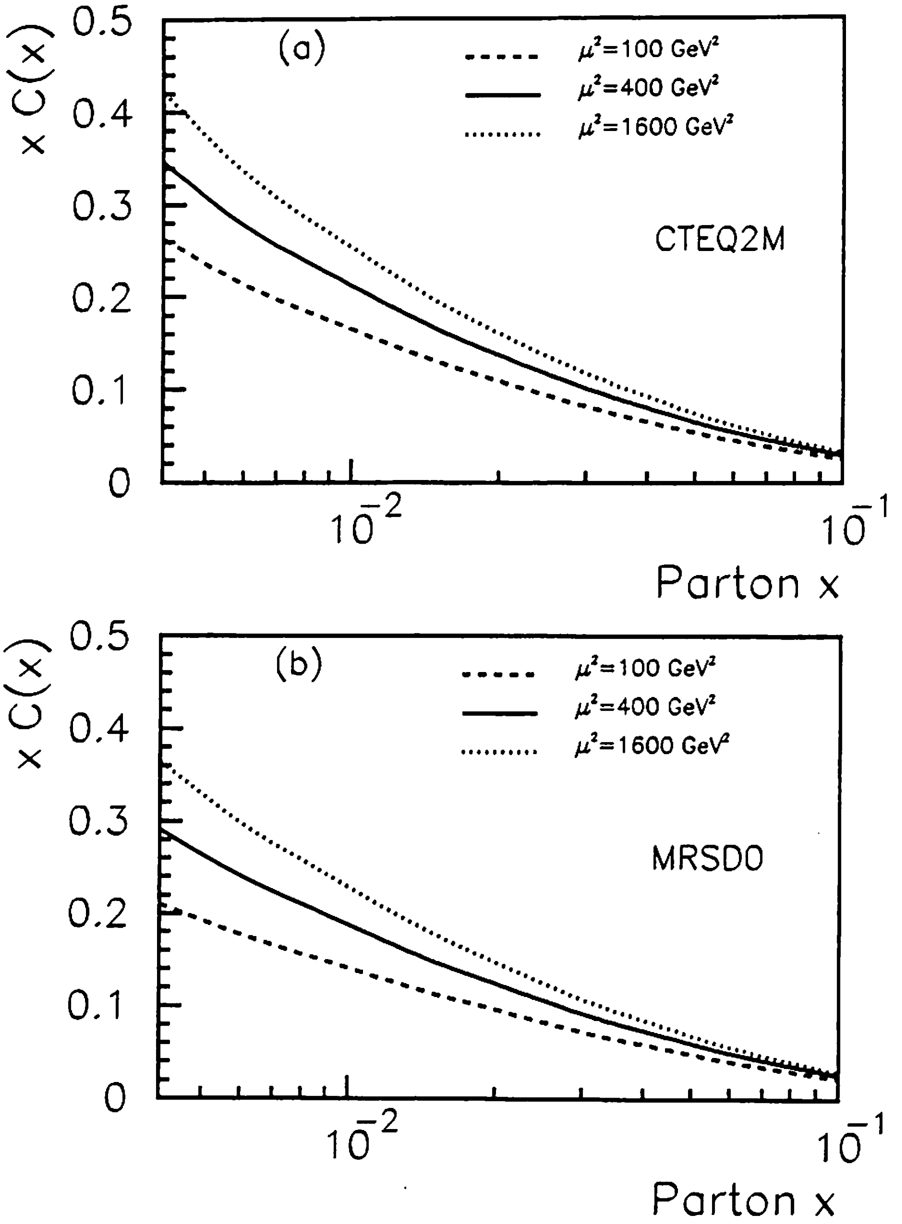

Figure 9.1: Dependence of the charm quark distribution functions on μ. The CTEQ2M and the MRSD$_0$' distribution functions were used.

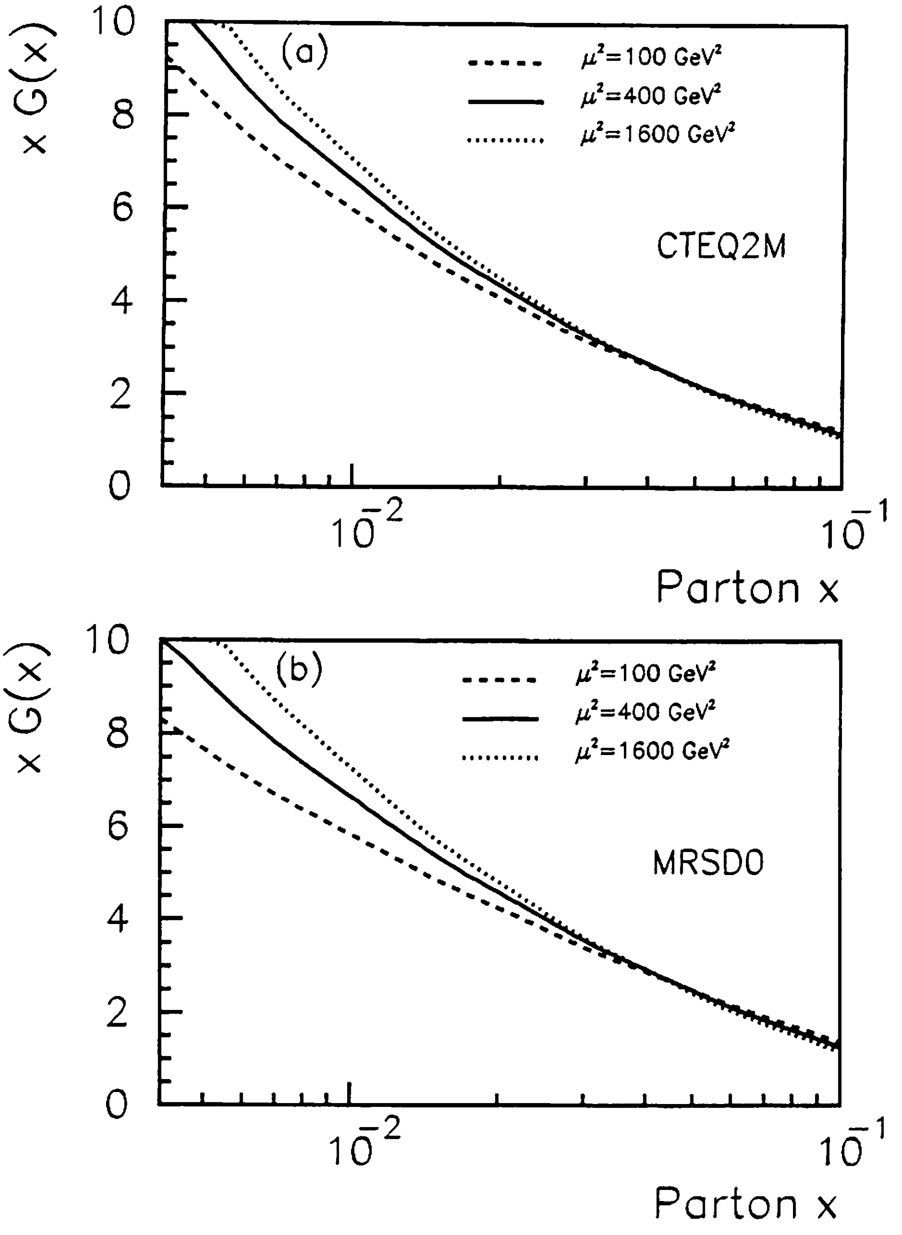

Figure 9.2: Dependence of the gluon distribution functions on μ. The CTEQ2M and the MRSD$_0$' distribution function were used.

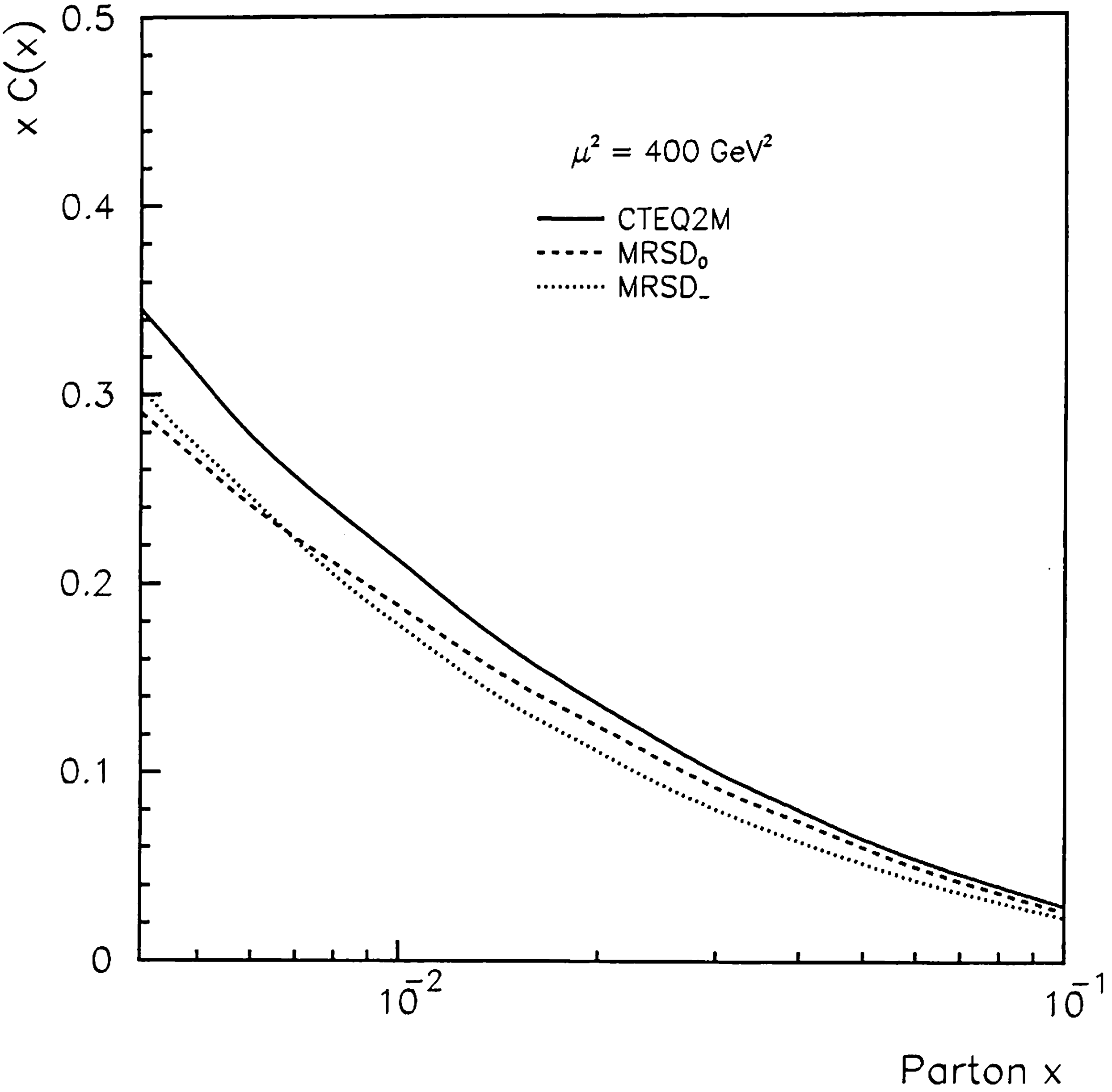

Figure 9.3: Charm quark distribution functions for the CTEQ2M, MRSD$_0$', and MRSD$_-$' with $\mu^2 = 400$ GeV^2.

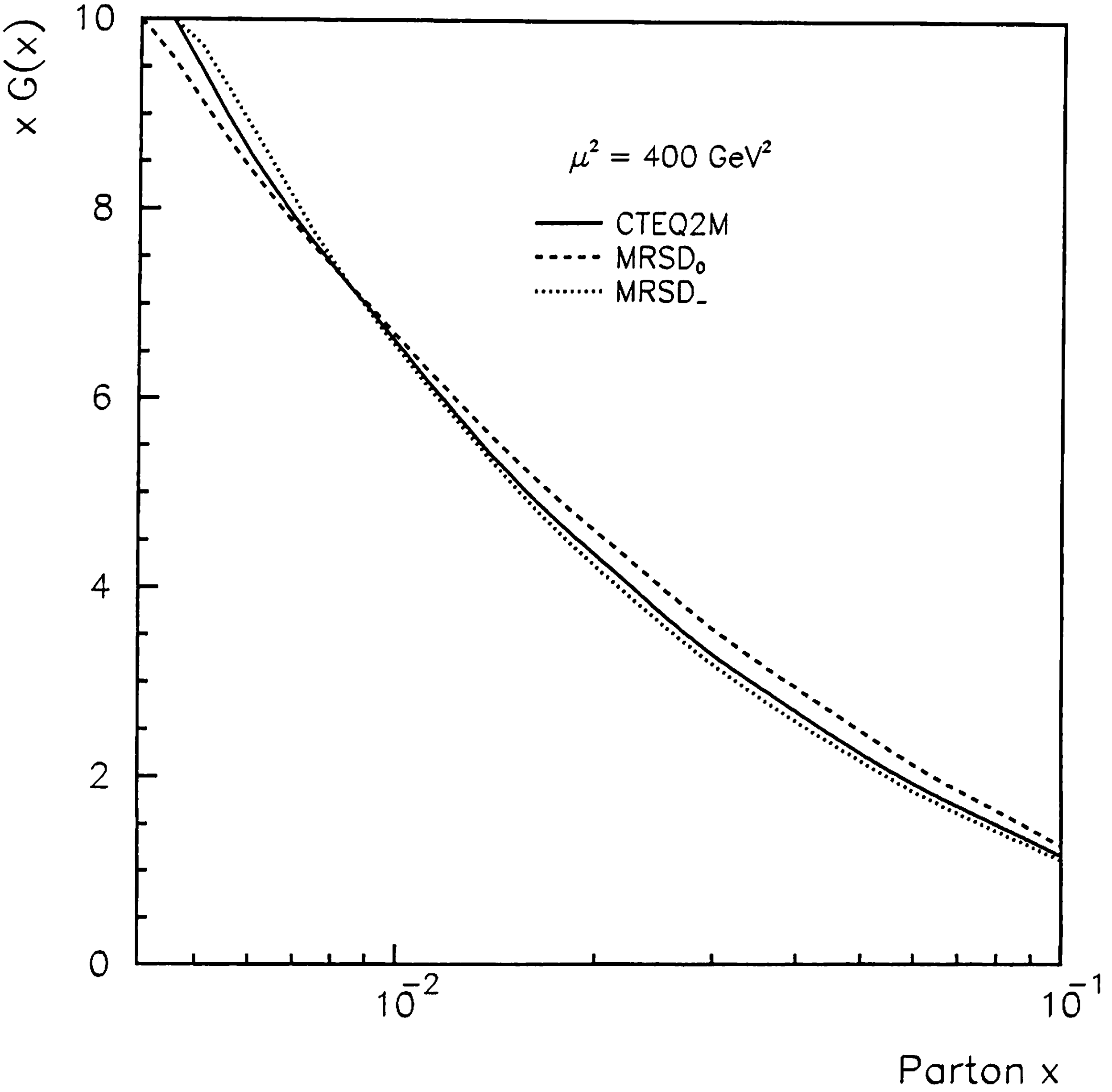

Figure 9.4: Gluon distribution functions for the CTEQ2M, MRSD$_0$', and MRSD$_-$' with μ^2 = 400 GeV^2.

Chapter 10

Results and Conclusion

The proton-antiproton collision data at $\sqrt{s} = 1.8$ TeV were collected with the CDF detector during 1992 and 1993. The inclusive photon events were taken with the E_{T} threshold of 16 GeV. The integrated luminosity of the data was 16.4 pb^{-1}. In the photon candidate events, $D^{*\pm}$ mesons were fully reconstructed through the sequential decays of $D^{*\pm} \rightarrow D^0(\rightarrow K^{\mp}\pi^{\pm})\pi^{\pm}$ and $D^{*\pm} \rightarrow D^0(\rightarrow K^{\mp}\pi^{\mp}\pi^{\pm}\pi^{\pm})\pi^{\pm}$. The significant peaks were observed at 145.5 MeV/c^2 in the mass difference distributions. The background events against prompt photons were statistically subtracted using the CES χ^2 method. The combinatorial background events against $D^{*\pm}$ mesons were subtracted by using the parameterization of the fake $D^{*\pm}$ ΔM distribution. After subtracting these background events, we found 29.9 ± 10 γ+$D^{*\pm}(\rightarrow K^{\mp}\pi^{\pm}\pi^{\pm})$ events and 31.9 ± 16 γ+$D^{*\pm}(\rightarrow K^{\mp}\pi^{\mp}\pi^{\pm}\pi^{\pm}\pi^{\pm})$ events. The $D^{*\pm}$ reconstruction efficiency and the detection efficiency of photons were estimated from the data, the electron test beam data, and the Monte Carlo data. The overall efficiencies for detecting $\gamma + D^{*\pm}$ events were estimated to be

0.150±0.024 and 0.067±0.011 for the reconstructions using $D^0 \rightarrow K^-\pi^+$ and $D^0 \rightarrow K^-\pi^-\pi^+\pi^+$, respectively. The systematic uncertainty in the cross section was evaluated to be $^{+14}_{-16}$ % from the Monte Carlo events and the real events. We determined the cross section for $\gamma + D^{*\pm}$ production in the kinematical range of 16 GeV/c $< p_{\mathrm{T}}(\gamma) <$ 40 GeV/c, $|y(\gamma)| < 0.9$, $p_{\mathrm{T}}(D^{*\pm}) >$ 6 GeV/c, and $|y(D^{*\pm})| < 1.2$. The measured cross section is $0.48 \pm 0.15(\mathrm{stat.})\ ^{+0.07}_{-0.08}\ (\mathrm{syst.})$ nb, where the first and the second errors show statistical and systematic ones, respectively. The contributions of the gluon splitting and the b decay processes in $\gamma + D^{*\pm}$ events were studied using the PYTHIA Monte Carlo data and the real dijet data. From the real dijet events, the estimated number of the events from the gluon splitting processes was 7.4 ± 2.3 events in the observed 61.8 ± 19 $\gamma + D^{*\pm}$ events. The measured cross section was compared to the lowest-order calculations. The predicted cross section was 0.211 nb using the CTEQ2M parton distribution function, where the renormalization scale was taken as photon transverse momentum ($\mu = p_{\mathrm{T}}$).

The measured cross section is 1.5 standard deviation higher than the lowest order calculation.

Bibliography

[1] NMC collaboration, P. Amaudruz *et al.* Phys. Lett. **B295**, 159 (1992).

[2] CCFR collaboration, A. O. Bazarko *et al.* NEVIS-1502, June 1994, 21pp. Submitted to Phys. Lett. **B**.

[3] H1 collaboration, T. Ahmed *et al.* Phys. Lett. **B299**, 385 (1993).

[4] ZEUS collaboration, M. Derrick *et al.* Phys. Lett. **B316**, 412 (1994).

[5] P. Amaudruz *et al.* Phys. Rev. Lett. **66**, 2712 (1991).

[6] J. Botts *et al.* Phys. Lett. **B304**, 159 (1993).

[7] S. A. Rabinowitz *et al.* Phys. Rev. Lett. **70**, 134 (1993).

[8] F. Bedeschi *et al.* Nucl. Instrum. Methods Phys. Res. Sect. **A268**, 50 (1988).

[9] B. Barnett *et al.* Nucl. Instrum. Methods Phys. Res. Sect. **A315**, 125(1992).

[10] F. Snider *et al.* Nucl. Instrum. Methods Phys. Res. Sect. **A268**, 75 (1988).

[11] L. Balka *et al.* Nucl. Instrum. Methods Phys. Res. Sect. **A267**, 272 (1988).

[12] S. Bertolucc *et al.* Nucl. Instrum. Methods Phys. Res. Sect. **A267**, 301 (1988).

[13] CDF collaboration, F. Abe *et al.* Nucl. Instrum. Methods Phys. Res. Sect. **A271**, 387 (1988).

[14] G. Foster *et al.* Nucl. Instrum. Methods Phys. Res. Sect. **A269**, 93 (1988).

[15] E710 collaboration, N. M. Amos *et al.*, Phys. Lett. **B243**, 158 (1990).

[16] S. Belforte *et al.*, CDF internal note. (to be published.)

[17] R. Brun *et al.*, GEANT3, Report No. CERN DD/EE/84-1.

[18] Particle Data Group, K. Hikasa *et al.* Phys. Rev. D**45**, S1 (1992).

[19] CDF Collaboration, F. Abe *et al.*, Phys. Rev. **D** 48, 2998(1993).

[20] CDF Collaboration, F. Abe *et al.* Fermilab Report No. Fermilab-PUB-92/01-E,1992.

[21] CDF Collaboration, F. Abe *et al.* Phys. Rev. **D40**, 3791 (1989).

[22] G. Hanson *et al.* Phys. Rev. Lett. **35**, 1609 (1975).

[23] T. Sjiöstrand *et al.* PYTHIA 5.6 and JETSET 7.3, Physics and JETSET Manual, CERN Preprint CERN-TH-6488/92.

[24] CDF Collaboration, F. Abe *et al.*, Submitted to Phys. Rev. Lett.

[25] H. Plothow-Besch, CERN-PPE, PDFLIB: User's Manual.

[26] P. Avery, K. Read, and G. Trahern, Cornell Internal Note CSN-212, Mar. 25, 1985 (unpublished).

[27] CDF collaboration, A. Abe *et al.* Phys. Rev. Lett. (To be submitted.)

[28] A. D. Martin, W. J. Stirling, and R. G. Roberts Phys. Lett. **B306**, 145 (1993).